



Quantum Phases of a Spin-1 Bose Gas in an Optical Lattice: A Focus on Mean Field and Perturbative Approaches

A THESIS SUBMITTED FOR THE AWARD OF THE
DEGREE OF DOCTOR OF PHILOSOPHY IN PHYSICS BY

SK NOOR NABI

Supervisor: Prof. Saurabh Basu



INDIAN INSTITUTE OF TECHNOLOGY GUWAHATI

DEPARTMENT OF PHYSICS

GUWAHATI-781039, ASSAM, INDIA

Guwahati, July 2018



The thesis investigates the ground state properties of a spin-1 ultracold Bose gas in an optical lattice. We have employed a spin-1 Bose Hubbard model (SBHM) which includes an additional spin dependent interaction potential due to the presence of the hyperfine degrees of freedom. The primary motivation is to explore various quantum phases, such as, Mott insulator (MI), superfluid (SF) and the density ordered phases in the SBHM for either sign (positive or negative) of the spin dependent interaction potential. The phase diagrams are obtained using a site decoupling mean field approximation (MFA) by considering the SBHM in presence of different types of the interaction potential. The formation of the singlet and nematic MI phases and their transition to the SF phase have been carefully scrutinized by analyzing the behaviour of the order parameter and the spin eigenvalues. All the numerical mean field phase diagrams are then compared with the analytical phase diagrams obtained by using a strong coupling perturbative expansion (PMFA) technique. The effects of an on-site random disorder in the SBHM results in a glassy phase, known as the Bose glass (BG) phase in addition to the MI and SF phases. The site inhomogeneities in the MFA is taken care of by defining an indicator which is the fraction of lattice sites having finite SF order parameter and non-integer occupation densities. The transition between these three phases shows a percolation phenomena similar to the statistical mechanics and the phase diagrams are obtained based on the appearance of the SF percolating cluster computed using Hoshen-Kopelman (HK) algorithm. Further, the inclusion of a synthetic and an external magnetic fields is found to be competing against each other on the formation of the spin singlet MI phase. The synthetic magnetic field tries to stabilize the insulating phase while the external magnetic field destabilizes the even MI lobes by suppressing the spin singlet pair formation. As a next, the inclusion of a long range density density extended interaction in the SBHM gives charge density wave (CDW) phase which appears in between the MI and the SF phases. A signature of the formation of the spin singlet and nematic CDW phases are observed at larger values of the extended interaction strength similar to the spin singlet and nematic MI phases. Apart from studying the SBHM in presence of two body interactions, we have extended our calculations up to multi-body, namely, three body interaction potential. The formation of the spin singlet-nematic and hence the odd-even asymmetry in the MI lobes is found to remain unaffected in presence of both the two and three body repulsive interaction strengths. Although such asymmetry in the MI lobes is absent and the higher order MI lobes except the first one stabilizes in case of a purely repulsive three body interaction strengths. An attractive three body interaction potential helps in stabilizing the third MI lobe and destroys the odd-even asymmetry in the

neighbouring even MI lobes. The first and third MI lobes show different orders of phase transition from the MI to the SF phase for higher values of the attractive three body strength.









Dedicated to my parents . . .



Acknowledgement

First and foremost, I would like to express my sincere gratitude to my research adviser, Prof. Saurabh Basu for giving me the opportunity to join in his research group. His intelligent ideas and constant guidance have helped me to complete my thesis work successfully well in time. He has always given me the complete freedom to choose whatever is right in order to finish my research work. Despite his own busy official responsibilities, he gave me time for discussion and all the encouragement I needed throughout all these years. The most important thing, I have tried to learn in these five years is his ability to represent things in a compact way. Finally, It has been a pleasure for me to work under his guidance.

I would like to thank the chairman of my doctoral committee Prof. Dilip Pal, doctoral committee members Dr. Debaprasad Maity, Dr. Sumana Dutta and Dr. Swati Bhattacharya for reviewing my progress every year and for their frank comments and valuable suggestions.

I sincerely acknowledge the help and assistance received from Prof. R. V. Pai, Prof. M. O. Oktel and Dr. O. Umucalilar during the early days of my Ph.D work.

I am thankful to all other faculty members and the HoDs of the Physics department for their friendly behaviour. I am grateful to Indian Institute of Technology Guwahati, and Government of India, Ministry of Human Resource Development for the financial support. I wish to thank Department of Physics, IIT Guwahati for providing me the necessary computational facilities. I thank all the technical assistants of the department of physics, especially Mr. Basab Bijoy Purkayastha, for their assistance in various ways during my research period.

I would like to thank my seniors Dr. Apurba Barman and Dr. Sudin Ganguly for their silent cooperation. I feel very fortunate to have Dr. Sudin Ganguly, sometimes we call him Dr. Cool, as a senior during my PhD period. I would also like to thank my other group members Priyadarshini, Sunayana, Priyanka and Shilpi for their cooperation and assistance.

I am thankful to my seniors, Dr. Jahir Ahmed, Dr. Ramesh Ghosh, Dr. Tapash Singha, Dr. Bappaditya Roy, Dr. Sk Obaidulla, Dr. Biswajit Karmakar, Dr. Kartik Sau, Dr. Amit Dutta Banik, Dr. Ashis Kundu and Dr. Koushik Pal for their help and support.

My special thanks go to Himangsu, Arnab, Kallol, Ramiz, Sourav, Abhijit and Anabil (Bhatnagar) with whom I have so much fun during last five years. I would also like to thank my lab members, Biplob, Sandeep, Subhadeep, Nawaz, Purusottam, Sheuly for maintaining a peaceful environment inside the lab.

I wish to thank all my friends from 2013 research batch, Prahlad, Ram, Pankaj, Bijita, Arun, Subhasish, Srikrishna (Kesta), Pulak, Deep, Srimoy, Sangkha, Susmita, Rajkumar, Camelia, Eshita, Pratap, Kajwal, Kamal and Krishnanjan for

their friendly behaviour and support.

I feel fortunate for having Dr. Sanjib Nayak, Somnath Layek and Raj Hossain as my best friends with whom I enjoyed so much fun, friendship and excitement. No word is enough to express their help and support during the last 10 years of my friendship.

I am also thankful to my M.Sc friends, Ayan, Moin, Arup, Suman, Indranil (the future P.M. of India), Raja and finally the man whom I admire so much, Roopam for the unlimited fun and friendship.

I am grateful to all my family members and particularly, my uncle, Eyar Mahammad for their love and encouragement during my entire academic career. Finally, I am deeply indebted to my parents, my sister, Jannat Ul Firdous and brother-in-law, Mehaboob Ali for their unconditional love and constant support throughout my endeavor. They always stood by me and their constant support makes what I am today.

Guwahati, July 2018

Sk Noor Nabi

Declaration

The work contained in the thesis entitled “Quantum phases of a spin-1 Bose gas in an optical lattice: A focus on mean field and perturbative approaches” has been carried out at the Department of Physics, Indian Institute of Technology Guwahati, India by me under the supervision of Prof. Saurabh Basu. The material of this thesis has not been submitted elsewhere for any other degree. Works presented in the thesis are all my own unless referenced to the contrary in the text.

The majority of this work has already been published in Ref.[144], Ref.[170], Ref.[189], Ref.[199] and has been included in this thesis with prior permission from the editorial office of the respective journal.

(Sk Noor Nabi)

July 2018

Department of Physics

Indian Institute of Technology Guwahati

Guwahati - 781039



Disclaimer

The bibliography included in this thesis is, by no means complete but contains the ones which are consulted thoroughly by me. I apologize for inadvertently missing out some of the research papers, review articles and other scientific documents pertaining to the focus of this thesis which should also have been cited. For illustration purpose some of the figures in this thesis are taken from other sources and properly cited.





Certificate

This is to certify that the work contained in the thesis entitled “Quantum phases of a spin-1 Bose gas in an optical lattice: A focus on mean field and perturbative approaches” by Mr. Sk Noor Nabi (Roll no.-136121007), a Ph.D. student of the Department of Physics, Indian Institute of Technology Guwahati is carried out under my supervision and has not been submitted elsewhere for the award of any other degree.

(Prof. Saurabh Basu)

July 2018

Department of Physics

Indian Institute of Technology Guwahati

Guwahati - 781039





List of Publications

Journal Articles:

1. *Percolation analysis of a disordered spinor Bose gas**¹,
Sk Noor Nabi and Saurabh Basu, J. Phys. B: At. Mol. Opt. Phys., **49**, 125301 (2016).
2. *Competition between external and synthetic magnetic fields on a spin-1 ultracold Bose gas**,
Sk Noor Nabi and Saurabh Basu, Europhysics Letters, **116**, 46001 (2016).
3. *Spin-1 Bose Hubbard Model with Nearest Neighbour Extended Interaction**,
Sk Noor Nabi and Saurabh Basu, Ann. Phys. (Berlin), **530**, 1700245 (2018).
4. *Quantum phases of a spin-1 ultracold Bose gas with three body interaction**,
Sk Noor Nabi and Saurabh Basu, Europhysics Letters **121**, 46002 (2018).
5. *Effects of an attractive three body interaction on a spin-1 Bose Hubbard model*,
Sk Noor Nabi and Saurabh Basu, arXiv:1806.11450, Annals of Physics (submitted).

Conference Proceedings:

1. *Disordered spin dependent interactions in a spinor ($S=1$) Bose gas: A percolation analysis*,
Sk Noor Nabi and Saurabh Basu, AIP Conference Proceedings, **1731**, 030015 (2016).
2. *Three body interaction effects on the phase diagram of spinor bosons*,
Sk Noor Nabi and Saurabh Basu, J. Phys.: Conf. Ser., **759**, 012034 (2016).
3. *Disorder, three body interaction and Bose glass phase in a spinor atomic gas in an optical lattice*,
Sk Noor Nabi and Saurabh Basu, J. Phys.: Conf. Ser., **759**, 0120345 (2016).
4. *Spin-1 Bose Hubbard model with three body interaction and magnetic field*,
Sk Noor Nabi and Saurabh Basu, AIP Conference Proceedings **1953**, 0040003 (2018).

Conference/School Attended:

1. **XXVII IUPAP International Conference on Computational Physics**, CCP2015,

¹* These journal articles are included in this thesis.

Dec 2-5 2015, I.I.T. Guwahati, Guwahati, Assam, India.

2. 60th Department of Atomic Energy-Solid State Physics Symposium, DAE-SSPS 2015, Dec 21-25 2015, Amity University, Noida, U.P, India.

3. 25th National Conference on Condensed Matter Physics, CMDAYS-2017, August 29-31 2017, Tezpur University, Tezpur, Assam, India.

4. 2nd International Conference on Concended Matter and Applied Physics, ICC-2017, November 24-25 2017, Govt. Engineering College, Bikaner, Rajastan, India.

5. International Conference on Recents Trends in Cold and Ultracold Matter, Ultracold 2018, March 27-29 2018, I.I.T. Guwahati, Guwahati, Assam, India.

5. International Conference on Quantum Dynamics of Disordered interacting Systems, SMR 3212, June 11-15 2018, The Abdus Salam International Centre for Theoretical Physics, Strada Costiera, 111-34151, Trieste, Italy.

6. SERB School on Frontiers on Quantum Optics, Dec 01-19 2017, I.I.T Guwahati, Guwahati, Assam, India.

Contents

Abstract	1
Acknowledgement	7
Declaration	9
Disclaimer	11
Certificate	13
Publication	15
1 Introduction	27
1.1 Bose Einstein condensation (BEC)	29
1.2 Optical lattice	31
1.2.1 Optical lattice potential	31
1.2.2 Laser cooling	33
1.2.3 Atom-atom interaction: Feshbach resonance	33
1.3 Ultracold atoms in optical lattices	35
1.3.1 Bose Hubbard model (BHM)	35
1.3.2 Superfluid to Mott insulator transition: QPT	37
1.4 Optical dipole trap (ODT)	38
1.5 Spin-1 Bose gas: An era of quantum magnetism	40
1.6 A comparison between spin-0 and spin-1 Bose gases	42
1.7 Various aspects of ultracold atoms in optical lattices	43
1.7.1 Disorder optical potential	43
1.7.2 Synthetic magnetic field	45
1.7.3 Dipole-dipole interaction	46
1.7.4 Multi-body interaction potential	48
2 Spin-1 Bose Hubbard model	53
2.1 Spin dependent interaction potential	53
2.2 Spin-1 Bose Hubbard model (SBHM)	54
2.3 SBHM in the atomic limit ($t = 0$)	57
2.4 Tools to solve SBHM	59
2.4.1 Single site mean field theory (SSMFT)	59
2.4.1.1 Ground state energy variation with occupation densities	61
2.4.1.2 Phase diagrams	62
2.4.1.3 Order parameter and variational energy behaviour	63

2.4.1.4 Spin eigenvalue and spin nematic order parameter . . .	64
2.4.2 Perturbative mean field approximation (PMFA)	66
2.4.3 Quantum Monte Carlo (QMC)	68
2.4.4 Density matrix renormalization group (DMRG)	69
2.4.5 Multi-site mean field theory (MMFT)	69
3 Percolation analysis of a disordered spinor Bose gas	73
3.1 Model	75
3.2 Results	76
3.2.1 Antiferromagnetic case ($U_2/U_0 = 0.1$)	76
3.2.1.1 The behavior of the SF order parameter and com- pressibility	77
3.2.1.2 Spin eigenvalue and spin nematic order parameter . . .	78
3.2.1.3 Indicator for the MI, BG and SF phases	79
3.2.1.4 Observation of the percolation phenomena	81
3.2.1.5 Percolation probability and finite size scaling	82
3.2.1.6 Phase diagrams	85
3.2.1.7 Phase diagram with disorder in spin dependent inter- action potential	85
3.2.2 Ferromagnetic case ($U_2/U_0 = -0.2$)	87
3.2.2.1 The behaviour of the order parameters and the indicator	87
3.2.2.2 Phase diagrams	88
3.3 Conclusions	89
4 Competition between synthetic and external magnetic field on a spin-1 ultracold Bose gas	91
4.1 Model	92
4.2 Results	95
4.2.1 Antiferromagnetic case	95
4.2.1.1 Phase diagrams	95
4.2.1.2 SF order parameter variation	98
4.2.1.3 Energy spectrum and magnetization	99
4.2.2 Ferromagnetic case	101
4.3 Conclusion	102
5 Spin-1 Bose Hubbard model with nearest neighbour extended interac- tion	105
5.1 Model	107
5.2 Results	108
5.2.1 Antiferromagnetic case	108
5.2.1.1 MFA phase diagrams	108

5.2.1.2 SF order parameter and occupation density variation	111
5.2.1.3 Spin eigenvalue behaviour	112
5.2.1.4 PMFA phase diagrams	114
5.2.1.5 Effects of harmonic trapping potential	115
5.2.2 Ferromagnetic case	118
5.3 Conclusion	120
6 Quantum phases of a spin-1 ultracold Bose gas with three body interaction potential	123
6.1 Model	124
6.2 Results	125
6.2.1 Antiferromagnetic case	125
6.2.1.1 MI lobes width in the atomic limit with ($W > 0$)	125
6.2.1.2 MFA phase diagrams ($W > 0$)	127
6.2.1.3 Spin population fraction and spin eigenvalue ($W > 0$)	130
6.2.1.4 PMFA phase diagrams ($W > 0$)	132
6.2.1.5 Phase diagrams for attractive three body interaction ($W < 0$)	133
6.2.1.6 Phase diagrams for purely three body interaction ($U_0 = U_2 = 0$)	134
6.2.2 Ferromagnetic case	135
6.3 Conclusion	135
7 Effects of an attractive three body interaction on a spin-1 Bose Hubbard model	137
7.1 Model	138
7.2 Results	139
7.2.1 Antiferromagnetic case	139
7.2.1.1 MI lobes in the atomic limit	139
7.2.1.2 MFA phase diagrams	141
7.2.1.3 Spin eigenvalue and spin nematic order parameter	142
7.2.1.4 PMFA phase diagrams	144
7.2.1.5 Phase diagram for $U_3 = -1.4U_0$	145
7.2.2 Ferromagnetic case	147
7.3 Conclusion	147
8 Conclusions	149
Appendices	153
A Matrix elements and the PMFA calculation	155

B Derivation of the repulsive three body interaction potential	159
Bibliography	173
Vita	175



List of Figures

1.1	Experimental realization of a Bose-Einstein condensate	31
1.2	3D optical lattice potential	32
1.3	Scattering length variation in a magnetically tuned Feshbach resonance	34
1.4	Phase diagram of a spin-0 BHM in a homogeneous case	36
1.5	Absorption images of multiple matter wave interference pattern for different potential depths	38
1.6	Laser detuning of an optical dipole trap	40
1.7	Spin-1 BEC of a ^{23}Na atom using optical dipole trap	41
1.8	Transverse and longitudinal magnetization of a ^{87}Rb spinor condensate in an external Zeeman field	41
1.9	A synthetic dimension of a spinor Bose gas by coupling different hyperfine levels.	42
1.10	Appearances of a BG phase in between MI and SF phases and a disordered optical lattice potential.	45
1.11	Synthetic magnetic field of a spin-1 BEC of ^{87}Rb atoms	46
1.12	The dipolar interaction potential between two interacting dipoles	47
1.13	Multi-body interactions under variable lattice potential depth	48
2.1	The MI lobe widths in the atomic limit ($t = 0$)	59
2.2	The decoupling of hopping term in a single site mean field theory	60
2.3	The ground state energy variation with occupation densities, n	62
2.4	Mean field phase diagrams corresponding to the AF and ferromagnetic cases.	63
2.5	The SF order parameter and variational energy behaviour in the AF case for the odd and even MI lobes.	64
2.6	The spin eigenvalue and spin nematic order parameter for the odd and even MI lobes in the AF case.	65
2.7	The PMFA phase diagram corresponding to the AF case with $U_2/U_0 = 0.05$	67
2.8	The QMC phase diagram corresponding to the AF case with $U_2/U_0 = 0.1$	68
2.9	The DMRG phase diagram corresponding to the AF case with $U_2/U_0 = 0.1$	69
2.10	The decoupling of hopping term in a 2-site mean field theory	70
2.11	The phase diagram in 2-site MFT in the AF case with $U_2/U_0 = 0.1$	71
3.1	The probability distribution of the on-site disorder potential	75

3.2	The variation of averaged SF order parameter and compressibility in the AF with disorder strengths.	77
3.3	Spin eigenvalue and spin nematic order parameter variation in the antiferromagnetic case with disorder strengths	79
3.4	The variation of the indicator, χ in the antiferromagnetic case	80
3.5	The real space plots of the occupation densities, ρ_i for lattice size $L \times L = 50 \times 50$ at $\Delta/U_0 = 0.5$ with $U_2/U_0 = +0.1$	81
3.6	The percolation probability, P_{perc} and the mean cluster size, M_{cs}	83
3.7	The percolation probability, P_{perc} corresponding to different lattice sizes, L	84
3.8	The phase diagrams in the AF case with different disorder strengths	86
3.9	The phase diagram in the AF case with disorder in spin dependent interaction potential	87
3.10	The variation of order parameters and the indicator in the ferromagnetic case	88
3.11	The Phase diagrams for the ferromagnetic case with disorder	88
4.1	The phase diagrams in AF case for different values of ϕ corresponding to $B_s = B_e$	96
4.2	Phase diagrams in AF case for different values of ϕ corresponding to $B_s > B_e$	97
4.3	Color map of SF order parameter, ψ_q with ϕ is shown near the MI-SF transition point.	98
4.4	The one dimensional behaviour of ψ_l in AF case corresponding to the odd and the even MI lobes with ϕ	99
4.5	The energy spectrum in the AF case for complete range of ϕ for odd and even MI lobes.	100
4.6	The site averaged transverse and longitudinal magnetization in the AF case with ϕ for the odd and the even MI lobes.	100
4.7	Phase diagram for different values of ϕ and the energy spectrum in the ferromagnetic case	101
5.1	The phase diagrams in the AF case for different values of zV/U_0	109
5.2	The one dimensional behaviour of order parameters and ground state energy in AF case for different values of zV/U_0	111
5.3	The one dimensional behaviour of the spin eigenvalues in the AF case with zV/U_0	113
5.4	Relative spin eigenvalues in the AF case for $zV/U_0 = 1.7$	113
5.5	The variation of occupation density and the order parameter in the AF case with $zV/U_0 = 0.7$ and trapping potential, $V_T = 0.0002$	116

5.6	The variation of $\langle S_i^2 \rangle$ in the AF case with $zV/U_0 = 0.7$ and trapping potential, $V_T = 0.0002$	117
5.7	Magnitude of the Fourier transform of ψ_i , ρ_i and S_i^2 with k_x in SF, SS and CDW phases for AF case.	118
5.8	Phase diagrams in the ferromagnetic case with zV/U_0 for $U_2/U_0 = -0.04$	119
6.1	The width of the MI lobes in the atomic limit in AF case with repulsive three body interaction strength.	127
6.2	The phase diagrams from MFA and PMFA for $U_2/U_0 = 0.05$ with repulsive three body interaction potential.	128
6.3	The MFA and PMFA phase diagrams with W/U_0 for higher values of spin dependent interaction strength, $U_2/U_0 = 0.3$	129
6.4	The spin population fraction, N_σ/N and the total spin eigenvalue, $\langle S^2 \rangle$ in the AF case with W/U_0 in the MI lobes.	131
6.5	The MFA phase diagram for an attractive three body interaction strength, $W/U_0 = -0.1$ with $U_2/U_0 = 0.05$	133
6.6	The phase diagram in the AF case for a purely repulsive three body spin dependent interaction strength.	134
6.7	The MFA and PMFA phase diagrams in the ferromagnetic case with repulsive three body interaction strength.	135
7.1	MI lobe widths in the atomic limit in AF case for attractive three body interaction potential.	140
7.2	Phase diagrams from MFA and PMFA for $U_2/U_0 = 0.05$ with attractive three body interaction potential.	141
7.3	The population fraction, N_σ/N in the AF case with U_3/U_0 for the MI lobes.	142
7.4	The total spin eigenvalue and the spin nematic order parameter in the AF case corresponding to the even MI lobes for $U_3/U_0 = -0.5$. .	143
7.5	The total spin eigenvalue and the spin nematic order parameter in the AF case corresponding to the odd MI lobes for $U_3/U_0 = -1.4$. .	144
7.6	Variational energy behaviour in the AF case for attractive three body interaction strength, $U_3/U_0 = -1.4$	146
7.7	The detailed mean field phase diagram depicting the first and second order transition for $U_2/U_0 = 0.05$ corresponding to $U_3/U_0 = -1.4$. .	146
7.8	The MFA and PMFA phase diagrams in the ferromagnetic case with attractive three body interaction strength.	147



List of Tables

1.1	A comparison between the spin-0 and the spin-1 Bose gases	43
1.2	Magnetic dipole moment of various species where μ_B : Bohr magneton. Source Lahaye <i>et al.</i> [96].	47
2.1	Nature of on-site spin independent and dependent interaction potentials for ^{23}Na and ^{87}Rb atoms.	56
2.2	Different possible combinations between n_σ with $n = n_+ + n_0 + n_-$ for $n = 1$ which gives the matrix dimension, $D = 4$	61
2.3	The matrix dimension of the mean field Hamiltonian with n in MSMFT.	71
3.1	The transition points for the MI-BG and BG-SF phases obtained from χ and P_{perc} for both the AF and the ferromagnetic cases.	90





Chapter 1: Introduction

Understanding phase transitions from a theoretical as well as an experimental perspective even now covers a major research area in condensed matter physics. For example, consider the phase transition of an Ising ferromagnet as a function of temperature and an applied magnetic field. Below a critical temperature T_c , the system shows a discontinuous transition from a state of positive magnetization, commonly known as "spin-up" to a state of negative magnetization, that is "spin down" owing to the variation of the applied magnetic field. However, in the other case, by changing the temperature at zero magnetic field, the magnetization shows a continuous transition at a critical point given by, $T = T_c$. The discontinuous variation in the order parameter, such as, the magnetization or the latent heat (in liquid to vapour transition) is a signature of first order phase transition where the correlation length of the system is finite. While the continuous variation of order parameter signifies a second order phase transition and leads to the divergence of the correlation length in the vicinity of the critical point.

All these phase transitions are driven by the thermodynamic fluctuations where the system migrates from an ordered phase to a disordered phase, and they immediately raise concern whether there will be any phase transition if one continues to decrease the temperature and approaches absolute zero, that is, $T \rightarrow 0$? As soon as one approaches $T \rightarrow 0$, although all the thermodynamic fluctuations will be frozen, but the fluctuations, that persist owing to the Heisenberg's uncertainty principle are going to be responsible for a new kind of phase transition, known as the quantum phase transition (QPT) [1, 2].

Study of QPT in the context of different systems has gained much momentum following the success of attaining extremely low temperature near nanokelvin, (nK) using laser cooling technique [3–6] and subsequently the successful observation of Bose-Einstein condensation (BEC) in dilute atomic gases [7–9]. The BEC was first theoretically predicted in 1925 by A. Einstein who first extend the idea of photon statistics, put forward by S. N Bose to identical particles with integral degrees of freedom [10]. At extremely low temperatures, all the identical particles that obey the BE statistics can microscopically occupy the ground state of the system and thus behaves as a collective matter wave which is known as a BEC. Although predicted theoretically, observing BEC experimentally was out of imagination due to the constraints in reaching such extremely low temperatures. However an intense research from the atomic, optical and condensed matter physics community finally made it possible to reach such ultra low temperatures of the order of nK , using, among other techniques, laser and evaporative cooling.

Besides, the confinement of the constituent particles of the atomic gas can be achieved by using a periodic optical lattice potential [2]. A smooth crossover

from a weakly interacting region to a strongly interacting region can be achieved by changing the optical lattice potential parameters, which in turn can control the inter-atomic interactions [1, 2]. Also, the inter-atomic interaction potential which arises due to a scattering phenomena can be controlled using a Feshbach resonance [11]. Owing to such exquisite control over various experimental parameters, ultracold atoms in optical lattices nowadays act as a quantum simulator and thus provide a new insight in exploring quantum many body phenomena.

Such breakthrough in achieving ultra low temperatures immediately resulted in successful observation of BEC using dilute, weakly interacting atomic gases which shows a coherent superfluid (SF) behaviour, independently by two groups led by E. A Cornell [7] and W. Ketterle [9] after 70 years of its theoretical prediction. Although a BEC was experimentally realized, but one may ask how such coherent behaviour is relevant to the study of quantum phase transition in many body systems that host complicated interactions. In 1998, Jacksh *et al.* showed that the ultracold atoms cooled and trapped in an optical lattice can be described by a Bose-Hubbard model (BHM) that will act as an ideal platform to explore the many body phenomena in strongly correlated systems [1]. They predicted that by tuning the system parameters, such as the hopping and the interaction potential of the Hamiltonian, one can easily go from a state of coherent superfluid to an insulating phase, commonly known as Mott insulating (MI) phase. Following the proposal by Jacksh *et al.*, Griener *et al.* in 2002 designed an experiment by magnetically trapping ^{87}Rb atoms in an optical lattice and hence experimentally observe the SF to the MI transition by controlling the optical lattice potential [2].

In experiments, the cooling and trapping of ultracold atoms in optical lattice involve the magneto-optical trap (MOT) [4, 12] as well as a purely optical dipole trap [12–15] techniques. Although the neutral alkali atoms trapped by the MOT successfully shows the quantum phase transition, however such trapping technique suffers from the following drawback. For an atomic Bose gas, each atom can have multiple degrees of freedom, such as the hyperfine degrees of freedom, F which is the sum of the nuclear spin, I in addition to the electron spin, J that is, $F = I + J$ [16]. In MOT, the atoms are polarized in a single magnetic sublevel and thus it freezes all the hyperfine degrees of freedom and yields a spin-0 or a scalar Bose gas. With technological breakthrough, such limitation of MOT was removed by the invent of optical dipole trap where the interaction between the electric field of the laser beams and the dipole force of neutral atoms help in retaining all the hyperfine spin degrees of freedom. Thus these systems can be treated as spinor Bose gases [17, 18].

In 1998, following such proposal, the MIT group experimentally observed spin-1 ($F = 1$) condensates by optically trapping all of $(2F + 1)$ magnetic sublevels of ^{23}Na atoms which has a nuclear spin, $I = 3/2$ using optical dipole trap [16, 19–21].

Such observation of spinor condensates shows a unique characteristic which have no analogue with the scalar Bose gas, and thus opens up a new possibilities in the study of quantum magnetism using spin-1 ultracold Bose gases.

The presence of spin degrees of freedom yields an additional spin dependent interaction potential, (U_2) which determines the ground state properties of a spin-1 Bose gas. The theoretical description of a spin-1 BEC was first illustrated by Ho and Machida by generalizing the Gross-Pitaevskii equation in the low energy limit [17, 18]. They showed that unlike the scalar Bose gas, the SF order parameter of a spinor gas is a vector quantity comprising of $(2F + 1)$ spinor components. Also these hyperfine components can transform to each other in the spin space through spin-gauge rotational symmetry and thus show different spin textures as well as topological excitations [17, 18, 22, 23].

After such a prediction, an intense theoretical research has ensued to explore and understand various exotic phases along with the SF and the MI phases of a spin-1 Bose gas in an optical lattice using an extended Bose Hubbard model induced by an additional spin dependent interaction [17, 18, 24–31]. For positive value of the spin dependent interaction, the ground state of a spin-1 BHM (SBHM) consists of a spin singlet phase corresponding to even occupation densities, and a spin nematic phase with odd occupation densities [24–34]. Besides the spin singlet and nematic MI phases, a fractionalized phase that breaks both the charge and spin symmetries [27] and a dimerized phase [28, 34–36] have been studied.

Also the SF phase of a spinor Bose gas can be a polar phase, such as, a longitudinal polar (LP) and a transverse polar (TP), and as well as a broken axis symmetry phase has been identified in presence of an external magnetic field [37–43]. Moreover, the use of hyperfine degrees of freedom of spinor Bose gas as a short lattice dimension known as synthetic dimension generates a spin-orbit coupled (SOC) state that gives rise to various density ordered SF phases such as charge density or spin density wave phases [44–50].

The presence of such rich ground state properties and hence the existence of various quantum phases motivate us to study the spin-1 ultracold Bose gas in optical lattices using the mean field approach (MFA) and a strong coupling perturbative mean field approximation (PMFA).

1.1 Bose Einstein condensation (BEC)

The physics of non-interacting distinguishable particles is described by the Maxwell-Boltzmann (MB) statistics which applies at high temperature or low particle density region in order to minimize the quantum effects. The average particle

distribution, n_i^{MB} over an energy state, ϵ_i with degeneracy, g_i is given by,

$$n_i^{MB} = \frac{g_i}{e^{(\epsilon_i - \mu)/k_B T}} \quad 1.1$$

where k_B is the Boltzmann constant, μ is the chemical potential and T is the temperature of the system.

As the temperature is continuously lowered towards absolute zero, the quantum nature of the particle starts to dominate due the Heisenberg's uncertainty principle and hence they are described in terms of their atomic wave functions. In the quantum region, particles are indistinguishable and they are broadly divided into two categories based on their internal degrees of freedom. Particles with integral degrees of freedom whose wave functions are symmetric obey the Bose Einstein (BE) statistics, while for half integral degrees of freedom whose wave functions are anti-symmetric obey the Fermi Dirac (FD) statistics. The average particle distribution corresponding to the BE and FD statistics are given by,

$$n_i^{BE/FD} = \frac{g_i}{e^{(\epsilon_i - \mu)/k_B T} \mp 1} \quad 1.2$$

where "-" is for BE statistics [10] and "+" in the denominator is for FD statistics [51].

In room temperature, the thermal de Broglie wavelength, $\lambda_{DB} = \frac{h}{\sqrt{2\pi m k_B T}}$ of an atom is much smaller than the size of the atom or the mean interparticle separation. As the atoms are cooled enough below the critical temperature, then λ_{DB} becomes comparable or larger than the interparticle separation between the atoms. In this scenario, the atomic wave functions begin to overlap with each other and become degenerate by losing their identity. Thus a Bose Einstein condensation (BEC) occurs where all the identical atoms microscopically occupy the lowest energy levels and behaves as a single quantum state. The critical temperature, T_c at which a transition from a thermal state to BEC happens depend upon the phase space density as [52],

$$T_c = \frac{h}{2\pi k_B m} \left[\frac{n}{\xi(3/2)} \right]^{2/3} \quad 1.3$$

where $\xi(3/2) \approx 2.61$ is the Riemann Zeta function [53] and the temperature, T_c is known as quantum degeneracy temperature.

The average particle density of an atomic BEC is of the order of $10^{13}/cm^3$ which is much lower than the molecular density of air ($10^{19}/cm^3$) at room temperature implies that $T_c \geq 100nK$ and requires very sophisticated cooling and trapping techniques. Using laser and evaporative cooling, the macroscopic matter wave coherence properties of a BEC was experimentally observed in dilute atomic gases

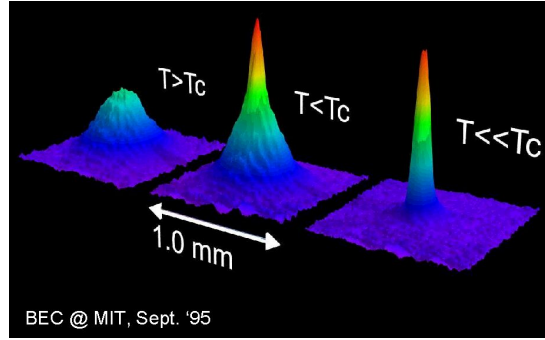


Figure 1.1: *Experimental realization of a Bose-Einstein condensate. From left to right, the momentum distribution in the gas is shown for three different decreasing temperatures. In the left, above the critical temperature and right one is far below the critical temperature. The middle one is just below the critical temperature. The peaks denote a macroscopic accumulation of particles corresponding to $\mathbf{k} = 0$ state. Figure courtesy of W. Ketterle et al., MIT [9].*

in 1995 independently by Cornell, Wiemann at JILA using Rubidium atoms [7] and Ketterle at MIT using a sodium vapor [9] [Fig. 1.1]. Thus the ground state of a non-interacting BEC at zero temperature is essentially a superfluid phase and the many body ground state for N particles is the product of single particle ground state $\psi(\mathbf{x})$ written as [54],

$$\Psi_N(\mathbf{x}_1, \mathbf{x}_1, \dots, \mathbf{x}_N) = \prod_{i=1}^N \psi(\mathbf{x}_i) \quad 1.4$$

For large particle numbers, N , the BEC can be characterized by a macroscopic wave function or order parameter, $\phi(\mathbf{x}) = \sqrt{N}\psi(\mathbf{x})$ and the particle density, $n(\mathbf{x}) = |\phi(\mathbf{x})|^2$. However, for interacting Bose gas, the many body ground state in the system results a non linear term in the order parameter and such an interacting BEC in optical lattices is described by a mean field Gross Pitaevskii equation (GPE) [55, 56].

1.2 Optical lattice

1.2.1 Optical lattice potential

The understanding of correlated many body phenomena in usual solid state physics are extremely difficult due to the complicated band structure, complexity in Coulomb interactions between the constituent particles, the presence of disorder and impurities etc. Sometimes it is quite impossible to take care of all the underlying consequences in a single theoretical model and often hard to gauge out the relevance of a particular effect while synthesizing the outcome of an ex-

periment. An alternate way to bypass such restrictions is to use of an artificial, known as optical lattice potential [2] and thus provides a gateway to explore the phenomena at the interface of solid state physics and (ultracold) atomic physics.

An optical lattice is formed due to the interference of counter propagating laser beams from all directions that renders a periodic potential which replicates lattice structures as perceived by an electron in a real crystal. To create a one dimensional optical lattice potential, consider two counter propagating laser beams each of amplitude E_0 , and linearly polarized in the x -direction with wave vector $\mathbf{k} = (\pm k, 0, 0)$ then the resultant electric field is written as,

$$\mathbf{E}(x) = E_0 \hat{e}_z [e^{ikx} + e^{-ikx}] \quad 1.5$$

The field intensity is given by,

$$I(x) = |\mathbf{E}(x)|^2 = 4|E_0|^2 \cos^2(kx) \quad 1.6$$

Thus the optical lattice potential becomes,

$$V_{op}(x) = V_0 \cos^2(kx) \quad 1.7$$

where V_0 is the depth of the optical lattice and the lattice periodicity, $a = \pi/2$. Using further two pair of laser beams in y and z direction, a three dimensional optical lattice potential is formed as shown in [Fig.1.2] [2],

$$V_{op}(\mathbf{r}) = V_{0x} \cos^2(kx) + V_{0y} \cos^2(ky) + V_{0z} \cos^2(kz) \quad 1.8$$

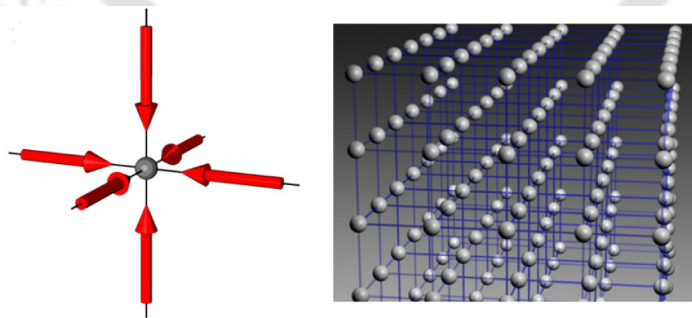


Figure 1.2: A 3-dimensional optical lattice potential is formed by superimposing three orthogonal standing waves. In the 3D case, the optical lattice can be approximated by a 3D simple cubic array of tightly confining harmonic oscillator potentials at each lattice site. Figure courtesy of I. Bloch [57].

The height of the optical lattice potential, V_{0i} is often expressed in terms of recoil energy via $E_R = \hbar^2 k^2 / 2m$. The superiority of the optical lattice potential

originates from the vast control of the lattice parameters as well as the potential height by smoothly calibrating only the laser intensity. More so, it is free from defects, impurities and lattice vibrations etc. Thus the tunability of different parameters that are agents of the phase transition yields an edge over experiments performed in the context of usual condensed matter physics.

1.2.2 Laser cooling

An optical lattice allows the neutral atoms to cool down at extremely low temperature using various cooling mechanism such as laser cooling [3–6], evaporative cooling [58] techniques etc. Thermal velocity of an atom is directly related with the temperature and hence slowing down their motion will help in decreasing the temperature. The central idea of laser cooling is to decelerate an atom by using a radiation (or scattering) pressure of a laser light near atomic resonance. In this process, an atom in the ground state absorbs a photon from an incident laser beam. After absorbing a photon of energy $h\nu$, the atom acquires a momentum impulse of $h\nu/c$ along the incoming direction. In order to absorb a photon again, the atom has to return to the ground state by emitting a photon. After emitting a photon, the atom recoils in the opposite direction which results in their slowing down for a span of few microseconds, a phenomenon responsible for the origin of "optical molasses" [3] and subsequently producing low temperature. Apart from the laser cooling, few other techniques such as polarization gradient cooling [59], Raman cooling [59], Sisyphus cooling [4, 6, 60] etc have been developed to reach ultralow temperatures.

1.2.3 Atom-atom interaction: Feshbach resonance

In optical lattices, experimental navigation from a weak to a strong interaction region is possible by simply changing the optical lattice potential. However, without disturbing the lattice geometry so much, a strong interaction region can be achieved by controlling the atom-atom interaction using a Feshbach resonance [11, 54] which in turn determine the on-site interaction potential. For ultracold gases at extremely low temperature, the two body interaction potential is essentially short range in nature and hence entirely depends upon the s -wave scattering length, a_s . The Feshbach resonance was first introduced in the context of nuclear physics which was later extended for ultracold atomic gases to tune the scattering lengths via magnetic field.

Apart from the Feshbach resonance, few other resonances such as a 'shape resonance' which occurs in a potential barrier where the scattering cross section is a function of the angular momentum and a 'potential resonance' that happens in a single channel where the s -wave phenomena is dominant [61]. Unlike shape and

potential resonances, a Feshbach resonance involves two particle collision process between multi channels and hence occurs when a bound state in a closed channel resonantly coupled with the scattering state of an entrance or open channel [11, 54]. Here the open and the closed channels correspond to the two different spin configurations of the molecule. Further by simply changing the magnetic field, the energy difference and hence the interaction potential can be controlled over a wide range of values. Instead of a magnetically induced resonance, a Feshbach resonance can be obtained by inducing an optical transition by detuning the light from the atomic resonance [11]. In a magnetically tuned Feshbach resonance, the s -wave atomic scattering length, a_s is now a function of the magnetic field, B as [62],

$$a_s(B) = a_{bg}(1 - \Delta/B - B_0) \quad 1.9$$

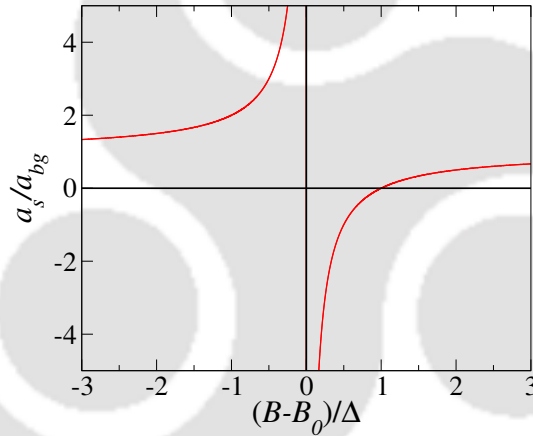


Figure 1.3: The variation of the scattering length, a_s/a_{bg} in a magnetically tuned Feshbach resonance. Figure courtesy of Chin et al. [11].

Here a_{bg} is the background scattering length as a result of the background collision in the open channel represents an off-resonant value. B_0 is the resonance field at which scattering length diverges ($a \rightarrow \pm\infty$) and Δ is called resonance width over which the scattering length changes sign. Fig. 1.3 shows a schematic plot of the atomic scattering length as a function of magnetic field, B . Both a and a_{bg} can have positive as well as negative values which implies a repulsive and an attractive interactions respectively can be realized for the cold atoms. Such tunability of the interaction by using Feshbach resonances have resulted in successful observation of BEC [63], physics of the BEC-BCS crossover [64], and the existence of Efimov states [65] etc.

1.3 Ultracold atoms in optical lattices

1.3.1 Bose Hubbard model (BHM)

In 1963, J. Hubbard introduced a simple Hamiltonian, commonly known as Fermi-Hubbard model to describe the electronic structure of strongly correlated systems which also aided in understanding of high-temperature superconductivity to a certain extent [66]. In 1989, Fisher *et al.* [67] first extended the idea of a Fermi Hubbard model for correlated bosonic system in a lattice, leading to the birth of the Bose Hubbard model (BHM) to study the Mott insulator (MI) and the superfluid (SF) phases. Later, in 1998, Jacksh *et al.* showed that, ultracold atoms cooled and trapped in optical lattices can also be mapped into similar BHM consisting of a hopping term as well as an on-site interaction potential [1].

The BHM in the second quantized form is written as [1],

$$H = -t \sum_{\langle ij \rangle} (a_i^\dagger a_j + h.c.) + \frac{U_0}{2} \sum_i n_i(n_i - 1) - \sum_i (\mu - \epsilon_i) n_i \quad 1.10$$

The first term is the hopping term where $\langle \ \rangle$ denotes the two nearest neighbour sites of a lattice and t is the hopping amplitude from site i to j . The operator a_i^\dagger (a_i) is the boson creation (annihilation) operator at site i . The second term includes the two body on-site interaction potential, U_0 and the number operator is $n_i = a_i^\dagger a_i$. μ is the chemical potential which controls the particle number of the system and ϵ_i is the on-site energy which can be an external confining potential or a random disorder potential etc. The parameters, t as well as U_0 of the Hamiltonian are related to the optical lattice as,

$$t = - \int d^3x w^*(\mathbf{x} - \mathbf{x}_i) \left[-\frac{\hbar^2}{2m} \nabla^2 + V_{op}(\mathbf{x}) \right] w(\mathbf{x} - \mathbf{x}_j)$$

$$U_0 = \frac{4\pi\alpha_0\hbar^2}{m} \int d^3x |w(\mathbf{x})|^4. \quad 1.11$$

where $V_{op}(\mathbf{x})$ is the optical lattice potential, α_0 being the s-wave scattering length and $w(\mathbf{x})$ is the Wannier orbital of the lowest vibrational band localized at the origin.

The ground state of a BHM can be a SF or a MI phase depending upon the competition between the system parameters, such as the hopping (t) and the on-site interaction potential (U_0). It is therefore necessary to gather more familiarity on different quantum phases of the ultracold Bose gases corresponding to both the weak as well as strong interaction limits.

A SF phase is observed in the limit of vanishing interaction strength, that is, when the kinetic energy is overwhelmingly larger than the interaction potential

strength ($t \gg U_0$). In the non interacting limit ($U_0 = 0$), the many body ground state is essentially a BEC where all the atoms occupy identical Bloch states with zero momentum ($\mathbf{k} = 0$) in the lowest band which is essentially a superfluid phase. Since the hopping strength is dominant which is responsible for delocalizing the atoms across the lattice sites and thus a quantum correlation in atom numbers is negligible. Under this condition, the system can be described by a giant wave function and subsequently, the many body ground state for N atoms is just the sum over all the Bloch states as [54],

$$|\Psi\rangle_{U_0=0} \propto \left(\sum_i a_i^\dagger \right)^N |0\rangle \quad 1.12$$

An MI phase on the other hand is observed when the on-site interaction potential dominates over the tunneling amplitude ($U_0 \gg t$). In the strong interacting limit, atoms tend to localize across the lattice site and remain so as long as the hopping amplitude remains below the on-site potential and hence a perfect correlation in atom numbers exist. Thus in the MI phase, the many body ground state is a product of local Fock state with fixed numbers of atoms (n) per lattice site is given by [54],

$$|\Psi\rangle_{t=0} \propto \prod_i \left(a_i^\dagger \right)^n |0\rangle \quad 1.13$$

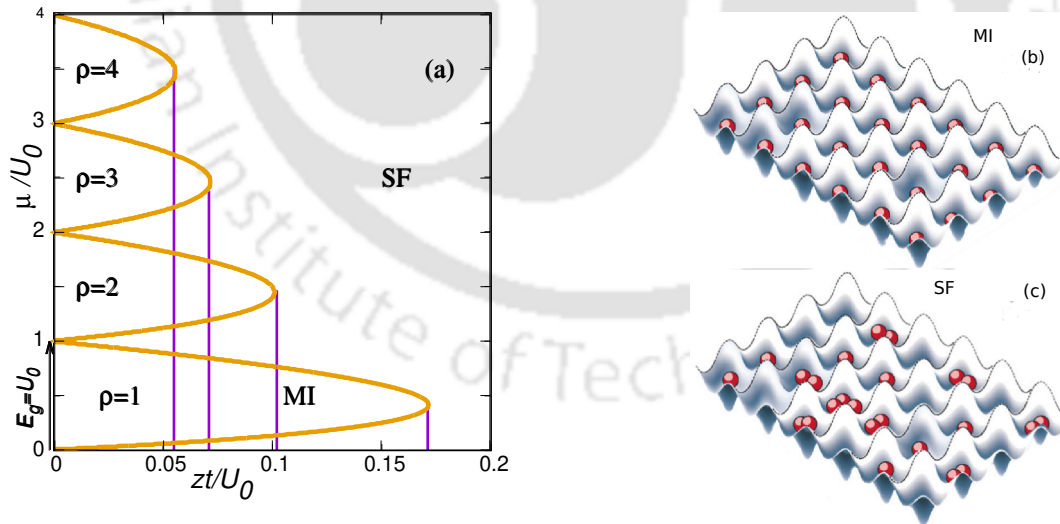


Figure 1.4: The zero temperature phase diagram of a homogeneous BHM in (a). The lobes indicate MI phase with occupation densities, ρ . The vertical line corresponds to the critical tunneling strength, $z t_c / U_0$ from the MI to SF phase. Pictorial representations of the occupation densities in the MI lobe ($\rho = 1$) in (b) and in the SF phase in (c) of bosons on an optical lattice. Figure courtesy of Markus Greiner [12].

The zero temperature phase diagram of a homogeneous BHM in the μ/U_0 - $z t / U_0$

plane which schematically shows the MI and SF phases is presented in Fig1.4 (a). Here z is the coordination number which is related with the lattice dimension, d as $z = 2d$. At smaller values of zt/U_0 , each lobe denotes a Mott insulating phase with integer occupation densities per lattice site, that is $\rho = 1, 2, \dots$ due to localization [Fig1.4 (b)]. The compressibility, $\kappa = \partial\rho/\partial\mu$ vanishes inside the MI lobes implying that the MI phase is an incompressible phase. Also, there exists an energy gap ($E_g = U_0$) in the particle-hole excitation spectrum and it is equal to the on-site interaction potential, U_0 at zero hopping limit ($t = 0$). As soon as the tunneling strength is increased, the system will remain in the MI phase below a certain critical value, zt_c/U_0 since the kinetic energy required for an atom to hop from one site to another is still insufficient to overcome the potential energy cost. Further increase in hopping amplitude above this critical value will push the system to undergo a phase transition to an SF phase which corresponds to a non-integer number of bosons per lattice site that is $\rho \neq 1, 2, \dots$ due to delocalization and hence shows finite compressibility Fig1.4 (c). The point in the vicinity of the two MI lobes with $\rho = n$ and $\rho = n + 1$ is degenerate along the vertical axis (μ) and corresponds to the SF phase. Thus a quantum phase transition from a gapped, incompressible MI phase is accompanied to a gapless, compressible SF phase with the existence of finite values for the off-diagonal long range order. The mean field calculation shows that the tunneling strength, zt/U_0 for the MI-SF phase transition now depends on the occupation density of the MI lobes, n and lattice dimension, d as [68]

$$\frac{1}{zt} = \left[\frac{n+1}{nU_0 - \mu} - \frac{n}{(n-1)U_0 - \mu} \right] \quad 1.14$$

1.3.2 Superfluid to Mott insulator transition: QPT

After such theoretical prediction by Jacksh *et al.*, the first experimental signature of the quantum phase transition involving the SF and MI phases was demonstrated by Greiner *et al.* by loading ^{87}Rb atoms from a BEC into a three-dimensional optical lattice potential using a magneto optical trap (MOT) [2]. They recorded the absorption spectra via a 'Time of flight (TOF)' experiment, a commonly used method for a system of cold atoms loaded in optical lattices [54]. In TOF, the system is initially prepared in a BEC state and trapped by using a confining potential. Later, all the trapping as well as optical lattice potentials are suddenly turned off to allow the atoms to expand for a certain interval of time, τ . After such expansion, the wave packets associated with the atoms confined at each lattice site grow and start to overlap with each other giving rise to the interference pattern in the momentum space. The absorption image in Fig.1.5 corresponding to different optical lattice potential, V_0 shows a SF-MI phase transition. In absence of lattice potential, a sharp absorption spectra, which corresponds to a construc-

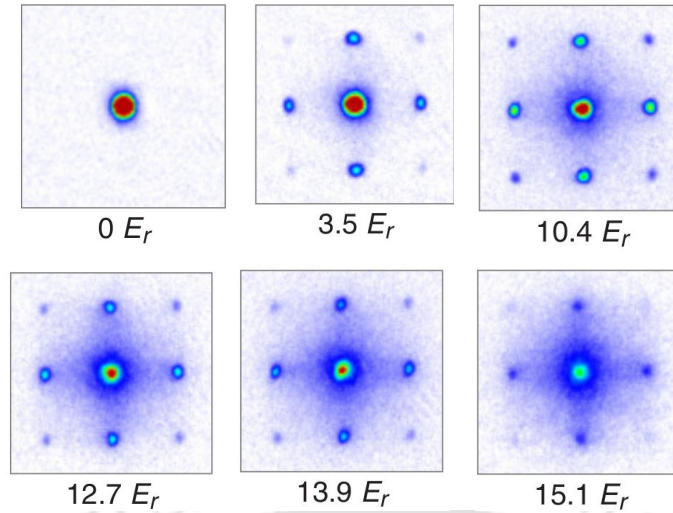


Figure 1.5: Absorption images of multiple matter wave interference pattern for different potential depths, after a time of flight period of 15 ms. In the superfluid regime for potential depth, $V_0 = 0$, a sharp peak in the interference pattern is observed and such trend is visible up to about $V_0 = 12E_r$. For a potential depth, $V_0 \geq 13E_r$, such interference peaks are gradually diminishing indicating a transition to the Mott insulator phase. Figure courtesy of Markus Greiner [12].

tive interference pattern at $\mathbf{k} = 0$, indicates that the system is in the SF phase. In that phase, since atoms are delocalized across the lattice sites, a coherent matter wave prevails during the expansion which results in sharp peaks in the interference pattern and similar trend is maintained for relatively smaller values of the potential strength. With further increase in the potential height beyond a critical value $V_0^c \simeq 13E_r$ [2], sharp peaks in the absorption spectra disappears indicating a destructive interference pattern, thereby signaling the transition to the MI phase. In MI phase, the atoms are localized at the lattice sites and hence demonstrates a destructive interference pattern with no definite phase relationship. Surprisingly, this critical value of the potential strength at which the absorption spectra shows a transition is in excellent agreement with the theoretical prediction of the BHM.

1.4 Optical dipole trap (ODT)

A neutral atom can be cooled and trapped using various mechanism such as a magneto-optical trap (MOT) [12, 59] and a purely optical dipole trap (ODT) [12–15] techniques. In MOT, ultracold atoms are exposed in a simple Helmholtz coil arrangement where the applied magnetic field in opposite direction orient the ultracold atoms in a single magnetic sublevel despite the presence of different hyperfine states, m_F . To unlock all hyperfine states, an optical dipole trap can be employed which works on the principle of energy shifts induced by the radiation on the atomic internal energy levels. In ODT, the interaction between the electric

field of a laser beam with the induced dipole moment on a neutral atom paves the way in retaining the hyperfine degrees of freedom and make them as a spinor Bose gas. In order to see how a dipole force arises, consider a spatially varying electric field of a laser beam which oscillates with frequency ω_l of the form

$$\mathbf{E}(\mathbf{r}, t) = 2E_0 \cos(\mathbf{k} \cdot \mathbf{r} - \omega_l t) \quad 1.15$$

and the induced dipole moment on the atom at a position \mathbf{r} is $\mathbf{d} = -e \sum \mathbf{r}$ which oscillates with same frequency of the laser field. Thus the Hamiltonian for the atom-light interaction is given by

$$H_{AL}(t) = -\mathbf{d} \cdot \mathbf{E}(\mathbf{r}, t) \quad 1.16$$

Using atom-light Hamiltonian, the energy shifts after including the second order correction is given by,

$$\Delta E(\mathbf{r}) = -\frac{1}{2} a_{m_F}(\omega_l) \overline{\mathbf{E}(\mathbf{r}, t)^2} \quad 1.17$$

where $\overline{\dots}$ denotes the time average of the electric field and $I(\mathbf{r}) = \overline{\mathbf{E}(\mathbf{r}, t)^2}$ is the intensity of the laser field. $a_{m_F}(\omega_l)$ is the atomic polarizability which is given by,

$$a_{m_F}(\omega_l) = \sum_{\gamma} |\langle \gamma | \mathbf{d} \cdot \mathbf{e} | g \rangle|^2 \left(\frac{1}{E_{\gamma} - E_g + \hbar \omega_l} + \frac{1}{E_{\gamma} - E_g - \hbar \omega_l} \right) \quad 1.18$$

Here \mathbf{e} is the unit vector in the direction of the electric field and $|g\rangle = |F, m_F\rangle$ is the ground state of the atom and the summation is taken over all the excited states, $|\gamma\rangle$. For a far off resonance laser light, the polarizability, $a_{m_F}(\omega_l)$ takes the form,

$$a_{m_F}(\omega_l) \simeq -\frac{|\langle \gamma | \mathbf{d} \cdot \mathbf{e} | g \rangle|^2}{\hbar \Delta} \quad 1.19$$

where Δ is the detuning parameter from the resonance, $\hbar \Delta = \hbar \omega_l - (E_{\gamma} - E_g)$. Thus the effective dipole potential and hence the force experience by an atom is given by,

$$\begin{aligned} U_{dipole}(\mathbf{r}) &= -\frac{1}{2} a_{m_F}(\omega_l) \overline{\mathbf{E}(\mathbf{r}, t)^2} \propto \frac{I(\mathbf{r})}{\Delta} \\ \mathbf{F}_{dipole}(\mathbf{r}) &= -\nabla U_{dipole}(\mathbf{r}) \end{aligned} \quad 1.20$$

For red detuned light, $\Delta < 0$ ($\omega_l < \omega_0$), atoms are attracted towards potential minima, that is, the regions of maximum field intensity, $I(\mathbf{r})$, while for blue detuned light, $\Delta > 0$ ($\omega_l > \omega_0$), atoms are attracted towards potential maxima, that is, the regions of minimum field intensity, $I(\mathbf{r})$ [12] [Fig.1.6].

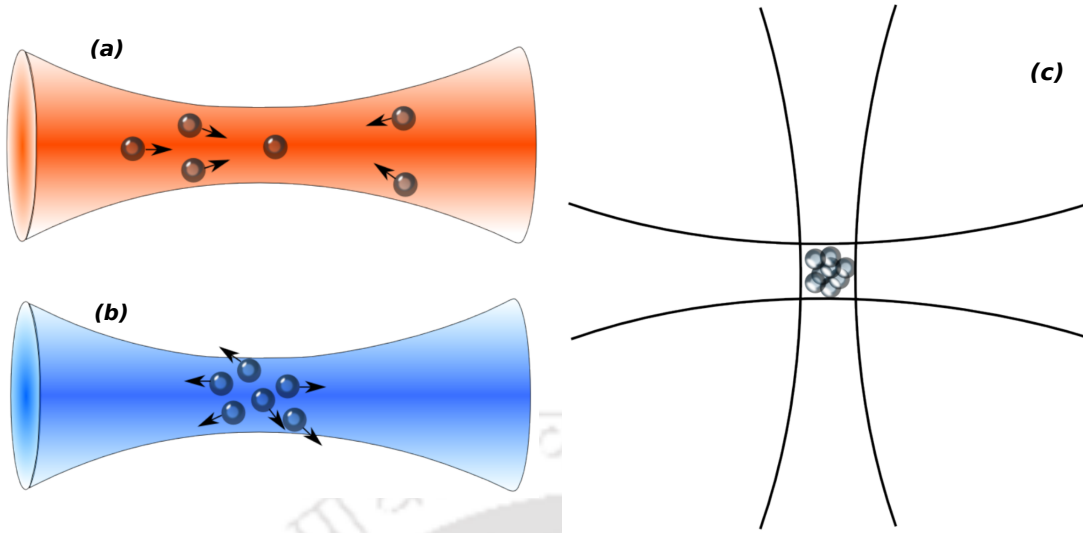


Figure 1.6: *Laser detuning of a dipole potential trap (ODT) using a Gaussian laser beams. For a red tuned ODT, atoms are trapped in the maximum intensity (a). For a blue detuning ODT, atoms are scattered from the trap center (b). A crossed ODT to trap the atoms at the center of maximum intensity in (c). Figure courtesy of J. Wernsdorfer [69].*

For a system with hyperfine spin, $F = 1$, the detuning parameter, Δ involves different nS to nP transition where $\Delta = \omega_l - \omega_{PS}$ and the atomic polarizability, $a_{m_F}(\omega_l)$ can be approximated as [17],

$$a_{m_F}(\omega_l) = -\frac{1}{\omega_{PS}^2 - \omega_l^2} \left(\sum_{\gamma \in P} |ed_{\gamma,g}|^2 \omega_{\gamma,g} \right) + O\left(\frac{1}{\Delta}\right) \quad 1.21$$

where $ed_{\gamma,g}$ are the dipole matrix elements between the ground state $|g\rangle$ and the excited state $|\gamma\rangle$.

1.5 Spin-1 Bose gas: An era of quantum magnetism

Although the commonly used MOT during the early days of experiment successfully shows the BEC as well as the QPT of ultracold atoms in optical lattices. But such trapping technique comes at a cost of dropping most of then rich phase properties due to the suppression of the internal degrees of freedom. On the contrary, experiments involving the ODT which purely uses an electric field instead of a magnetic field has opened up a new window of opportunity in studying the quantum degenerate Bose gases with atomic hyperfine spin and hence treat them as spinor Bose gases. Remarkably, a spin-1 ($F = 1$) condensation [19] was experimentally observed using ^{23}Na atoms where all three hyperfine states are populated by transferring the spin-0 BEC into a far off resonant optical trap [Fig.1.7], initiated following a theoretical studies by Ho [17] and Machida [18] in

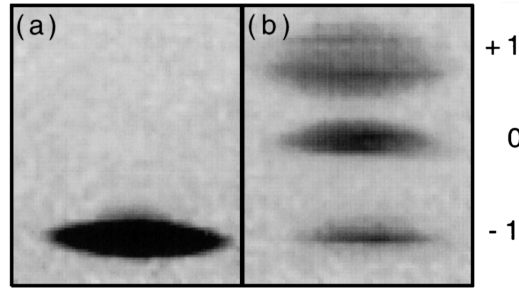


Figure 1.7: *Optical trapping of a spin-1 ($F = 1$) BEC using ^{23}Na atom where all three hyperfine states are populated. Absorption images are captured after 250 ms in (a) where atoms remains polarized. After 340ms of optical confinement in (b), hyperfine states are separated by a magnetic field gradient of pulse duration 40 ms. Figure courtesy of Stamper-Kurm et al. [19].*

the low energy limit. Latter, spinor condensates of ^{87}Rb atoms corresponding to hyperfine spin state $F = 1$ [70] as well as $F = 2$ [71, 72] and ^{23}Na atoms with $F = 2$ [73] were observed and it was found that the higher spin manifolds ($F = 2$) of ^{23}Na atoms are very much unstable compared to those for ^{87}Rb atoms.

The vector nature of the order parameter of a spin-1 condensates which is invariant under the spin-gauge rotation provides a new insights in exploring various spin textures, topological aspects and quantum magnetization properties present therein [16–18]. The application of an external magnetic field which breaks the rotational symmetry of the system shows a transition between easy-axis and easy-plane ferromagnetism. The transition was observed by applying an in-situ magnetization of a ^{87}Rb ($F = 1$) spinor condensates [16] [Fig. 1.8]. Also different topological properties such as Shankar skyrmions and knot solitons which are characterized by the linking number or Hopf invariant, classified by the third homotopy group have been studied in the context of spin-1 BEC [37].

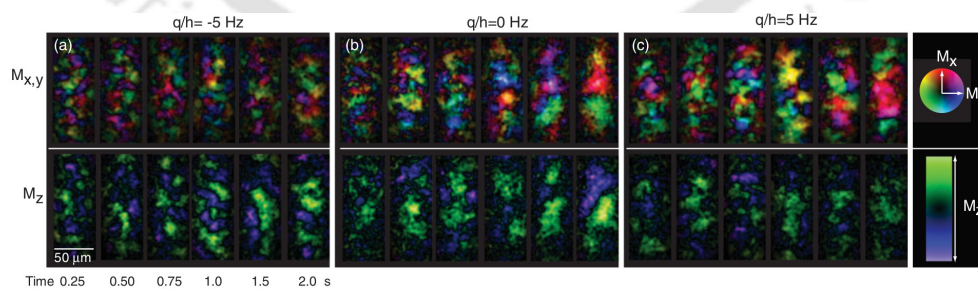


Figure 1.8: *Transverse (top) and longitudinal (bottom) magnetization of a $F = 1$ ^{87}Rb spinor Bose gas that was prepared initially in a non degenerate incoherent ($1/3, 1/3, 1/3$) population mixture of the Zeeman states and then cooled to quantum degeneracy. The degenerate spin texture evolves for a variable time at a quadratic shift of (a) $q/h = -5$, (b) $q/h = 0$ and (c) $q/h = 5$ before column density of the vector magnetization is measured. Figure courtesy of Stamper-Kurm et al. [16].*

Apart from such intriguing aspects of spinor condensates, the ground state

of a spin-1 Bose gas in optical lattices is determined completely by the magnetic sublevels. Recently, it was shown that the different hyperfine spin states can be coupled sequentially to form an extra dimension, known as a synthetic dimension, similar to the spatial dimension of an optical lattice [47, 74] [Fig.1.9]. For ^{87}Rb ($F = 1$) atoms, a Raman transition which splits the three spin states $m_F = \pm 1, 0$, thus provide the synthetic dimension can be used along with an optical lattice dimension to create a synthetic magnetic flux due to Peierl's coupling [47]. Moreover, a synthetic dimension can be used to generate high synthetic magnetic field of the order of unit flux per plaquette to overcome the rotational limitation of the neutral atoms in optical lattices.

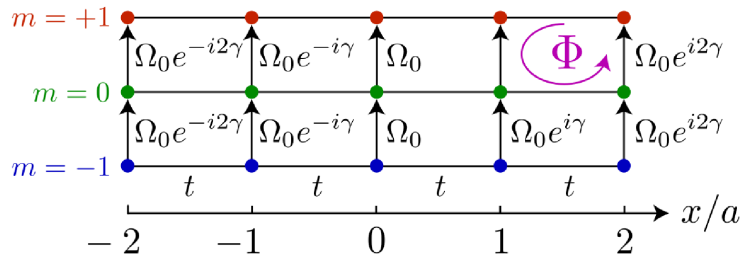


Figure 1.9: A synthetic dimension is created by illuminating a $F = 1$ ^{87}Rb spinor Bose gas in a pair of Raman laser beam of wavelength λ_R . A synthetic 2D lattice with magnetic flux $\Phi = \gamma/2\pi$ per plaquette ($\gamma = 2k_R a$, a : lattice spacing). Figure courtesy of Celi et al. [47]

1.6 A comparison between spin-0 and spin-1 Bose gases

The above section shows that the spin-1 Bose gas exhibits an edge in the direction of quantum magnetism compared to spin-0 Bose gas due to its spin degrees of freedom. Particularly, the spin dependent interaction plays an important role in determining different kinds of spontaneous symmetry breaking of the ground state which in turn directly affects the properties of the MI and SF phases. Thus a comparison between the spin-0 and spin-1 Bose gases with regard to different quantities will help us to get a comprehensive overview on these two systems which are listed in the following table 1.1. We have included few properties of a spin-1 Bose gas here but this table does not include the complete list of phase properties that a spin-1 Bose gas exhibits.

Parameters	Spin-0	Spin-1
Interaction potential	U_0	$U_0 \propto a_0 + 2a_2$ $U_2 \propto a_2 - a_0$
Nature of interaction		Antiferromagnetic (AF): $U_2/U_0 > 0$ Ferromagnetic: $U_2/U_0 \leq 0$
SF order parameter	scalar quantity: ψ	vector quantity: $\vec{\psi} = (\psi_+, \psi_0, \psi_-)$
Symmetry of BHM	$U(1)$	$U(1) \times \mathbf{S}^2$: AF $SO(3)$: Ferromagnetic
MI phase	Insulating phase $\rho = 1, 2..$	Spin singlet: ($\rho = \text{even}$) Spin nematic: ($\rho = \text{odd}$)
SF phase	Atomic SF	Transverse or longitudinal polar, Ferromagnetic, Broken axis symmetry
Order of MI-SF phase transition	2^{nd} order	1^{st} order: Spin singlet MI-SF phase 2^{nd} order: Spin nematic MI-SF phase

Table 1.1: A comparison between the spin-0 and spin-1 Bose gases

1.7 Various aspects of ultracold atoms in optical lattices

1.7.1 Disorder optical potential

Although the correlated bosons described by the BHM successfully demonstrate the presence of an incompressible MI and a compressible SF phases in a disorder free scenario, however some kind of impurities, such as, disorder, defects etc are always present in an interacting system. Thus understanding the interplay between disorder and interaction still remains a controversial topic from theoretical as well as experimental point of view and shows a plethora of physics at the boundary between a "clean" and "dirty" bosons problem.

Motivated by the experimental observation of the superfluidity in a weakly interacting ^4He absorbed in a porous Vycor glass [75], the effects of a random potential, "disorder" was first studied in a correlated Bose system by Giamarchi *et al.* [76] and Fisher *et al.* [67]. They found that apart from the usual SF and MI phases in a clean state, an additional phase, known as a Bose glass (BG) phase, which is compressible, but a gapless yet insulating in nature appears due to the boson localization in presence of disorder. They showed that a BG phase is sandwiched between a SF and a MI phases, that is, a direct transition from the MI to the SF phase is interrupted by the presence of such glassy phase, however a direct transition is not fundamentally impossible.

While the theoretical understanding of the location and appearance of the BG

phase still remains a contradictory subject but the possible scenarios at which the BG phase intervenes in between the SF and the MI phases are the following- (i) A BG phase appears in between the MI and the SF phases [Fig. 1.10 (left)] (ii) A BG phase appears between the MI and the SF phases except at the tip of the MI lobes where a direct transition from a MI to a SF phase is possible (iii) A BG phase appears only in between the MI lobes and a direct transition from MI to SF phases is possible. Several numerical studies, such as, quantum Monte Carlo (QMC), Renormalization Group (RG) [77–79] show that for a weakly disorder system, the disorder is insufficient to introduce a BG phase and thus paves the way for a direct transition from the MI to the SF phase.

Recently, Pollet *et al.* gave rigorous proof which forbids possible direct transition from the MI to the SF phase in scenarios (ii) and (iii) and pointed out that for a generic bounded disorder, a BG phase always intervenes in between the MI and the SF phases (scenario (i)) [80]. They formalized a theorem (Theorem 1) which was introduced earlier in Refs. [67, 81] and further postulated another theorem, known as, "*theorem of inclusions*" in support of scenario (i).

Theorem 1 states that when the critical strength of a bounded disorder (Δ_c) is larger than the half of the width of the energy gap ($E_g/2$) in the MI phase then the transition inevitably occurs to a compressible and gapless phase, that is, the BG phase. Such theorem is based on the fact that for an infinite system, the chemical potential is homogeneously shifted upwards or downwards by an amount Δ since there exists an arbitrarily large "Lifshitz" region where no energy gap exists for particle transfer in that region [80]. The "*theorem of inclusions*" says that for a generic bounded disorder, there exists a rare but arbitrary large region on either side of a transition line. This implies that if one phase across the transition line is gapless, then the other phase across the transition line is automatically gapless because of arbitrarily large rare regions which locally look exactly same as the previous phase [80].

Study of the BG phase in the context of ultracold Bose gas in optical lattices has attracted much attention due to the ability to introduce disorder in a controlled manner. Although an optical lattice is free from disorder or defects, but one can easily create a disordered optical lattice potential by several methods, such as, using speckle laser beams [83–85], two color superlattices [86–88] etc.

Recently Fallani *et al.* designed an experiment to create a disordered optical lattice potential using different laser beams and thus observed a transition from a MI to the BG phase by loading the ^{87}Rb atoms in optical lattices [82]. A primary laser beam of wave length, λ_1 was used to create an optical lattice (main) along with an auxiliary laser beam with slightly different wavelength, λ_2 ($< \lambda_1$) to introduce the disorder and thus controlling the auxiliary laser beam, a transition from weak to strong disorder strength is possible [Fig. 1.10 (right)]. They initially

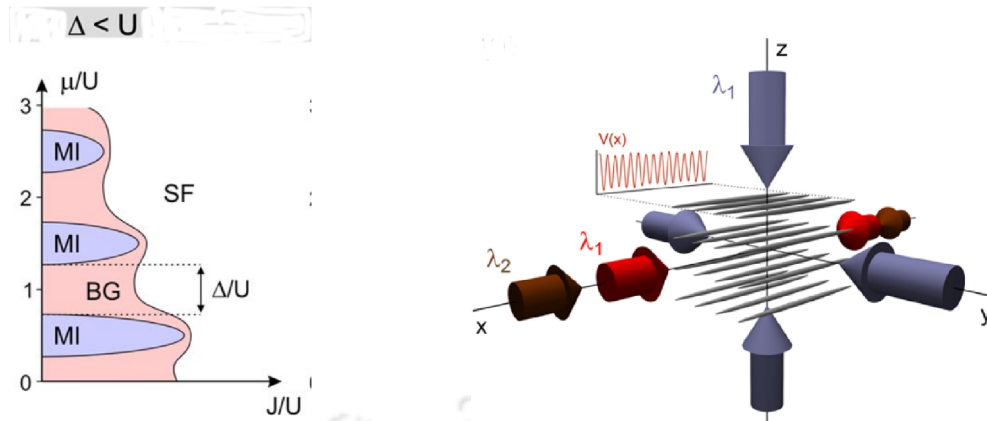


Figure 1.10: The appearances of a BG phase in between MI and SF phases in scenario (i) in presence of disorder, Δ (left). A disorder optical lattice potential is created using an auxiliary laser beam with slightly different wavelength along with a primary laser beam to create an optical lattice (main) potential (right). Figure courtesy of Fallani *et al.* [82]

prepared the system in the MI phase by turning off the disorder potential ($\beta_2 = 0$) and measured the excitation spectra in different phases via TOF at different disorder strengths. The peaks in the excitation spectra show that the system is in MI phase in the clean state but with increasing disorder potential (β_2), the disappearances of such peaks in the excitation spectra indicates a transition to the Bose glass phase.

1.7.2 Synthetic magnetic field

Ultracold atoms suffer a serious drawback due to the charge neutrality despite the fact of their unchallenging ability in tuning the Hamiltonian parameters which simulates the quantum behaviour. Unlike a charge particle which rotates around a field axis, it is quite difficult to know the true response of an ultracold Bose gas in presence of a magnetic field because of their charge neutrality.

One possible way to overcome such limitation is to put these neutral atoms in rotational motion so that they can mimic the effects of a charge particle. They use the equivalence between the Lorentz force experienced by a charge particle and the Coriolis force on the neutral atoms due to rotation. Thus the neutral atoms in rotation generates an artificial gauge field, known as synthetic magnetic vector potential (\mathbf{A}^*) which was observed by the appearances of quantized vortices in BEC [89–91] [Fig. 1.11 (left)]. However large synthetic vector potential requires large rotation of the quantum gases which may cause the atoms to fly apart.

Later Lin *et al.* engineered a large synthetic magnetic field $\mathbf{B}^* = \nabla \times \mathbf{A}^*$ by introducing a Berry phase which arises due to the coupling between the different hyperfine levels of an atom and does not depend explicitly on the rotational motion

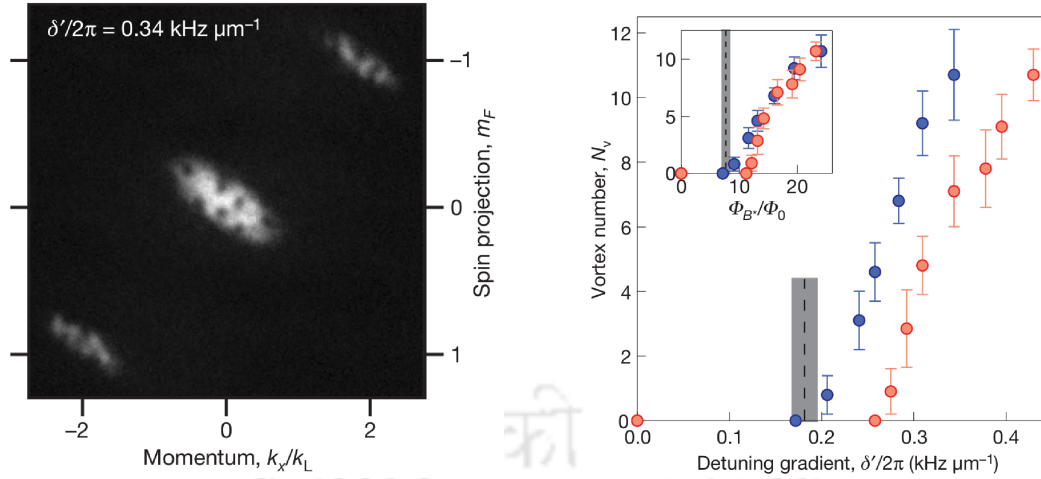


Figure 1.11: Dressed BEC image of three hyperfine states of ^{87}Rb atoms after a TOF of 25.1 ms in a crossed optical dipole trap with a magnetic field, $B = (B_0 - b'y)\hat{y}$, that is, with a detuning gradient, $\delta' \propto b'$ (left). Vortex number, N_v versus δ' at Raman coupling $\hbar\Omega_R = 5.85E_L$ (blue circles) and $\hbar\Omega_R = 8.20E_L$ (red circles) (right). The inset displays N_v versus the synthetic magnetic flux, Φ_B/Φ_0 . Figure courtesy of Lin et al. [92]

[92]. For that purpose, they created a spatially varying synthetic vector potential by illuminating ^{87}Rb BEC ($F = 1$) by a pair of Raman laser beams with momentum difference and a real magnetic field which varies in a single direction. At first the BEC was formed in a uniform motion at the Raman resonance and then by tuning the laser beams and applying a magnetic field gradient (b'), a non uniform motion is created. Such non uniform motion where atoms swirl in a whirlpool-like motion generates quantized vortices which are the signature of the synthetic vector potential. The number of vortices which determine the strength of the synthetic vector potential depends upon the detuning gradient ($\delta \propto b'$) and thus possible to create large vector potential without the restriction of large rotation [92] [Fig. 1.11 (right)]. After the observation of vortices in the BEC, study of Abrikosov vortex lattice which shows a structural transition due to the pinning [93, 94] and observation of Dirac mono-pole [95] are now of great importance.

1.7.3 Dipole-dipole interaction

For correlated Bose systems, the interaction between the constituent particles, which can be either short or long range, plays an important role in determining the ground state properties of the system. Although most of the BHM have been analyzed by taking care the effects of two body short range interaction which certainly raises the concern to revisit such quantum phase properties by considering the long range interaction such as a dipole-dipole interaction (DDI). In contrast to the s -wave dominated two body pseudopotential which is isotropic in nature,

the DDI is highly anisotropic and has a direct consequences in the stability of the BEC, that is, leads to the d -wave collapse in the dipolar condensates.

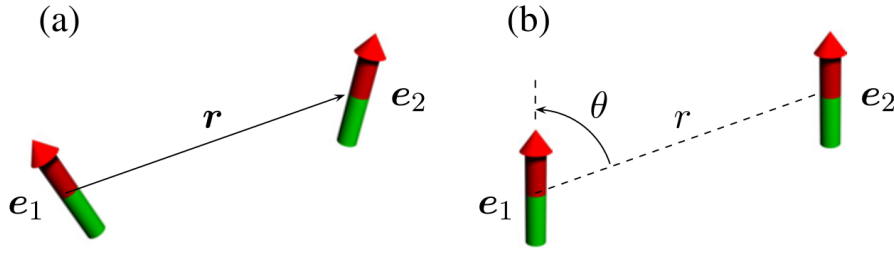


Figure 1.12: Two particles interacting via dipole-dipole interaction for non-polarized atoms in (a) and polarized atoms in (b). r and θ are the relative distance and angle between the two dipoles. Figure courtesy of Lahaye et al. [96]

Consider two dipoles are separated by a relative distance r and their dipole moments are pointed along two different directions with the unit vectors \mathbf{e}_i then the interaction potential of the two dipoles is given by [96]

$$U_{DDI}(\mathbf{r}) = \frac{C_{DDI}}{4\pi} \frac{(\mathbf{e}_1 \cdot \mathbf{e}_2)r^2 - 3(\mathbf{e}_1 \cdot \mathbf{r})(\mathbf{e}_2 \cdot \mathbf{r})}{r^5} \quad 1.22$$

where C_{DDI} is the strength of the DDI which is $C_{DDI} = \mu_0 \mu_m^2$ for particles with magnetic dipole moments, μ_m and $C_{DDI} = d^2 \epsilon_0$ for electric dipole moments, d . Such dependency of $1/r^3$ shows that the DDI is a long range interaction and the anisotropy which depends upon the relative angles between two dipoles are now responsible for the phase shift where all partial wave contributes to the scattering phenomena [96] [Fig.1.12].

Species	I	F	Dipole moment
${}^7\text{Li}$	3/2	1	$0.94\mu_B$
${}^{23}\text{Na}$	3/2	1	$0.91\mu_B$
${}^{39}\text{K}$	3/2	1	$0.95\mu_B$
${}^{87}\text{Rb}$	3/2	1	$0.73\mu_B$
${}^{52}\text{Cr}$	0	3	$6\mu_B$

Table 1.2: Magnetic dipole moment of various species where μ_B : Bohr magneton. Source Lahaye et al. [96].

It was found that for polarized molecules, the electric nature of the DDI is dominant, while for spinor particles, the DDI is essentially magnetic origin. The strengths of magnetic DDI of few spinor particles are listed in table 1.2 and till now the maximum value of the experimentally observed DDI corresponds to the ${}^{52}\text{Cr}$ atoms which has a hyperfine spin $F = 3$ [97, 98]. The effects of such long range interaction in the context of the BHM can be studied by considering the off-site interaction term to be the interaction between the density imbalanced nearest

neighbour sites which often referred as an extended interaction potential [99]. Thus the inclusion of such extended interaction in the ultracold Bose gas shows a plethora of interesting phases such as solid as well as crystalline along with the usual quantum phases of the system [100–102].

1.7.4 Multi-body interaction potential

The ability to control the inter-particle interactions using Feshbach resonance in ultracold atoms paves the way to explore the ground state phase properties in presence the three and higher body interaction strengths in addition to the usual two body interaction potential. In contrast to inelastic three body process which shows Efimov effect [103], an effective three body interaction can lead to quantum Hall phenomena described by the Pfaffian state [104]. For a sufficient deep optical lattice potential, the three body interaction can be dominated and independently controlled by tuning the two body collisions process.

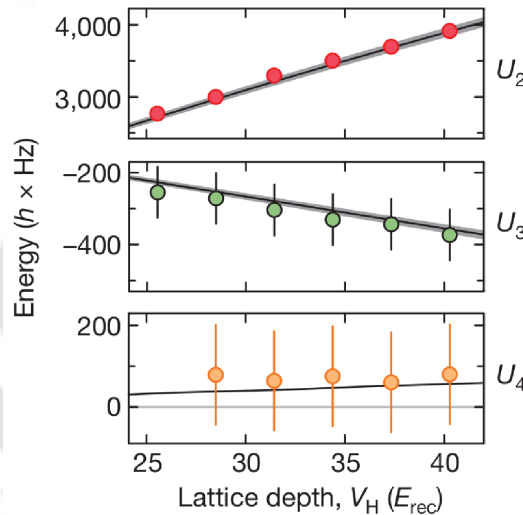


Figure 1.13: *Effective multi-body, that is, two (top), three (middle) and four (bottom) body interaction strength derived from the experiment using multi orbital energies using a collapse and revival technique under variable lattice potential depth, V_H . Figure courtesy of Will et al. [105]*

Recently, Will *et al.* experimentally observed the signature of three and higher body interaction by inducing a virtual transition of the atoms from lowest to the excited energy band by loading the ^{87}Rb BEC in a sufficiently deep optical lattice potential [105]. They measured up to six body interaction in a time resolved quantum phase collapse and revival oscillation using an atom interferometry. A collapse and revival of coherent matter wave of BEC is a direct outcome of two body interaction in which atoms occupy a single spatial orbital of the system. However by controlling the atom-atom interaction, a virtual transition of atoms

to the higher excited orbitals which in turn reshape the spatial distribution of the wave function gives rise to the multi-body interaction [Fig. 1.13].

In contrast to the single orbital case where the visibility of the interference pattern depends on the single frequency, U_0/h (U_0 : two body strength), for multi orbital effects, the collapse and revival of the visibility is now function of multiple frequency components, that is, lU_0/h (l : integer) [105]. Thus the effective multi-body interaction can be determined iteratively from the multi orbital energies and both the three and four body interactions are in agreement with the theoretical prediction. Apart from such multi-body interaction, Safavi-Naini *et al.* proposed a mechanism to engineer a tunable on-site three body interaction [106]. Such types of three body interaction can be observed by coupling a triply occupied state using a radio frequency field to an excited hyperfine state so that they can form a trimer state.

Outline of the thesis

In the following, we present a more specific plan of the thesis by including a description of the various problems that have been tackled in the form of the chapters of the thesis. There are total seven chapters in this thesis. We proceed with a brief description of the context of each one by one.

Chapter 1 contains an overview of the quantum phase transition of ultracold atoms in optical lattices and the quantum magnetism of spin-1 Bose gas.

Chapter 2 will outline the BHM for the spinor Bose gas in an optical lattice along with the single site mean field theory (SSMFT) with a necessary note on the ground state properties and the phase diagrams. We shall also extend our single site MFA to a multi-site mean field theory (MMFT) to increase the accuracy of the work and the computational limitation related to the MMFT therein. A strong coupling perturbative mean field approximation (PMFA) is also discussed to obtain the analytical phase diagrams for a check with the MFA phase diagrams. A short discussion on the QMC results is included to demonstrate the comparison with the results obtained from the MFA and PMFA techniques.

Chapter 3 we explore the effects of a random disorder on the spin-1 Bose Hubbard model (SBHM) to study the MI to the SF phase transition intervened by a BG phase. The transition from a MI to a BG phase is analyzed by introducing a simple physical quantity, defined as the fraction of the sites with finite SF order parameter and non integer occupation densities, that is, used as an indicator for the onset of the MI, BG or SF phases. The transition to the BG phase either from a MI or a SF phase is found to have an unusual similarity with the random percolation phenomena familiar in the context of statistical physics. A percolation threshold is found to have a surprisingly close value to the one obtained at the

onset of a SF phase in our interacting spinor Bose gas using Hohen-Kopelman (HK) algorithm. All the MFA phase diagrams are shown to be in qualitative agreement with the results obtained using probabilistic mean field approaches.

Chapter 4 deals with the consequences of the synthetic magnetic field on the phase diagrams of the spinor Bose gas. An external magnetic field which causes the Zeeman splitting among the different magnetic sublevels of a spinor Bose gas is included for comparison. For the AF case, the spin singlet state is found to be stable at low values of the external field strength and the system is more likely to be in the Mott insulating phase as the synthetic field is enhanced. But at large field strengths, due to a competition between the synthetic and the external magnetic fields, the former tends to stabilize the MI phase compared to the superfluid phase, while the latter tries to destabilize the MI phase by suppressing the formation of singlet pairs. Further, the energy spectrum shows a symmetry as a function of the magnetic flux for both spin singlet and nematic phases.

Chapter 5 we investigate the effects of density-density extended interaction on a SBHM. Such an interaction not only paves the way for the CDW phase, but also an additional compressible phase, known as the supersolid (SS) phase which depicts a coexistence of both the crystalline and superfluid phases. In the weak interaction limit, a charge density wave (CDW) phase emerges which is sandwiched between the MI and the supersolid (SS) phases. In the strong interaction limit, when the extended interaction is larger than the width of the odd and even MI lobes, the CDW phase completely occupies all the MI lobes. Since at this critical value, both the CDW and the MI phases become degenerate, it opens up the possibilities of spin singlet and nematic CDW insulating phases. The variation of spin eigenvalues confirmed the formation of the spin singlet and nematic CDW phases. In the CDW phase, the spin eigenvalues oscillate between 0 and 1 replicating a spin density wave (SDW) pattern. Further, we have obtained the phase diagrams through the PMFA calculation and the location of the boundaries between the CDW-SS and the MI-SF phases in the phase diagrams are compared with the mean field (MFA) results. They are found to be in qualitative agreement with each other.

Chapter 6 we study the effects of a repulsive three body interaction in addition to an usual two body interaction term on a spin-1 ultracold Bose gas. We have found that the odd-even asymmetry in the MI lobes remains intact in presence of both the two and three body interactions in the AF case. However, for a purely three body repulsive interaction, the higher order MI lobes, except the first one, extend and encroach into the SF phase. Also the spin nematic-singlet formation occurs for all the odd-even MI lobes which are confirmed based on the spin eigenvalue and spin nematic order parameter for the former case. While there is neither any asymmetry in the MI lobes, however the spin nematic-singlet formation being

observed beyond second MI lobe for the latter case. We have compared our MFA results with the analytic phase diagrams obtained using the PMFA expansion and recorded a good agreement between the two approaches.

Chapter 7 we extend our calculations for an attractive three body interaction potential on a SBHM. The phase diagrams show that the third MI lobe is severely affected and it breaks odd-even asymmetry in the neighborhood of the second and fourth MI lobes at higher values of the interaction strength. At higher values of the three body interaction, we have found different order of phase transition from the MI to the SF phase corresponding to the first and third MI lobes. This was confirmed by meticulous observation of the spin eigenvalues and the nematic order parameter. All phase diagrams are completely in agreement with the analytical PMFA phase diagrams.

Chapter 8 concludes with the highlights of the results obtained in the previous chapters.





Chapter 2: Spin-1 Bose Hubbard model

In this chapter, we shall discuss the Bose Hubbard model and its relevance to spin-1 ultracold atoms in an optical lattice. The theoretical formalism is hence outlined with a view to solve the spinor BHM (SBHM) for studying various quantum phases. In this regard, we briefly enumerate various theoretical techniques, such as, mean field approximation (MFA), quantum Monte Carlo (QMC) and density matrix renormalization group (DMRG) theory and hence a qualitative comparison between them.

2.1 Spin dependent interaction potential

At ultralow temperatures, the interaction between two $F = 1$ atoms is described by a pseudo-potential which is defined as [17, 34],

$$V_{int}(\mathbf{r}_1 - \mathbf{r}_2) = \delta(\mathbf{r}_1 - \mathbf{r}_2) \sum_{F_{tot}=0}^{2F} g_{F_{tot}} \mathbf{P}_{F_{tot}} \quad 2.1$$

$$g_{F_{tot}} = \frac{4\pi\hbar^2 a_{F_{tot}}}{M}$$

where the coupling constant, $g_{F_{tot}}$ depends upon the s -wave scattering length corresponding to the spin channel with total spin, F_{tot} and M is the atomic mass. Here $\mathbf{P}_{F_{tot}}$ is the projection operator which defined as,

$$\mathbf{P}_{F_{tot}} = \sum_{m_{F_{tot}}=-F}^F |F_{tot}, m_{F_{tot}}\rangle \langle F_{tot}, m_{F_{tot}}| \quad 2.2$$

Due to the symmetry of the BE statistics, the total spin, F_{tot} must be even and hence the only allowed values for two $F = 1$ atoms are $F_{tot} = 0$ and $F_{tot} = 2$. Thus the normalization condition for the projection operator, $\mathbf{P}_{F_{tot}}$ is given by,

$$1 = \sum_{F_{tot}=0}^2 \mathbf{P}_{F_{tot}} = \mathbf{P}_0 + \mathbf{P}_2 \quad 2.3$$

Also the interaction between the two spin F atoms is given by,

$$\mathbf{F}_1 \cdot \mathbf{F}_2 = \sum_{F_{tot}=0}^2 \mathbf{F}_1 \cdot (\mathbf{F}_2 \mathbf{P}_{F_{tot}}) = \sum_{F_{tot}=0}^2 \hat{\mathcal{H}}_{F_{tot}} \mathbf{P}_{F_{tot}} \quad 2.4$$

$$\hat{\mathcal{H}}_{F_{tot}} = \frac{F_{tot}(F_{tot} + 1) - 2F(F + 1)}{2}$$

Using Eq.(2.3) and Eq.(2.4), finally the projection operator corresponding to the $F_{tot} = 0$ and $F_{tot} = 2$ channels are given by,

$$\mathbf{P}_0 = \frac{1 - \mathbf{F}_1 \cdot \mathbf{F}_2}{3}, \quad \mathbf{P}_2 = \frac{2 + \mathbf{F}_1 \cdot \mathbf{F}_2}{3} \quad \text{2.5}$$

Thus the spin dependent interaction potential [Eq.(2.1)] using Eq.(2.5) is written as,

$$V_{int}(\mathbf{r}_1 - \mathbf{r}_2) = \delta(\mathbf{r}_1 - \mathbf{r}_2) \left[\frac{g_0 + 2g_2}{3} + \frac{g_2 - g_0}{3} \mathbf{F}_1 \cdot \mathbf{F}_2 \right] \quad \text{2.6}$$

The first and second terms of the coefficient represent the spin independent and dependent interactions respectively.

2.2 Spin-1 Bose Hubbard model (SBHM)

To derive the Bose Hubbard model for the spin-1 Bose gas in an optical lattice, we start from the second quantized Hamiltonian in a grand canonical ensemble [17, 18, 34]

$$\begin{aligned} H = & \sum_a \int d^3x \psi_a^\dagger(\mathbf{x}) \left[-\frac{\hbar^2}{2M} \nabla^2 + V_0(\mathbf{x}) + V_T(\mathbf{x}) - \mu \right] \psi_a(\mathbf{x}) \\ & - \eta \sum_{a,\beta} \int d^3x \psi_a^\dagger(\mathbf{x}) F_{a\beta}^z \psi_a(\mathbf{x}) + \frac{c_0}{2} \sum_{a,\beta} \int d^3x \psi_a^\dagger(\mathbf{x}) \psi_\beta^\dagger(\mathbf{x}) \psi_\beta(\mathbf{x}) \psi_a(\mathbf{x}) \\ & + \frac{c_2}{2} \sum_{a,\beta,\gamma,\delta} \int d^3x \psi_a^\dagger(\mathbf{x}) \psi_\gamma^\dagger(\mathbf{x}) \mathbf{F}_{a\beta} \cdot \mathbf{F}_{\gamma\delta} \psi_\delta(\mathbf{x}) \psi_\beta(\mathbf{x}) \end{aligned} \quad \text{2.7}$$

where μ is the chemical potential, $V_0(\mathbf{x})$ is the periodic optical lattice potential, $V_T(\mathbf{x})$ is the trapping potential and η includes the external magnetic field. The constants $c_{0,2}$ are related with the atomic scattering lengths, $a_{0,2}$ as

$$c_0 = \frac{4\pi\hbar^2}{3M}(a_0 + 2a_2), \quad c_2 = \frac{4\pi\hbar^2}{3M}(a_2 - a_0) \quad \text{2.8}$$

Here $\mathbf{F}_{a,\beta}$ are the spin-1 matrices which fulfill the commutation relations as, $[\mathbf{F}_\alpha, \mathbf{F}_\beta] = i \sum_\gamma \epsilon_{\alpha\beta\gamma} \mathbf{F}_\gamma$,

$$\mathbf{F}_x = \frac{1}{\sqrt{2}} \begin{pmatrix} 0 & 1 & 0 \\ 1 & 0 & 1 \\ 0 & 1 & 0 \end{pmatrix} \quad \mathbf{F}_y = \frac{i}{\sqrt{2}} \begin{pmatrix} 0 & -1 & 0 \\ 1 & 0 & -1 \\ 0 & 1 & 0 \end{pmatrix} \quad \mathbf{F}_z = \frac{1}{\sqrt{2}} \begin{pmatrix} 1 & 0 & 0 \\ 0 & 0 & 0 \\ 0 & 0 & -1 \end{pmatrix}$$

The bosonic field operator, $\psi_a(\mathbf{x})$ annihilates a particle in a hyperfine state $|F = 1, m_F = a\rangle$ where $a = +1, 0, -1$ which obey the following commutation relations,

$$[\psi_a(\mathbf{x}), \psi_\beta(\mathbf{x}')] = [\psi_a^\dagger(\mathbf{x}), \psi_\beta^\dagger(\mathbf{x}')] = 0 \quad [\psi_a(\mathbf{x}), \psi_\beta^\dagger(\mathbf{x}')] = \delta_{a,\beta} \delta(\mathbf{x} - \mathbf{x}') \quad 2.9$$

Assuming all the particles are in the lowest band of the optical lattice then the field operator can be expressed in terms of Wannier wave functions as,

$$\psi_a(\mathbf{x}) = \sum_i a_{ia} w_0(\mathbf{x} - \mathbf{x}_i), \quad \psi_a^\dagger(\mathbf{x}) = \sum_i a_{ia}^\dagger w_0(\mathbf{x} - \mathbf{x}_i) \quad 2.10$$

where $w_0(\mathbf{x} - \mathbf{x}_i)$ is the Wannier wave function of the lowest Bloch band and $a_{ia}^\dagger(a_{ia})$ is the bosonic creation(annihilation) operator at the site i with hyperfine spin $m_F = a$ and obeys the bosonic commutation relation, $[a_{ia}, a_{j\beta}^\dagger] = \delta_{a,\beta} \delta_{ij}$. Now inserting Eq.(2.10) into Eq.(2.7) and making an approximation that Wannier wave functions are strongly localized at lattice sites, that is, the overlap between them at different sites can be neglected then the Hamiltonian for the spin-1 BHM can be written as,

$$H = -t \sum_{\langle i,j \rangle} \sum_a (a_{ia}^\dagger a_{ja} + h.c.) + \sum_i \left[- \sum_a \mu_i a_{ia}^\dagger a_{ia} - \eta \sum_{a,\beta} a_{ia}^\dagger F_{a\beta}^z a_{i\beta} \right. \\ \left. + \frac{U_0}{2} \sum_{a,\beta} a_{ia}^\dagger a_{i\beta}^\dagger a_{i\beta} a_{ia} + \frac{U_2}{2} \sum_{a,\beta,\gamma,\delta} a_{ia}^\dagger a_{i\gamma}^\dagger \mathbf{F}_{a\beta} \cdot \mathbf{F}_{\gamma\delta} a_{i\delta} a_{i\beta} \right] \quad 2.11$$

where $\sum_{\langle i,j \rangle}$ includes the summation between nearest neighbour sites, t is the hopping matrix element and dropping the site indices due to the translational invariance in case of nearest neighbour hopping then

$$t = -t_{ij} = - \int d^3x w_0^*(\mathbf{x} - \mathbf{x}_i) \left(- \frac{\hbar^2 \nabla^2}{2M} + V_0(\mathbf{x} + V_T(\mathbf{x})) \right) w_0(\mathbf{x} - \mathbf{x}_j) \quad 2.12$$

U_0 and U_2 refers the on-site spin independent and dependent interaction respectively which are given by,

$$U_{0,2} = c_{0,2} \int d^3x |w_0(\mathbf{x} - \mathbf{x}_i)|^4 \quad 2.13$$

To simplify the spin dependent interaction term, we rearrange the following term as,

$$\sum_{a,\beta,\gamma,\delta} a_{ia}^\dagger a_{i\gamma}^\dagger \mathbf{F}_{a\beta} \cdot \mathbf{F}_{\gamma\delta} a_{i\delta} a_{i\beta} = \sum_{a,\beta,\gamma,\delta,v} (a_{ia}^\dagger \mathbf{F}_{a\beta}^v a_{i\beta}) (a_{i\gamma}^\dagger \mathbf{F}_{\gamma\delta}^v a_{i\delta}) - \sum_{a,\beta,\delta,v} \mathbf{F}_{a\beta}^v \mathbf{F}_{\beta\delta}^v a_{ia}^\dagger a_{i\delta} \quad 2.14$$

Now defining the spin operator, $\mathbf{S}_i = \sum_{\alpha,\beta} a_{i\alpha}^\dagger \mathbf{F}_{\alpha\beta} a_{i\beta}$ and the number operator, $n_{i\alpha} = a_{i\alpha}^\dagger a_{i\alpha}$, $n_i = \sum_{\alpha} n_{i\alpha}$, Eq.(2.11) becomes

$$H = -t \sum_{\langle i,j \rangle} \sum_{\alpha} (a_{i\alpha}^\dagger a_{j\alpha} + h.c.) + \sum_i \left[-\mu n_i - \eta S_{iz} + \frac{U_0}{2} n_i(n_i - 1) + \frac{U_2}{2} (S_i^2 - 2n_i) \right] \quad 2.15$$

The spin operator, \mathbf{S}_i behaves like an angular momentum or spin operator where each component of the spin operator is given by,

$$\begin{aligned} S_i^x &= \frac{1}{\sqrt{2}} (a_{i0}^\dagger a_{i+} + a_{i+}^\dagger a_{i0} + a_{i0}^\dagger a_{i-} + a_{i-}^\dagger a_{i0}) \\ S_i^y &= \frac{i}{\sqrt{2}} (a_{i0}^\dagger a_{i+} - a_{i+}^\dagger a_{i0} - a_{i0}^\dagger a_{i-} + a_{i-}^\dagger a_{i0}) \\ S_i^z &= a_{i+}^\dagger a_{i+} - a_{i-}^\dagger a_{i-} = n_{i+} - n_{i-} \end{aligned} \quad 2.16$$

Using Eq.(2.16), the total spin, S_i^2 is

$$\begin{aligned} S_i^2 &= \underbrace{2n_{i+}n_{i0} + 2n_{i0}n_{i-} + n_{i+} + 2n_{i0} + n_{i-} + n_{i+}^2 - 2n_{i+}n_{i-} + n_{i-}^2}_{S_i^{2diag}} \\ &+ \underbrace{2a_{i+}^\dagger a_{i-}^\dagger a_{i0}^2 + 2(a_{i0}^\dagger)^2 a_{i+} a_{i-}}_{S_i^{2offdiag}} \end{aligned} \quad 2.17$$

The on-site spin independent and dependent interactions can be positive as well as negative depending upon the values of the atomic scattering lengths, $a_{0,2}$. Experimentally the measured values of U_2/U_0 for ^{23}Na ($F = 1$) and ^{87}Rb ($F = 1$) are shown in table 2.1 where a_B is the Bohr magneton [Source T. L. Ho, [17]].

Species	F	a_0	a_2	U_2/U_0	Remarks
^{23}Na	1	$(46 \pm 5)a_B$	$(52 \pm 5)a_B$	$\simeq 0.04$	Antiferromagnetic (AF)
^{87}Rb	1	$(110 \pm 4)a_B$	$(107 \pm 4)a_B$	$\simeq -0.04$	Ferromagnetic

Table 2.1: Nature of on-site spin independent and dependent interaction potentials for ^{23}Na and ^{87}Rb atoms.

The ground state of the SBHM [Eq.(2.15)] exhibits different kind of symmetry depending upon the values of U_2/U_0 . Now introducing a superfluid order parameter as,

$$\Psi_a = \langle |a_a| \rangle, \quad \Psi = \begin{pmatrix} \Psi_+ \\ \Psi_0 \\ \Psi_- \end{pmatrix} \quad 2.18$$

where $\langle |..| \rangle$ is the equilibrium ground state of Eq.(2.15). All the spinors, (Ψ_+, Ψ_0, Ψ_-)

can transform to each other by a gauge transformation, $e^{i\theta}$ and a spin rotation $u(a, \beta, \tau) = e^{-iS_z a} e^{-iS_y \beta} e^{-iS_z \tau}$ where (a, β, τ) are the Euler angles [17, 25].

(I) Antiferromagnetic (AF) case ($U_2/U_0 > 0$): In the AF case, the ground state of Eq.(2.15) is polar (or antiferromagnetic) state and the symmetry group is $[U(1) \times S^2]/Z_2$ where $U(1)$ denotes the phase ϑ , S^2 refers to the direction $\hat{\mathbf{n}}$ on the surface of a unit sphere (on which orientations are specified by angles (a, β) of the spin quantization axis) and Z_2 arises because of the symmetry of this state under the simultaneous transformation $\vartheta \rightarrow \vartheta + \pi$, $\hat{\mathbf{n}} \rightarrow -\hat{\mathbf{n}}$ [17, 25]. Thus the spinor components can be written as,

$$\begin{pmatrix} \Psi_+ \\ \Psi_0 \\ \Psi_- \end{pmatrix} = e^{i\vartheta} u \begin{pmatrix} 0 \\ 1 \\ 0 \end{pmatrix} = e^{i\vartheta} \begin{pmatrix} -\frac{1}{\sqrt{2}} e^{-ia} \sin\beta \\ \cos\beta \\ \frac{1}{\sqrt{2}} e^{ia} \sin\beta \end{pmatrix} \quad 2.19$$

For a spatially uniform superfluid, the order parameter is taken to be real. Thus for polar SF, we have the following two possibilities:

- (i) $\vartheta = a = \beta = \pi/2$ or $\vartheta = -a = \beta = \pi/2$ then $\Psi_+ = \Psi_- > 0$ and $\Psi_0 = 0$
- (ii) $\beta = \vartheta = 0$ or π and $0 \leq a \leq 2\pi$ then $\Psi_+ = \Psi_- = 0$ and $\Psi_0 > 0$

(I) Ferromagnetic case ($U_2/U_0 \leq 0$): In the ferromagnetic case, the ground state of Eq.(2.15) is a ferromagnetic state and the symmetry group is $SO(3)$ and the spinor components can be written as [17, 25],

$$\begin{pmatrix} \Psi_+ \\ \Psi_0 \\ \Psi_- \end{pmatrix} = e^{i\vartheta} u \begin{pmatrix} 1 \\ 0 \\ 0 \end{pmatrix} = e^{i\vartheta} \begin{pmatrix} e^{-ia} \cos^2\beta/2 \\ \sqrt{2} \cos\beta/2 \sin\beta/2 \\ e^{ia} \sin^2\beta/2 \end{pmatrix} \quad 2.20$$

If $\beta = \pi/2$ and $a = 0$ then $\Psi_+ = \Psi_-$, $\Psi_0 = \sqrt{2}\Psi_+$.

2.3 SBHM in the atomic limit ($t = 0$)

In order to see how the spin dependent interaction potential, U_2 will modify the ground state properties of the SBHM, let us first consider the atomic limit, that is, $t = 0$ and without an external magnetic field, $\eta = 0$. Thus in the atomic limit, the SBHM [Eq.(2.15)] can be expressed in term of the single site Hamiltonian, that is, $H = \sum H^0$ (site index i is removed since we are only considering the homogeneous case) where,

$$H^0 = -\mu n + \frac{U_0}{2} n(n-1) + \frac{U_2}{2} (\mathbf{S}^2 - 2n) \quad 2.21$$

Since the operators associated with Eq.(2.21) commute with each other, that is, $[n, \mathbf{S}^2] = 0$ then the eigenstate of H^0 can be expressed by a simultaneous eigenstate

$|n, S, m\rangle$ such that

$$H^0|S, m, n\rangle = E^0(\mu, U_0, U_2, n, S)|S, m, n\rangle \quad 2.22$$

where,

$$\begin{aligned} n|S, m, n\rangle &= n|S, m, n\rangle & 2.23 \\ S^2|S, m, n\rangle &= S(S+1)|S, m, n\rangle \\ E^0(n, S, \mu, U_0, U_2) &= -\mu n + \frac{U_0}{2}n(n-1) + \frac{U_2}{2}[S(S+1) - 2n] \end{aligned}$$

In the atomic limit, the ground state of Eq.(2.15) is totally an insulating phase. The chemical potential width, μ for a particular MI lobe with occupation density n can be found from the following condition [107]

$$E^0(S_1, n-1, \mu, U_0, U_2) < E^0(S, n, \mu, U_0, U_2) < E^0(S_2, n+1, \mu, U_0, U_2) \quad 2.24$$

where $S_{1,2}$ are the spin eigenvalues corresponding to the occupation densities $n \mp 1$.

(I) AF case ($U_2/U_0 > 0$): In AF case, the minimum of $E^0(n, S, \mu, U_0, U_2)$ corresponds to the minimum of S which depends upon the occupation density, n . Since the only quantum numbers related with Eq.(2.15) are S and n , thus the symmetry of BE statistics implies that for $n = \text{even}$, the minimum spin eigenvalue $S = 0$ and for $n = \text{odd}$, $S = 1$ [107]. Thus the boundary of each MI lobe can be calculated using the Eq.(2.24) as follows -

(i) $n = \text{odd}$ ($S = 1$): The condition $E^0(0, n-1) < E^0(1, n) < E^0(0, n+1)$ leads to the following inequality,

$$(n-1)U_0 < \mu < nU_0 - 2U_2 \quad 2.25$$

Equating these two μ values give a critical value of spin dependent interaction, $U_2/U_0 \leq 0.5$ below which odd MI lobes survive.

(ii) $n = \text{even}$ ($S = 0$): For $U_2/U_0 \leq 0.5$, the condition $E^0(1, n-1) < E^0(0, n) < E^0(1, n+1)$ gives

$$(n-1)U_0 - 2U_2 < \mu < nU_0 \quad 2.26$$

while for $U_2/U_0 > 0.5$, for all even MI lobes, $E^0(0, n-2) < E^0(0, n) < E^0(0, n+2)$ implies

$$U_0(n-1/2) - U_2 < \mu < U_0(n+1/2) - U_2 \quad 2.27$$

(II) Ferromagnetic case ($U_2/U_0 \leq 0$): In the ferromagnetic case, the minimum of E^0 corresponds to the maximum of $S = n$ and hence the boundary of each MI lobe is given by,

$$(n-1)(U_0 + U_2) < \mu < n(U_0 + U_2) \quad 2.28$$

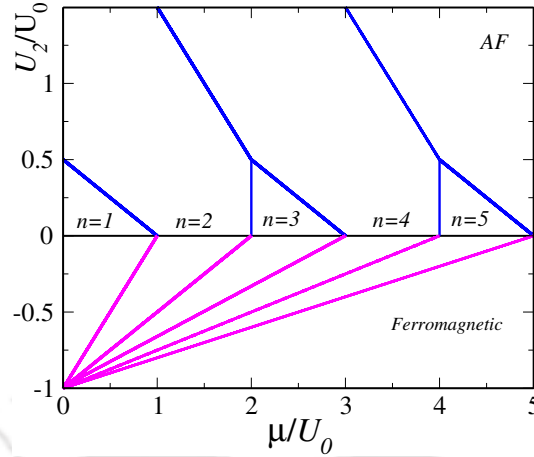


Figure 2.1: The MI lobe widths in the atomic limit ($t = 0$) corresponding to both the antiferromagnetic (AF) and ferromagnetic spin dependent interactions.

Finally the resultant phase diagram of the MI lobes in the atomic limit is shown in Fig.2.1. For smaller values of U_2/U_0 , both the odd and even MI lobes exist and the chemical potential width of even MI lobes increases with increasing the spin dependent interaction values and completely occupies the whole phase diagram beyond $U_2/U_0 > 0.5$. In the ferromagnetic case, the MI lobes are identical to that of the spin-0 case with equal chemical potential width at $U_2 = 0$ and gradually shrinks at $U_2 = -U_0$.

2.4 Tools to solve SBHM

2.4.1 Single site mean field theory (SSMFT)

In the previous section, we have seen how the spin dependent interaction potential affects the MI lobes in the atomic limit. To get a complete picture, now we shall obtain the phase diagrams by turning on the hopping strength, t . A single site mean field approximation can be used to decouple the hopping term which gives a qualitative phase diagram in the $\mu/U_0 - t/U_0$ plane at zero temperature in the homogeneous case.

In a site decoupling MFT (SSMFT), each operator is replaced by its original value with some fluctuations and then the hopping term can be written as [25, 108]

$$\begin{aligned}
 a_{i\sigma} &\rightarrow a_{i\sigma} + \delta a_{i\sigma} \\
 a_{i\sigma}^\dagger a_{j\sigma} &\simeq \langle a_{i\sigma}^\dagger \rangle a_{j\sigma} + a_{i\sigma}^\dagger \langle a_{j\sigma} \rangle - \langle a_{i\sigma}^\dagger \rangle \langle a_{j\sigma} \rangle \\
 &= \psi_{i\sigma} a_{j\sigma} + a_{i\sigma}^\dagger \psi_{j\sigma} - \psi_{i\sigma} \psi_{j\sigma}
 \end{aligned} \tag{2.29}$$

where $\delta a_{i\sigma}$ is the fluctuations in a_σ and we have neglected the quadratic fluctuation in Eq.(2.29).

Here we have defined the superfluid order parameter as,

$$\psi_{i\sigma} = \langle G.S. | a_{i\sigma} | G.S. \rangle = \langle G.S. | a_{i\sigma}^\dagger | G.S. \rangle \quad 2.30$$

where $|G.S.\rangle$ is the equilibrium ground state of the system. In SSMFT, each operator at site i is replaced by the average SF order parameter coming from the nearest neighbour sites, that is, $\phi_{i\sigma} = (1/z) \sum_{j=1}^z \psi_j$ where $z = 2d$ is the coordination number and d is the lattice dimension [Fig.2.2].

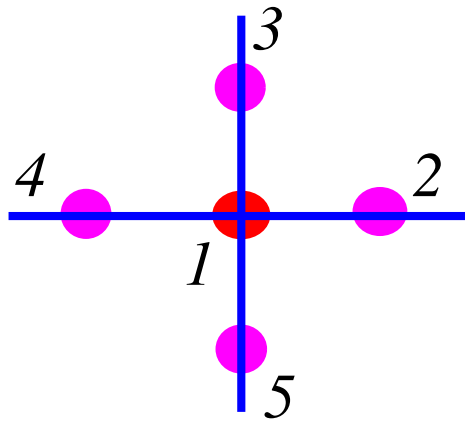


Figure 2.2: The decoupling of hopping term in a single site mean field theory (SSMFT). The circles represent the bosons at the lattice sites and the line indicates the hopping direction. In SSMFT, the average SF order parameter at site i (say 1) is coming from four nearest neighbouring sites, j ($j = 2 - 5$).

Now using Eq.(2.29), the Hamiltonian in Eq.(2.15) can be expressed as a sum of single site mean field Hamiltonian, $H = \sum_i H_i^{MF}$ where,

$$H_i^{MF} = \underbrace{-t \sum_{\sigma} (\phi_{i\sigma} a_{i\sigma}^\dagger + h.c.) + t \sum_{\sigma} \phi_{i\sigma}^* \psi_{i\sigma}}_H - \underbrace{\mu n_i + \frac{U_0}{2} n_i (n_i - 1) + \frac{U_2}{2} (S_i^2 - 2n_i)}_{H^0} \quad 2.31$$

For a homogeneous system, we can omit the site index and hence the order parameter at all sites are same, that is, $\phi_{i\sigma} = \psi_{i\sigma} = \psi_\sigma$ [Fig.2.2]. The mean field Hamiltonian in this approximation is given by,

$$H^{MF} = -t \sum_{\sigma} (\psi_{\sigma} a_{\sigma}^\dagger + h.c.) + t \sum_{\sigma} \psi_{\sigma}^* \psi_{\sigma} - \mu n + \frac{U_0}{2} n(n-1) + \frac{U_2}{2} (S^2 - 2n) \quad 2.32$$

To find the self consistent ground state energy of the system, we first form the

matrix elements of H^{MF} in the site occupation number basis, $|n_\sigma\rangle$ as,

$$\langle n'_+, n'_0, n'_- | H^{MF} | n_+, n_0, n_- \rangle = h^d + h^{od} \quad 2.33$$

where the h^d and h^{od} part includes the matrix elements coming from the diagonal and off-diagonal part of the mean field Hamiltonian respectively. Assuming the SF order parameters are real and starting with some guess values of ψ_σ , we diagonalize the matrix in Eq.(2.33) to obtain the ground state energy $E^g(\psi_\sigma)$ and the eigenfunction $\Psi_g(\psi_\sigma)$. Then from the updated wave function $\Psi_g(\psi_\sigma)$, we again reconstruct the matrix and repeat the diagonalization procedure until self consistency is reached [109]. Finally, the equilibrium SF order parameter and local density are given by,

$$\begin{aligned} \psi_\sigma^{eq} &= \langle \Psi_g(\psi_\sigma) | a_\sigma | \Psi_g(\psi_\sigma) \rangle \\ \rho_\sigma^{eq} &= \langle \Psi_g(\psi_\sigma) | n_\sigma | \Psi_g(\psi_\sigma) \rangle \end{aligned} \quad 2.34$$

Since for a spin-1 Bose gas, the SF order parameter is a vector quantity thus the total SF order parameter and occupation density are (we drop the superscript eq from hereafter)

$$\psi = \sqrt{\psi_\sigma^2} = \sqrt{\psi_+^2 + \psi_0^2 + \psi_-^2}, \quad \rho = \rho_+ + \rho_0 + \rho_- \quad 2.35$$

2.4.1.1 Ground state energy variation with occupation densities

The matrix in Eq.(2.33) needs to be diagonalized over a *sufficient Fock basis* $|n\rangle$ in order to find the self consistent ground state energy, $E^g(\psi_\sigma)$ of the system. For that purpose, we have plotted E^g for the MI-SF phase transition corresponding to both the odd ($\rho = 3$) [Fig.2.3 (a)] and the even ($\rho = 4$) [Fig.2.3 (b)] MI lobes in the AF case with different Hilbert spaces. It shows that E_g is diverging for smaller value of $|n\rangle$ ($= 3$) and still fluctuating for $n \leq 5$, while it saturates for $n \geq 6$. Thus it is reasonable to work with $n = 7$ for which matrix dimension, D is $D = 120$ after considering all possible combination between n_+ , n_0 and n_- [For example see Table 2.2].

possibilities	n_+	n_0	n_-	n	D
1	0	0	0	0	4
2	0	0	1	1	
3	0	1	0	1	
4	1	0	0	1	

Table 2.2: Different possible combinations between n_σ with $n = n_+ + n_0 + n_-$ for $n = 1$ which gives the matrix dimension, $D = 4$.

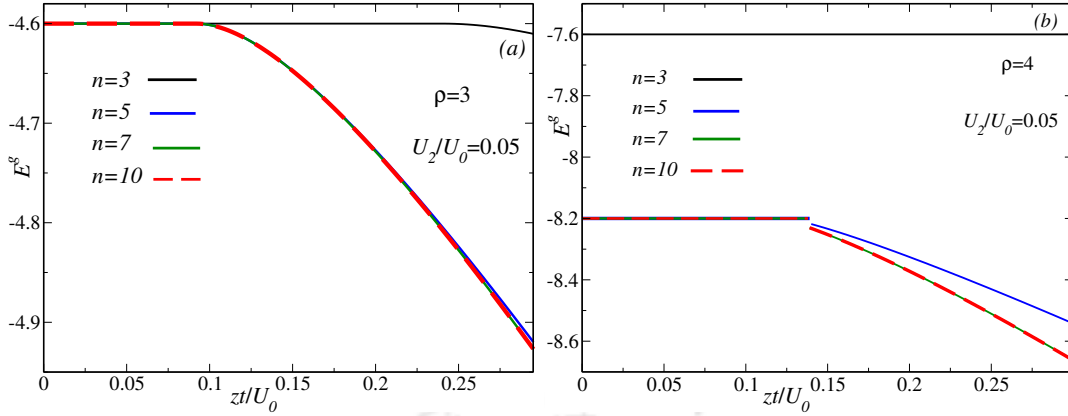


Figure 2.3: The ground state energy variation as a function of the occupation densities, n for the odd ($\rho = 3$) in (a) and the even ($\rho = 4$) MI lobes in (b) shows that E_g is saturated for $n \geq 5$. Also a first order transition is observed for the even MI lobes in the AF case.

We shall use this Hilbert dimension throughout this thesis to obtain the ground state phase properties for both the AF and ferromagnetic cases. Further, the ground state energy shows a jump from an MI to a SF phase indicating a first order phase transition for the even MI lobes and a continuous transition for the odd MI lobes.

2.4.1.2 Phase diagrams

The zero temperature phase diagrams computed based on the self consistent values of ψ and ρ in the homogeneous case for both values of the spin dependent interactions are shown in Fig.2.4. Although the two phase diagrams look similar but the major intriguing aspects appear in the AF case.

For $U_2/U_0 = 0.05$ [Fig.2.4 (a)], the even MI lobes ($\rho = 2, 4, \dots$) expand by encroaching into the SF phase compared to the odd MI lobes ($\rho = 1, 3, \dots$). Such asymmetry is due to the formation of the spin singlet (nematic) phase corresponding to the even (odd) MI lobes and hence leads to the stability of the even MI phase. While the outer boundary of each odd MI lobe is suppressed but for the even MI lobes, it remains constant at $\rho = \text{even}$ which is also expected from the atomic limit (see Fig.2.1). This shows that the chemical potential width and hence the energy gap, E_g for the odd MI lobes corresponds to $U_0 - 2U_2$, while for the even MI lobes, it is $U_0 + 2U_2$. Further the dashed line represents a first order phase transition from spin singlet MI to the SF phase and solid line indicates a second order transition from spin nematic MI to SF phase [25, 27, 29, 34, 110, 111].

In the ferromagnetic case [Fig.2.4 (b)], the phase diagram is similar to the spin-0 (scalar) case and the MI lobes are gradually decreasing with increasing chemical potential. The phase transition from the MI to the SF phase is second order and the chemical potential width for all MI lobes is now $U_0 + U_2$ (see Fig.2.1).

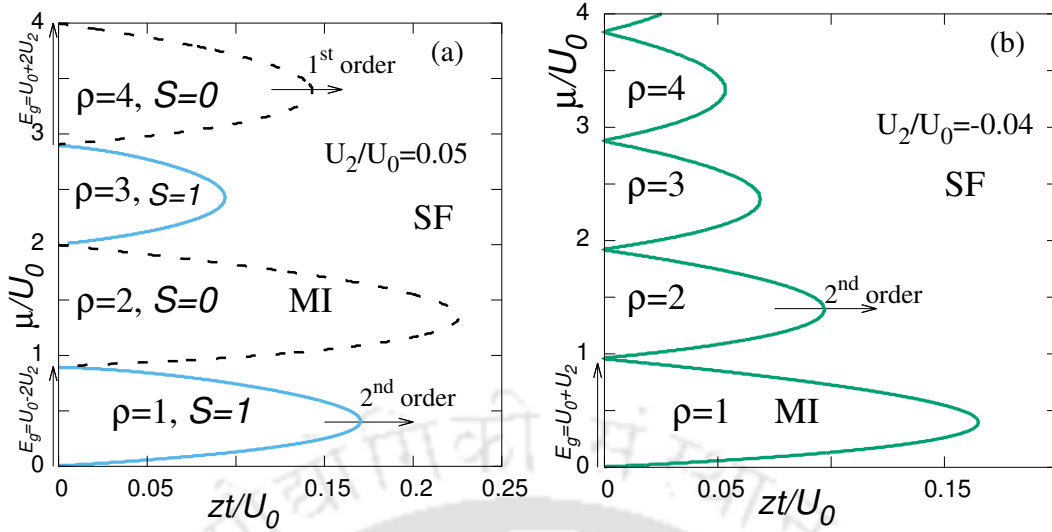


Figure 2.4: The mean field phase diagram corresponding to AF case ($U_2/U_0 = 0.05$) in (a) and ferromagnetic case ($U_2/U_0 = -0.04$) in (b). The solid line represents a second order and dashed line represents a first order transition respectively.

2.4.1.3 Order parameter and variational energy behaviour

To ascertain the various orders of the phase transition involved in the MI and the SF phases, particularly in the AF case, we shall study the order parameter variation as a function of tunneling strength, zt/U_0 . In the AF case, we have found that the spinor components behave as $\psi_{\pm} \neq 0$ and $\psi_0 = 0$ in the SF phase which is one of the possibilities as discussed in sec 2.2. For the odd MI lobes ($\mu/U_0 = 0.5$), the SF order parameter shows a continuous variation which is a signature of second order transition from the spin nematic MI to the SF phase for all values of $U_2/U_0 > 0$ [Fig.2.5 (a)]. While for the even MI lobes ($\mu/U_0 = 1.5$), the SF order parameter demonstrates a discontinuous variation from the MI to the SF phase indicating a first order transition at $U_2/U_0 = 0.05$. Subsequently at an increased value of the spin dependent interaction, namely, $U_2/U_0 \geq 0.15$, the scenario indicates a second order phase transition [111].

We have also studied the behaviour of the variational ground state energies, (E^v) at different locations of the MI and the SF phases in the AF case. The behaviour of E^v with the $\psi_+ = \psi_-$ and ψ_0 corresponding to three different values of zt/U_0 for $U_2/U_0 = 0.05$ are shown in Fig.2.5. For the even ($\rho = 2$) MI lobe ($\mu/U_0 = 1.5$), E^v has a single minimum in the MI phase at $zt/U_0 = 0.05$ [Fig.2.5 (b)] and then shows the formation of four degenerate minima, each corresponding to ψ_{\pm}, ψ_0 at $zt/U_0 = 0.22$ [Fig.2.5 (c)]. This implies that the system is gradually approaching towards the SF phase and finally a discontinuous evolution of the the global minimum to the four degenerate minima at $zt/U_0 = 0.3$ is a signature of the first order transition to the SF phase [Fig.2.5 (d)]. For the odd MI lobe ($\mu/U_0 = 2.5$), the continuous evolution of the global minimum signifies a second

order transition to the SF phase. In the ferromagnetic case, the ground state is infinitely degenerate for $U_2 = 0$ and has four degenerate minima for $U_2/U_0 = -0.04$, where the latter shows that the MI-SF phase transition is second order [25].

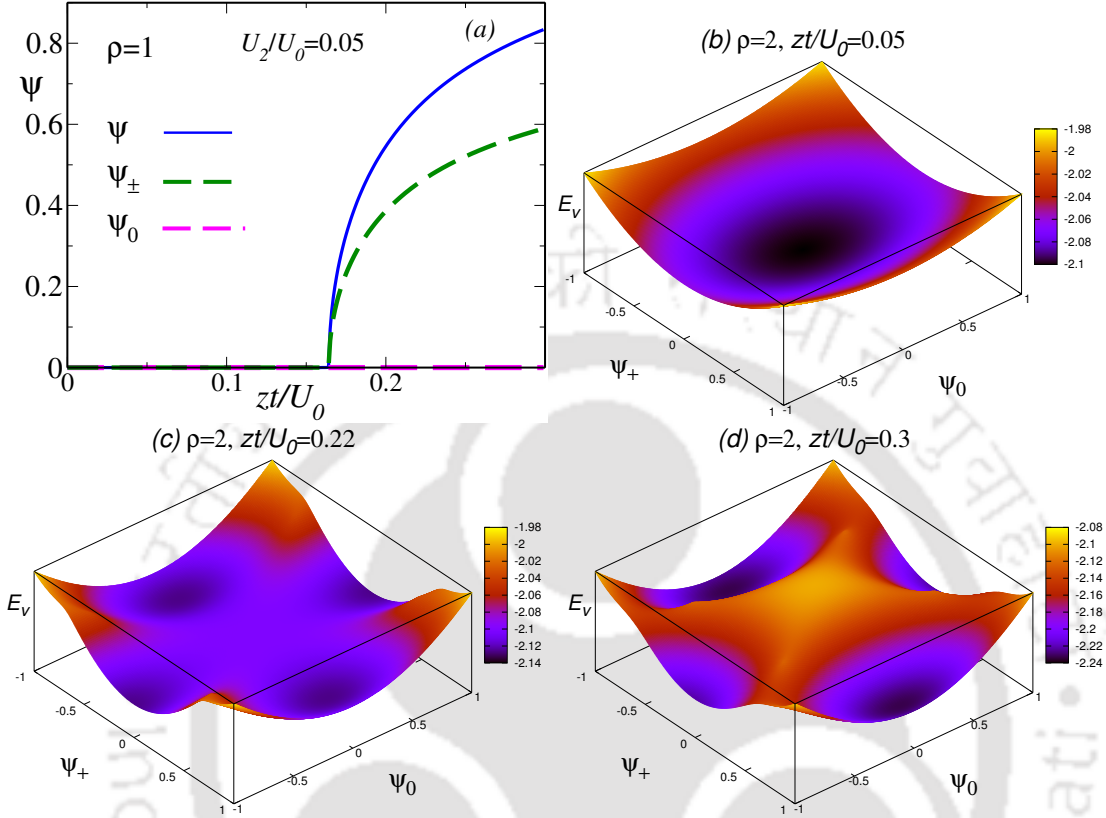


Figure 2.5: The SF order parameter variation for the first odd MI lobe ($\rho = 1$) in the AF case shows a second order transition (a). The variational energy (E^v) behaviour for the first even MI lobe ($\rho = 2$) shows a discontinuous evolution of the global minimum to four degenerate minima which is a signature of first order transition (b)-(d).

2.4.1.4 Spin eigenvalue and spin nematic order parameter

We have seen an asymmetry and different order of phase transition in the MI lobes due to the formation of spin singlet (nematic) phase in the AF case. To get a complete picture on the formation of the spin singlet-nematic states, we shall compute the total spin eigenvalue, S^2 [see Eq.(2.17)] corresponding to the even and odd MI lobes and they are shown in Fig.2.6 for $U_2/U_0 = 0.05$.

For the even MI lobes ($\mu/U_0 = 1.5$), $S^2 = S(S + 1) = 0$ implies that the spin eigenvalue, $S = 0$ in the MI phase which is a signature of the spin singlet pair formation and then shows a first order transition to the SF phase [Fig.2.6 (a)]. A spin singlet state is formed corresponding to an even number of bosons per lattice site, where each of $m_F = \pm 1$ can combine together to form a pair of $m_F = 0$ or the inverse scenario is also possible. Thus a spin singlet state appears to be

more stable due to the pair formation which requires a large hopping strength to break such pairs and push them to the SF phase. While for the odd MI lobes ($\mu/U_0 = 0.5$), $S^2 = S(S + 1) = 2$ implies that the spin eigenvalue, $S = 1$ in the MI phase corresponds to a spin nematic state, and hence follows what is a second order phase transition to the SF phase [Fig.2.6 (c)]. In the odd MI lobes, there is always an extra boson which can not form a pair and hence can easily hop at smaller values of the tunneling strength. Due to the formation of such spin singlet pair corresponding to the even MI lobes, which is more stable than the spin nematic phase, results in an odd-even asymmetry in the MI lobes.

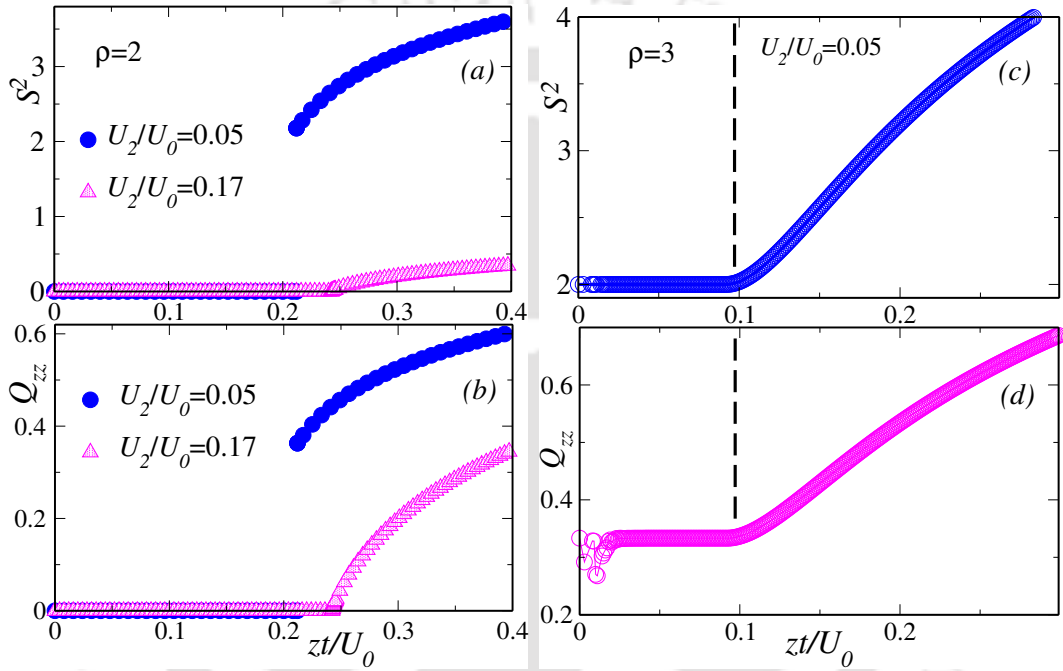


Figure 2.6: The spin eigenvalue, S^2 and spin nematic order parameter, Q_{zz} for the even ($\rho = 2$) (left) and the odd ($\rho = 3$) (right) MI lobes in the AF case. $Q_{zz} = 0$ for the spin singlet MI phase and a first order transition to the SF phase at $U_2/U_0 = 0.05$. For $U_2/U_0 = 0.17$, the spin singlet MI to the SF phase transition has a second order nature. For the spin nematic MI phase, $Q_{zz} \neq 0$ and shows a second order transition to the SF phase.

Also the magnetic properties of the spin singlet-nematic phases can be obtained from the z-component of the spin nematic order parameter which is defined as [27, 110, 111],

$$Q_{zz} = \langle S_z^2 \rangle - \frac{1}{3} \langle S^2 \rangle \quad 2.36$$

The variation of Q_{zz} from the spin singlet (nematic) MI to the SF phase as a function of tunneling strength, zt/U_0 for $U_2/U_0 = 0.05$ is shown in Fig.2.6. For the even MI lobes ($\mu/U_0 = 1.5$), the spin nematic order parameter, $Q_{zz} = 0$ in the MI phase indicates an on-site spin isotropy for the spin singlet phase following a first order transition to the SF phase for $U_2/U_0 = 0.05$ [Fig.2.6 (b)]. At $U_2/U_0 =$

0.17, the phase transition from spin singlet MI to the SF phase shows a second order character [111]. For the odd MI lobes ($\mu/U_0 = 0.5$), the finite values of the Q_{zz} implies an on-site spin anisotropy for the spin nematic state and then a second order transition is observed to the SF phase [Fig.2.6 (d)]. An oscillating behaviour of Q_{zz} is observed in the odd MI lobes for small values of zt/U_0 due to the limitation involved in the MFA. However, for smaller values of the spin dependent interaction, $U_2/U_0 \leq 0.025$, a first order phase transition from a spin singlet to nematic state is possible inside the MI lobes with even occupation densities in two dimensions a fact that was pointed out in Refs. [27, 34, 110, 111].

2.4.2 Perturbative mean field approximation (PMFA)

So far we have presented the mean field numerical phase diagrams for both values of the spin dependent interaction. In this section, we shall obtain an analytical phase diagram using perturbation theory and compare it with the mean field phase diagram. Using H' as a perturbation and H^0 as the unperturbed Hamiltonian in Eq.(2.31), the ground state energy after incorporating the first (E^1) and second (E^2) order corrections can be expressed in terms of series expansion of the order parameter ψ as,

$$E_n(\psi) = E^0 + E^1 + E^2 = E^0 + C_2(\mu, n, U_0, U_2, zt) \sum_{\sigma} \psi_{\sigma}^2 \quad 2.37$$

where $C_2(\mu, n, U_0, U_2, zt)$ includes the first, E^1 and the second, E^2 correction terms which can be calculated using the following eigenstate of H^0 defined as [24, 30, 112],

$$\begin{aligned} |S, S, n\rangle &= \frac{1}{\sqrt{f(Q, S)}} (a_+^\dagger)^S (\Theta^\dagger)^Q |\text{vacuum}\rangle \\ \Theta &= a_0^2 - 2a_+ a_-, \quad Q = \frac{n - S}{2} \\ f(Q, S) &= \frac{S! Q! 2^Q (2Q + 2S + 1)!!}{(2S + 1)!!} \end{aligned} \quad 2.38$$

The boundary between the MI-SF phase can be obtained by minimizing $E_n(\psi)$ with respect to ψ . In the MI phase, $\psi = 0$ thus $C_2 > 0$, while for the SF phase, $\psi > 0$ requires $C_2 < 0$. Thus at the boundary between the MI and the SF phases, $C_2(\mu, n, U_0, U_2, zt) = 0$.

As we have seen that for the even MI lobes, the spin eigenvalue $S = 0$, so using a non-degenerate perturbation theory, the equation for the boundary line is given by [24, 30] [see Appendix A],

$$\frac{1}{zt} = \frac{1}{3} \left[\frac{n+3}{nU_0 - \mu} + \frac{n}{\mu + 2U_2 - U_0(n-1)} \right] \quad 2.39$$

The critical tunneling strength, zt_c below which the system remain in the MI phase can be found by equating the two μ values of the above equation and is given by [24],

$$zt_c = (1/3)(U_0 + 2U_2)[(2n + 3) - \sqrt{4n^2 + 12n}] \quad 2.40$$

while for the odd MI lobes, the spin eigenvalue $S = 1$ and using a degenerate perturbation theory yields [24, 30],

$$\frac{1}{zt} = \frac{(n+2)/3}{a} + \frac{4(n-1)/15}{a+3U_2} + \frac{(n+1)/3}{\beta-2U_2} + \frac{4(n+4)/15}{\beta+U_2} \quad 2.41$$

where $a = \mu - (n-1)U_0$, $\beta = -\mu + nU_0$. Finally the phase diagram is obtained by using Eq.(2.39) for the even MI lobes and Eq.(2.41) for the odd MI lobes corresponding to $U_2/U_0 = 0.05$ is shown in Fig.2.7 (magenta line). The mean field phase diagram Fig.2.7 (green line) is also included in order to compare with the analytic PMFA phase diagram.

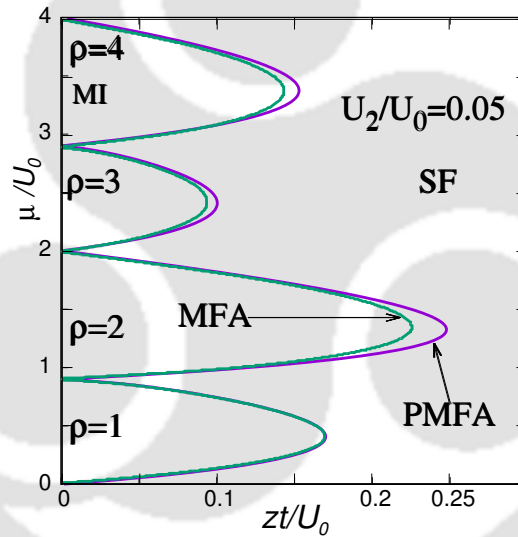


Figure 2.7: PMFA phase diagram corresponding to the AF case with $U_2/U_0 = 0.05$ (magenta line). The MFA phase diagram is included for comparison with the PMFA phase diagram (green line).

The PMFA phase diagram shows that the asymmetry is present in the insulating phase and the chemical potential width for each odd and even MI lobes is $U_0 \mp 2U_2$. Also the PMFA phase diagram is in complete agreement with the mean field phase diagram well inside the MI lobes. However a small discrepancy appears near the tip of the MI lobes and particularly such disagreement is prominent for the even MI lobes compared to the odd MI lobes [24, 30]. This suggests that the PMFA holds true for smaller values of the tunneling strength, that is, region having smaller ψ values where the perturbation is small. Further, it is relevant to point out that the MFA only holds deep inside the MI lobes where the fluctuations are small but near the tip of the MI lobes, MFA fails to handle the

fluctuations because it has limitations in lower dimensions. The phase diagrams in the ferromagnetic case are in complete agreement with each other.

2.4.3 Quantum Monte Carlo (QMC)

We have obtained the phase diagrams of the spin-1 Bose gas using the MFA as well as PMFA techniques and discussed the limitations present therein. Apart from such numerical methods, another elegant technique, such as, quantum Monte Carlo (QMC) can be used for obtaining an accurate estimate of the ground state properties of the BHM. The properties of the MI and the SF phases of a spin-0 BHM have been explored using various QMCs which are based on stochastic series expansion [113] and variational wave function methods [114, 115] etc. Recently, the ground state properties of the SBHM were studied using a variational QMC [116] and an exact QMC which is based on the stochastic Green function algorithm with directed updates and thus enable to calculate the many body Green functions [31, 111, 117, 118].

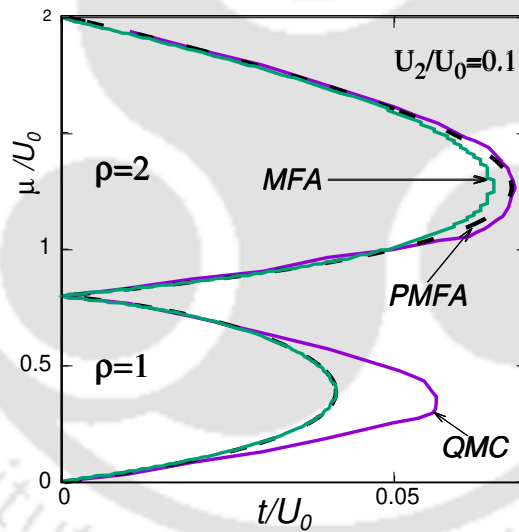


Figure 2.8: The QMC phase diagram obtained in Ref. [111] for the AF case with $U_2/U_0 = 0.1$ (magenta line). The MFA (green line) and the PMFA (dashed line) are also included for comparison with the QMC result. Figure courtesy for QMC data Parny et al., [111].

The zero temperature phase diagram corresponding to the AF case obtained using exact QMC method in Ref. [111] is shown in Fig.2.8 (magenta line) where the MFA [Fig.2.8 (green line)] and PMFA [Fig.2.8 (dashed line)] results are included for comparison. The QMC phase diagram is in complete agreement with the MFA and PMFA phase diagrams deep inside the MI lobes. But near the tip of the MI lobes, both the MFA and PMFA results shows a discrepancy with the QMC due to their limitations as pointed out in section 2.4.2. The QMC results also show a first

order transition from a spin singlet MI to SF phase as long as $U_2/U_0 \leq 0.15$ and supports a possible spin singlet to nematic phase transition for smaller values of $U_2/U_0 \leq 0.005$ [111] which was earlier predicted by the mean field theory in two dimensions [27, 29, 34, 110].

2.4.4 Density matrix renormalization group (DMRG)

So far we have discussed the various properties of the spin singlet and nematic MI phases and different order of phase transition to the SF phase using MFA and QMC techniques which are mostly valid for two and three dimensions. On the other hand, one dimensional studies of SBHM using a density matrix renormalization group (DMRG) shows the signature of a dimerized phase that breaks translational symmetry corresponding to the odd occupation densities along with the spin singlet phase for the even MI lobes [119, 120]. The DMRG phase diagram shows signature of such odd-even asymmetry in the AF case, and subsequently, the dimerized phase gradually vanishes at larger values of the spin dependent interaction strength [Fig.2.9]. Recently, a QMC study in one dimension also indicates the signature of a spin singlet and a dimerized phase and found the signature of a second order transition, since first order transition generally absent in one dimension [31].

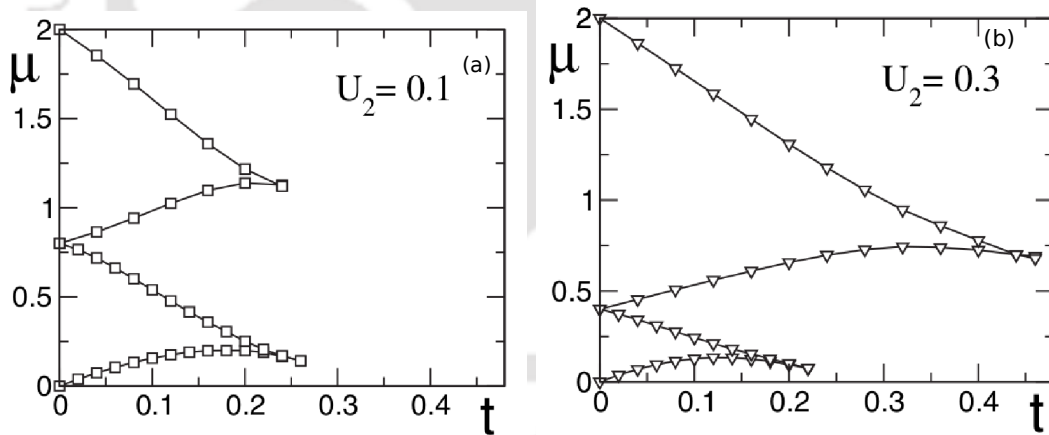


Figure 2.9: The DMRG phase diagrams obtained in Ref. [119] for the AF case with $U_2/U_0 = 0.1$ show the dimerized phase for odd MI lobes along with the spin singlet MI phase (a). The dimerized phase vanishes with increasing the spin dependent interaction value, $U_2/U_0 = 0.3$ (b). Figure courtesy for DMRG phase diagrams Rizzi et al., [119]

2.4.5 Multi-site mean field theory (MMFT)

We have seen the discrepancy between the mean field (SSMFT) phase diagram with that of the PMFA and QMC results near the tip of the MI lobes. Such

discrepancy arises since mean field often neglects the quantum fluctuations of various quantities. In order to improve the accuracy of the mean field results, one can extend the idea of SSMFT to a multi-site mean field theory (MSMFT) where the hopping between neighbouring sites are treated exactly assuming a cluster of sites N . For example, in a 2-site cluster mean field theory, the neighbouring sites, 1 and 2 are treated exactly while the other three sites for each are replaced by their mean field values [Fig.2.10]. In such case, the Hamiltonian can be written as,

$$H = -t \sum_a \left[(a_{1a}^\dagger a_{2a} + a_{2a}^\dagger a_{1a}) - \sum_{\langle ij \rangle} (a_{ia}^\dagger a_{ja} + h.c.) \right] \quad 2.42$$

$$+ \sum_{i=1}^2 \left[-\mu n_i + \frac{U_0}{2} n_i(n_i - 1) + \frac{U_2}{2} (\mathbf{S}_i^2 - 2n_i) \right]$$

where $\langle i, j \rangle$ includes only the nearest neighbours of sites 1 and 2 which can be found by applying the similar mean field approximation as used in section 2.4.1. To form the matrix elements of Eq.(2.42), the basis state now changes to $|n_{1\sigma}, n_{2\sigma}\rangle$

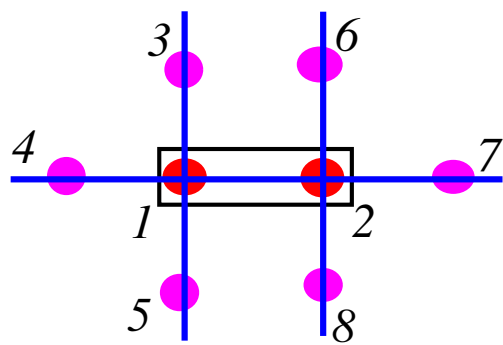


Figure 2.10: The decoupling of hopping term in a 2-site mean field theory. In 2-site MFT, sites 1 and 2 are treated exactly while the rest of the sites are replaced by the average SF order parameter from the nearest neighbouring sites, j ($j = 3 - 8$).

and hence,

$$\langle n_{1\sigma}, n_{2\sigma} | H^{MF} | n'_{1\sigma}, n'_{2\sigma} \rangle = -t \sum_{\sigma} \left[(\sqrt{n_1 + 1} \sqrt{n_2} \delta_{n_1+1, n'_1} \delta_{n_2-1, n'_2} + h.c.) + \quad 2.43 \right.$$

$$\left. 3\psi_{\sigma} (\sqrt{n_1 + 1} \delta_{n_1+1, n'_1} \delta_{n_2, n'_2} + \sqrt{n_1} \delta_{n_1-1, n'_1} \delta_{n_2, n'_2} + h.c.) - 6\psi_{\sigma}^2 \right]$$

$$+ \sum_{i=1}^2 \left[-\mu n_i + \frac{U_0}{2} n_i(n_i - 1) + \frac{U_2}{2} (\mathbf{S}_i^{2diag} - 2n_i) \right] \delta_{n_1, n'_1, n_2, n'_2}$$

$$+ \frac{U_2}{2} \sum_{i=1}^2 \langle n_{1\sigma}, n_{2\sigma} | \mathbf{S}_i^{2offdiag} | n'_{1\sigma}, n'_{2\sigma} \rangle$$

where \mathbf{S}_i^{2diag} and $\mathbf{S}_i^{2offdiag}$ can be calculated from Eq.(2.17).

n	SSMFT	2-site MFT	3-site MFT	4-site MFT
7	120	120^2	120^3	120^4
8	165	165^2	165^3	165^4
9	220	220^2	220^3	220^4
10	286	286^2	286^3	286^4

Table 2.3: The matrix dimension of the mean field Hamiltonian with n in MSMFT.

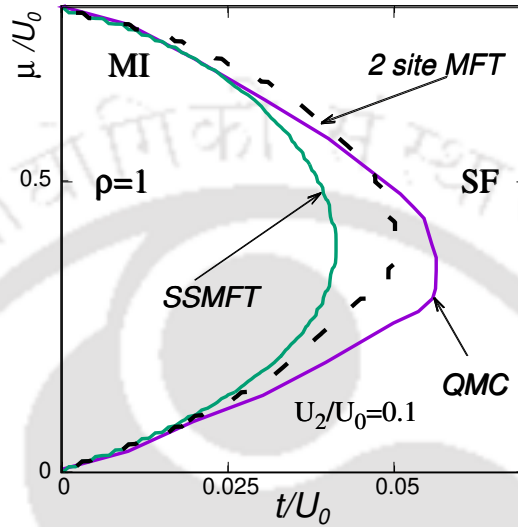


Figure 2.11: The phase diagrams obtained using 2-site MFT (dashed line) in the AF case with $U_2/U_0 = 0.1$. The single site MFT (solid green line) and the QMC (magenta solid line) phase diagrams are included for comparison. The 2-site MFT phase diagram is approaching towards the QMC phase diagram. Figure courtesy for QMC data Parry et al., [111].

Due to the change of the basis state structure, the matrix dimension of Eq.(2.43) dramatically increases to $|n_+, n_0, n_-\rangle^{c_s}$ where c_s is the cluster size. For a 2-site mean field theory, c_s corresponds to 2, that is $c_s = 2$ and say for $n = 7$, now the matrix dimension becomes 120^2 . Similarly, the matrix dimension for 3-site and 4-site MFT becomes extremely large as shown in Table 2.3 which is quite difficult to diagonalize due to the memory shortage. Keeping this fact in mind, we have used only 2-site MFT to see its consequences on the phase diagram and restricted our calculation up to the first MI lobe only. The phase diagram of 2-site MFT is shown in Fig.2.11 where we have included the QMC as well as SSMFT results for comparison. It shows that the critical tunneling strength, zt_c/U_0 for the MI-SF phase transition increases in the 2-site MFT and the resultant phase diagram is slightly approaching towards the PMFA and QMC results. This suggests that one can use multi-site, that is, a cluster mean field theory to remove the discrepancy near the tip of the MI lobes. Recently, the phase diagrams and the entanglement entropy of a spin-1 Bose gas have been studied using cluster mean field theory in Ref. [121]. However implementing a cluster MFT for spin-1 system will be much

more difficult due to the large matrix dimensions in presence of different type of interaction potential. Due to this limitation, we shall only focus on the SSMFT for our calculation throughout this thesis work.



Chapter 3: Percolation analysis of a disordered spinor Bose gas

In a spinor Bose gas, the bosonic atoms have multiple internal degrees of freedom, namely the orientation of their spins. These additional features compared to those corresponding to the spinless case should create new possibilities of studying physical phenomena, such as, quantum entanglement of spins [122], ground state properties [123], superfluidity of spin current [124] etc. However the experimental progress in spinor gases is hindered owing to the instability of the internal atomic or molecular states. The cause for the instability can be understood as follows. The excited states typically decay through spontaneous emission on time scales faster than that what is needed for the gas to equilibrate via collisions. However, due to the huge technological success, dilute atomic gases with internal degrees of freedom have been realized. Optically trapped spin-1 ^{23}Na is among the first ones to be reported [19, 21, 112, 125, 126]. The progress has been rapid since then with the discovery of spin-1 [70] and spin-2 manifold of ^{87}Rb [71, 72, 126, 127]. A flurry of activities have taken place since then. It is beyond the scope of the present work to furnish the large volume of literature that exists on the progress of the study of spinor Bose gases [16].

An interesting offshoot of the study of phase diagram of spinor Bose gases is to investigate the role of disorder present therein. Since inclusion of disorder in the context of an atomic gas loaded in an optical lattice is experimentally possible via speckle or periodic potentials [82, 85, 88, 128, 129], investigation of its influence on the phase diagram is a pertinent task. The phase diagram of the spinor particles is in general richer owing to the different signs of the spin dependent interaction that render among other features, a polar or a ferromagnetic nature for the SF phase [25, 112, 130].

The '*theorem of inclusions*' [80] forbids a direct MI to a SF phase transition in presence of disorder. A BG phase always intervenes in between. Since a BG phase originates due to arbitrarily large, although rarely occurring clusters of one type of phase present amidst another, and as statistically rare events are difficult to sample, elegant methods such as stochastic mean-field theory (SMFT) [131–133], QMC [79, 134–136] etc were formulated and used to study the BG phase.

In the homogeneous case, the mean field approach (MFA) [109], Gutzwiller [137] or the strong coupling expansion [81] can accurately locate the MI-SF phase transition. While in the disordered case, neither the MFA nor the Gutzwiller approach can reduce the site dependent Hamiltonian into a single site Hamiltonian. The other methods generally overestimate the location of BG-SF phase boundary. This is because, in presence of disorder, the SF order parameter varies randomly from one site to another and at the transition point there are some sites with vanishing SF order parameter, while the rest have finite SF order parameter.

To overcome the site inhomogeneities and for exact location of the phase boundaries, powerful numerical approaches, such as QMC [79, 80, 134–136], SMFT [131–133] and strong coupling expansion [81] etc have been applied on the disordered spin-0 (scalar) BHM. In QMC, the location of BG-SF phase transition is obtained from the finite size scaling, while the MI-BG boundary is determined from the energy gap data owing to a gap in the particle hole excitation spectra in the MI phase [80, 138]. The central idea of SMFT approach is to compute the local SF order parameter self consistently from a probability distribution function thereby showing a direct BG-SF phase transition [131–133].

Unlike the disordered scalar BHM, the disordered spinor BHM lacks such studies, except for the probabilistic mean field perturbative approximation (PMFA) which is the simplest version of SMFT have been developed to overcome the site inhomogeneity in local order parameter and obtained the phase diagram with the help of the Gutzwiller ansatz. This methods however gives no indication for the location of the transition points for the MI, BG and SF phases [107].

In this work, we take a different approach where we focus on the site decoupled mean field theory [109], and in order to take into account the site inhomogeneities, we introduce a simple physical quantity, χ defined as the fraction of the sites with finite SF order parameter and non-integer occupation density that will be used as indicator for the MI, BG or SF phases [139]. Although the location of MI-BG phase boundary can be determined depending on whether the indicator is zero or finite, but for determining the extent of the BG phase, we turn our attention into the percolation analysis and finite size scaling [140].

A percolation of the insulating sites is seen to occur with patches of the SF order surviving, thereby maintaining a zero macroscopic superfluid order, although compressible. The percolation scenario is robustly tested and a percolation threshold, implying the onset of a SF phase is obtained with the help of Hoshen-Kopelman (HK) algorithm [141]. Equipped with all of the above, we map out a phase diagram for the ($F = 1$) spinor bosons in a two dimensional square lattice, where we specifically focus on the emergence and sustenance of the BG phase in both antiferromagnetic and ferromagnetic cases based only on the critical value of the indicator and compared our phase diagrams with the results obtained by Lacki *et al.* [107].

We organize this chapter as follows. In the next section, we briefly outline the theoretical formalism of the MFA to study the disordered SBHM and the relevant quantities to characterize three different phases. After that, we have included an elaborate discussion on the results for the order parameters, indicator and percolation analysis that are required to obtain the phase diagrams in details.

3.1 Model

The behavior of ultracold atoms loaded in an optical lattice with hyperfine spin $F=1$ can be well described by a SBHM [17, 18] which is written as,

$$H = -t \sum_{\langle i,j \rangle} \sum_{\sigma} (a_{i\sigma}^{\dagger} a_{j\sigma} + h.c.) - \sum_i (\mu - \epsilon_i) n_i + \frac{U_0}{2} \sum_i n_i (n_i - 1) + \frac{U_2}{2} \sum_i (\mathbf{S}_i^2 - 2n_i) \quad 3.1$$

where all the symbols are carrying the same meaning as discussed in section 2.2 of the chapter 2. ϵ_i is the on-site disorder at site i , which is randomly chosen from a uniform probability distribution extended over $[-\Delta, \Delta]$ where Δ is the strength of the disorder. The probability distribution, $P(\epsilon_i)$ of ϵ_i is given by,

$$\begin{aligned} P(\epsilon_i) &= \frac{1}{\Delta} : -\Delta \leq \epsilon_i \leq \Delta \\ &= 0 : \text{otherwise} \end{aligned} \quad 3.2$$

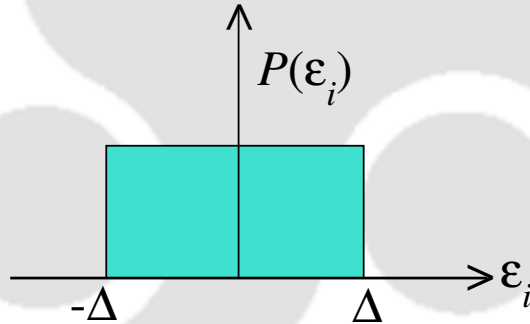


Figure 3.1: The schematic representation of the probability distribution, $P(\epsilon_i)$ of the on-site disorder potential, ϵ_i .

Here we shall use the SSMFT as discussed in section 2.4.1 of chapter 2 and finally the SBHM [Eq.(3.1)] can be written as a sum of single site Hamiltonian as, $H = \sum_i H_i^{MF}$ where,

$$H_i^{MF} = -t \sum_{\sigma} (\phi_{i\sigma} a_{i\sigma}^{\dagger} + h.c.) + t \sum_{\sigma} \phi_{i\sigma}^* \psi_{i\sigma} - (\mu - \epsilon_i) n_i + \frac{U_0}{2} n_i (n_i - 1) + \frac{U_2}{2} (\mathbf{S}_i^2 - 2n_i) \quad 3.3$$

with $\phi_{i\sigma} = (1/z) \sum_j \psi_{j\sigma}$. The sum j includes all nearest neighbors at the site i of a square lattice with $z = 4$, z being the coordination number.

In order to see the effects of disorder, we first diagonalize the $\langle n_{i\sigma} | H_i^{MF} | n'_{i\sigma} \rangle$ with $n_i = 7$ self consistently as discussed in section 2.4.1 of chapter 2 on a two dimensional square lattice of size $L \times L$ and the equilibrium value of the SF order

parameter and compressibility are given by,

$$\begin{aligned}\psi_{i\sigma} &= \langle \Psi_g(\psi_{i\sigma}) | a_{i\sigma} | \Psi_g(\psi_{i\sigma}) \rangle \\ \rho_i &= \langle \Psi_g(\psi_{i\sigma}) | n_{i\sigma} | \Psi_g(\psi_{i\sigma}) \rangle \\ \kappa_i^2 &= \langle \rho_i^2 \rangle - \langle \rho_i \rangle^2\end{aligned}\tag{3.4}$$

Finally the site averaged SF order parameter, $\bar{\psi}$ and compressibility, $\bar{\kappa}$ are given by,

$$\bar{\psi} = \left[\frac{1}{L^2} \sum_{i=1}^{L^2} \psi_i \right]_{sample} \quad \text{and} \quad \bar{\kappa} = \left[\frac{1}{L^2} \sum_{i=1}^{L^2} \kappa_i \right]_{sample}\tag{3.5}$$

where we have considered a system of size $L \times L = 30 \times 30$ and has been kept the same throughout our calculations (unless mentioned otherwise) and the *sample* in the subscript refers to the fact that results are averaged over different realizations of disorder. Here we have used 100 different disorder realizations and confirmed that the fluctuations are remarkably negligible.

In the clean state, the mean field Hamiltonian is homogeneous and hence the order parameters are uniform throughout the entire lattice. In the strong interaction limit, the system is in the MI phase, while the system shows a SF behaviour in the weak interaction limit as pointed out in section 2.4.1 of chapter 2.

In presence of disorder, the mean field Hamiltonian becomes inhomogeneous and hence the SF order parameter will vary from one site to another. Further, in the pure case, the system can make direct phase transition from MI to SF phase controlled by the system parameter t and U_0 . But as soon as disorder is present, the BG phase always intervenes between the SF and the MI phases. The BG phase is defined as the zero SF order parameter with no gap in the particle hole excitation spectra. Thus the three types of phases that are likely to be present in a system of disordered interacting bosons in an optical lattice can be characterized as,

- (i) SF phase: $\psi_i \neq 0$, $\rho_i \neq \text{integer}$ and $\kappa_i > 0$
- (ii) BG phase: $\psi_i = 0$, $\rho_i \neq \text{integer}$ and $\kappa_i > 0$
- (iii) MI phase: $\psi_i = 0$, $\rho_i = \text{integer}$ and $\kappa_i = 0$

3.2 Results

3.2.1 Antiferromagnetic case ($U_2/U_0 = 0.1$)

At first, we shall study the effects of the disorder (ϵ_i) present in the chemical potential (μ) corresponding to the AF case with $U_2/U_0 = 0.1$. Two different strengths of disorder will be considered in order to see the appearance of the BG

phase. The reason for choosing different disorder strengths can be understood as follows. In the AF case, the energy gap, E_g for the odd MI lobes is $U_0 - 2U_2$, while for the even MI lobes, it corresponds to $U_0 + 2U_2$ which are calculated in section 2.3 of chapter 2. In order to go from a gapped MI phase to a gapless BG phase, the disorder strength, Δ/U_0 should be greater than or equal to the width of the respective MI lobes. Since we are using a uniform probability distribution of disorder from $-\Delta$ to Δ , so the critical disorder strength, Δ_c should extend from $-E_g/2$ to $+E_g/2$, that is, $\Delta_c/U_0 = 0.4$ for the odd MI lobes and $\Delta_c/U_0 = 0.6$ for the even MI lobes corresponding to $U_2/U_0=0.1$. In this work, we are using the same parameter values as used in Ref. [107] in order to see the closeness of the results obtained among the two cases.

3.2.1.1 The behavior of the SF order parameter and compressibility

The variation of the averaged SF order parameter, $\bar{\psi}$ and the compressibility, $\bar{\kappa}$ are shown for the first odd ($\mu/U_0 = 0.4$) in Fig.3.2 (left) and first even ($\mu/U_0 = 1.4$) in Fig.3.2 (right) MI lobes for two different strengths of the disorder. In the pure case, the system remains in the MI phase with $\bar{\psi}$ and $\bar{\kappa}$ as zero till $zt/U_0 = 0.16$ for the first odd [Fig.3.2 (a), (b)] and $zt/U_0 = 0.26$ for the first even [Fig.3.2 (c), (d)] MI lobes. These values are below the critical tunneling strength zt_c/U_0 [see Eq.(2.40)] and beyond this critical value, the system goes to the SF phase.

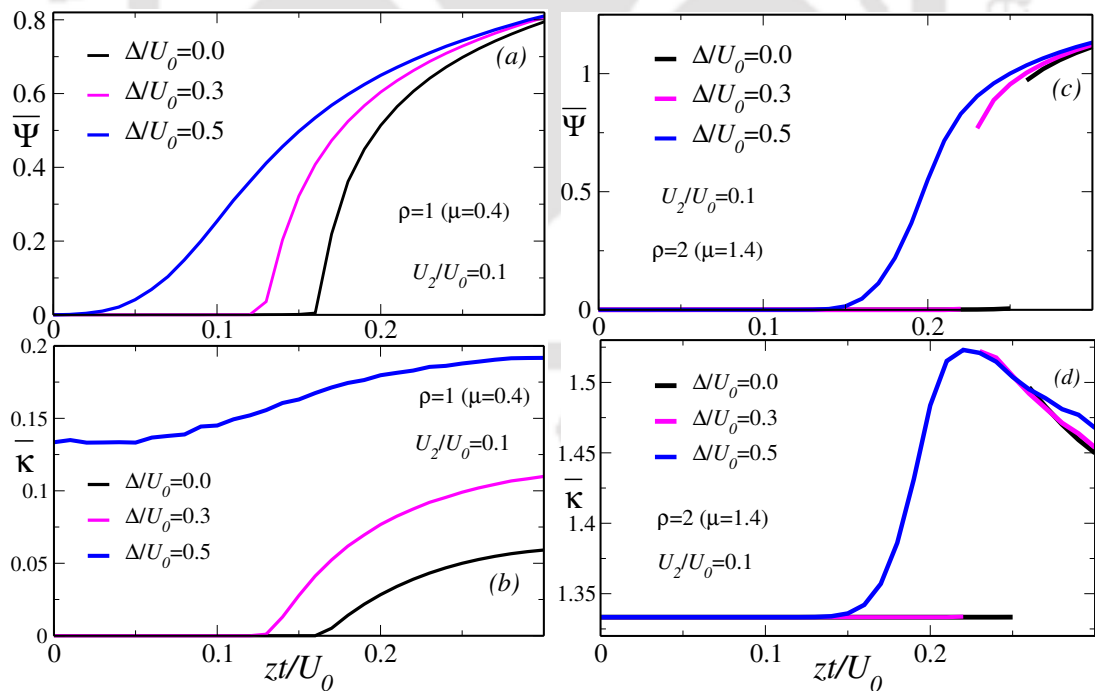


Figure 3.2: The variation of averaged SF order parameter, $\bar{\psi}$ and compressibility, $\bar{\kappa}$ at $U_2/U_0 = +0.1$ with disorder strengths Δ/U_0 for the odd ($\mu/U_0 = 0.4$) in (left) and even ($\mu/U_0 = 1.4$) in (right) MI lobes.

In presence of disorder, the BG phase intervenes in between the MI and the SF

phases and the region spanned by the MI phase gradually decreases with increasing Δ/U_0 . For the odd MI lobe, the MI region starts to shrink due the appearance of the BG phase at $\Delta/U_0 = 0.3$ and shows a continuous phase transition to the SF phase [Fig.3.2 (left)]. At $\Delta/U_0 = 0.5$, the BG phase completely destroys the MI phase since this value exceeds the critical value of disorder strength and results only the existence of the BG and SF phases as pointed out earlier in section 1.7.1 of chapter 1 [Fig.3.2 (left)]. Thus by looking through naked eye, one can say that the BG region extends up to $zt/U_0 \simeq 0.067$ as perceived from the vanishing of $\bar{\psi} \leq 0.02$ and $\bar{\kappa} > 0$ at $\Delta/U_0 = 0.5$. However determination of an exact location for the BG-SF phase transition based on $\bar{\psi}$ and $\bar{\kappa}$ is absolutely impossible due to their site dependency.

For the even MI lobe, the MI phase starts to diminish due to the appearance of the BG phase and the MI-SF phase transition continues to be first order for $\Delta/U_0 = 0.3$. While at $\Delta/U_0=0.5$, the MI phase still survives since this value is well below the critical disorder strength ($\Delta_c/U_0 = 0.6$) but the MI-SF transition becomes a second order phase transition [Fig.3.2 (right)]. We have also investigated the behavior of the individual spinor, $\bar{\psi}_\sigma$ and compressibility, $\bar{\kappa}_\sigma$ components with disorder strengths and they are also showing similar behaviour as that of $\bar{\psi}$ and $\bar{\kappa}$ corresponding to both the odd and even MI lobes.

3.2.1.2 Spin eigenvalue and spin nematic order parameter

In the disorder free case, we have studied the spin eigenvalue as well as magnetic properties of the spin singlet-nematic MI phases in section 2.4.1.4 of chapter 2. Therefore it is necessary to study how the spin eigenvalue and spin nematic order parameter behave as a function of disorder strength particularly in the BG phase. We have shown the variation of site averaged $\bar{\mathbf{S}}^2$ and \bar{Q}_{zz} in the AF case with Δ/U_0 for the odd ($\mu/U_0 = 0.4$) in Fig.3.3 (left) and the even ($\mu/U_0 = 1.4$) in Fig.3.3 (right) MI lobes. To compute $\bar{\mathbf{S}}^2$ and \bar{Q}_{zz} , we have increased the *sample* average up to 500 different realization of different disorder strengths for both the MI lobes.

At $\Delta/U_0 = 0.3$, $\bar{\mathbf{S}}^2 = 2$ for the odd and $\bar{\mathbf{S}}^2 = 0$ for the even MI lobes and the corresponding transition to the SF phase still remains a second and first order respectively. However, at $\Delta/U_0 = 0.5$, since the BG phase completely destroys the first odd MI lobe thus the spin eigenvalue for the BG phase oscillates between 0 and 2, that is, $0 < \bar{\mathbf{S}}^2 < 2$ [Fig.3.3 (a)] [107]. For the even MI lobe, $\bar{\mathbf{S}}^2 = 0$ in the MI phase and then shows a second order phase transition to the SF phase at $\Delta/U_0 = 0.5$ [Fig.3.3 (c)].

The spin nematic order parameter vanishes for the spin singlet MI phase and it is showing similar behaviour as that of SF order parameter and $\bar{\mathbf{S}}^2$ for both values of the disorder strengths [Fig.3.3 (d)]. For the odd MI lobe, \bar{Q}_{zz} is finite for

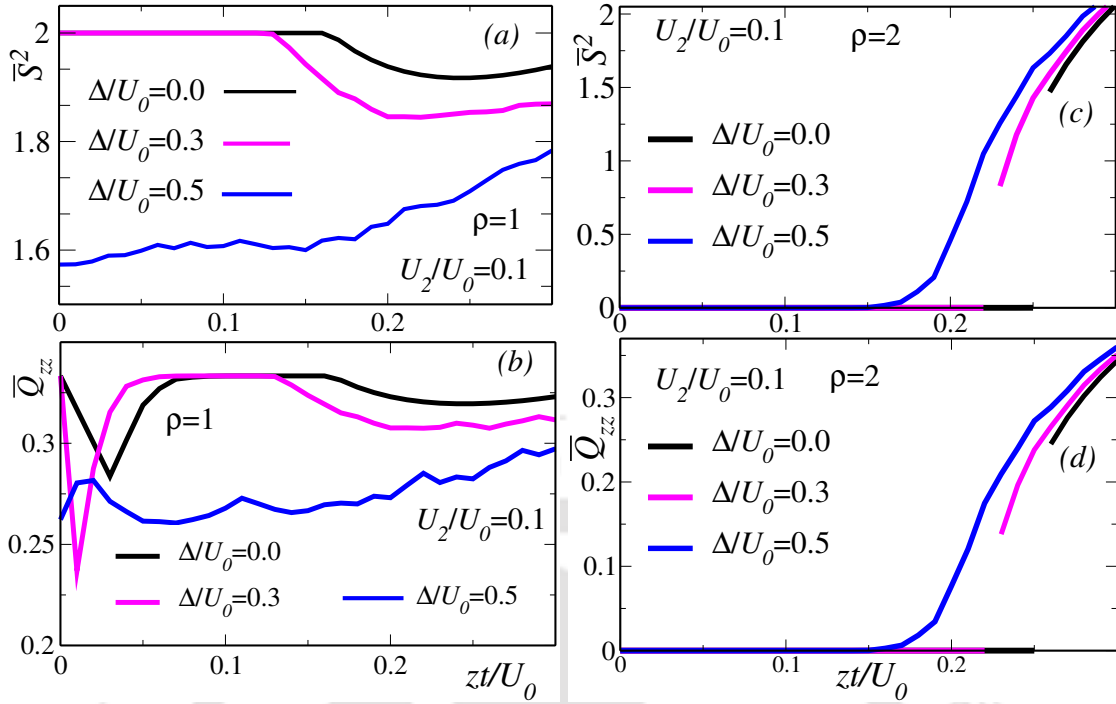


Figure 3.3: The variation of averaged spin eigenvalue, \bar{S}^2 and spin nematic order parameter, \bar{Q}_{zz} with $U_2/U_0 = +0.1$ for the odd ($\rho = 1$) in (left) and even ($\rho = 2$) in (right) MI lobes with different Δ/U_0 .

the spin nematic MI phase at $\Delta/U_0 = 0.3$ but it is also oscillating similar to \bar{S}^2 for the BG phase at $\Delta/U_0 = 0.5$ [Fig.3.3 (b)].

3.2.1.3 Indicator for the MI, BG and SF phases

Although the average $\bar{\psi}$ and $\bar{\kappa}$ shows the signature of the BG phase but via these averaged quantities, it is quite difficult to locate the precise location for the MI-BG and the BG-SF phase transition, owing to the fact that the ψ_i and the ρ_i are explicitly site dependent. Thus at the transition point there are some sites with zero SF order parameter and integer occupation densities, while other sites may have zero SF order parameter and non integer occupation densities.

In order to circumvent this difficulty, we define a measurable quantity, χ which is defined as,

$$\chi = \frac{\text{Sites with } \psi_i \neq 0 \text{ and } \rho_i \neq \text{integer}}{\text{Total numbers of sites}} \quad 3.6$$

The main reason to define χ is to distinguish between the MI, BG and the SF phases where depending upon the value of χ , we will be able to easily characterize the three different types of phases.

At this point, one can ask, what will be the value of ψ_i and ρ_i which can define the MI or the SF phase. Since we see from the behavior of $\bar{\psi}$ and $\bar{\kappa}$ corresponding to the pure case that the system will remain in the MI phase till $zt < zt_c$ having vanishingly small $\psi_{i\sigma}$ (values below $O(2 \times 10^{-1}) \pm \delta$) and the occupation density

$\rho_i = N \pm \delta$ where $N = 0, 1, 2, 3, \dots$ and δ is of $O(10^{-3})$. These values are set for numerical convergence of the parameters corresponding to the MI phase. The variation of χ with tunneling strength, zt/U_0 with Δ/U_0 is shown in Fig.3.4 (a) for the odd and Fig.3.4 (b) for the even MI lobe.

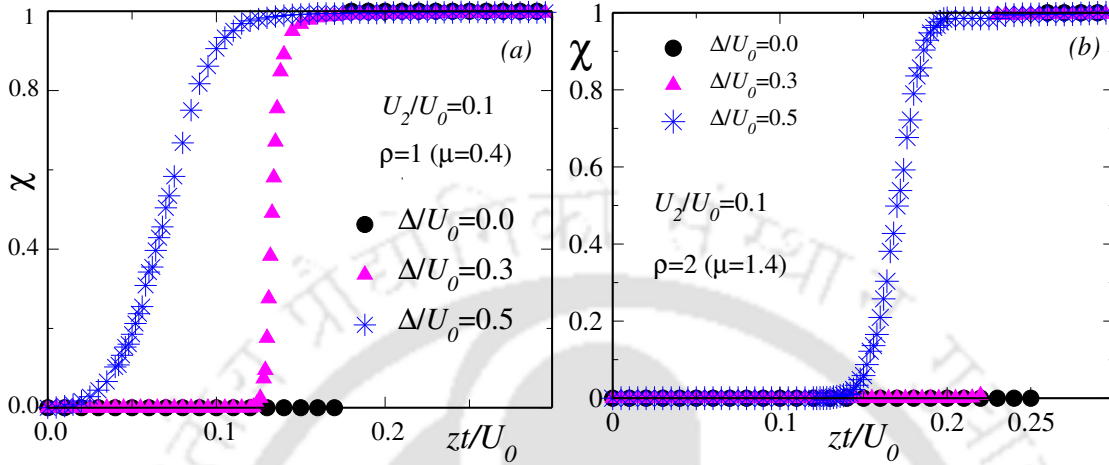


Figure 3.4: The variation of χ in the AF case with $U_2/U_0 = +0.1$ for the odd ($\mu/U_0 = 0.4$) in (a) and even ($\mu/U_0 = 1.4$) in (b) MI lobes with different Δ/U_0 .

In the disorder free case, we see that χ makes direct transition from 0 to 1 emphasizing an unhindered MI-SF transition for both the odd [Fig.3.4 (a)] and even [Fig.3.4 (b)] MI lobes. When $zt < zt_c$, the system is in MI phase, that is all sites have $\psi_i = 0$ and $\rho_i = \text{integer}$ and thus χ takes the value 0. While for $zt > zt_c$, the system becomes a SF phase with $\psi_i \neq 0$ and $\rho_i \neq \text{integer}$ and thereby χ assumes a value 1.

As soon as disorder is introduced, the direct transition of χ from 0 to 1 is prohibited, as indicated by a gradual increase due to the presence of the BG phase. For the odd MI lobe ($\mu/U_0 = 0.4$), χ remains zero till $zt/U_0 = 0.133$, beyond which χ starts to increase ($0 < \chi < 1$) indicating that some sites with $\rho_i = \text{integer}$ in the MI regime start evolving and the system moves towards the BG regime with $\rho_i \neq \text{integer}$ at $\Delta/U_0 = 0.3$ [Fig.3.4 (a)]. With increase of disorder strength, that is, at $\Delta/U_0 = 0.5$, we see that χ only takes finite values and ultimately goes to unity as a function of zt/U_0 , indicating that the region spanned by the BG phase continues to increase and results in vanishing of the MI phase [Fig.3.4 (a)].

For the even MI lobe ($\mu/U_0 = 1.4$), although χ only takes values between 0 and 1, however the region occupied by the MI phase shrinks as compared to the pure case due to the emergence of the BG phase at $\Delta/U_0 = 0.3$ [Fig.3.4 (b)]. At $\Delta/U_0 = 0.5$, χ again takes finite values owing to the presence of the BG phase between 0 and 1, while the MI phase still exists since the critical disorder strength is higher for the even MI lobe as discussed in the previous section.

In a similar manner, we can also define the χ_σ involving $\psi_{i\sigma}$ and $\rho_{i\sigma}$ which will

aid in the study of the individual spinor components. The χ_{\pm} are computed by suitably modifying the numerator of the Eq.(3.6) with $\psi_{i\pm} \neq 0$ and $\rho_{i\pm} \neq 0.5$ for the odd ($\rho = 1$) and $\psi_{i\pm} \neq 0$ and $\rho_{i\pm} \neq 0.667 \pm \delta$ for the even ($\rho = 2$) MI lobes respectively. For determining χ_0 , we set the condition $\psi_{i0}=0$ and $\rho_{i0} > 0.001$ for the first and $\psi_{i0} = 0$ and $\rho_{i0} \neq 0.667 \pm \delta$ for the second MI lobes respectively. The components of χ_{σ} show similar kind of behavior as that of χ in presence of disorder.

3.2.1.4 Observation of the percolation phenomena

At this point we will try to figure out one of our earlier questions that was posed in this regard, whether is it possible to locate the transition point for the BG-SF phase transition in the presence of disorder with confidence. Further what will be the extent of the BG phase, that is, whether the whole region ($0 < \chi < 1$) is a BG phase, or there is certain amount of SF phase still left in presence of disorder. To answer these questions, we have to really look at the concept of the appearance of SF percolating cluster of sites with non integer occupation densities and finite values of the SF order parameter.

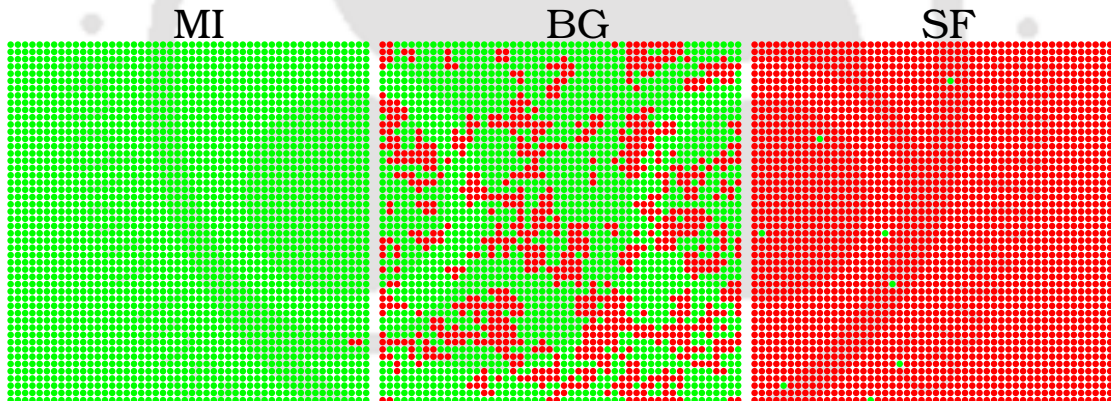


Figure 3.5: The real space plots of the occupation densities, ρ_i for lattice size $L \times L = 50 \times 50$ at $\Delta/U_0 = 0.5$ with $U_2/U_0 = +0.1$ and $\mu/U_0 = 0.4$ corresponding to the MI phase at $zt/U_0 = 0.001$ (left), a BG phase at $zt/U_0 = 0.06$ (middle) and finally the SF phase at $zt/U_0 = 0.3$ (right). The light green circles (light shades) represent integer densities and deep red circles (deep shades) represent the non integer densities.

In order to understand what do we mean by a SF percolating cluster, we have shown typical real space plots of ρ_i for three values of zt/U_0 corresponding to the three different phases of the system in Fig.3.5. The plots illustrate the values of the local density ρ_i in a square lattice of size $L \times L = 50 \times 50$ for a single realization of disorder. The parameter corresponding to the plots are $\Delta/U_0 = 0.5$ and $\mu/U_0 = 0.4$ ($\rho = 1$) in the AF case ($U_2/U_0 = +0.1$). The light green circles are the indicators for the integer densities, while the deep red circles denote the

non integer densities. The figures shown in each column depicts MI phase at $zt/U_0 = 0.001$ [Fig.3.5 (left)], a BG phase at $zt/U_0 = 0.06$ [Fig.3.5 (middle)] and the SF phase at $zt/U_0 = 0.3$ [Fig.3.5(right)].

In the clean state, the system splits into two, the MI patches with all sites having zero ψ_i (not shown here) and integer densities ρ_i as shown by light dots in Fig.3.5 (left) till $zt/U_0 < zt_c/U_0$ and the SF island with finite ψ_i and non integer densities ρ_i at $zt/U_0 > zt_c/U_0$ separated by a sharp boundary. As soon as disorder is introduced, the BG phase tries to mix two phases by removing the boundary between them. So the sites with zero ψ_i and integer densities attempt to evolve towards zero ψ_i and non integer densities as shown in Fig.3.5 (middle) which is a BG phase and then finally percolates for the first time towards the SF phase with non zero ψ_i and non integer occupation densities Fig.3.5 (right).

3.2.1.5 Percolation probability and finite size scaling

To extract different phases of the system, we shall concentrate on the appearance of the SF clusters which percolate throughout the entire lattice for the first time. In the MI phase, all sites have integer particle densities and hence there will be no SF cluster, while in the BG phase, some of the sites have non integer densities and thus the SF clusters will be trapped by other clusters with sites having integer densities. Finally with the increase in the tunneling strength, the SF clusters will start to percolate throughout the lattice resulting in a SF phase for the system. Thus the BG region can be identified in between the MI and the SF phases where SF clusters exist, however do not percolate across the lattice [133].

When a SF cluster percolates through an infinite lattice it is known as an infinite cluster, while when it percolates through a finite lattice it is known as a percolating or spanning cluster. Since we are dealing with a finite size of the system for our numerical work, we shall aim to find a spanning cluster using Hoshen-Kopelman (HK) algorithm [141].

Whether a SF cluster will percolate can be well understood from the following quantity, P_{perc} which is defined as [140],

$$P_{perc} = \frac{\text{Sites in a spanning cluster}}{\text{Total number of occupied sites}} \quad \mathbf{3.7}$$

Here we briefly outline the idea used in the HK algorithm for the sake of completeness. It is based on the special application of the union-find algorithm where it aims to assign a label to each cluster. For that we represent our 2D lattice as a matrix and label all occupied sites initially with -1 and unoccupied sites with 0. Our cluster index starts with 1. Corresponding to each occupied site, every time we check the neighbours at the top and left corner of the current site. If both sites are empty, we label a new cluster number that has not used

so far. Else, if the site has one occupied neighbour, then we assign same cluster number to the current site. If both neighbouring sites are occupied, then we set the smallest number cluster label of the occupied neighbours to use as the label for the current site. To link two clusters, we create a union between both labels and set the site as the lowest of the two labels. When we burn the lattice for a second time, we collect the unions and update the lattice.

In Fig.3.6(a) we study P_{perc} as a function of χ at a disorder strength $\Delta/U_0 = 0.5$ and $\mu/U_0 = 0.4$ in the AF case. It is found that P_{perc} is zero till $\chi = \chi_c = 0.581$ for a lattice size $L \times L = 128 \times 128$ which is close to the critical threshold value for the occupation probability $p_c = 0.592$ for random site percolation problem in an infinite 2D square lattice [140] and shows finite value above $\chi > \chi_c$. This similarity is only coincidental as the random site percolation model is a classical problem where sites are randomly occupied, while we have a system of quantum particles and the driving parameters are systematically varied at a given value of random disorder.

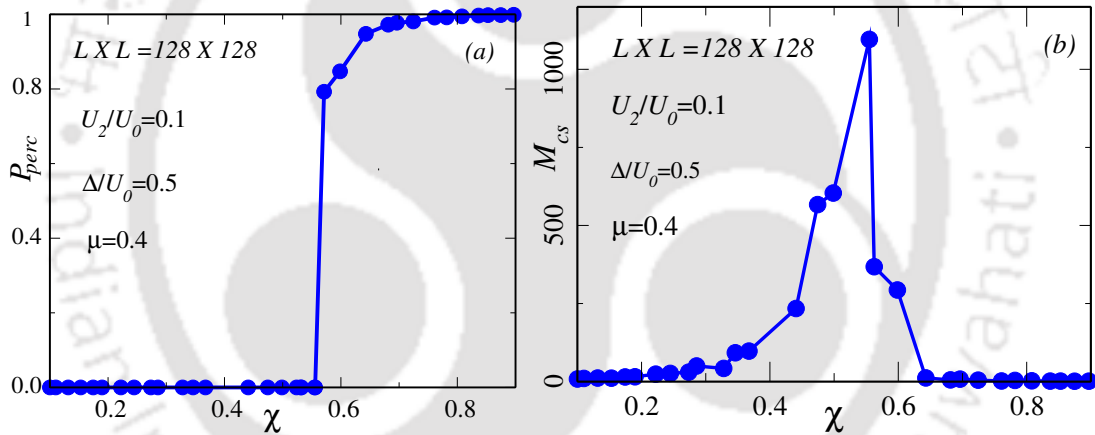


Figure 3.6: The percolation probability, P_{perc} in (a) and the mean cluster size, M_{cs} in (b) corresponding to a lattice size $L \times L = 128 \times 128$ at $\Delta/U_0 = 0.5$ for $U_2/U_0 = +0.1$ and $\mu/U_0 = 0.4$.

Another useful quantity in this regards, is the mean cluster size, M_{cs} defined as [140]-

$$M_{cs}(\chi) = \frac{\sum_p^\infty p^2 s_p(\chi)}{\sum_p^\infty p s_p(\chi)} \quad 3.8$$

where ps_p is the number of occupied sites belonging to a p -th cluster and the spanning clusters are excluded from the sum. Since the spanning clusters are excluded from the sum, the mean cluster size continues to increase with χ till the appearance of a spanning cluster for the first time and starts to decay immediately after that. The variation of M_{cs} with χ at a disorder strength $\Delta/U_0 = 0.5$ for $\mu/U_0 = 0.4$ [Fig.3.6(b)] shows that it reaches its peak value just below the χ_c and falls off after χ_c which confirms that the system is in the BG phase till χ_c , and

beyond that it goes toward the SF phase.

To deal with the finite size effects and also to determine the percolation transition, we resort to the finite size scaling. For a given system size L , we shall now study the percolation probability P_{perc} which is the probability of having a percolating cluster with the system parameter $\eta = zt/U_0$. Fig.3.7(a) shows the variation of P_{perc} with different lattice sizes L at a particular disorder strength, $\Delta/U_0 = 0.5$ and $\mu/U_0 = 0.4$ in the AF case. We averaged our results over 1500 different realizations of disorder for the system size, $L = 10$ and 150 different realizations of disorder for $L = 30, 50$.

The P_{perc} is assumed to follow a scaling law near the critical tunneling strength, η_c [140] and is described by,

$$P_{perc}(L, \eta) = \tilde{p}(L^{1/\nu}(\eta - \eta_c)) \quad \text{3.9}$$

where P_{perc} for different L values intersect approximately at one critical point given by $\eta_c = zt_c/U_0$ and \tilde{p} is the scaling function which approaches zero in $(\eta - \eta_c) \ll 0$ and unity for $(\eta - \eta_c) \gg 0$, ν is the critical exponent which is equal to 1.33 for conventional random site percolation problem in two dimensions. The finite size scaling plot, where all data corresponding to different system sizes collapse on a single curve, is shown in Fig.3.7(b) corresponding to the critical tunneling strength, $\eta_c = zt_c/U_0 = 0.073$.

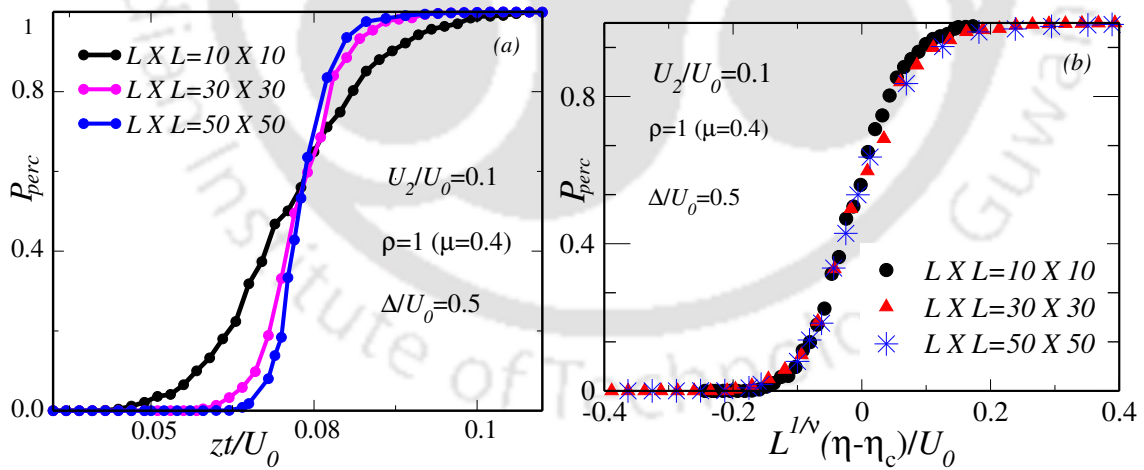


Figure 3.7: The percolation probability, P_{perc} corresponding to different lattice sizes, L with system parameter, $\eta = zt/U_0$ in (a) and finite size scaling in (b). The critical tunneling strength η_c where P_{perc} for different L values intersect at $\eta_c = zt_c/U_0 = 0.073$.

We are now in a position to distinguish the three different types of phases and able to ascertain the critical tunneling strength, η_c corresponding to the MI-BG and the BG-SF phase transitions. As we have already pointed out earlier that the MI regime corresponds to $\chi=0$, while the BG regime corresponds to $0 < \chi < \chi_c$ till

$P_{perc} = 0$ and the SF regime is given by, $\chi_c \leq \chi \leq 1$ when $P_{perc} \neq 0$. For this purpose we shall tune zt/U_0 in a controlled manner to closely monitor the value of χ and P_{perc} for a given lattice size namely, $L = 30$. For the odd MI lobe ($\mu/U_0 = 0.4$), $\chi = 0$ till $zt/U_0 = 0.122$ indicates the onset for the MI-BG phase transition and the BG phase extends up to $zt/U_0 = 0.133$, where $\chi_c = 0.524$ with $P_{perc} = 0$ for $\Delta/U_0 = 0.3$. Hence the BG-SF phase transition takes place at $zt/U_0 = 0.133$ corresponding to $\Delta/U_0 = 0.3$. For $\Delta/U_0 = 0.5$, since there is no MI phase and the phase transition from the BG to the SF occurs at $zt/U_0 = 0.073$ with $\chi_c = 0.549$.

3.2.1.6 Phase diagrams

Now we shall present the phase diagram in $t - \mu$ plane for both the pure and disorder cases based upon the information obtained from ψ_i , χ and P_{perc} . In the pure case, the phase diagram can be easily obtained based on ψ_i while in the disordered case, phase diagrams are obtained based upon the range of χ as discussed in the previous section.

The phase diagram for the disorder free case shows spin singlet-nematic MI phase with $\chi = 0$ in the MI phase and the SF phase with $\chi = 1$ [Fig.3.8 (a)]. In presence of disorder, for obtaining the phase diagram, we set $\chi = 0$ as the indicator for the MI phase, $0 < \chi < \chi_c (= 0.524)$ for the BG phase and $0.524 \leq \chi \leq 1$ for the SF phase at $\Delta/U_0 = 0.3$ [Fig.3.8 (c)]. Similarly for $\Delta/U_0 = 0.5$, the BG phase corresponds to $0 < \chi < \chi_c (= 0.549)$ and $0.549 \leq \chi \leq 1$ for the SF phase [Figs.3.8 (d)]. At $\Delta/U_0 = 0.3$, the intervening BG region for the odd MI lobes is more noticeable as compared to the even MI lobes [Fig.3.8(c)]. At $\Delta/U_0 = 0.5$, the BG phase completely destroys the first odd MI lobe, but the even MI lobe still exists as expected from the earlier discussion [Fig.3.8(d)]. The small spike inside the BG region for $\Delta/U_0 = 0.5$ appears due to large step size of μ/U_0 which can be minimized by considering a smaller step size. The phase diagrams obtained using probabilistic mean field perturbative approximation (PMFA) of Ref. [107] for $\Delta/U_0 = 0.3$ with $U_2/U_0 = 0.1$ in Fig.3.8 (b) is included for comparison. We found that our phase diagrams in presence of disorder obtained using percolation analysis in (b) is in qualitative agreement with that of the PMFA phase diagram in (c) and holds true for higher values of disorder strengths as well.

3.2.1.7 Phase diagram with disorder in spin dependent interaction potential

So far we have considered the effects of disorder in the chemical potential (μ) and hence obtained the phase diagrams using percolation analysis and found that they are in good agreement with that of Ref. [107]. Now we shall include the disorder in the spin dependent interaction potential, that is, $U_{2i} = U_2 + \epsilon_i$ which

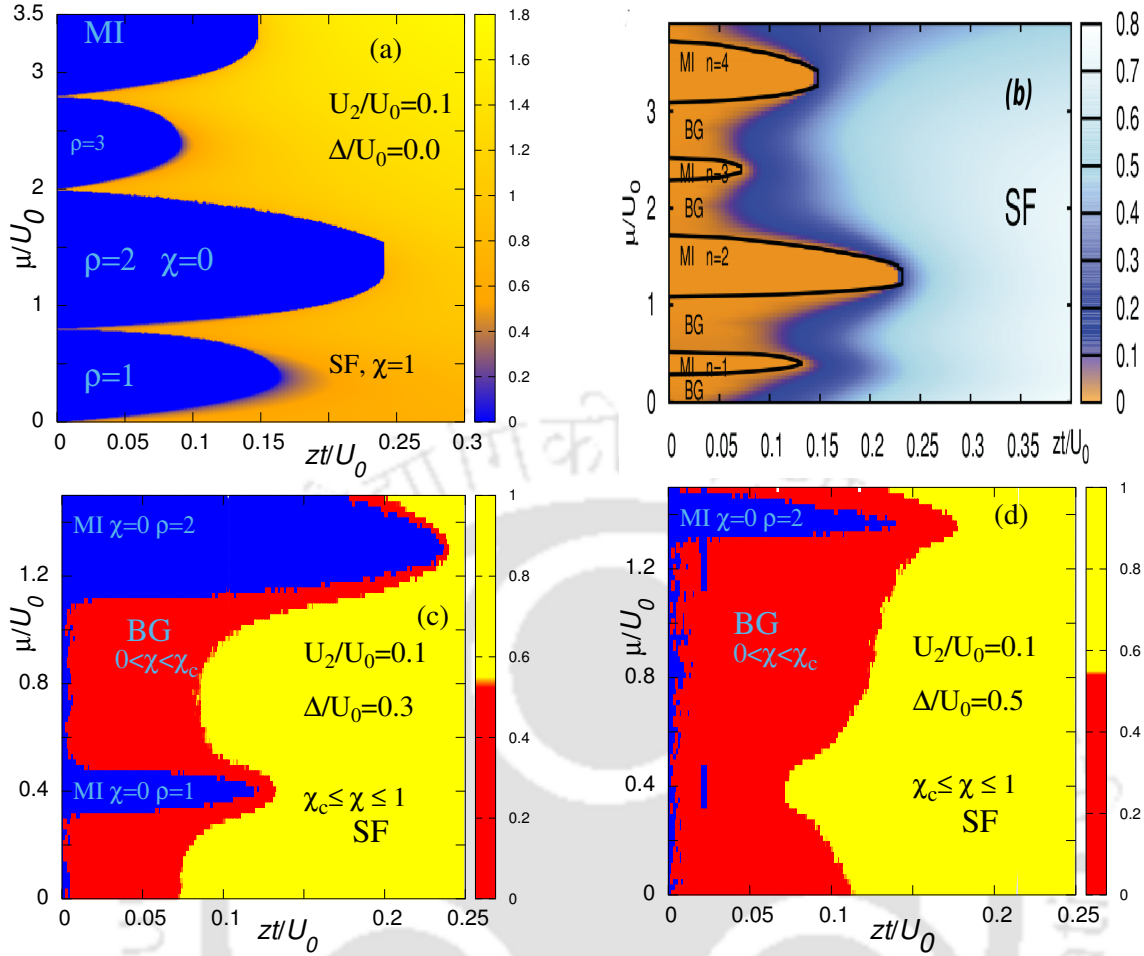


Figure 3.8: The phase diagrams in the AF case with $U_2/U_0 = +0.1$ corresponding to $\Delta/U_0 = 0.0$ is shown in (a). Phase diagram based on the information obtained from χ for the disordered cases, namely $\Delta/U_0 = 0.3$ is shown in (c) and $\Delta/U_0 = 0.5$ in (d). The phase diagram obtained using PMFA of Ref. [107] with $\Delta/U_0 = 0.3$ for $U_2/U_0 = 0.1$ is included for comparison with our phase diagram in (b). The phase diagrams in (b) and (c) are in qualitative agreement with each other. Figure courtesy of (b) Lacki et al., [107].

becomes site dependent interaction potential. We shall consider $\Delta/U_0 = 0.06$ with $\Delta/U_0 \ll U_2/U_0$ so that the nature of spin dependent interaction potential remains unaltered and the resultant phase diagram is shown in Fig.3.9 (b). In a similar manner like earlier, the critical value of χ for the BG phase corresponds to $\chi_c < 0.56$ and for the SF phase, we set the condition $0.56 \leq \chi \leq 1$.

Interestingly, compared to the disorder in chemical potential [Fig.3.8], here the BG phase appears only in between the MI lobes characterized by the odd and even occupation densities Fig.3.9 (b). While there is no BG phase observed in between the even and odd MI lobes Fig.3.9 (b). The reason for such appearance of the BG phase can be understood as follows. As we have seen in section 2.3 of chapter 2 that in the atomic limit ($t = 0$), the outer boundary of the even MI lobes are independent of U_2 , while for the odd MI lobes, it depends upon U_2 for

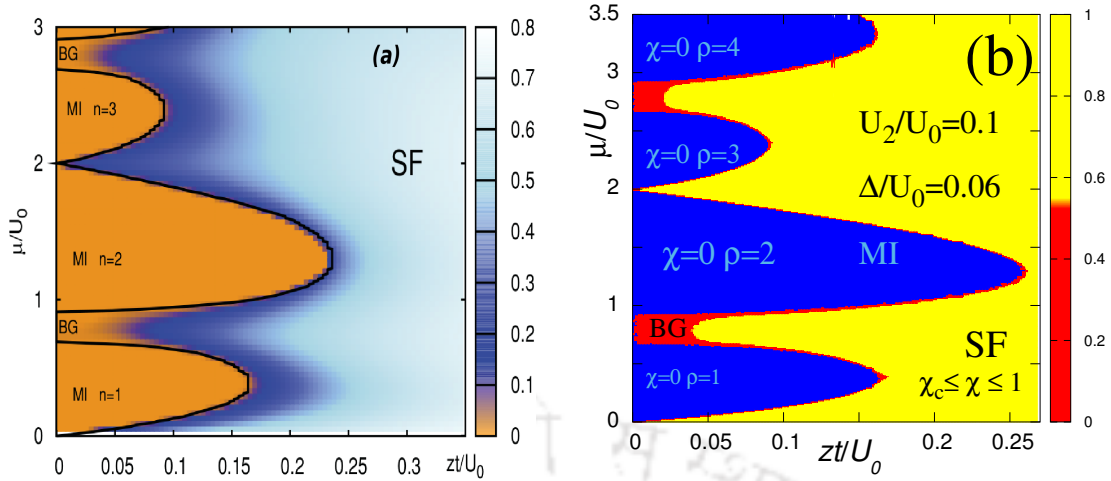


Figure 3.9: The phase diagram with disorder in spin dependent interaction potential with $U_2/U_0 = +0.1$ and $\Delta/U_0 = 0.06$ (b). The phase diagram obtained using PMFA of Ref. [107] with $\Delta/U_0 = 0.06$ for $U_2/U_0 = 0.1$ is included for comparison with our phase diagram in (a). The phase diagrams in (a) and (b) are in good agreement with each other. Figure courtesy of (a) Lacki et al., [107].

$U_2/U_0 \leq 0.5$. Thus adding disorder in U_2 will only change the chemical potential of the odd MI lobes, but the outer boundary of the even MI lobes will remain unchanged. Due to this reason, the BG phase appears only in between the odd-even MI lobes but not in the even-odd MI lobes. The phase diagram obtained using PMFA in Ref. [107] is included for same parameter values in Fig.3.9 (a). We found that our results are in complete agreement with [107] and certainly signifies that within the mean field level, one can use a percolation analysis to study the disordered BHM with a reasonable accuracy.

3.2.2 Ferromagnetic case ($U_2/U_0 = -0.2$)

Since in the ferromagnetic case with $U_2/U_0 = -0.2$, there is no distinction between the odd and the even MI lobes thus we shall only focus on the first MI lobe ($\mu/U_0 = 0.4$) with different disorder strengths. Also the energy gap of each MI lobe corresponds to $E_g = U_0 + U_2$ and hence the critical disorder strength is given by, $\Delta_c/U_0 = 0.4$.

3.2.2.1 The behaviour of the order parameters and the indicator

The variation of $\bar{\psi}$ and $\bar{\kappa}$ for the first MI lobe with Δ/U_0 is shown in Fig.3.10 (a). At $\Delta/U_0 = 0$, the system is in MI phase till $zt/U_0 = 0.13$ and then smoothly goes toward the SF regime with finite $\bar{\psi}$ and $\bar{\kappa}$. With disorder, the BG phase intervenes in between the MI and the SF phases. At $\Delta/U_0 = 0.5$, the region spanned by the MI phase is completely occupied by the BG phase, resulting in the survival of the BG and the SF phases.

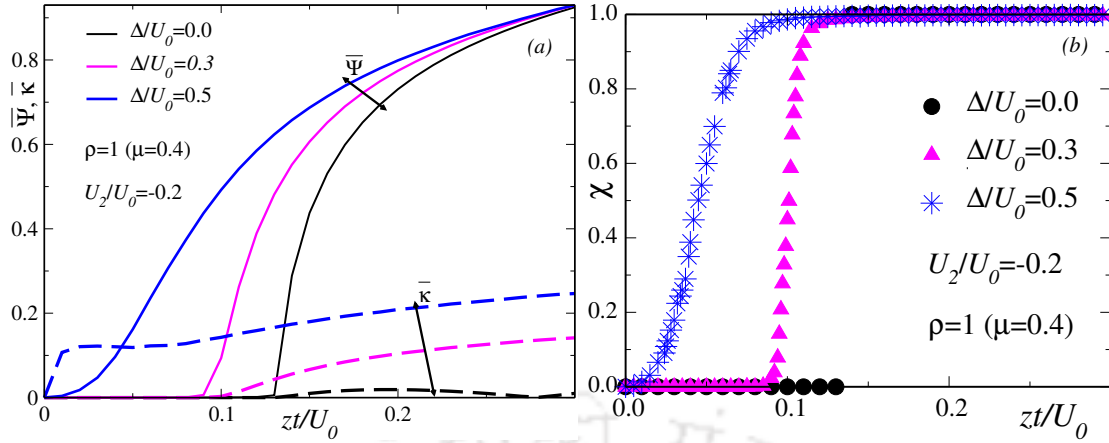


Figure 3.10: The variation of $\bar{\psi}$ (solid line) and $\bar{\rho}$ (dashed line) for $U_2/U_0 = -0.2$ with disorder strengths Δ/U_0 is shown in Fig.(a). The variation of χ in the ferromagnetic case with disorder Δ/U_0 is shown in (b).

The variation of χ with Δ/U_0 is shown in Fig.3.10 (b). At $\Delta/U_0 = 0.3$, χ remains zero till $zt/U_0 = 0.085$, beyond which χ starts to increase and finally takes a value unity in the SF phase. At $\Delta/U_0 = 0.5$, χ only takes the value between 0 and 1, indicating that the system consists of only the BG and the SF phases. In the latter case, disorder completely annihilates the MI phase because the disorder strength crosses the critical disorder value, $\Delta_c/U_0 = 0.4$.

3.2.2.2 Phase diagrams

Using the similar percolation analysis, we have obtained the phase diagrams based on χ and P_{perc} with Δ/U_0 .

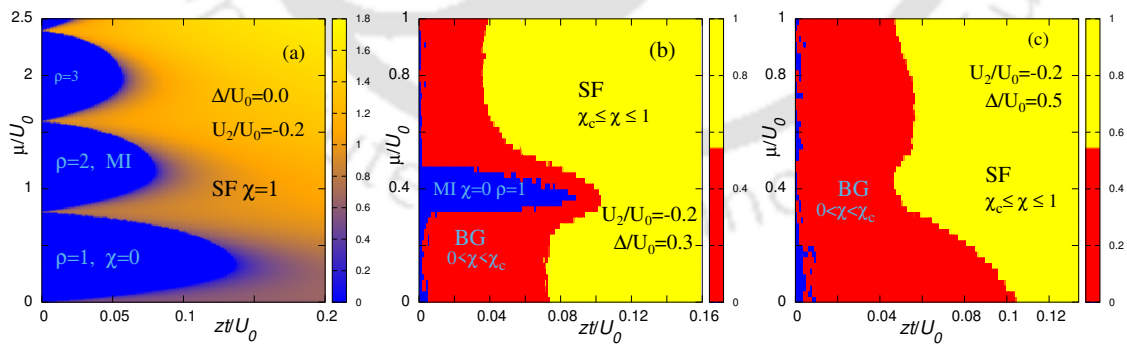


Figure 3.11: The phase diagrams for the ferromagnetic case with $U_2/U_0 = -0.2$. In the pure case ($\Delta/U_0 = 0.0$), the phase diagram is similar to that of scalar Bose gas (a). Phase diagram based on the information obtained from χ for the disordered cases, namely $\Delta/U_0 = 0.3$ is shown in (b) and $\Delta/U_0 = 0.5$ in (c).

In the disorder free case, the phases bear similar characteristic features as that of scalar Bose gas [Fig.3.11 (a)]. In the disordered case, as earlier, the phase diagrams are obtained by invoking the critical value of $\chi_c = 0.5034$ at

$\Delta/U_0 = 0.3$ [Fig.3.11(b)] and $\chi_c = 0.557$ at $\Delta/U_0 = 0.5$ [Fig.3.11(c)] corresponding to the onset of the SF phase. For $\Delta/U_0 = 0.5$, the MI lobes disappear since the disorder strength is higher than the critical disorder strength and the system is left only with the BG and the SF phases. The phase diagrams obtained using percolation analysis also show behaviour similar to the results obtained in Refs. [80, 107, 129, 131–133, 139, 142].

3.3 Conclusions

We have studied the effects of an on-site disorder in a two dimensional SBHM for both the AF and ferromagnetic interactions. The presence of the BG phase is observed via the average SF order parameter and compressibility. In the AF case, the MI- SF phase transition for odd MI lobes is always second order, while for even MI lobes, it shows a second order phase transition with increasing disorder strength. We also find that the MI phase exists till the disorder strength is below a critical value, while it vanishes above the critical value.

Three different types of phases, namely MI, BG and SF phases are characterized by an indicator which is defined as the fraction of the lattice sites having finite SF order parameter and non integer local densities. Further a percolation phenomenon is observed based on the concept of the SF percolating clusters. We define the MI phase where no SF cluster exists and the SF phase with at least one SF percolating cluster exists. The BG region occurs in between the MI and SF phases, that is, the SF cluster exists but does not percolate. The location for the MI-BG and the BG-SF phase transitions are identified by calculating the probability of having a percolating cluster. A percolation analysis of SF percolating cluster is studied using HK algorithm with different system sizes as a function of tunneling strength which obey finite size scaling law.

Finally, we obtain our phase diagram based on the indicator values for the AF and the ferromagnetic cases. For that purpose, we determine the critical value of the indicator where a SF cluster percolates throughout the lattice first time and set the respective ranges for three different phases. The resultant phase diagrams obtained by us using percolation analysis are in good agreement with the phase diagrams obtained via PMFA of ref. [107]. Thus a reliable enumeration of different phases can be obtained at desired parameter values of the SBHM Hamiltonian. Significantly, we have been able to compute the transition points between the MI, BG and SF phases even at the mean field level with reasonable accuracy with the help of finite size scaling. The transition points between the various phases obtained from the percolation analysis are presented in the table 3.1 for both the AF and the ferromagnetic interactions in pure and disordered cases.

Now we shall include some comments concerning the drawbacks in the mean

Interactions	MI lobes	μ/U_0	$\Delta/U_0=0$	$\Delta/U_0=0.3$		$\Delta/U_0=0.5$	
			MI-SF	MI-BG	BG-SF	MI-BG	BG-SF
			zt/U_0	zt/U_0	zt/U_0	zt/U_0	zt/U_0
AF	first odd	0.4	0.16	0.122	0.133	No	0.073
	first even	1.4	0.26	0.210	0.225	0.123	0.174
Ferro	first	0.4	0.133	0.085	0.103	No	0.047

Table 3.1: *The transition points for the MI-BG and the BG-SF phases obtained from χ and P_{perc} for both the AF and the ferromagnetic cases.*

field theory. Since our work is mainly a focus on the effects of disorder in SBHM, thus the single site mean field theory always is not able to handle the site inhomogeneity of the system properly, although it shall work well in higher dimensions, $d \geq 2$. Although we take into the effect the site inhomogeneity by defining the indicator, but ignoring quadratic fluctuations introduces a tiny error in the calculations. For example, the MI phase will vanish above the critical disorder strength, our results are in good agreement against this claim within a 3% error.

Chapter 4: Competition between synthetic and external magnetic field on a spin-1 ultracold Bose gas

The vector property of the SF order parameter in the spinor condensate shows significant modification of the ground state structures and yields new topological excitation as compared to its scalar counterpart [17, 18]. Later several studies on spinor Bose gas include the study of spin dynamics [130, 143], effects of disorder [107, 144], spin orbit coupling [45, 48, 145, 146] etc now under the lens from theoretical as well as experimental perspectives.

In the previous chapter, we have studied how the appearance of a Bose glass (BG) phase due to the presence of disorder affects the spin singlet-nematic state and gets an even-odd asymmetry of the MI lobes in the SBHM in details. Apart from studying disorder, this chapter will focus on how a (synthetic) magnetic field can modify the phase diagram of a spinor Bose gas. The primary motivation to study the synthetic magnetic field in the context of spinor bosons is as follows.

There are large number of review articles which include the study of spinor Bose gas subjected to an external magnetic field which enter the Hamiltonian through the Zeeman term [147-153]. In particular, the effect of an external magnetic field on the SF-MI phase transition was studied in details by considering the linear Zeeman term in Refs. [147, 148] and a quadratic Zeeman term in Refs. [38, 38], where the sole effect of the magnetic field is to affect the states with high spin configurations and thereby suppress the spin singlet formation that destabilizes the MI phase.

Although the external magnetic field causes the Zeeman splitting of the different magnetic sublevels of a spinor Bose gas, but because of their charge neutrality, they are unable to simulate most of the behaviour of a charge particle in a magnetic field. A quick remedy that can be prescribed is to set these neutral atoms in a rotational motion, where the role of the Lorentz force on a charge is executed by the Coriolis force due to rotation of the neutral particles [93, 154-156]. There will be a corresponding vector potential of the form $\vec{\Omega} \times \vec{r}$ (Ω being the rotation frequency) and hence a magnetic field will be generated that will be proportional to Ω . This magnetic field is called artificial or synthetic magnetic field and the motion of the charge particles are obligatory to be similar to that the charged fluid in an external magnetic field. The appearance of the vortices in Bose Einstein condensate are trademark signatures of the presence of the synthetic magnetic fields [89-91, 155].

After successful observation of vortices, it was tried to create pinning in vortices that had shown a structural transition from a triangular Abrikosov vortex lattice [94] to a lattice structure which are pinned by the optical lattice potential.

In a superconductor the pinning appears due to the impurities and defects. However in optical physics the pinning can be generated by using another rotating optical lattice. Tung *et. al.*, designed an experimental set up where the rotating BECs are combined with a co-rotating optical lattice with masks which yields pinning in the vortex phase [93]. Since one has vast tunability over the optical lattice potential, lattice parameters etc, the pinning in the SF phases vortex state can be controlled by the lattice parameters, optical potential, rotational velocity and putting large numbers of masks in the rotating optical lattice.

However this approach has a limitation on obtaining very large synthetic fields as that would require large rotational velocities which may cause the atoms to fly apart. To circumvent this difficulty, approaches such as, photon assisted tunneling [157] or by generating phase difference by coupling different hyperfine atomic states using a laser beam are developed recently [92].

In this chapter, we shall consider the spinor Bose gas in presence of a synthetic magnetic field which enters via Peierls couplings and simultaneously include the effect of an external magnetic field through the Zeeman interaction. Our goal is to study the phenomenon of SF-MI phase transition as a competition between these two magnetic fields for both signs of the spin dependent interactions.

We organize this chapter as follows. In the next section, we provide a detailed theoretical formalism of the MFA on a square lattice for a spinor Bose gas in presence of the synthetic and the external magnetic fields. After which, we have computed the phase diagrams for different relative strengths of the synthetic and the external magnetic fields. Then we discuss about the energy spectrum and magnetization properties and finally conclude with the highlight of our main results.

4.1 Model

Consider a spin-1 ultracold atomic gas in a synthetic magnetic field acting in the z-direction, namely, $\mathbf{B}_s = B_s \hat{z}$. This magnetic field can be described by a vector potential \mathbf{A}_s which is known to depend on the choice of a gauge. In a chosen gauge, namely the Landau gauge, \mathbf{A}_s can be taken as, $\mathbf{A}_s = B_s x \hat{y}$. The Bose Hubbard Hamiltonian for a system of spin -1 ultracold atoms in presence of a synthetic and an external magnetic fields is written as [17, 147, 158],

$$\begin{aligned}
 H = & - \sum_{\langle ij \rangle} \sum_{\sigma} (t_{ij} a_{i\sigma}^{\dagger} a_{j\sigma} + h.c) - \mu \sum_i n_i + g \mu_B B_e \sum_i S_{iz} \\
 & + \frac{U_0}{2} \sum_i n_i (n_i - 1) + \frac{U_2}{2} \sum_i (S_i^2 - 2n_i)
 \end{aligned} \tag{4.1}$$

where all the symbols carry same meaning as discussed in section 2.2 of the chapter 2. t_{ij} is the hopping matrix elements from site i to nearest neighbour site j which has acquired a phase shift given by,

$$t_{ij} = t e^{-i \frac{2\pi}{\phi_0} \int_i^j \mathbf{A}_s \cdot d\mathbf{l}} \quad 4.2$$

where \mathbf{A}_s enters in the hopping term of the Hamiltonian through this phase factor via Peierls coupling and ϕ_0 is the magnetic flux quantum. For this particular choice of the gauge field, the integral assumes the value as $\phi = B_s l_0^2 / \phi_0$, l_0 being the lattice spacing taken to be unity. g is Lande g factor and μ_B is the Bohr magneton and $S_{iz} = a_{i+}^\dagger a_{i+} - a_{i-}^\dagger a_{i-} = n_{i+} - n_{i-}$ is the z component of the spin vector at site i , namely \mathbf{S}_i . Here we consider a two dimensional square lattice where every lattice site i can be expressed by two indices as $i = [l, m]$, l corresponds to lattice site along x direction and m along y direction of the lattice.

Here B_e being the external magnetic field responsible for the Zeeman coupling. Mostly from an academic point of view, we have included a linear Zeeman term to compare with the synthetic magnetic field. Particularly, for a spinor Bose gas this term and its interplay with B_s may yield interesting consequences on the study of the MI to the SF phase transition.

Using similar SSMFT as discussed in section 2.4.1 of chapter 2, the hopping term can be decoupled as [25, 159],

$$a_{(l,m)\sigma}^\dagger a_{(l+1,m+1)\sigma} \simeq \langle a_{(l,m)\sigma}^\dagger \rangle a_{(l+1,m+1)\sigma} + a_{(l,m)\sigma}^\dagger \langle a_{(l+1,m+1)\sigma} \rangle \quad 4.3$$

where $\langle \rangle$ denotes the equilibrium value of an operator. Defining the superfluid order parameter at a site (l, m) as, $\psi_{(l,m)\sigma} = \langle a_{(l,m)\sigma} \rangle$, the total SF order parameter is given by, $\psi_{l,m} = \sqrt{\psi_{(l,m)\sigma}^2}$. Substituting this in Eq.(4.1), the SBHM can be written as a sum of single site Hamiltonian as, $H = \sum_{l,m} H_{l,m}^{MF}$ where,

$$\begin{aligned} H_{l,m}^{MF} = & - \sum_{\sigma} \left[t_{l+1,m} \psi_{l+1,m}^* a_{l,m} + t_{l-1,m} \psi_{l-1,m}^* a_{l,m} + t_{l,m+1} \psi_{l,m+1}^* a_{l,m} \right. \\ & \left. + t_{l,m-1} \psi_{l,m-1}^* a_{l,m} + h.c \right] - \mu n_{l,m} + \eta \left[n_{(l,m)+} - n_{(l,m)-} \right] \\ & + \frac{U_0}{2} n_{l,m} (n_{l,m} - 1) + \frac{U_2}{2} (\mathbf{S}_{l,m}^2 - 2n_{l,m}) \end{aligned} \quad 4.4$$

where $\eta = g\mu_B B_e$ and we define a dimensionless quantity, $\hat{\eta} = B_s / B_e$. Using the Bloch periodic boundary condition and calculating the hopping matrix element

between site (l, m) to a nearest neighbour $(l \pm 1, m \pm 1)$, we can write,

$$t_{l\pm 1, m\pm 1} \psi_{l\pm 1, m\pm 1} = \begin{cases} t \psi_{l\pm 1, m}; & l, m = l \pm 1, m \\ t e^{\mp i 2\pi l \phi} \psi_{l, m}; & l, m = l, m \pm 1 \end{cases} \quad 4.5$$

Now to compute the ground state energy of the system, we first evaluate the matrix elements of the mean field Hamiltonian, $H_{l, m}^{MF}$ in the occupation number basis, $|n_{(l, m)\sigma}\rangle$ as,

$$\langle n_{l, m+}, n_{l, m0}, n_{l, m-} | H_{l, m}^{MF} | n'_{l, m+}, n'_{l, m0}, n'_{l, m-} \rangle = h_{l, m}^d + h_{l, m}^{od} \quad 4.6$$

where the $h_{l, m}^{od}$ correspond to the matrix elements coming from the off diagonal terms and are written as,

$$h_{l, m}^{od} = -t \sqrt{n_{l, m}} \left[\psi_{l+1, m}^* + \psi_{l-1, m}^* + (e^{-i 2\pi \phi l} + e^{i 2\pi \phi l}) \psi_{l, m}^* \right] \quad 4.7$$

and the diagonal part, $h_{l, m}^d$ are calculated using,

$$h_{l, m}^d = \frac{U_0}{2} n_{l, m} (n_{l, m} - 1) + \frac{U_2}{2} (S_{l, m}^2 - 2n_{l, m}) - \mu n_{l, m} + \eta [n_{(l, m)+} - n_{(l, m)-}] \quad 4.8$$

After diagonalizing Eq.(4.6) with $n_i = 7$ self consistently as discussed in section 2.4.1 of chapter 2, we compute the equilibrium SF order parameter and local densities as,

$$\psi_{l, m\sigma} = \langle \Psi_g(\psi_{l, m\sigma}) | a_{l, m\sigma} | \Psi_g(\psi_{l, m\sigma}) \rangle \quad 4.9$$

$$\rho_{l, m\sigma} = \langle \Psi_g(\psi_{l, m\sigma}) | n_{l, m\sigma} | \Psi_g(\psi_{l, m\sigma}) \rangle \quad 4.10$$

In absence of a magnetic field, the Hamiltonian and hence the order parameters are independent of the lattice sites. The system shows a direct MI-SF phase transition which can be controlled by tuning zt/U_0 . In the AF case, the ground state is a polar SF which could be either transverse polar (TP), with spinor components $(1, 0, 1)^T / \sqrt{2}$ or the longitudinal polar (LP) with spinor components $(0, 1, 0)^T$. These two states can transform to each other by a rotation of $\pi/2$, since all spinor components are related to each other through rotation in spin space and are degenerate in the absence of external magnetic field as discussed in section 2.4.1 of chapter 2. The spin properties of the polar SF phase and the symmetry of the ground state were studied in details with and without an external magnetic field in Ref. [26]. Moreover the phase transition between the spin singlet and nematic MI state have been studied without an external field in Ref. [110] and spin singlet to partially polarized MI state in presence of external magnetic field in Ref. [160]. In the ferromagnetic case, the ground state is either a longitudinal

ferromagnetic (LF) with spinor components $(1, 0, 0)^T$ and $(0, 0, 1)^T$ or a LP state or a broken axis symmetry phase in presence of an external magnetic field [38, 161].

In presence of a synthetic magnetic field, the Hamiltonian and hence the order parameters are site dependent. In the non-interacting limit, the single particle energy spectrum of the Hamiltonian demonstrates a Hofstadter butterfly [162] which can be obtained by solving the Harper equation [47]. But in the interacting limit, this single particle energy spectrum leads to the modification of phase boundary near the SF-MI transition which we shall discuss in the next section.

4.2 Results

Let us start our discussion by considering bosons in a synthetic magnetic field by choosing the magnetic flux to be expressible in the form of a rational fraction, that is, $\phi = p/q$ where p and q are integers [163]. In the chosen Landau gauge, from Eq.(4.6), the system is translationally invariant along the y direction and quasi-periodic (as explained below) in the x direction. For a two dimensional square lattice with lattice site indices as (l, m) , the system maintains its periodicity along x direction with period $l = q$. This implies that we shall have to diagonalize the mean field Hamiltonian over a one dimensional chain of length q , that is, a $1 \times q$ magnetic supercell with periodic boundary conditions in the x direction in order to obtain the ground state energy. Due to invariance along the y axis, the SF order parameter, $\psi_{l,m}$ and the occupation density, $\rho_{l,m}$ are independent of m that is $\psi_{l,m} = \psi_l$ and $\rho_{l,m} = \rho_l$. Further owing to the periodicity in the x -direction, we also have $\psi_l = \psi_{l+q}$ and $\rho_l = \rho_{l+q}$. We shall obtain the phase diagrams based on the site averaged SF order parameter, $\bar{\psi} = \sum_q \psi(q)/q$ and local density, $\bar{\rho} = \sum_q \rho(q)/q$ for different values of the magnetic flux, ϕ and B_e [159].

4.2.1 Antiferromagnetic case

4.2.1.1 Phase diagrams

The phase diagrams corresponding to the AF case with different values of ϕ for the cases concerning the relative strengths of the synthetic and external magnetic fields, namely, when they are equal, that is, $B_s = B_e$ ($\lambda = 1$) is shown in Fig.4.1 and unequal, that is, $B_s > B_e$ ($\lambda > 1$) in Fig.4.2. Here we consider $U_2/U_0 = 0.05$ throughout our calculation for the AF interaction.

For $B_s = B_e$ ($\lambda = 1$) [Fig.4.1], we found that at low values of the magnetic field strength, that is, $\phi = 0.02$, the MI-SF phase boundary for the odd MI lobes shift towards larger t/U_0 , indicating a stabilization of the insulating phase. However for the even MI lobes, the singlet pair formation continues to play a dominant role as pointed out in Ref. [24, 25].

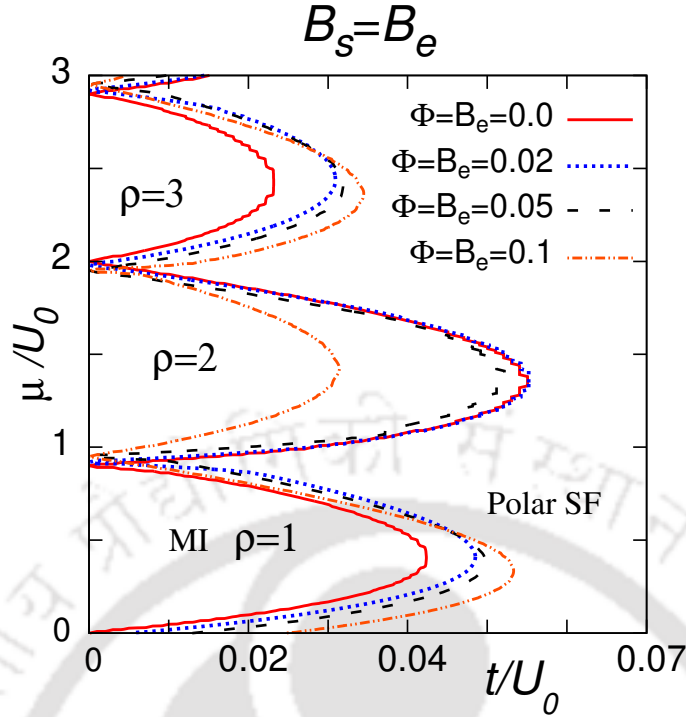


Figure 4.1: The phase diagrams in the AF case with $U_2/U_0 = 0.05$ for different values of ϕ corresponding to $B_s = B_e$. At higher values of the magnetic flux, the even MI lobes become unstable due to the suppression of the spin singlet pair formation.

At larger flux strengths, say for example, $\phi = 0.05$, we found that the even MI lobes shrink noticeably, while the other (odd) MI lobes are significantly enhanced, indicating further increase of the location (towards larger t/U_0) for the MI-SF phase transition. This is quite interesting because the MI phase becomes more stable compared to the SF phase, whereas in Refs. [147, 148], the MI phase seems to vanish when solely an external magnetic field is applied. Thus the role of an equal amount of synthetic magnetic field, in addition to the external field, is to push the system towards an insulating phase. Hence the MI phase breaks the lattice translational symmetry that disturbs the SF phase stability.

For the other case, namely, $B_s > B_e$ [Fig.4.2], corresponding to $B_e \leq 0.05$ in the AF phase, we found that the even MI lobes no longer diminish, however with increasing flux strengths (ϕ), the system acquires a tendency to be in insulating regime. This suggests that at low values of Zeeman interaction strength, the spin dependent interaction favours formation of the singlet pairs to make the even MI phase more stable. However at higher values of the external magnetic field strength (B_e), the Zeeman term penalizes the states with higher spin configurations, thereby suppressing the phenomena of spin singlet formation. So at large B_e values, the Zeeman term pushes the system towards the SF regime, while the magnetic flux included through the hopping term moves the system towards the

MI regime. These are the central results of this work, which distinctly emphasize the competition between the synthetic and external fields with regard to the emergence of the superfluid and the insulating phases. We explain these features more clearly in the upcoming discussion. In the AF case, the SF phase is a polar state where the components of the spinor are in transverse polar (TP or AF) [16,26,161]. The scenario corresponding to the third possibility, namely, $B_s < B_e$ is just the opposite to that of $B_s > B_e$ and thus we have shown the results corresponding to these two cases for brevity.

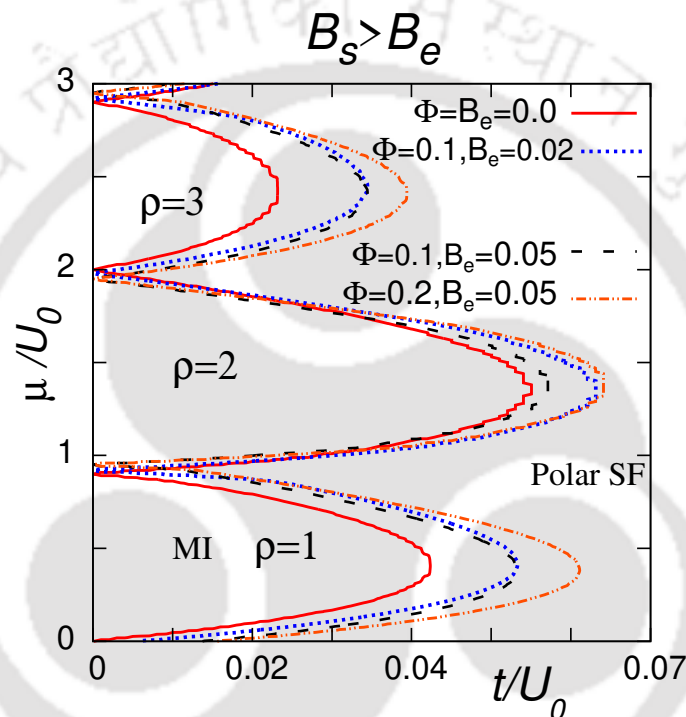


Figure 4.2: Phase diagrams in AF case with $U_2/U_0 = 0.05$ for different values of ϕ corresponding to $B_s > B_e$. At higher magnetic flux, the odd MI lobes becomes stable and occupy more regime compared to the SF phase.

Also the instability of the even MI lobes at higher external fields can be understood from the following discussion. At low magnetic fields, the formation of spin singlet (nematic) pair corresponding to the even (odd) MI lobes still continues and hence the ground state for even MI lobes is $|0, 0, n\rangle$, while for the odd MI lobes, it is $|1, S_z, n\rangle$. But at high field strengths, the ground state now changes from $|0, 0, n\rangle$ to $|2, S_z, n\rangle$ for the even MI lobes and $|1, S_z, n\rangle$ to $|3, S_z, n\rangle$ for the odd MI lobes. This implies that the spin eigenvalue changes from S to $S + 1$ since the formation of singlet or the nematic pair no longer occurs due to the change in the ground state structure at higher values of the magnetic field strength in the Zeeman term [147, 148].

4.2.1.2 SF order parameter variation

We now try to get a visualization of the SF order parameter ψ_q with flux, ϕ near the MI-SF transition point. We have plotted the order parameter, ψ_q (plotted along y axis) with t/U_0 (plotted along x axis) in the AF case ($U_2/U_0 = 0.05$) for $\mu/U_0 = 0.5$ without ϕ in Fig.4.3(a) and with ϕ in Fig.4.3(b). We consider ψ_q below 0.05 to denote the MI phase and above 0.05 as SF phase. The black dots correspond to the MI phase and red dots denote the SF phase. In Fig.4.3(a), we see that all lattice sites are in MI phase below $t/U_0 = 0.042$ ($= t_c/U_0$), and above it all are in the SF phase. Further they are separated by a sharp boundary for $\phi = 0.0$. In Fig.4.3(b), we found that the sharp boundary between the MI-SF phase is now destroyed for $\phi = 0.1$ because some lattice sites have become insulating above $t/U_0 = 0.049$ ($= t_c/U_0$) which used to denote the SF phase for $\phi = 0.0$. This makes the MI phase stable, as it breaks the translational symmetry of the SF phase locally and explains a shift of the location for the MI-SF phase transition to larger values of t/U_0 with increasing magnetic flux strength.

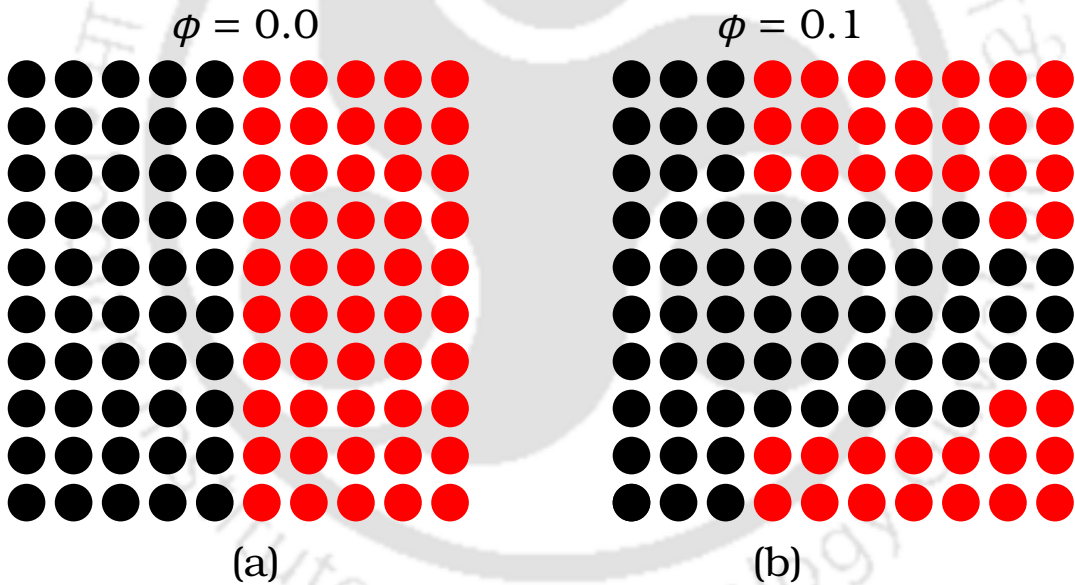


Figure 4.3: Color map of SF order parameter, ψ_q (along y axis) with t/U_0 (along x axis) is shown near the MI-SF transition point for $\Phi = 0.0$ in (a) and $\Phi = 0.1$ in (b). The black dots represent MI phase and red dots represent SF phase. At $\phi = 0.1$, the boundary between the MI-SF phase is now destroyed since some lattice sites in the MI phase now encroach into the SF phase above $t/U_0 = 0.049$ ($= t_c/U_0$).

In Fig.4.4, we study the one dimensional behaviour of the SF order parameter corresponding to the even and the odd MI lobes in the AF case for different values of ϕ corresponding to $\tilde{n} = 1$. It is seen that the location of the MI-SF phase transition occurs at the same value of the hopping strength, t_c/U_0 corresponding to l number of lattice sites (of the magnetic supercell of dimension $1 \times q$) and obeys the periodicity condition, $\psi_l = \psi_{l+q}$.

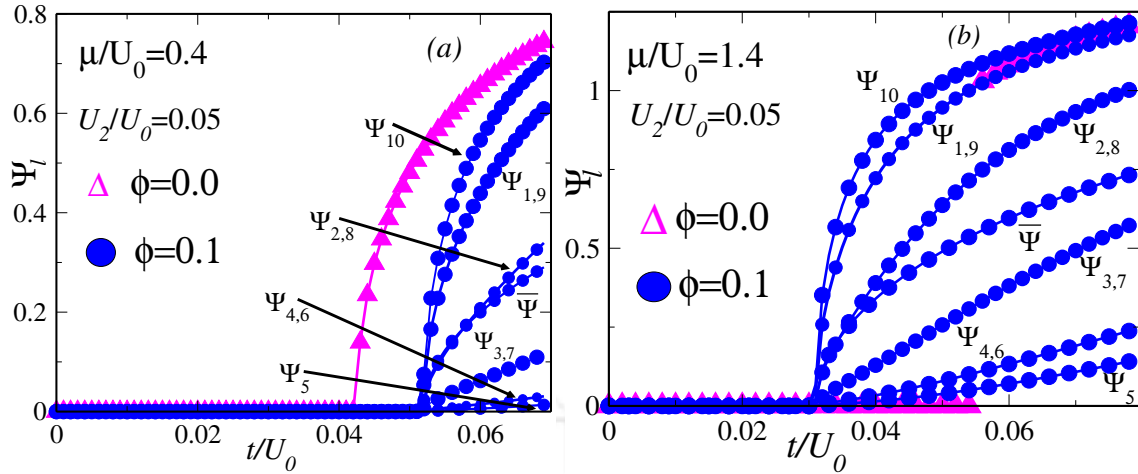


Figure 4.4: The one dimensional behaviour of ψ_l in AF case corresponding to the odd MI lobe (a) and the even (b) are shown with ϕ . The MI-SF phase transition for the odd MI lobe ($\mu/U_0 = 0.4$) is second order for all values of ϕ , while for the even MI lobes ($\mu/U_0 = 1.4$), it is first order only when $\phi \leq U_2/U_0$, but shows a second order character for higher values of the magnetic flux, that is, $\phi > U_2/U_0$.

Interestingly, for the odd MI lobes ($\mu/U_0 = 0.4$), the MI-SF phase transition is second order in nature due to the continuous variation of the SF order parameter and an increase in t_c/U_0 value with increasing flux strengths [Fig.4.4(a)]. While for the even MI lobes ($\mu/U_0 = 1.4$) and for low flux strengths, that is, $\phi \leq U_2/U_0$, the MI-SF phase transition has a first order character due to the jump of the order parameter. However for higher field strengths, that is $\phi > U_2/U_0$, the order parameter shows continuous variation from the MI to the SF phase and hence shows a second order transition for all ψ_l [38]. Also the critical tunneling strength, t_c/U_0 decreases with increasing magnetic flux values because of the absence of singlet pair formations [Fig.4.4(b)].

4.2.1.3 Energy spectrum and magnetization

In Fig.4.5, we have shown the discrete energy spectrum for a full range of $\phi = [0, 1]$ with $B_s = B_e$ as a function of t/U_0 in AF case. It shows a periodicity of $\phi = \phi + N$, N being an integer as seen from Eq.(4.6) and also symmetric about $\phi = 0.5$ for both the odd ($\mu/U_0 = 0.4$) and the even ($\mu/U_0 = 1.4$) cases. Interestingly for the odd MI lobes, the insulating phase increases with ϕ till a value of 0.5, but for the even MI lobes, it shows an increase till $\phi \leq 0.05$, after which the MI phase decreases, as it is obvious from the preceding discussion. Also an asymmetry appears in the even MI lobe ($\mu/U_0 = 1.4$) for $\phi > 0.93$ since the Zeeman term starts to dominate over the term containing the synthetic magnetic field.

In Fig.4.6, we have shown the transverse and longitudinal magnetization av-

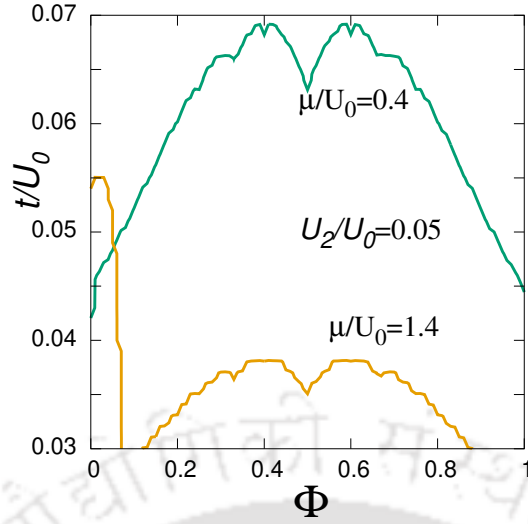


Figure 4.5: The energy spectrum in the AF case for a complete range of ϕ corresponding to the odd ($\mu/U_0 = 0.4$) and the even ($\mu/U_0 = 1.4$) MI lobes. It shows a symmetry about $\phi = 0.5$ for both the MI lobes. An asymmetry appears in the even MI lobe for $\phi > 0.93$ since the Zeeman term is dominating over the synthetic magnetic field.

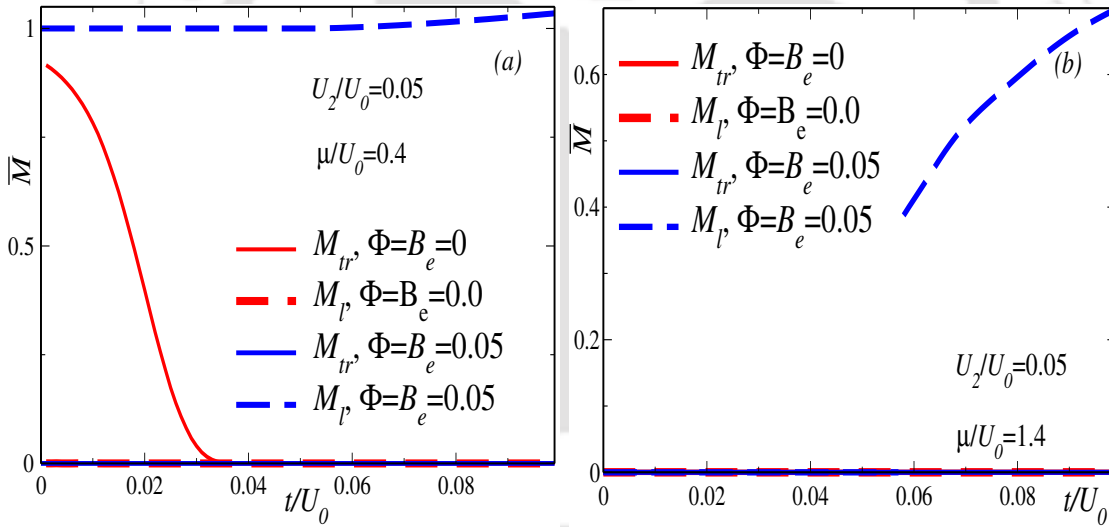


Figure 4.6: The site averaged transverse, \bar{M}_{tr} (solid lines) and longitudinal, \bar{M}_l (dashed lines) magnetization in the AF case with $B_s = B_e = 0.05$ for the odd ($\mu/U_0 = 0.4$) in (a) and the even ($\mu/U_0 = 1.4$) in (b) MI lobes. $\bar{M}_{tr} = 0$ for both the MI lobes, but \bar{M}_l shows a first order for the even and a second order transition for the odd MI lobes.

eraged over q sites in the AF case corresponding to $B_s = B_e$ value, where

$$M_{tr} = \sqrt{\langle S_{ix} \rangle^2 + \langle S_{iy} \rangle^2} \quad 4.11$$

$$M_l = \sqrt{\langle S_{iz} \rangle^2}$$

In the AF case, for $B_s = B_e = 0.0$ (red lines), \bar{M}_{tr} is finite for odd MI lobes, while

\bar{M}_l is zero for the spin nematic phase [Fig.4.6 (a)]. For the even MI lobes, both \bar{M}_{tr} and \bar{M}_l are zero, which is a signature for the spin singlet phase [24, 25] [Fig.4.6 (b)]. At $B_s = B_e = 0.05$ (blue lines), \bar{M}_{tr} is zero for both the MI lobes, but \bar{M}_l shows a first order transition as a function of the hopping strength for the even MI lobes and second order transition for the odd MI lobes [Fig.4.6]. Further magnitude of \bar{M}_l is of the order of B_e/nU_2 [16, 161], which shows a linear dependence on external magnetic field, B_e [160] [Fig.4.6 (b)].

4.2.2 Ferromagnetic case

The phase diagrams in the ferromagnetic case with $U_2/U_0 = 0.0$ for $B_s = B_e$ is shown in Fig.4.7 (a).

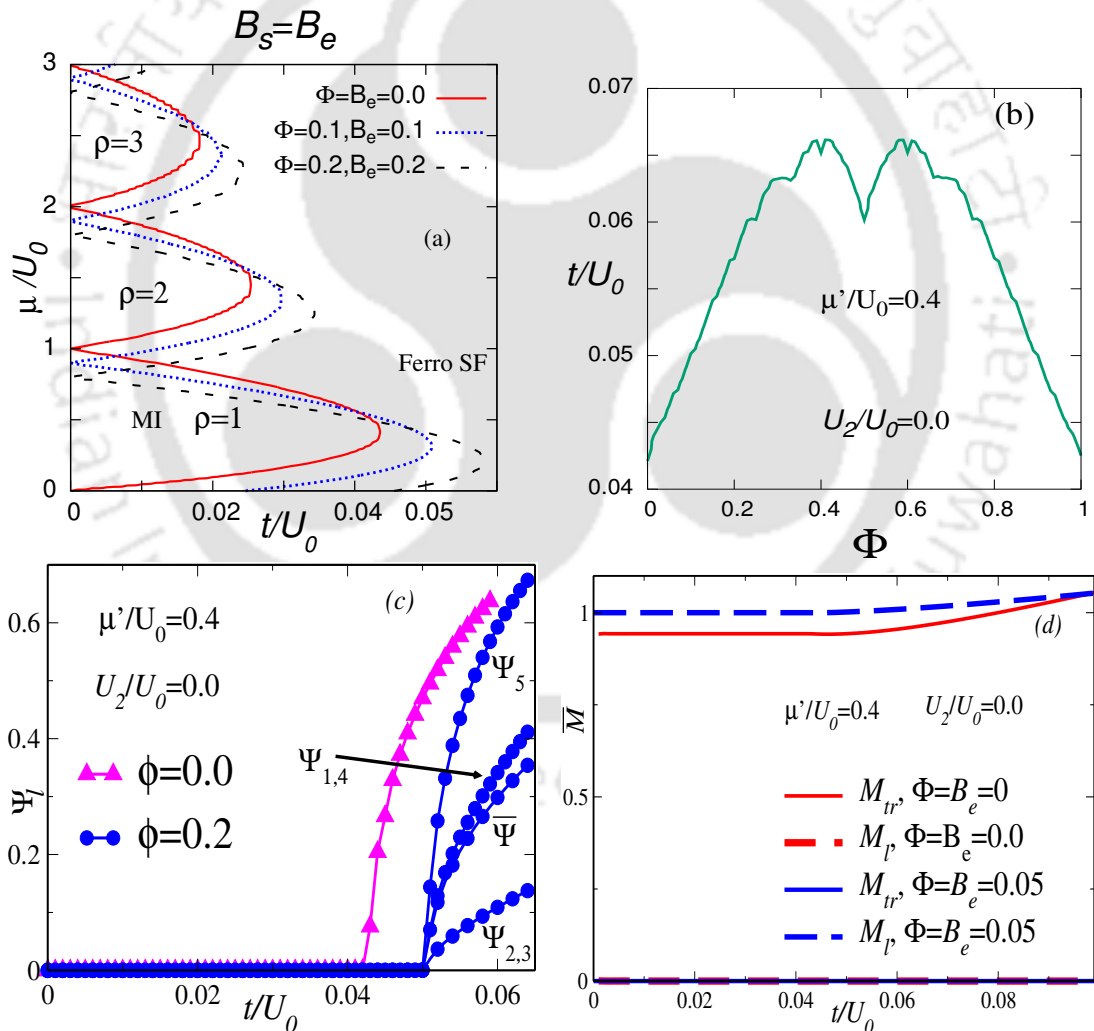


Figure 4.7: Phase diagram for different values of ϕ in ferromagnetic case with $U_2/U_0 = 0.0$ in (a). At higher magnetic flux, the MI lobes become stable compared to the SF phase. The energy spectrum in AF case for complete range of ϕ shows symmetry in (b). The SF order parameter in (c) obeys the periodicity. The longitudinal magnetization is of the order unity in the ferromagnetic case (d).

For the ferromagnetic interaction, the phase diagrams are similar to that of the spin-0 (scalar) system, except for only the chemical potential width now gets rescaled with the Zeeman interaction strength, η as $\mu + \eta \rightarrow \mu'$ [148, 159].

Unlike the AF case, in the ferromagnetic case, all the MI phases become more stable with increasing magnetic flux strengths due to the phase decoherence of the SF order parameter at the transition point as discussed above. Further, each MI lobe now gets shifted along the vertical axis (μ/U_0) by an amount η/U_0 due to rescaling of the chemical potential. The phase diagram for $\phi = 0.1$ is in agreement with the results obtained in Ref. [159]. Here the SF phase is a longitudinal ferromagnetic (LF) state where the spinor SF order parameter behaves as $\psi_\sigma = (1, 0, 0)^T$ [16, 161].

The energy spectrum in the ferromagnetic case also shows symmetry about $\phi = 0.5$ for all MI lobes and is in agreement with the results obtained in Ref. [159] [Fig.4.7 (b)]. We have also studied ψ_l in the ferromagnetic case as a function of flux, ϕ and the results are in agreement with those obtained in Ref. [159]. The SF order parameter obeys the periodicity condition similar to the AF case and the MI-SF phase transition occurs at larger hopping strength [Fig.4.7 (c)]. The magnetization in Fig.4.7 (d) shows that \bar{M}_l is 1 for $B_e = 0.0$, while the longitudinal magnetization is of the order of unity for $B_e = 0.05$ implying that we have a LF superfluid phase [16, 161].

4.3 Conclusion

In this work, we have studied the competition between the external and the synthetic magnetic fields on the superfluid to the Mott insulator transition on a spin-1 ultracold Bose gas. In the AF case, for external fields to have numerical values smaller than the spin dependent interaction, the even MI lobes continue to play a dominant role compared to the odd MI lobes due to formation of spin singlet pairs. While at large external fields, the Zeeman interaction term suppresses the singlet pair formation by penalizing the states with the higher spin configurations, and at the same time the synthetic magnetic field emerging through the phase of the hopping term, included via Peierls couplings, pushes the system towards the MI regime. As a result, all the MI lobes, except the spin singlet states, encroach more into the SF regime. In the ferromagnetic case, the phase diagrams are similar to that of the scalar Bose gas and the system is more likely to be in the MI regime compared to the SF phase with increasing flux strengths.

Also the nature of MI-SF phase transition for the even MI lobes is first order as long as flux is less than the spin dependent interaction (scaled by U_0) but changes over to a second order transition for higher flux strengths in the AF case. The SF phase is polar and longitudinal ferro (LF) phase corresponding to AF and

ferromagnetic cases. Further, the transverse magnetization is zero, while the longitudinal magnetization is finite in the AF case in presence of magnetic fields. The energy spectrum shows a symmetry with the magnetic flux for both the spin singlet and nematic MI phases. However an asymmetry is observed for the spin singlet phase at higher values of the flux strength.

It is relevant to point out that most of the experiments have focused with quadratic Zeeman interaction term [16,38,38,161], however we restrict ourselves only up to the linear Zeeman term in order to maintain the dimensional homogeneity with the synthetic magnetic field. We find that the linear Zeeman term explores most of the phase properties that are needed for our purpose.





Chapter 5: Spin-1 Bose Hubbard model with nearest neighbour extended interaction

In chapter 3 and chapter 4, we have studied the effects of disorder and magnetic fields on a spin-1 Bose gas including the s -wave dominated short range two body interaction potential. This immediately raises concern to revisit the ground state properties of the SBHM in presence of a longer range interaction potential which is the primary motivation of this chapter.

The phase diagrams of spin-1 Bose gas, particularly for the AF case shows an odd-even asymmetry in the MI phase and also the different order of phase transitions involved therein using different techniques, such as, MFA [25], DMRG [119] as well as Quantum Monte Carlo (QMC) [31, 118] methods in presence of the two body interaction strengths. Besides, various types of the MI phases, including the spin singlet, nematic as well as exotic fractionalized phase that break both the spin and charge symmetry and the SF phases were studied in Refs. [27, 34, 35]. Later, possible ground state structures of the spin nematic and spin singlet MI phases and the transition between them were investigated in Refs. [34, 110]. Further the existence of the dimerized phase is explored using an effective spin Hamiltonian in Refs. [28, 36].

Apart from all these activities, a large number of review articles on the spinor Bose gas exist that emphasize studies in presence of disorder [107, 144], external magnetic field through the linear [29, 164, 165] and the quadratic Zeeman strengths [38, 164, 166–168], spin-orbit couplings (SOC) [48, 49, 145, 146, 169] and synthetic magnetic fields [170] etc. Among them, the inclusion of SOC after its recent experimental realization using Raman coupling between hyperfine levels [171] gives rise to more than one minima in the single particle dispersion relation which leads to different exotic ground state structures like plane and standing wave [145] and various striped ferromagnetic phases [169]. Also usages of the hyperfine spin states as a short lattice dimension, known as the synthetic dimension [47], to create spatially varying SOC gives rise to multiple density ordered SF phases such as the charge density or the spin density wave phases [74].

Although the different density ordered SF phases have been proposed for a spin-1 system using SOC, a specific concern is the possibility to study also the charge density wave (CDW) insulating phase by employing a spin-1 BHM with nonlocal nearest neighbour extended interactions apart from the usual on-site interaction, that may help in realizing the CDW phase. We feel such an extended interaction is relevant in the present context. Although the issues are reasonably well studied in the context of scalar particles [100–102, 172, 173], however it has not been explored for systems with internal degrees of freedom. The CDW phase

which breaks the crystal translational symmetry and thus have different density modulation corresponding to different sublattices, forms a new crystalline phase which is also an incompressible phase like the MI phase defined by an integer occupancy at each lattice site. The extended interaction, which is long range in nature may be realized through the dipole-dipole interaction (DDI) between the dipolar atoms, not only paves the way for realizing the CDW phase, but also yields an additional compressible phase known as the supersolid (SS) phase which depicts a coexistence of both the crystalline and the superfluid phases.

The experimental realization of DDI using bosonic condensates of ^{52}Cr atoms, which have no nuclear spin but have hyperfine spin-3 [97, 98], has created much interest to study the extended BHM from a theoretical perspective. Also for small dipole interaction strengths, the ground state structure of spin-1 dipolar condensate has been studied through single mode approximation (SMA) in Ref. [174] and different spin textures like polar core vortices, chiral spin vortex in ferromagnetic case beyond SMA in Refs. [22, 175]. Apart from the bosonic dipolar condensates, recently experimental efforts to observe the DDI in a gas of fermionic atoms, such as, ^{52}Cr [176], ^{167}Er [177], ^{161}Dy [178] and molecules like $^{23}\text{Na}^{40}\text{K}$ [179] etc. have been made.

Motivated from such studies on magnetic dipole-dipole interaction which has quite a complicated form, in this chapter we study the spin-1 BHM in presence of the density-density interaction term via the mean field approach (MFA). Our plan is to obtain the phase diagrams for both the AF and the ferromagnetic interactions in presence of extended interaction strengths. We have also performed a PMFA calculation to provide support for the mean field phase diagrams. We extend our calculations in presence of an external harmonic confinement and calculate the momentum distribution corresponding to different phases.

We organize this chapter as follows. In the next section, we briefly outline the theoretical formalism for the MFA to study the SBHM in presence of long range density-density interaction and characterized different phases based on the order parameters and occupation densities. After that, we present the phase diagrams which includes the CDW and other phases corresponding to different values of the extended interaction strengths. Finally we draw our conclusion at the end.

5.1 Model

The BHM for spin-1 ultracold atoms in presence of nearest neighbour extended interaction (NNI) can be written as [17, 18, 100],

$$\begin{aligned}
 H = & -t \sum_{\langle ij \rangle} \sum_{\sigma} (a_{i\sigma}^{\dagger} a_{j\sigma} + h.c) - \sum_i \mu_i n_i + V \sum_{\langle ij \rangle} n_i n_j \\
 & + \frac{U_0}{2} \sum_i n_i (n_i - 1) + \frac{U_2}{2} \sum_i (\mathbf{S}_i^2 - 2n_i)
 \end{aligned} \tag{5.1}$$

where all the symbols carry same meaning as discussed in section 2.2 of the chapter 2. $\mu_i = \mu - V_{ho}$ is the chemical potential at site i with μ being the global chemical potential and V_{ho} is the trapping potential for harmonic confinement which has the form $V_{ho} = V_T(\mathbf{x} - \mathbf{x}_i)^2$ [180] where $\mathbf{x} = (x, y)$ and $\mathbf{x}_i = (x_i, y_i)$ are the lattice coordinates at the center and i -site of the trap in a two dimensional square lattice, V_T being the strength of such trap. The last term includes nearest neighbour density-density extended interaction with a repulsive strength V .

To decouple both the hopping and the density-density interaction terms, we shall use the SSMFT as discussed in section 2.4.1 of chapter 2 [25, 181],

$$O_{i\sigma}^{\dagger} O_{j\sigma} \simeq \langle O_{i\sigma}^{\dagger} \rangle O_{j\sigma} + O_{i\sigma}^{\dagger} \langle O_{j\sigma} \rangle - \langle O_{i\sigma}^{\dagger} \rangle \langle O_{j\sigma} \rangle \tag{5.2}$$

where $\langle \dots \rangle$ denotes the equilibrium value of an operator, O . Using Eq.(5.2) in the Hamiltonian appearing in Eq.(5.1), its mean field form can be written as,

$$\begin{aligned}
 H_i^{MF} = & \underbrace{-zt \sum_{\sigma} (\phi_{i\sigma}^* a_{i\sigma} + \phi_{i\sigma} a_{i\sigma}^{\dagger}) + zt \sum_{\sigma} \phi_{i\sigma}^* \psi_{i\sigma}}_{H'_i} \\
 & - \underbrace{\mu_i n_i + \frac{U_0}{2} n_i (n_i - 1) + \frac{U_2}{2} (\mathbf{S}_i^2 - 2n_i) + zV \bar{\rho}_i (n_i - \rho_i)}_{H_i^0}
 \end{aligned} \tag{5.3}$$

where $\phi_{i\sigma} = (1/z) \sum_j \psi_{j\sigma}$ and $\bar{\rho}_{i\sigma} = (1/z) \sum_j \rho_{j\sigma}$ and the sum j includes all the nearest neighbours of the site i of a square lattice with the coordination number, $z = 4$. Here H'_i and H_i^0 are the perturbation term and the unperturbed Hamiltonian respectively.

The presence of an external trapping potential makes the mean field Hamiltonian, H_i^{MF} inhomogenous across the lattice. Thus it necessitates diagonalization of Eq.(5.3) on a full lattice. Here we have considered a square lattice of dimension $L \times L$ and obtain the ground state energy and the eigenfunction of the system.

Since the extended interaction term gives an extra CDW phase which has density modulations as one traverses from one lattice site to another, it is quite

reasonable to break the entire lattice into two sublattices, such as the A and B sublattices. So the unit cell has two types of atoms, namely A and B , where an A atom has B atom as all its neighbours and vice versa. In the CDW phase, one type of sublattice has higher occupancy than the other, so without much loss of generality, we assume $n_A > n_B$.

To begin with, let us consider $V_T = 0$. In the absence of trapping, we can diagonalize Eq.(5.3) over the unit cell consisting of two sites namely A and B . Thus for A type of sublattice ($\mu_A = \mu_B = \mu$), Eq.(5.3) can be written as,

$$H_A^{MF} = zt \sum_{\sigma} (-\psi_{B\sigma} a_{A\sigma} - \text{h.c.} + \psi_{B\sigma} \psi_{A\sigma}) + \frac{U_0}{2} n_A (n_A - 1) - \mu n_A + \frac{U_2}{2} (\mathbf{S}_A^2 - 2n_A) + zV\rho_B (n_A - \rho_A) \quad 5.4$$

Similarly one can easily obtain H_B^{MF} by changing the indices from A to B (and B to A) and the total mean field Hamiltonian is just sum of two mean field Hamiltonians, that is, $H_i^{MF} = H_A^{MF} + H_B^{MF}$. The self consistent ground state energy and the eigenfunction are obtained by diagonalizing H_i^{MF} in the occupation basis $|n_i\rangle$ with $n_i = 7$ starting with some guess values for $\psi_{(A/B)\sigma}$ and $\rho_{(A/B)\sigma}$ as discussed in section 2.4.1 of chapter 2.

5.2 Results

5.2.1 Antiferromagnetic case

For an AF case, we shall consider the spin dependent interaction value, $U_2/U_0 = 0.03$ and present our numerical results for different strengths of the extended interaction, V .

5.2.1.1 MFA phase diagrams

The phase diagrams are calculated based on the self consistent values of the SF order parameters, $\psi_{(A/B)}^{eq}$ and the local densities, $\rho_{(A/B)}^{eq}$ (we shall drop the superscript, eq from here) to characterize different phases. Both the CDW and MI phases are incompressible phases with integer occupation densities and vanishing SF order parameters, however the CDW phase is characterized by unequal occupation densities in the A and B sublattices, that is, $\rho_A \neq \rho_B$, (the MI phase corresponds to $\rho_A = \rho_B$) where $\rho_{A/B}$ is an integer and denotes the occupancy of a site belonging to the sublattice, A/B . Also the SF and SS phases are the compressible phases with non integer densities and finite values of the SF order parameters. But in the SF phase, $\psi_A = \psi_B \neq 0$ and $\rho_A = \rho_B \neq \text{integer}$, while the SS phase is characterized by $\psi_A \neq \psi_B \neq 0$ and $\rho_A \neq \rho_B \neq \text{integer}$ respectively.

We present our phase diagrams corresponding to both the weak and strong interaction limits of zV/U_0 in Fig.5.1(a)-(d). The reason for choosing four different values zV/U_0 is justified in the upcoming discussion.

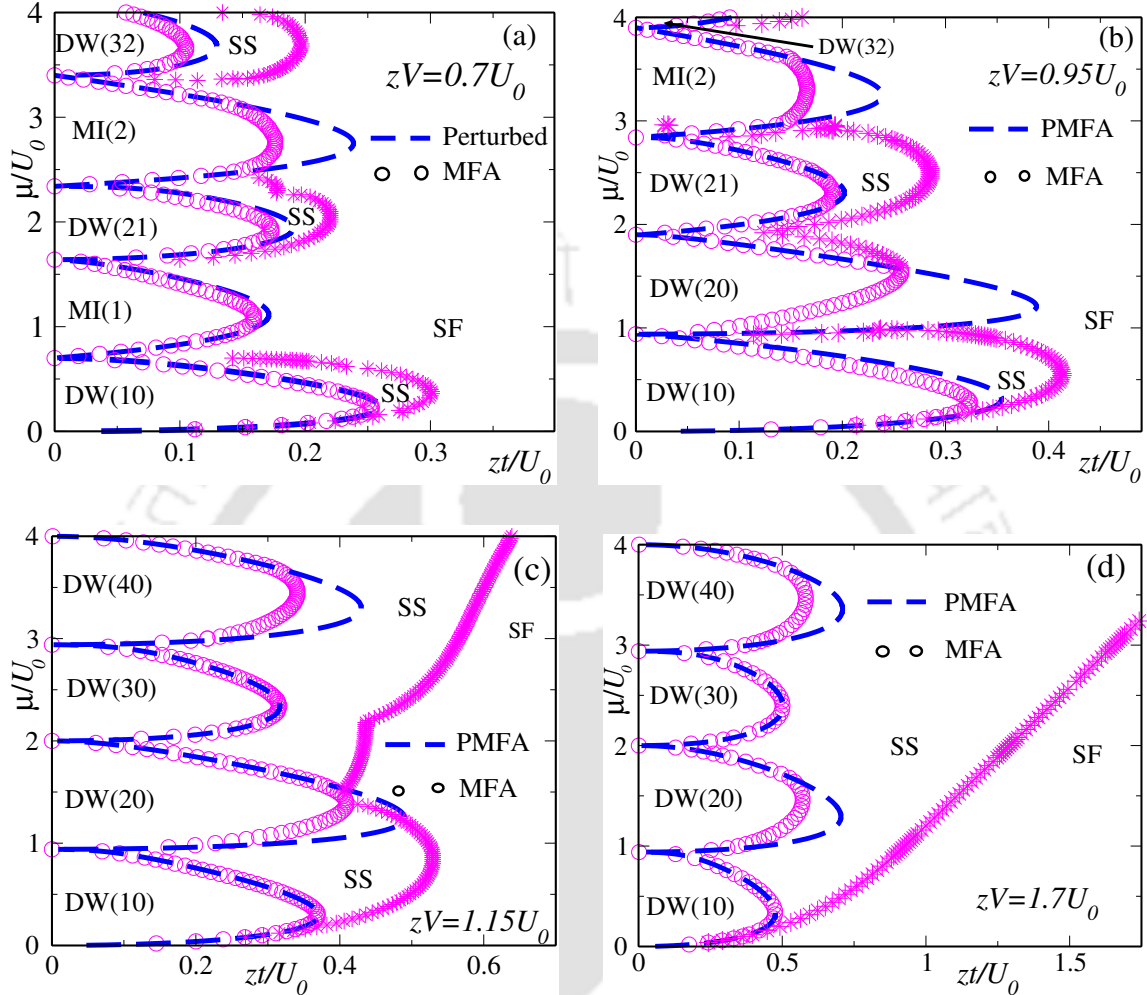


Figure 5.1: Phase diagrams in AF case with $U_2/U_0 = 0.03$ for different values of zV/U_0 are shown from (a)-(d). The dashed lines denote the results of the perturbation calculation (PMFA) and the circles represent the mean field (MFA) phase diagrams. At $zV/U_0 = 0.7$ [Fig.(a)], the phase diagram consists of various CDW phases, the even MI(2) and odd MI(1) phases. In Fig.(b), for $zV/U_0 = 0.95 > 1 - 2U_2/U_0$, the odd MI(1) lobes now gripped by the CDW(20) phase. In Fig.(c), the MI(2) phase is now occupied by the CDW(40) phase since $zV/U_0 = 1.15 > 1 + 2U_2/U_0$. In Fig.(d), at strong interaction limit, $zV/U_0 = 1.7$, all insulating phase are now the CDW phases.

In Fig.5.1(a), the phase diagram presented for $zV/U_0 = 0.7$ shows that the CDW phase appears in between the MI lobes, and thus a direct transition from the CDW to the SF is interrupted due to the appearance of the SS phase (region enclosed by the * symbol). The symbol DW($\rho_A\rho_B$) implies the CDW phase having occupation densities, ρ_A (corresponding to sublattice A) and ρ_B (corresponding to sublattice B) with average occupation density, $\bar{\rho} = (1/2)[\rho_A + \rho_B]$. The SS phase, which not only appears concomitantly with the DW(21) and DW(32) phases, but also

exists along with the DW(10) phase for $\bar{\rho} < 1/2$, as was predicted earlier through quantum Monte Carlo (QMC) studies in Ref. [101]. The MI(1) and MI(2) are the Mott insulating phases with occupation densities $\rho_A = \rho_B = 1$ and $\rho_A = \rho_B = 2$ respectively. The odd and even MI phases which form the spin nematic and singlet phases are the distinguishing features of a spinor Bose gas compared to a spin-0 Bose gas and the stabilization of the singlet phase over the nematic phase has been studied extensively without extended interaction in Refs. [24, 25].

In Fig.5.1(b), we found that corresponding to $zV/U_0 = 0.95$, although the phase diagram consists of all the compressible and incompressible phases, however, interestingly, the MI(1) phase is now completely occupied by the DW(20) phase and the chemical potential widths of the DW phases increase with zV/U_0 , which now has a value 0.95 [Fig.5.1(b)] compared to 0.7 in Fig.5.1(a).

The disappearance of the MI(1) phase can be understood by considering the atomic limit, that is, $t = 0$ where the system only consists of the MI and CDW phases. In the atomic limit, the ground state energy $E_g(n_A n_B)$ from Eq.(5.1) in the CDW phase is given by,

$$E_g(n_A n_B) = \frac{U_0}{4} \sum_{i=A,B} [n_i(n_i - 1)] - \frac{\mu}{2} \sum_{i=A,B} n_i + \frac{U_2}{4} \sum_{i=A,B} [S_i(S_i + 1) - 2n_i] + \frac{zV}{2} n_A n_B \quad 5.5$$

Following the calculations carried out in Ref. [107], we found that the chemical potential width for the odd MI lobes is $U_0 - 2U_2$, while for the even MI lobes, it is $U_0 + 2U_2$. Also we have checked that for the CDW phase, the chemical potential width is zV using the same assumption that for the odd occupation densities, we shall consider the spin eigenvalues to be $S = 1$ and for even occupation densities, $S = 0$ will be considered. So for $zV/U_0 = 1 \pm 2U_2/U_0$, there are possibilities of coexistence of different CDW and MI phases because of the degeneracy in their ground state energies. As a result, at $U_2/U_0 = 0.03$, when $zV/U_0 > 0.94$, the MI(1) phase now gets absorbed by the DW(20) phase and this applies for the other odd MI lobes as well for $U_2/U_0 < 0.5$.

At larger value of the extended interaction, that is, for $zV/U_0 = 1 + 2U_2/U_0 = 1.06$, the MI(2) phase becomes degenerate with the DW(40) phase and beyond this critical value, all insulating phases become CDW phases and the SS phase has now expanded significantly with increasing zV/U_0 [Fig.5.1(c)]. We have also obtained the phase diagrams at stronger values of the extended interaction strength, that is, $zV/U_0 = 1.7$ in Fig.5.1(d), which indicates that the system is more likely to be in the SS phase compared to the CDW or the SF phases.

Since the formation of spin singlet pairs corresponding to even occupation densities and their stabilization over the odd MI lobes has been studied in Refs. [24, 25, 110] without the extended interaction, one can ask, is it possible to have also the spin singlet phase corresponding to integer $\bar{\rho}$ for the CDW phase. If

we look at Fig.5.1(a)-(b), it can be concluded that although the critical tunneling strength, zt_c/U_0 for transition from the incompressible to the compressible phases still occurs at higher values of zt/U_0 for the MI(2) phase compared to that of the MI(1) phase, but zt_c/U_0 for the DW(20) phase is now enhanced with increasing zV/U_0 compared to the other insulating phases except for the DW(10) phase.

Interestingly, from Fig.5.1(c)-(d), we found that the zt_c/U_0 for a transition from the CDW to the SS phase corresponding to the DW(20) or DW(40) are higher than that of the DW(10) or DW(30), thereby indicating a possibility of spin singlet formation in these CDW phases which we shall confirm by calculating the local spin eigenvalue in the subsequent discussion.

5.2.1.2 SF order parameter and occupation density variation

It is also helpful to study the nature of phase transition for different phases in the AF case. In section 2.2 in chapter 2, the order parameters variation show

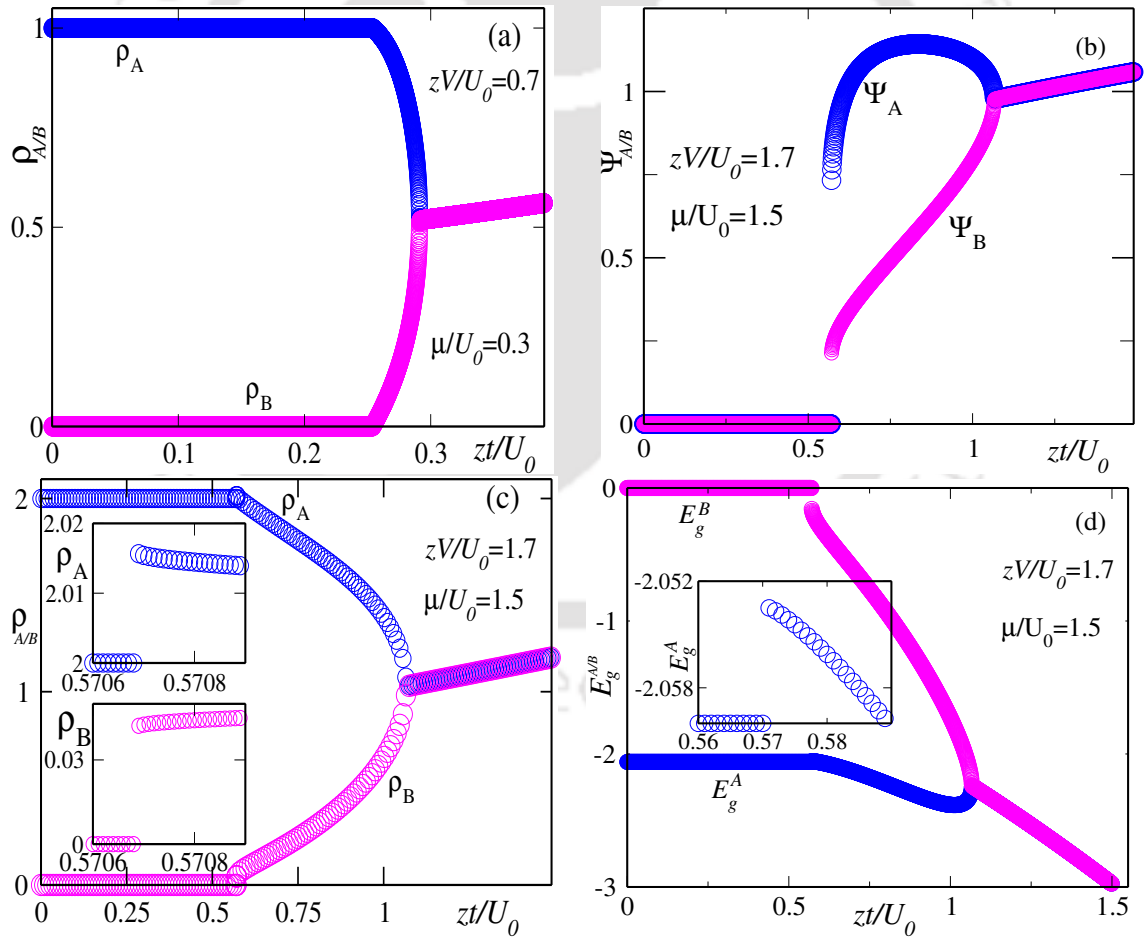


Figure 5.2: The one dimensional behaviour of the occupation densities $\rho_{A/B}$ in the AF case with $zV/U_0 = 0.7$ in (a) and $zV/U_0 = 1.7$ in (c). The variation of the SF order parameter, $\psi_{A/B}$ in (b) and the ground state energy, $E_g^{A/B}$ in (d) for $zV/U_0 = 1.7$. The discontinuity in the order parameters and $E_g^{A/B}$ indicate a first order transition for the DW(20)-SS transition while second order for the DW(10)-SS transition respectively.

that the MI-SF phase transition is first order for the even MI phase and second order for the odd MI lobes without an extended interaction in Refs. [24, 25].

In Fig.5.2(a), we have shown the one dimensional behaviour of $\rho_{A/B}$ for $zV/U_0 = 0.7$ at $\mu/U_0 = 0.3$ and it shows a continuous transition from DW(10) to the SS and then to the SF phases, indicating a second order transition. The same holds true for other DW phases. However, we have checked that the transition from DW to SF phase is found to be first order in nature, and the SF-MI transition for the even and odd MI phases still show first and second order transition respectively for $zV/U_0 = 0.7$ and $zV/U_0 = 0.95$.

For $zV/U_0 > 1.15$, the CDW phases indicate a first or a second order transition depending upon the even or the odd occupation densities respectively. The SF order parameters and occupation densities show a continuous transition from DW(10) or DW(30) to the SS and then SF phase for both values of zV/U_0 , namely, $zV/U_0 = 1.15$ and $zV/U_0 = 1.7$. While for the DW(20) or DW(40), $\psi_{A/B}$ [Fig.5.2(b)] and $\rho_{A/B}$ [Fig.5.2(c)] show a first order transition to the SS phase. The ground state energy, $E_g^{A/B}$ of the DW(20) or DW(40) also shows discontinuous transition to the SS phase, a behaviour similar to the spin singlet MI phase [Fig.5.2(d)].

5.2.1.3 Spin eigenvalue behaviour

It is also necessary to study the behaviour of the spin eigenvalue, $\langle S_i^2 \rangle$ with different values of zV/U_0 in order to verify our claims made in section 5.2.1.1 that the spin eigenvalue to be 0 for the even occupation densities and 1 for odd occupation densities to calculate the width of each of the CDW lobes and assess if there is any possibility of spin singlet formation for the CDW phase having integer $\bar{\rho}$ at larger values of zV/U_0 .

At $zV/U_0 = 0.7$, $\langle S_A^2 \rangle = 2$ and $\langle S_B^2 \rangle = 0$ for the DW(10) phase [Fig.5.3(a)] and we have found that for the DW(21) phase, the spin eigenvalue corresponds to $\langle S_A^2 \rangle = 0$ and $\langle S_B^2 \rangle = 2$. This implies that $S_A = 1$ for $\rho_A = \text{odd}$ and $S_B = 0$ for $\rho_B = \text{even}$ and vice versa for the CDW phases which holds true for other values of zV/U_0 as well. We have checked that $\langle S_i^2 \rangle = 0$ for the even and $\langle S_i^2 \rangle = 2$ for the odd MI phases and the transition to the SF phase still remain as the first and the second order respectively.

At $zV/U_0 = 1.7$, both the $\langle S_A^2 \rangle = \langle S_B^2 \rangle = 0$ for DW(20) phase, then followed by a jump to the SS phase [Fig.5.3(b)] and we found an identical behaviour also for the DW(40) phase. While for the DW(10) or the DW(30) phases, $\langle S_A^2 \rangle = 2$, $\langle S_B^2 \rangle = 0$ in the CDW phase and show continuous transition to the SS and the SF phases. It is important to point out that the discontinuity (signature of the first order transition) in $\rho_{A/B}$ and $\langle S_{A/B}^2 \rangle$ are very small corresponding to both the DW(20) and DW(40) phases which may be smoothed out by the quantum fluctuations. Since the SF order parameter [Fig.5.2(b)], $\rho_{A/B}$ [Fig.5.2(c)] and the ground state

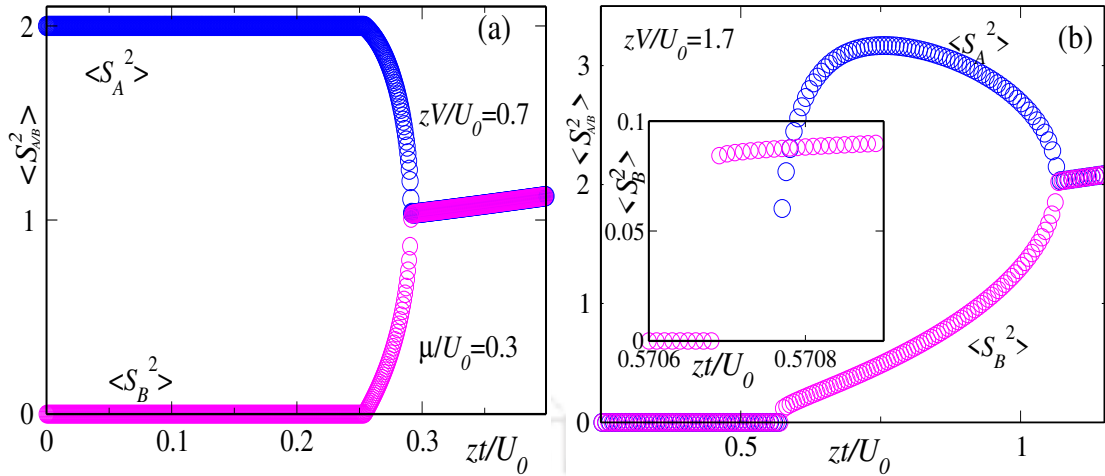


Figure 5.3: The one dimensional behaviour of $\langle S_{A/B}^2 \rangle$ in the AF case with $zV/U_0 = 0.7$ in (a) and $zV/U_0 = 1.7$ in (b). The discontinuity in $\langle S_i^2 \rangle$ indicates a first order transition for the DW(20)-SS transition (b) while second order for the DW(10)-SS transition respectively in (a). The total spin eigenvalue $\langle S_i^2 \rangle$ is either 2 or 0 signifies $S_i = 1$ or $S_i = 0$ since $\langle S_i^2 \rangle = S_i(S_i + 1)$ depending upon the odd or even occupation densities corresponding to the respective CDW phase.

energy, $E_g^{A/B}$ [Fig.5.2(d)] variation also show a discontinuity as well. Thus it is reasonable to conclude that the phase transition involved between the DW(20) or the DW(40) and the SS phase is essentially first order in nature.

Based on the above properties, so we infer that the DW(20) or the DW(40) behave as the spin singlet while the DW(10) or the DW(30) as spin nematic CDW insulator phases like the spin singlet and nematic phases corresponding to the even and the odd MI lobes.

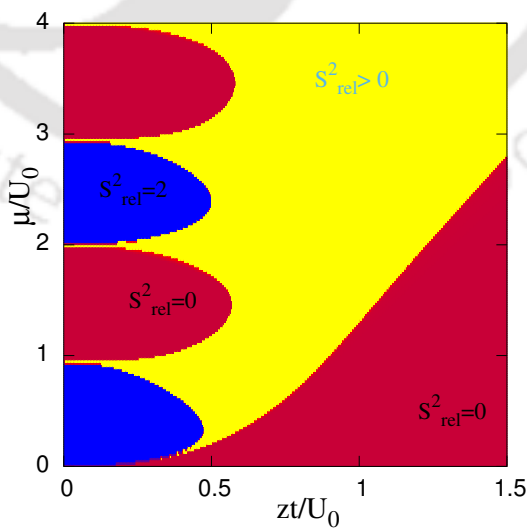


Figure 5.4: Relative spin eigenvalues, $S_{rel}^2 = \langle S_A^2 \rangle - \langle S_B^2 \rangle$ in the AF case for $zV/U_0 = 1.7$. For the even CDW phase, $S_{rel}^2 = 0$ and $S_{rel}^2 = 2$ for the odd CDW phase. This shows that the spin eigenvalue oscillates between 0 and 1 corresponding to the even and odd CDW phases and indicates a spin density wave (SDW) pattern.

Further we have plotted the relative spin eigenvalue, that is, $S_{rel}^2 = \langle S_A^2 \rangle - \langle S_B^2 \rangle$ as a function of zt/U_0 for $zV/U_0 = 1.7$ in Fig.5.4. At this value, S_{rel}^2 shows that, for the CDW phases, $S_{A/B}$ oscillates between 0 and 1 depending upon the density variations of these particular phases, that is, the blue and red lobes pertaining to the CDW phase having non integer and integer $\bar{\rho}$ respectively. The yellow region is for the SS phase where $S_{rel}^2 \neq 0$ and then the SF phase corresponds to the red region where $S_{rel}^2 = 0$. Thus we found signatures of a spin density wave (SDW) pattern, where S_i oscillates between 0 and 1 in a similar fashion as that of ρ_i in different CDW phases.

5.2.1.4 PMFA phase diagrams

We shall now turn on our attention to the second order perturbative mean field approach (PMFA) as discussed in section 2.4.2 of chapter 2 to obtain the phase boundaries between different phases in order to compare them with the mean field results discussed above. The ground state energy, E_n after incorporating the first order, E^1 and the second order, E^2 corrections can be expressed in terms of ψ and ϕ as [24],

$$E_n(\psi, \phi) = E^0 + E^1 + E^2 = E^0 + C_2(U_0, U_2, \mu, n, V)f(\psi_\sigma, \phi_\sigma) \quad 5.6$$

where C_2 is the coefficient arising from the perturbation correction, f includes the order parameter and E^0 is the eigenvalue of H^0 which is given by (site indices are skipped for the time being),

$$E^0 = \frac{U_0}{2}n(n-1) - \mu n + \frac{U_2}{2}[S(S+1) - 2n] + zV\bar{\rho}(n-\rho) \quad 5.7$$

Since the order parameter vanishes in the insulating phase, and it remains finite in the compressible phases, the boundary between them can be obtained by putting $C_2 = 0$. Following similar calculations of the PMFA as discussed in section 2.4.2 of chapter 2, the boundary equation for the even MI lobes leads to the following equation,

$$\left(\frac{1}{zt}\right)_{\text{even}} = \frac{(n_i+3)/3}{\beta_i + zV\bar{\rho}_i} - \frac{n_i/3}{-a_i - 2U_2 + zV\bar{\rho}_i} \quad 5.8$$

while for the odd MI lobes, it is given by,

$$\left(\frac{1}{zt}\right)_{\text{odd}} = \frac{(n_i+2)/3}{a_i - zV\bar{\rho}_i} + \frac{4(n_i-1)/15}{a_i + 3U_2 - zV\bar{\rho}_i} + \frac{(n_i+1)/3}{\beta_i - 2U_2 + zV\bar{\rho}_i} + \frac{4(n_i+4)/15}{\beta_i + zV\bar{\rho}_i + U_2} \quad 5.9$$

where $a_i = \mu - (n_i - 1)U_0$ and $\beta_i = -\mu + n_iU_0$ respectively. Thus the phase boundary between the MI and SF phases in presence of zV/U_0 is obtained by using either

of Eq.(5.8) or Eq.(5.9) separately, depending upon the even or odd MI lobes, with $\bar{\rho}_i = n_0$ for $i \in A, B$ since in MI phase, $\psi_A = \psi_B = 0$ and $\rho_A = \rho_B = n_0$, n_0 being the occupancy of that particular MI phase.

Now for the CDW-SS phase boundary, an immediate question arises, namely, since it has both even and odd occupation densities, which equation should one use for dealing with the different CDW phases. As we have seen before, the spin eigenvalue, $S_i = 0$ corresponding to $\rho_i = \text{even}$ and $S_i = 1$ for $\rho_i = \text{odd}$ in the CDW phases, we may use a combination of Eq.(5.8) and Eq.(5.9) depending upon the density to determine the phase boundary with $\psi_i = \psi_A$, $\rho_i = \rho_A$, $\bar{\rho}_i = \rho_B$ if $i \in A$ and vice versa for $i \in B$. For example, for the CDW(10) phase at $zV/U_0 = 0.7$, $n_A = 1$, $S_A = 1$ and $n_B = 0$, $S_B = 0$, the boundary equation is given by,

$$\frac{1}{z^2 t^2} = \left(\frac{1}{0.7 - x} \right) \left(\frac{1}{x} + \frac{2}{3(0.97 - x)} + \frac{4}{3(1.03 - x)} \right) \quad 5.10$$

In a similar fashion, we have calculated the boundary between all the compressible and incompressible phases using Eq.(5.8) or Eq.(5.9) at different values of zV/U_0 corresponding to the AF case and are superimposed in Fig.5.1 (dashed line).

It shows that the boundary curve of the MFA is in complete agreement with the PMFA for the first CDW phase, that is, DW(10) [Fig.5.1 (a)], but discrepancy appears for the other MI as well as CDW phases near the tip of the insulating phases [Fig.5.1 (b)]. Particularly, the deviation is prominent for the even occupancies as compared to the odd ones corresponding to the CDW phase for $zV/U_0 > 1.15$ [Fig.5.1 (c) and (d)]. In Refs. [24, 30], it was found that similar discrepancy appears and interestingly it exists also for the third MI lobes with much lower values of the spin dependent interaction without extended interaction strengths. So it is reasonable to conclude that the MFA only holds deep inside the MI lobes where the fluctuations are small but near the tip of the MI or CDW lobes, MFA fails to handle the fluctuations because of its limitations in lower dimensions.

5.2.1.5 Effects of harmonic trapping potential

So far the results presented above do not include the effects of a trapping potential. Now we shall consider a two dimensional trapping potential given by,

$$V_{ho} = V_T[(x - x_i)^2 + (y - y_i)^2] \quad 5.11$$

where V_T denotes the strength of the confining potential and the trap can be chosen to be located at the center of the lattice of size $L \times L$, that is, at $x = y = L/2$. Since the order parameter and the spin eigenvalues are now inhomogeneous over the lattice sites, here we shall show their one dimensional behaviour along the x -axis as a function of the distance, x_i from the center of the trap by choosing

$y = L/2$. Thus we will be able to scan both the sublattice, namely, A and B simultaneously.

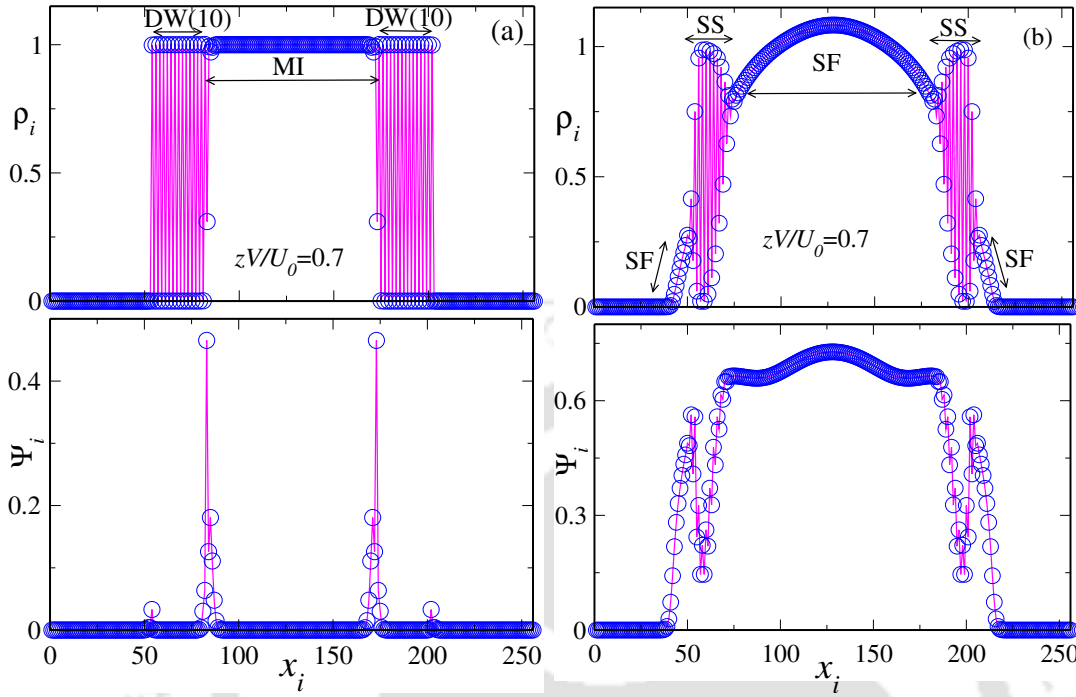


Figure 5.5: The variation of density, ρ_i and the order parameter, ψ_i in the AF case with $zV/U_0 = 0.7$ and trapping potential, $V_T = 0.0002$ for the CDW-MI phase at $\mu/U_0 = 1.1$ and $zt/U_0 = 0.05$ in (a) and the SS-SF phase at $\mu/U_0 = 1.25$ and $zt/U_0 = 0.25$ in (b).

In Fig.5.5, we have shown density, ρ_i (first row) and order parameter, ψ_i (second row) profile in the AF case with a trapping potential, $V_T = 0.0002$ for a square lattice of size $L = 256$. A careful scrutiny reveals that $V_T \sim 10^{-4}$ for a square lattice of dimension 256×256 will enable us to capture all the different phases and we choose μ/U_0 , zt/U_0 in such a way that the trap center is in the vicinity of the DW-MI and the SS-SF phases respectively. The open circles denote A type and solid lines denote B type sublattice.

From Fig.5.5(a), it is clear that they are symmetric about the center of x_i and as one advances from the center in either direction, we find, $\psi_i = 0$ while $\rho_i = 1$ which signals the MI(1) phase. Further movement along the x axis leads to a very narrow region where ψ_i is finite and both ψ_i , ρ_i are oscillatory in nature implying the presence of the SS phase. As we move with x_i , this narrow SS phase is now followed by a region where ψ_i vanishes but ρ_i oscillates between 0 and 1, thereby signifying the presence of the the DW(10) phase and finally lead to a vacuum with vanishing ψ_i and ρ_i at the edge of the trap.

In Fig.5.5(b), we have found that around the trap center, ψ_i and ρ_i are finite and they are equal for both the sublattices, indicating the signature of the SF phase. Upon moving away from the SF phase, one encounters the SS phase

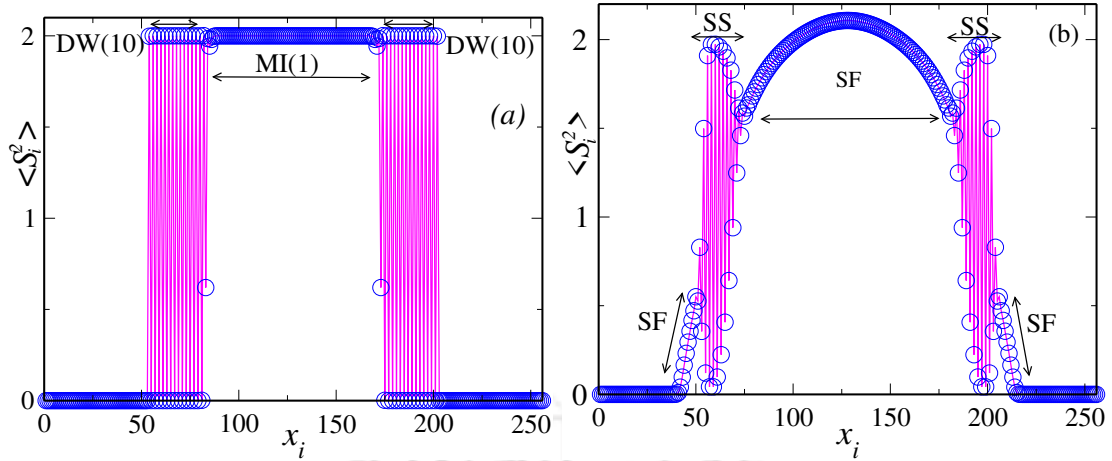


Figure 5.6: The variation of $\langle S_i^2 \rangle$ in the AF case with $zV/U_0 = 0.7$ and trapping potential, $V_T = 0.0002$ for the CDW-MI phase at $\mu/U_0 = 1.1$ and $zt/U_0 = 0.05$ in (a) and the SS-SF phase at $\mu/U_0 = 1.25$ and $zt/U_0 = 0.25$ in (b).

with oscillating ψ_i and ρ_i values which enters into the SF phase and eventually to a vacuum phase. We have also obtained the density and order parameter dependencies as a function of the lattice site, x_i for different values of zV/U_0 and V_T and they exhibit similar properties to those discussed above for different phases.

The variation of $\langle S_i^2 \rangle$ for different phases in the AF case with the trapping strength, $V_T = 0.0002$ are shown in Fig.5.6. It shows similar behaviour to that of ψ_i and ρ_i and found that the MI(1) phase with $\langle S_i^2 \rangle = 2$ is sandwiched between the DW(10) phases, where $\langle S_i^2 \rangle$ oscillates between 0 and 2 in Fig.5.6(a). Further an oscillatory behaviour of $\langle S_i^2 \rangle$ in the SS phase is observed which is located in between the SF phases in Fig.5.6(b).

Although the order parameter and the density modulation with lattice sites give an impression about the different phases, but to experimentally realize their signatures one has to record the interference pattern via a *time-of-flight* experiment. In a *time-of-flight* experiment, the trapped atoms in optical lattices are allowed to expand suddenly to register the interference patterns corresponding to a given Bloch state which is a superposition of plane waves with a spread in the momentum values.

In Fig.5.7, we have shown the Fourier transform amplitude of ρ_i , ψ_i and S_i^2 with the momentum along the x -direction, namely k_x in the SF, SS and CDW phases. The variation of ρ_k [Fig.5.7 (top)] shows the appearance of peaks at $k_x = 0$ and $k_x = 2\pi$ for all the phases, while an additional peak appears at $k_x = \pi$ for the CDW or the SS phase. The ψ_k [Fig.5.7 (middle)] and S_k^2 [Fig.5.7 (bottom)] shows similar behaviour as that of the SF and the SS phases except for the CDW phase, no peak is observed in k_x while the tiny peaks are due to inhomogeneity created by the trapping potential.

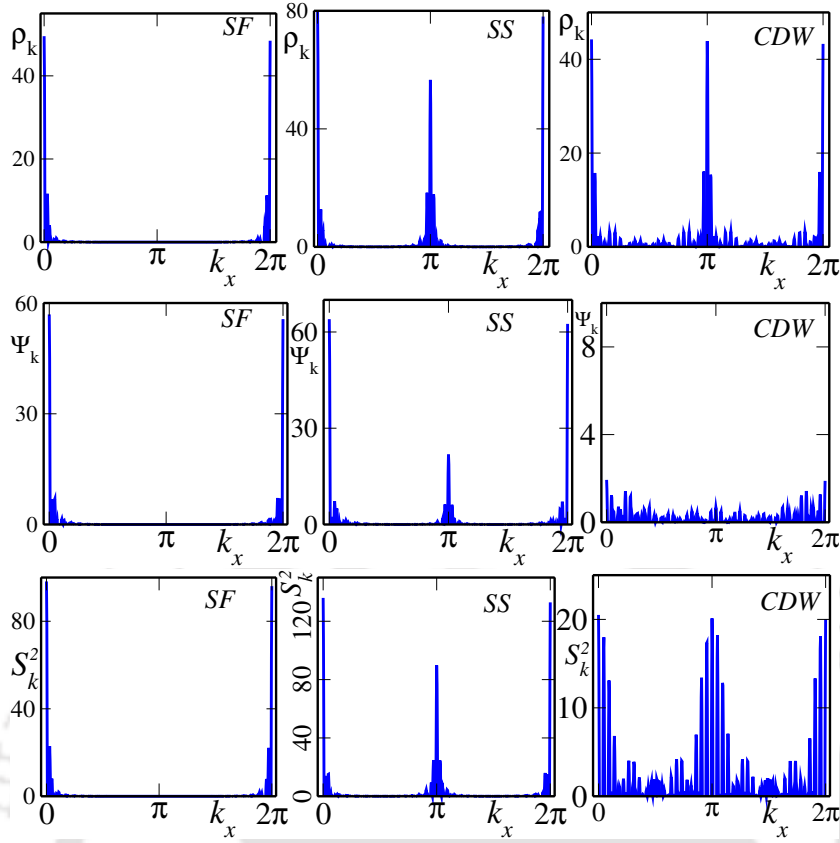


Figure 5.7: Magnitude of the Fourier transform of ψ_i , ρ_i and S_i^2 with k_x in SF, SS and CDW phases for AF case with $zV/U_0 = 1.7$ and $V_T = 0.0002$. The parameters are $\mu/U_0 = 1.0$ and $zt/U_0 = 1.6$ for the SF and $\mu/U_0 = 2.5$ and $zt/U_0 = 0.8$ for SS and $\mu/U_0 = 1.5$ and $zt/U_0 = 0.25$ for CDW phases respectively.

We have also considered the scenario in two dimensions by including k_y and found that the peaks in ρ_k corresponds to $(k_x, k_y) = (2\pi j, 2\pi m)$ for the SF or SS phases in addition to $(k_x, k_y) = (\pi j, \pi m)$ for the SS or CDW phases where j, m are integers and $k_{x,y}$ are defined in unit of lattice constant. The momentum profile of ψ_k and S_k^2 shows similar peak positions as that of ρ_k in the SF and SS phases, but no peak is observed at $(k_x, k_y) = (\pi j, \pi m)$ for the CDW phase.

5.2.2 Ferromagnetic case

In Fig.5.8, we have plotted the phase diagrams for two different values of zV/U_0 corresponding to the ferromagnetic case and found that they show similar characteristics as that of a scalar Bose gas. In this case, there is no distinction between the odd and the even MI lobes and hence all the MI lobes have densities, ρ_i equal to the maximum spin eigenvalue, that is, $S_i = n_i$ [107].

In the atomic limit, it turns out the the chemical potential width for each of the MI lobe is $U_0 + U_2$, while for the CDW phase, it is zV . The phase diagram with $zV/U_0 = 0.85$ for $U_2/U_0 = -0.04$ is shown in Fig.5.8 (a) demonstrates all the MI

and the CDW phases along with all the compressible phases, since the critical value at which both the MI and CDW phases become degenerate corresponds to $zV/U_0 = 0.96$.

We have also considered a strong interaction limit, namely $zV/U_0 = 1.4$, which is larger than the critical value 1 for $U_2/U_0 = 0.0$ in Fig.5.8 (b). Now all the CDW and the SS phases can be found, however there are no MI lobes. We have also checked for different values of zV/U_0 corresponding to $U_2/U_0 = 0.0$ and they are in complete agreement with the results obtained via Gutzwiller approximation in Ref. [100].

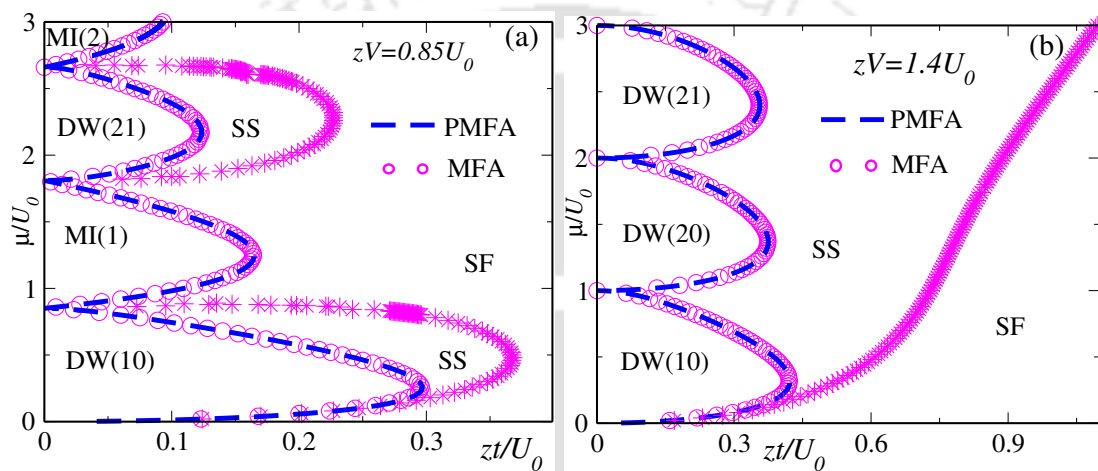


Figure 5.8: Phase diagrams in the ferromagnetic case with zV/U_0 for $U_2/U_0 = -0.04$ in (a) and $U_2/U_0 = 0.0$ in (b). At $zV/U_0 = 0.85 < 1 + U_2/U_0$ [Fig.(a)], both the MI and CDW phases exist with the SS and SF phases. In Fig.(b), phase diagram consists only the CDW phases since $zV/U_0 = 1.4 > 1$.

For the analytical phase boundary, we have done a similar perturbation (PMFA) calculation for the phase boundary for $U_2/U_0 \leq 0$ with maximum spin eigenvalue of S_i that is $S_i = n_i$. We found that both the MFA and phase diagrams obtained via perturbation calculations (dashed line) are in complete agreement with each other in Fig.5.8. Moreover the resultant boundary equations for the MI-SF and CDW-SS phase are identical with those obtained for different values of zV/U_0 in Refs. [100, 182].

The variations of ψ_i and ρ_i and the Fourier transform profiles are in complete agreement with the results obtained in Refs. [181, 183]. We have also checked the spin eigenvalues and the order parameter profiles in presence of one dimensional trapping potential without the extended term, zV/U_0 corresponding to both values of the spin dependent interactions and they are in agreement with the results obtained in Ref. [180].

5.3 Conclusion

In this work, we have studied the spin-1 BHM in presence of nearest neighbour extended interactions corresponding to both values of the spin dependent interactions using the mean field and the perturbation expansion approach. In the AF case, we have used different justifiable values of the extended interaction strength corresponding to the odd and the even MI lobes. In the weak interaction limit, the phase diagram consists of the CDW phase, the MI phase along with the compressible SF and SS phases. In the strong interaction limit, when extended interaction is larger than the width of the odd and even MI lobes, all the MI phases get captured by the CDW phase, since at this critical value, both the CDW and MI phases become degenerate. Further increase of the interaction strength leads to the stability of the SS phase over the other phases.

We have also found that the DW-SF phase shows a first order transition due to a jump in the order parameter. While the DW-SS phase transition is second order in nature for the odd occupancies and of first order for the even occupation densities. The MI-SF phase transition still remain the first and second order respectively for the even and odd MI lobes. We have also calculated the local spin values to confirm the formation of the spin singlet and nematic CDW phases. In the CDW phase, the spin eigenvalues oscillate between 0 and 1 replicating a spin density wave (SDW) pattern.

Further, we have obtained the phase diagrams through the perturbation calculation and the boundary between the CDW-SS and MI-SF phases to compare them with the mean field results. Although the phase diagrams are in agreement with each other, however small discrepancy appears at the tip of the insulating phases and particularly it is prominent for the incompressible phases with even occupation densities.

Also we have studied the order parameter and spin profile in presence of the trapping potential to characterize different phases. In order to get a close resemblance with that of the experimental observations, we have computed the Fourier transform of the order parameter that demonstrates the appearance of peaks at different momenta values which can be experimentally observed via *time-of-flight* experiment. In the ferromagnetic case, the phase diagrams are similar to the spin-0 Bose gas and both the mean field and the analytic results are in excellent agreement with each other.

Finally, the extended interaction strength which is closely related with the long range DDI can have either electric origin having coupling constant, $C_{dd} = \mu_e^2/\epsilon_0$ [96] or magnetic origin with $C_{dd} = \mu_0\mu_m^2$ [96]. For the alkali atoms with spin degrees of freedom, the magnetic dipole strength (μ_m) is considerable and all the results presented above will find relevance for the quantum dipolar gases with large μ_m .

The off-site coupling DDI is denoted by the 'dipolar length', $\alpha_{DDI} \propto M\mu_m^2$ [96] (M being the atomic mass) and hence due to large μ_m , along with high values of atomic masses of dipolar gases, such as *Cr*, *Dy* and *Er* etc, the DDI is significant. In fact further control in terms of enhancement of DDI can be achieved by altering the orientation of the magnetic dipoles [184]. Experimentally, it was found that for *Cr* atoms, $\mu_m = 6\mu_B$ [97], for *Dy* atoms, $\mu_m = 10\mu_B$ [185] and for *Er*, it is $7\mu_B$ [186] are reported. Inspired by such possibilities, we have considered the NNI to be comparable to the on-site energy. Specifically to quench the theoretical interests on the phenomena occurring in the parameter space, we have considered the extended interaction strength which denotes the width of the CDW lobes to have values lesser, greater or much greater than the width of the Mott insulating lobes.





Chapter 6: Quantum phases of a spin-1 ultracold Bose gas with three body interaction potential

The pioneering illustration of a spin-1 ultracold Bose gas were first portrayed simultaneously by Ho [17] and Machida [18] by generalizing the Gross-Pitaevskii equation using a low energy Hamiltonian for spinor particles. Contrary to the scalar Bose gas, the spinor Bose gas needs to be described by a vector order parameter and hence all the hyperfine components transform onto each other through a rotational symmetry in spin space. They also layout a change in the ground state structure of the system and analyzed different spin textures and topological excitation.

This predication allows several authors to rigorously go through the rich phase properties possessed by the SBHM owing to the presence of an additional spin dependent interaction term using diverse techniques, such as mean field approach (MFA) [25, 110, 130], quantum Monte Carlo (QMC) [31, 111, 117, 118] and perturbative expansion [24, 30, 187] etc. For an AF spin dependent interaction, it was found that the Mott insulating phase comprises of a spin singlet phase with even occupation densities and a spin nematic phase with odd occupation densities, where the latter is seen beyond one dimension. Besides, the formation of the spin nematic-singlet phase which is responsible for the odd-even asymmetry in the MI lobes pledge richer characteristics of a spinor Bose gas over a scalar gas.

However the density matrix renormalization group (DMRG) studies done in one dimension outlined that the MI phase with odd occupation densities seem to be a dimerized phase [28, 34, 36, 119]. Also, it displays odd-even asymmetry at higher values of the spin dependent interaction strength [119]. Further, the study on the spinor Bose gas appears to progress steadily in a variety of contexts, such as in presence of disorder [107, 144, 188], dipolar [22, 175] and extended [173, 189] interaction, magnetic field [26, 41, 47, 74, 153, 160, 170], spin-orbit coupling [45, 49, 169] etc.

All of these activities on a spin-1 Bose gas are examined by keeping in mind only the two body spin independent and spin dependent interaction terms which evidently generate curiosity to re-visit their properties in presence of a multi-body, especially the three body interaction strength. The effects of repulsive three body interaction on spin-0 (scalar) Bose gas have been subject of intense theoretical study in recent times after Will *et al.* [105] claimed to have experimentally observed the multi-body interactions [190, 191]. They found the signature up to six body interaction strength by measuring the multi-orbital energies using a collapse and revival technique. In their case, the ground state atoms occupying the single orbital energy are excited to higher-lying orbitals which in turn reshapes the

spatial structures of the wave functions. Unfortunately, effects of such interaction on spin-1 Bose gas remain unexplored and thus motivates us to explore their ground state properties in presence of such three body interaction.

The explicit form of the three body interaction was derived by the Tiesinga *et al.* [192] which consists of both the spin independent and dependent terms, similar to that of the two body interaction. Later Silva-Valencia *et al.* used this model to obtain the phase diagrams of the SBHM with only a three body term [193] and both the two and the three body interactions [194] using DMRG technique. In both the cases, they claimed that there is no signature of the formation of the spin singlet phase and hence the odd-even asymmetry in the MI lobes is absent which contradicts the results for a spinor Bose gas predicted in presence of a two body interaction potential. This surprising fact gives us an opportunity to study the SBHM by considering both two as well as three body interaction potentials using site decoupling MFA to compare and contrast with the DMRG results.

We organize this chapter as follows. In the following section, we outline the SBHM in presence of the three body interaction potential and a quick recapitulation of the mean field formalism. In the next section, we have presented the phase diagrams in presence of both the two and the three body repulsive interaction strengths. The formation of the spin singlet and nematic MI phase has been scrutinized by computing the spin eigenvalue and spin nematic order parameter. Then we consider a purely repulsive three body potential and its effects on the phase diagrams. Finally, we draw our conclusion.

6.1 Model

The Hamiltonian for spin -1 ultracold atoms in presence of a repulsive three body interaction in addition to the usual two body interaction can be written as [17, 18],

$$H = -t \sum_{\langle ij \rangle} \sum_{\sigma} (a_{i\sigma}^{\dagger} a_{j\sigma} + h.c) - \mu \sum_i n_i + \frac{U_0}{2} \sum_i n_i(n_i - 1) + \frac{U_2}{2} \sum_i (\mathbf{S}_i^2 - 2n_i) + H_3 \quad 6.1$$

where all symbols carry the same meaning as discussed in section 2.2 of the chapter 2. H_3 corresponds to the three body interaction potential which is assumed to have the form [192] [see Appendix B],

$$H_3 = \frac{W}{6} \sum_i n_i(n_i - 1)(n_i - 2) + \frac{V}{6} \sum_i (\mathbf{S}_i^2 - 2n_i)(n_i - 2) \quad 6.2$$

where W and V are the three body spin independent and dependent interaction strengths. H_3 can be a repulsive for $W > 0$ as well as an attractive for $W < 0$ in nature. It was found that the three body interaction strength is related to the

two body interaction strength by, $W \propto (V_0/E_r)^{3/4} a_s^2 k^2 U_0^2$ (a_s : s wave scattering length, and k : wave vector) [190], and experimentally the quantity $a_s^2 k^2$ is of the order of 10^{-2} to 10^{-8} [195]. Thus it is reasonable to consider $W \ll U_0$ and the relationship, $V/U_0 = 2(U_2/U_0)(W/U_0)$ only holds for $W \ll U_0$ and $V \ll U_2$ [192].

The hopping term of Eq.(6.1) can be decoupled using the SSMFT as discussed in section 2.4.1 of chapter 2 and the resultant Hamiltonian is written as a sum of the mean field Hamiltonian, namely, $H = \sum_i H_i^{MF}$ where H_i^{MF} is given by,

$$H_i^{MF} = \underbrace{-t \sum_{\sigma} (\phi_{i\sigma} a_{i\sigma} + h.c.) + t \sum_{\sigma} \psi_{i\sigma} \phi_{i\sigma}}_{H'} + \underbrace{\frac{U_0}{2} n_i (n_i - 1) + \frac{U_2}{2} (\mathbf{S}_i^2 - 2n_i) - \mu n_i + H_3}_{H^0} \quad (6.3)$$

where $\phi_{i\sigma}$ includes the SF order parameter from nearest neighbour sites, j , defined as, $\phi_{i\sigma} = (1/z) \sum_{j=1}^4 \psi_{j\sigma} = \psi_{i\sigma}$ due to the homogeneity of the system and $z = 4$ corresponds to a square lattice. H^0 and H' correspond to the unperturbed and perturbation Hamiltonians respectively. After diagonalizing Eq.(6.3) with $n_i = 7$ self consistently as discussed in section 2.4.1 of chapter 2, we compute the equilibrium SF order parameter and local densities as (dropping the superscript eq and the site index, i due to the homogeneity of the system),

$$\psi_{\sigma} = \langle \Psi_g | a_{\sigma} | \Psi_g \rangle; \quad \rho_{\sigma} = \langle \Psi_g | n_{\sigma} | \Psi_g \rangle \quad (6.4)$$

The total SF order parameter is, $\psi = \sqrt{\psi_+^2 + \psi_0^2 + \psi_-^2}$.

6.2 Results

6.2.1 Antiferromagnetic case

At first, we shall study the combined effects of the two body (U_0, U_2) and the three body (W, V) interactions for the AF case with $U_2/U_0 = 0.05$. The phase diagrams are obtained corresponding to both the repulsive ($W > 0$) as well as attractive ($W < 0$) three body interaction strengths. Then we shall explore the effects of only three body (W, V) interaction on the SBHM.

6.2.1.1 MI lobes width in the atomic limit with ($W > 0$)

To calculate the MI lobes width, let us consider the atomic limit ($t = 0$) in Eq.(6.1), where the system is completely in the insulating phase with an energy gap, E_g in the particle-hole excitation spectra, which is the difference between

the upper (μ_+) and the lower (μ_-) values of the chemical potential corresponding to a MI lobe for a given occupancy, n [107]. For $t = 0$, corresponding to the repulsive three body interaction strength ($W > 0$), the energy eigenvalue, $E^0(S, n)$ of H^0 consists of only the unperturbed terms which is given by (see section 2.3 in chapter 2),

$$E^0(S, n) = \frac{W}{6}n(n-1)(n-2) + \frac{V}{6}[S(S+1) - 2n](n-2) - \mu n + \frac{U_0}{2}n(n-1) + \frac{U_2}{2}[S(S+1) - 2n] \quad 6.5$$

Assuming the spin eigenvalue, $S = 0$ for the even and $S = 1$ for the odd MI lobes, similar to that in Ref. [107], the boundary of the MI lobe (μ_{\pm}) can be found from the relation, $E^0(S_1, n_1) < E^0(S, n) < E^0(S_2, n_2)$, where $S_{1,2}, n_{1,2}$ are the lower and higher spin and density values respectively corresponding to particular S, n values. This inequality gives the following conditions, which can be stated as,

(i) For the odd MI lobes (that is, $n = 1, 3, \dots$):

$$(n-1) + (n-1)(n-2)\frac{W}{2U_0} + (1-n)\frac{V}{3U_0} < \frac{\mu}{U_0} < n - 2\frac{U_2}{U_0} + n(n-1)\frac{W}{2U_0} - (n-1)\frac{V}{U_0} \quad 6.6$$

If we equate these two μ values, we shall obtain a critical U_2/U_0 , given by,

$$\frac{U_2^c}{U_0} = \frac{1}{2} + (n-1)\left[\frac{W}{2U_0} - \frac{V}{3U_0}\right] \quad 6.7$$

below which the odd MI lobes exist and above which the odd MI lobes vanish.

(ii) For even MI lobes (that is, $n = 2, 4, \dots$): similarly the boundary equations for $U_2/U_0 < U_2^c/U_0$ is given by,

$$(n-1) - 2\frac{U_2}{U_0} + (n-1)(n-2)\frac{W}{2U_0} + (2-n)\frac{V}{U_0} < \frac{\mu}{U_0} < n + n(n-1)\frac{W}{2U_0} - \frac{nV}{3U_0} \quad 6.8$$

and for $U_2/U_0 > U_2^c/U_0$,

$$n - \frac{3}{2} - \frac{U_2}{U_0} + (n-2)^2\frac{W}{2U_0} + 2(2-n)\frac{V}{3U_0} < \frac{\mu}{U_0} < n + \frac{1}{2} - \frac{U_2}{U_0} + n^2\frac{W}{2U_0} - 2n\frac{V}{3U_0} \quad 6.9$$

If we plot all these equations for different values of $W/U_0, V/U_0$, we shall obtain the structures for the MI lobes as shown in Fig.6.1. At $W/U_0 = 0.1$, which yields

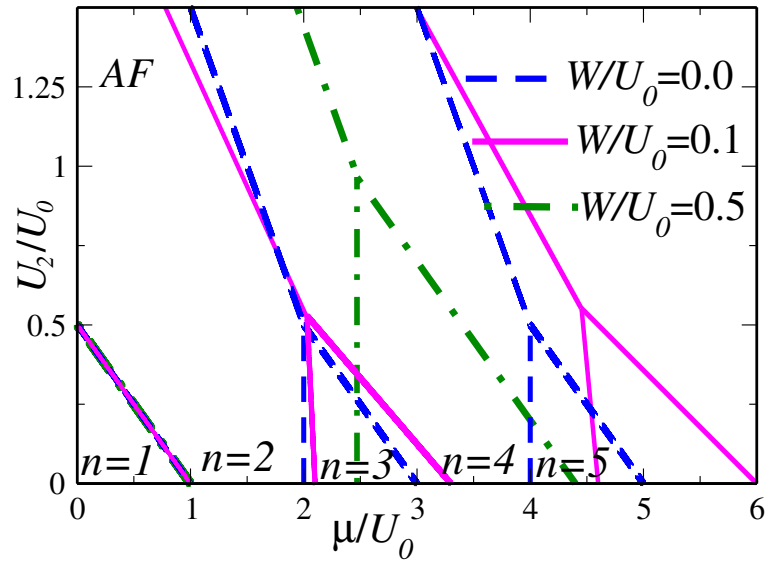


Figure 6.1: The width of the MI lobes in the atomic limit ($t = 0$) for AF case for different values of three body interaction potential, W/U_0 shows the odd-even asymmetry exists in the MI lobes.

$V/U_0 = 0.2U_2/U_0$, the even MI lobes become more stable compared to the odd MI lobes, and the width of the chemical potential for all the MI lobes, except the first one, increases with the three body interaction strength, W . Interestingly, the critical U_2^c/U_0 for the disappearance of all odd MI lobes in the absence of W/U_0 was 0.5 [107], which now changes to 0.53 and 0.553 at $W/U_0 = 0.1$ corresponding to the third and the fifth MI lobes respectively.

We have also considered a higher value of W/U_0 , namely, $W/U_0 = 0.5$, for which $V/U_0 = 0.05 \sim U_2/U_0$ and found that the chemical potential widths get enhanced, thereby making inroads for the MI phase. Thus the MI lobes become more stable compared to the SF phase. This clearly suggests of an existence of an odd-even asymmetry in the successive MI lobes even in presence of the three body interaction in the atomic limit.

6.2.1.2 MFA phase diagrams ($W > 0$)

Next we turn on the hopping strength and obtain the phase diagrams via the mean field approximation (MFA) for visualization of the existence of the odd-even asymmetry and hence to explore the nature of the MI-SF phase transition in presence of the three body interactions.

Recently, the phase diagrams of SBHM in presence of both the two and three body repulsive interaction were obtained for the AF case in Ref. [194] using DMRG technique, where the authors have claimed that the odd-even asymmetry only exists for small values of the hopping strength, that is, t/U_0 . But as t/U_0 is increased, such asymmetry vanishes and there is a signature of phase transition

from longitudinal polar (LP) to transverse polar (TP) SF phase.

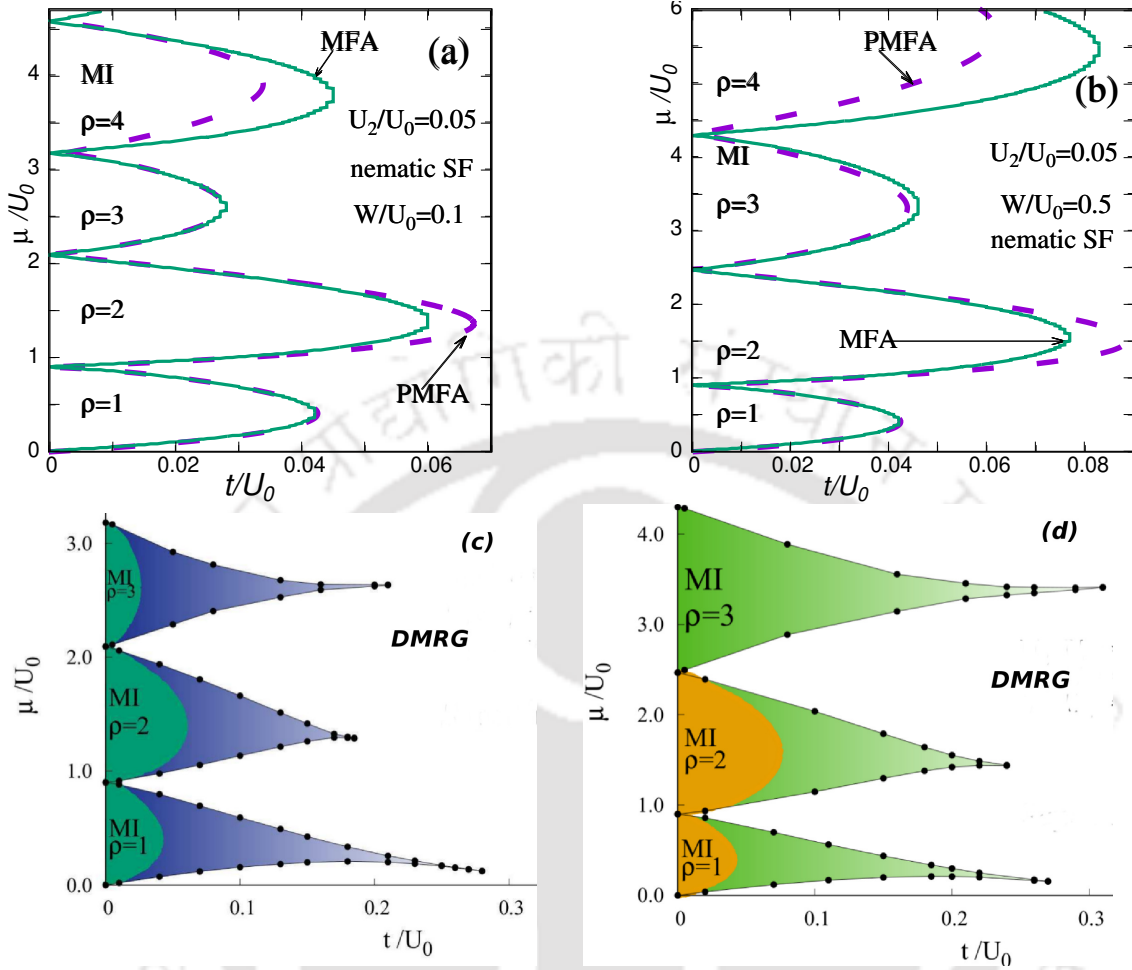


Figure 6.2: The phase diagrams from MFA (solid lines) and PMFA (dashed lines) for $U_2/U_0 = 0.05$ with repulsive three body interaction potential, $W/U_0 = 0.1$ in (a) and $W/U_0 = 0.5$ in (b). In both the cases, the MI lobes display an odd-even asymmetry in presence of W/U_0 . The DMRG phase diagrams (solid lines with points) of Ref. [194] are shown for $W/U_0 = 0.1$ in (c) and $W/U_0 = 0.5$ in (d) to compare with our results.

To crosscheck their claims, here we shall use same parameter values, that is, $U_2/U_0 = 0.05$ for the AF case. The MFA phase diagrams are shown in Fig.6.2 for different values of W/U_0 . At $W/U_0 = 0.1$, we found that although there is no modification of the first MI lobe, the second and the higher MI lobes get enhanced with W/U_0 as seen from Fig.6.2 (a). On increasing the three body interaction strength at $W/U_0 = 0.5$, the MI phase encroaches more into the SF regime, pushing the system towards an insulating phase which results in increase of the location for the MI-SF phase transition, t_c/U_0 [Fig.6.2 (b)]. We have also included the phase diagrams obtained using DMRG approach in Ref. [194] for similar values of W/U_0 in Fig.6.1 (c) and (d) to compare with the mean field phase diagrams. The DMRG phase diagrams show that the odd-even asymmetry only exists for smaller value of t/U_0 , but at higher values of the hopping strength, such asymmetry disappears.

Thus the MFA phase diagrams convincingly demonstrate the existence of such asymmetry in the insulating phase, where the even MI lobes grow due to formation of singlet pairs at the expense of the SF phase. These results differ from the DMRG results obtained in Ref. [194]

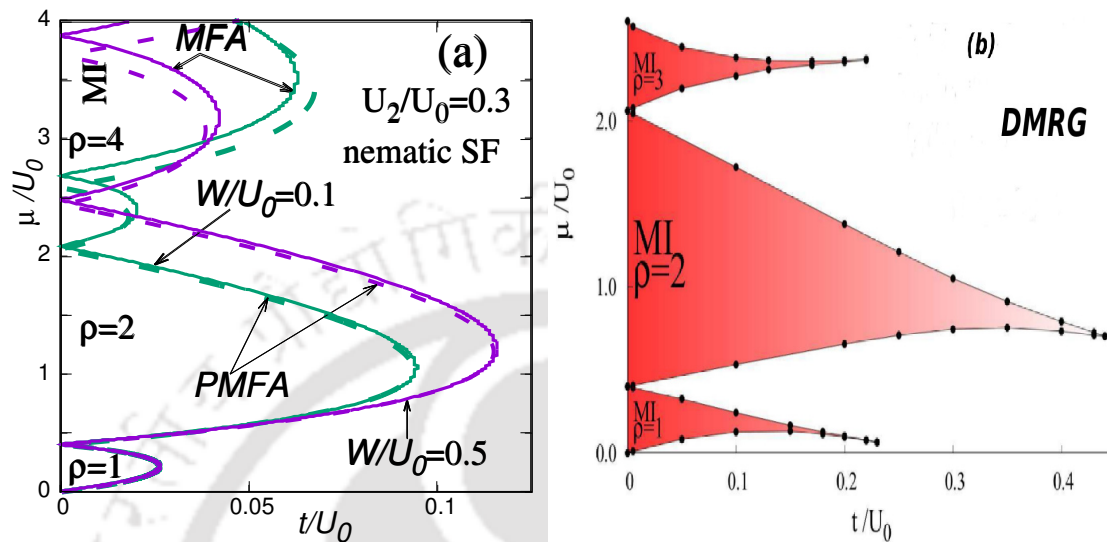


Figure 6.3: The MFA (solid lines) and PMFA (dashed lines) for higher values of spin dependent interaction potential, $U_2/U_0 = 0.3$ with W/U_0 in (a). The DMRG phase diagram of Ref. [194] for $W/U_0 = 0.1$ and $U_2/U_0 = 0.3$ is shown (b). In both the cases, the odd-even asymmetry is observed in the MI lobes.

Further, we have considered a larger value of the spin dependent interaction strength, that is, $U_2/U_0 = 0.3$ and the resulting phase diagrams with similar values of W/U_0 are shown in Fig.6.3 (a). At a higher value of $W/U_0 = 0.5$, we have chosen the three body spin dependent interaction potential, $V = 0.1 \neq 2U_2/U_0W$ so that it obeys $V \ll U_2$. However, at larger values of U_2/U_0 , the DMRG phase diagram obtained in Ref. [194] retains such asymmetry for the MI lobes corresponding to $W/U_0 = 0.1$ as shown in Fig.6.3 (b). We have also checked that the first and third odd MI lobes disappear when the spin dependent interaction value satisfies, $U_2/U_0 = 0.53 \geq U_2^c/U_0$ at $W/U_0 = 0.1$ and $U_2^c/U_0 = 0.967$ for $W/U_0 = 0.5$.

It is worthwhile to mention that the DMRG studies of Ref. [194] are relevant for one dimension, while the MFA studies here are mostly valid in higher dimensions. Thus a direct comparison of the MFA results with the DMRG studies may not be strictly legitimate. Also, the reason for the above mismatch can be explained as follows. Since the tip of the MI lobes in the MFA phase diagrams close quadratically [see Fig.6.2 (a),(b) and Fig.6.3 (a) and will be apparent from the solution of Eq.(6.11)], while they show an asymptotic trend due to the Kosterlitz-Thouless transition in the DMRG phase diagram [194, 196]. Such asymptotic trends in DMRG calculation is responsible for washing away the odd-even asymmetry in

the MI lobes at larger value of the hopping strength, t/U_0 .

6.2.1.3 Spin population fraction and spin eigenvalue ($W > 0$)

In order to verify the signature of the LP to TP SF phase transition reported in Ref. [194], we have plotted the population fraction, N_σ/N as a function of the occupation densities, ρ for $W/U_0 = 0.1$ and $W/U_0 = 0.5$ in Fig.6.4(a). At $U_2/U_0 = 0.05$, it shows that two hyperfine populations are equal, that is, $N_+/N = N_-/N$ and N_\pm/N dominates over N_0/N for all values of W/U_0 . This suggests that the SF phase obtained from the MFA is completely in the transverse polar phase since $N_\pm > N_0$, and that there is no crossover between the N_\pm/N and N_0/N indicates an absence of such a phase transition. This result again differs from the findings of Ref. [194]. Further, it tells us that the spin singlet formation occurs to all the even MI lobes, that is, the second ($\rho = 2$) and the fourth ($\rho = 4$) MI lobes where the hyperfine fractions obey, $N_\pm/N = N_0/N$ [31]. Thus one is justified in concluding that the MFA phase diagram elegantly captures the existence of the odd-even asymmetry in the MI lobes in presence of a three body interaction and emphasizes the rich phase properties of a spinor Bose gas.

The variation of the spin eigenvalue, $\langle S^2 \rangle$ with different values of W/U_0 corresponding to the even and the odd MI lobes in the AF case are shown in Fig.6.4 (b). For $U_2/U_0 = 0.05$, we have found that $\langle S^2 \rangle = 2$ for the first ($\rho = 1$) as well as the third ($\rho = 3$) MI lobes, while $\langle S^2 \rangle = 0$ for the second ($\rho = 2$) and fourth ($\rho = 4$) MI lobes at $W/U_0 = 0.1$ [Fig.6.4 (b)]. At larger values of W/U_0 , that is, $W/U_0 = 0.5$, the spin eigenvalue, $\langle S^2 \rangle$ still remains at 0 and 2 in the MI phase for all the even and the odd MI lobes respectively [Fig.6.4 (b)]. The second and the fourth MI lobes show a first order transition from MI to the SF phase [Fig.6.4 (b)]. This also re-emphasizes our previous prediction on possible spin singlet formation for all the even MI lobes. This was outlined earlier from N_σ/N behavior as a function of ρ . At $U_2/U_0 = 0.3$, we have observed similar $\langle S^2 \rangle$ variation for the odd and even MI lobes for all values of W/U_0 .

We have also checked that the SF order parameter and the ground state energy show a first order transition from the spin singlet MI to the SF phase and a second order transition for the odd MI lobes at both the values of the three body interaction strength for $U_2/U_0 = 0.05$. This was pointed out earlier in Refs. [25, 111] without including a three body interaction term. For larger $U_2/U_0 = 0.3$, there is no signature of the first order transition from the spin singlet MI to the SF phase, as it was found in Ref. [111] without a three body interaction, but all the MI-SF phase transitions are of second order in nature.

To make our point regarding the spin singlet formation more emphatic, we have computed the z-component of the spin nematic order parameter which is defined as, $Q_{zz} = \langle S_z^2 \rangle - (1/3)\langle S^2 \rangle$ [27, 34, 111, 160]. The results for Q_{zz} are shown

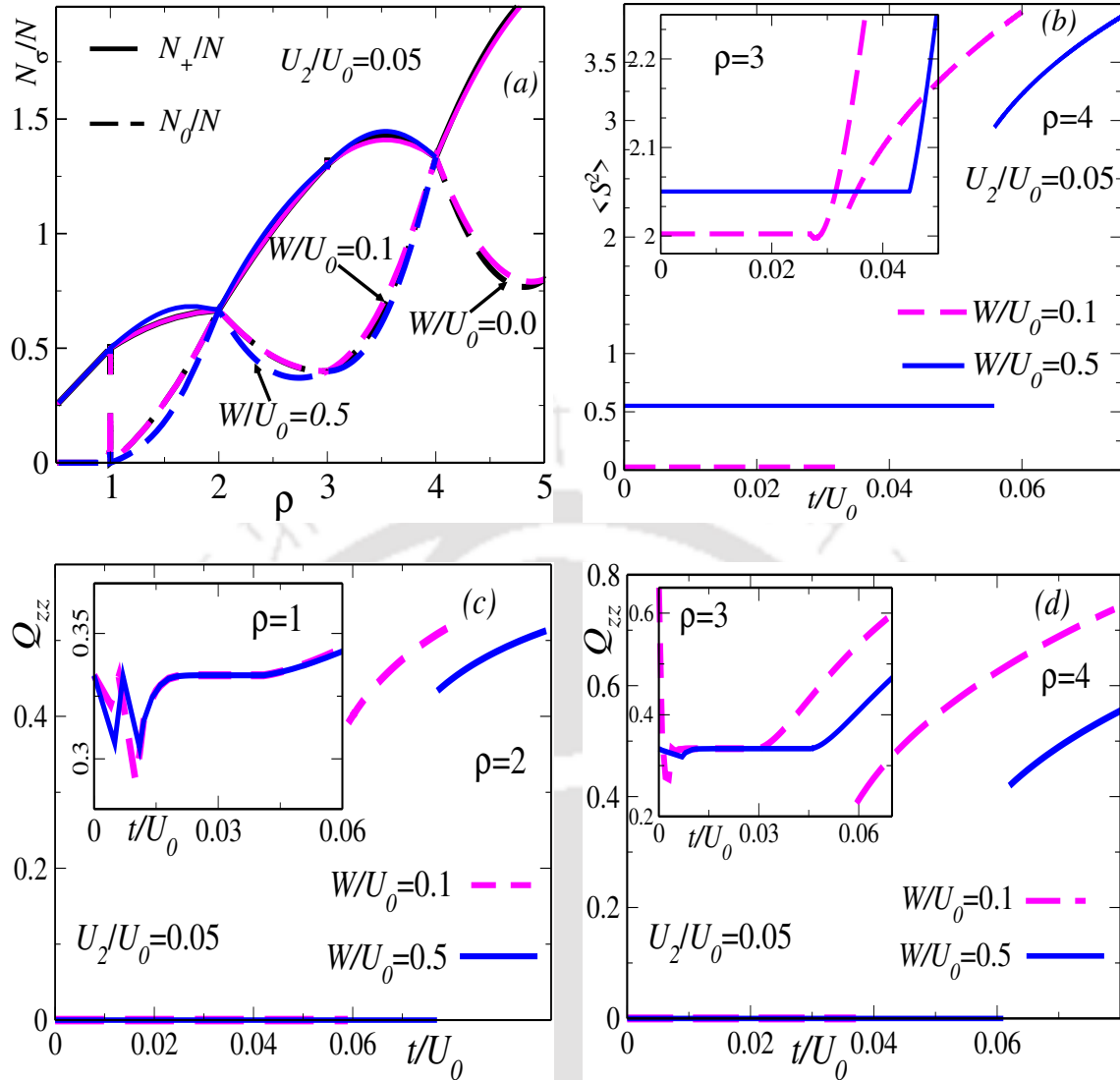


Figure 6.4: The spin population fraction, N_σ/N with occupation densities, ρ in (a) and the total spin eigenvalue, $\langle S^2 \rangle$ in (b) for $U_2/U_0 = 0.05$ indicates that the spin singlet formation is possible for the even MI lobes. The spin nematic order parameter, Q_{zz} for $U_2/U_0 = 0.05$ with different W/U_0 for the MI lobes with $\rho = 2$ in (c) and $\rho = 4$ in (d). The variation of Q_{zz} for the odd MI lobes with W/U_0 are shown in (c) and (d) (inset). For the second and fourth MI lobes, $Q_{zz} = 0$ in the MI phase then shows a first order transition to the SF phase.

in Fig.6.4 (c), (d) for different values of W/U_0 corresponding to all the MI lobes. For $U_2/U_0 = 0.05$, it shows that Q_{zz} is finite for the first as well as the third MI lobes and hence it shows a second order transition to the SF phase [Fig.6.4 (c), (d) (inset)]. Also for the second ($\rho = 2$) and fourth ($\rho = 4$) MI lobes, Q_{zz} completely vanishes in the MI phase, and hence shows a jump to a finite value in the SF phase at both values of W/U_0 [Fig.6.4 (d)]. At $U_2/U_0 = 0.3$, for the second and the fourth MI lobes, Q_{zz} exhibits similar variation in the MI phase and hence registers a second order transition to the SF phase. This finally supports the claim made earlier about the possible spin singlet formation for all the even MI lobes.

6.2.1.4 PMFA phase diagrams ($W > 0$)

Now in order to support our MFA phase diagrams more convincingly, we shall shift our attention to the perturbative mean field approaches (PMFA) as discussed in section 2.4.2 of chapter 2. At this point, we are ready to perform the perturbation expansion (PMFA) using the above information on the spin eigenvalues, $\langle S^2 \rangle$ to determine the modified ground state energy, E_n with H' as the perturbation term [see Eq.(6.3)]. After incorporating the first and the second order corrections, the modified ground state energy can be expressed in a series expansion of ψ having a form [24],

$$E_n(\psi) = E^0 + C_2(U_0, U_2, \mu, n, W, V) \sum_{\sigma} \psi_{\sigma}^2 \quad 6.10$$

Minimization of $E_n(\psi)$ with respect to ψ leads to $C_2(U_0, U_2, \mu, n, W, V) = 0$ which yields the boundary between the SF and the MI phases.

In presence of two and three body repulsive interaction potentials, the above condition for the even MI lobes with $\langle S^2 \rangle = 0$ yields,

$$\left(\frac{1}{t}\right) = \frac{n/3}{a + 2U_2 - (n-2)[\delta + V]} + \frac{(n+3)/3}{\beta + n\delta - nV/3} \quad 6.11$$

while for the odd MI lobes with $\langle S^2 \rangle = 2$, it corresponds to,

$$\begin{aligned} \left(\frac{1}{t}\right) &= \frac{(n+2)/3}{a - (n-2)\delta + \gamma/3} + \frac{4(n-1)/15}{a + 3U_2 - (n-2)\delta - (4n-10)V/3} \\ &+ \frac{(n+1)/3}{\beta - 2U_2 + n\delta - \gamma} + \frac{4(n+4)/15}{\beta + U_2 + n\delta + 2n\gamma/3} \end{aligned} \quad 6.12$$

where $a = \mu - (n-1)U_0$, $\beta = -\mu + nU_0$, $\delta = (n-1)W/2$ and $\gamma = (n-1)V$.

We have observed that $\langle S^2 \rangle = 2$ for all the odd and $\langle S^2 \rangle = 0$ for the even MI lobes and thus we shall extend our calculations up to the fourth ($\rho = 4$) MI lobe and the resulting phase boundaries are plotted as a function of W/U_0 in Fig.6.2 (a) (b) (dashed lines) and Fig.6.3 (a) (dashed lines). At both values of U_2/U_0 and W/U_0 , the analytical phase diagrams are in excellent agreement with the MFA results except at the tip of the second MI lobe.

It has to be noted that such disparity between the two approaches are due to less sensitivity of MFA in lower dimensions, since it scales as $1/D$ (D: dimension). Thus the MFA only holds deep inside the MI lobes where the fluctuations are suppressed, but near the tip of the MI lobes, MFA fails to handle the fluctuations [24, 30]. Further, the critical hopping strength, t_c/U_0 denoting the location of the MI-SF phase transition (by equating μ_+ and μ_- of Eq.(6.11) and Eq.(6.12)) is now a function of W and increases with the strength of the three body interaction

potential.

6.2.1.5 Phase diagrams for attractive three body interaction ($W < 0$)

So far we have studied the effects of the repulsive three body interaction potential in the AF case. However, for a spherically symmetric, deep optical lattice potential with harmonic frequency, ω_f , it was found that W is related to the two body interaction strength, U_0 via $W = -1.34U_0^2/\hbar\omega_f$ which implies that the three body interaction potential is attractive in nature [192].

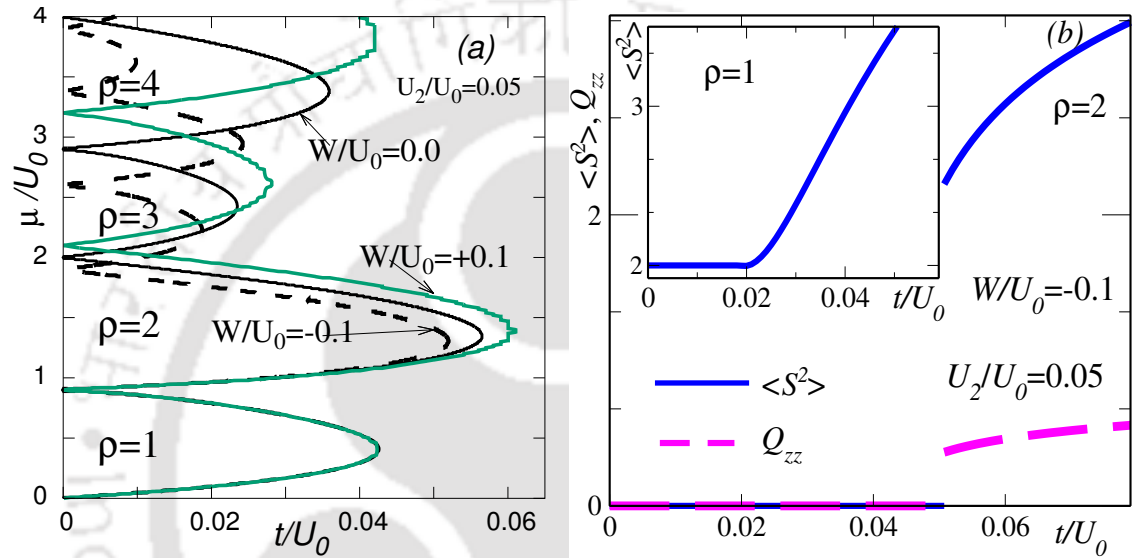


Figure 6.5: The MFA phase diagram for an attractive three body interaction strength, $W/U_0 = -0.1$ with $U_2/U_0 = 0.05$ in (a). Both the $W/U_0 = 0.1$ and $W/U_0 = 0.0$ phase diagrams are included in (a) to compare with the $W/U_0 = -0.1$ case. The total spin eigenvalue, $\langle S^2 \rangle$ behaviour in the AF case with $W/U_0 = -0.1$ for the odd ($\rho = 1$) (b) (inset) and the even ($\rho = 2$) (b). The spin nematic order parameter, Q_{zz} for the even ($\rho = 2$) MI lobe in (b) indicates that the spin singlet formation for all even MI lobes and then shows a first order transition to the SF phase.

Thus we have obtained the phase diagram for $W/U_0 = -0.1$ in the AF case and hence compared it to the repulsive case in Fig.6.5 (a). It shows that the chemical potential width, μ/U_0 is now contracted by an amount W/U_0 for the attractive case which is contrary to what happens for the repulsive three body interaction [Fig.6.5 (a)]. Also the critical tunneling strength, t_c/U_0 for the MI-SF phase transition now decreases for $W/U_0 = -0.1$. Similar effects are observed for another value of W/U_0 , namely, $W/U_0 = -0.05$. The most intriguing fact is that the odd-even asymmetry in the MI lobes remains intact in presence of the attractive three body interaction potential. Also the spin eigenvalue, $\langle S^2 \rangle$ replicates similar behaviour for the odd and even MI lobes as that corresponding to the repulsive case [Fig.6.5 (b)].

6.2.1.6 Phase diagrams for purely three body interaction ($U_0 = U_2 = 0$)

It is also interesting to investigate the effects of only the repulsive three body interaction (without a two body interaction) on a spin-1 ultracold Bose gas, which was studied in Ref. [193] using DMRG technique. For this purpose, we set $U_0 = U_2 = 0$, $W = 1$ and the resulting MFA phase diagrams with different values of the three body spin dependent interaction, V are shown in Fig.6.6(a).

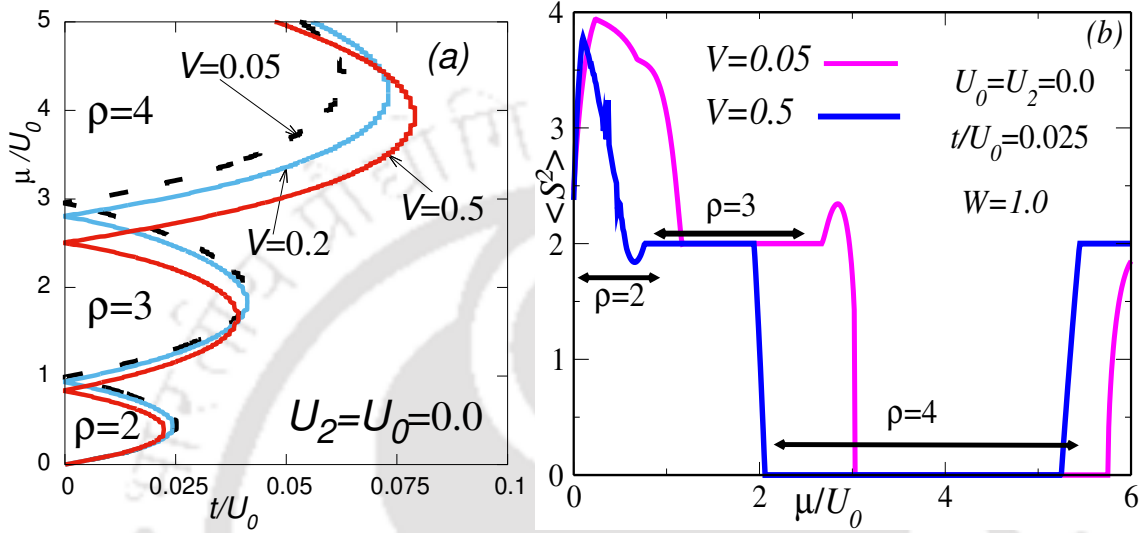


Figure 6.6: The MFA Phase diagrams for a purely three body repulsive spin dependent interaction strength, V taking the three body spin independent term, $W = 1$ as parameter and the two body interaction terms have been put to zero, that is, $U_2 = U_0 = 0.0$ in (a). The phase diagrams show that the MI lobe with unit occupancy ($\rho = 1$) is absent, however the higher order MI lobes become more stable compared to the low occupancy MI lobes. The spin eigenvalue, $\langle S^2 \rangle$ variation in (b) shows $\langle S^2 \rangle = 2$ for the $\rho = 3$. While for $\rho = 4$ MI lobe, $\langle S^2 \rangle = 0$ and $\rho = 2$ shows an oscillatory behavior with V in (b).

The results show that although the MI lobe with unit occupancy ($\rho = 1$) is absent, however the second and the higher order MI lobes are stable and expand into the SF phase. At larger values of V , that is, at $V = 0.5$, the chemical potential widths of the second and the third MI lobes shrink, thereby resulting in the stability of the fourth MI lobes. This clearly indicates that the odd-even asymmetry is completely absent when only the three body interaction is present and these phase diagrams are in qualitative agreement with the results in Ref. [193].

We have also noticed that for a purely repulsive three body interaction, the spin eigenvalue is $\langle S^2 \rangle = 2$ for the odd (that is $\rho = 3$) and $\langle S^2 \rangle = 0$ for the fourth ($\rho = 4$) MI lobes, while $\rho = 2$ shows an oscillatory behavior as a function of V [Fig.6.6(b)]. Further, the population fraction shows that the SF phase is completely in the TP phase since $N_{\pm}/N > N_0/N$.

Finally, by comparing the results of Fig.6.2(a), (b), Fig.6.3(a) and Fig.6.6(a), we conclude that the two body spin dependent interaction is solely responsible

for the odd-even asymmetry in the MI lobes, while the three body interaction just adds to the stability of the insulating phases.

6.2.2 Ferromagnetic case

In the ferromagnetic case, the MI lobes are identical with a spin-0 (scalar) Bose gas and the chemical potential width increases for the second and higher order MI lobes with the inclusion of a three body interaction potential. The mean field phase diagrams are identical to that of the scalar Bose gas as obtained earlier in Refs. [190, 197, 198] [Fig.6.7 (solid lines)]. All the MI lobes stabilize with increasing repulsive three body strength, W/U_0 . We have also performed similar perturbation (PMFA) calculations [Fig.6.7 (dashed lines)] and they are in complete agreement with the MFA phase diagrams.

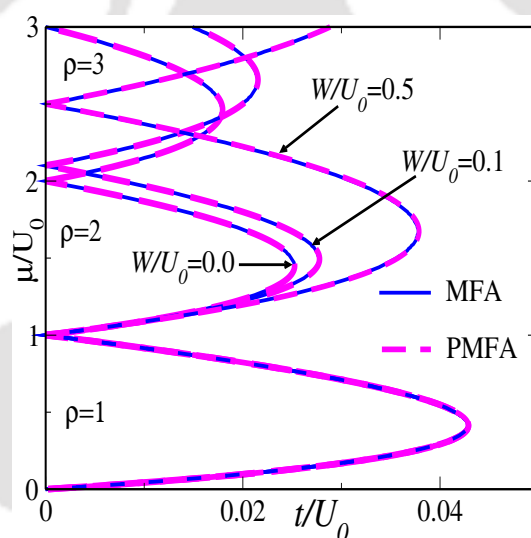


Figure 6.7: The MFA (solid lines) and PMFA (dashed lines) phase diagrams in the ferromagnetic case $U_2/U_0 = 0.0$ with the repulsive three body interaction strength, W/U_0 . Both the MFA and PMFA phase diagrams are in complete agreement with each other.

6.3 Conclusion

In this work, we have explored the consequences of a repulsive three body interaction on the phase diagrams of a spin-1 Bose Hubbard model (SBHM) using mean field approximation.

For AF spin dependent interaction, we first consider both the two as well as three body interactions strengths together and have found the existence of the odd-even asymmetry in the MI lobes which differs from the results obtained in Ref. [194]. We have also found that the spin nematic (singlet) formation occurs

for all the odd (even) MI lobes, which were subsequently confirmed by computing the total spin eigenvalue and spin nematic order parameter. Further, we have confirmed that the superfluid (SF) phase is completely in transverse polar (TP) state and there is no signature of any kind of phase transition therein which, again differs from the findings of Ref. [194]. All the MFA phase diagrams are compared with the analytical phase diagrams obtained using perturbative expansion (PMFA) and they are found to be in good agreement with each other except at the tip of the MI lobes where a small discrepancy is observed.

But in case of only three body repulsive interaction, the phase diagram shows that the higher order MI lobes, excluding the first one, expand into the SF phase and there is no indication of the odd-even asymmetry in the MI lobes which are qualitatively in agreement with the results of Ref. [193]. The spin eigenvalue is $\langle S^2 \rangle = 2$ for the third ($\rho = 3$) and $\langle S^2 \rangle = 0$ for the fourth ($\rho = 4$) MI lobes, while the second ($\rho = 2$) MI lobes show an oscillatory behaviour. Thus we can infer that the two body interaction is totally responsible for such an asymmetry in the MI lobes, while the three body interaction acts as a catalyst to stabilize the MI phases, against the SF phase.

In the ferromagnetic case, the phase diagrams are similar to that of the spin-0 Bose gas for the repulsive [190, 198] three body interaction. Finally, all these MFA phase diagrams receive total support from the analytical phase diagrams obtained using perturbative expansion (PMFA).

Chapter 7: Effects of an attractive three body interaction on a spin-1 Bose Hubbard model

The general dynamics of spin-1 ultracold Bose gas in an optical lattice is described by an extended Bose Hubbard model which includes an additional spin dependent interaction potential due to the presence of hyperfine degrees of freedom [17, 18, 34]. Such a spin dependent interaction can be antiferromagnetic (AF) or ferromagnetic in nature and thus possesses a wealth of rich phase properties and quantum magnetism as a result of spontaneous symmetry breaking of the ground state. It was found that the ground state shows a $U(1) \times \mathbf{S}^2$ symmetry in the AF case and a $SO(3)$ symmetry in the ferromagnetic case in contrast to the usual $U(1)$ symmetry of a standard spin-0 BHM [17, 18].

To understand the origin of various phases in a spinor gas, several numerical techniques, such as mean field approximation (MFA) [25, 110, 130], quantum Monte Carlo (QMC) [31, 111, 117, 118] and strong coupling perturbative expansion (PMFA) [24, 30, 187] have been developed to gain an in-depth knowledge on how different extent of the Mott insulating and superfluid phases will affect the ground state phase diagram. In the AF case, the MI state with even occupation densities form a spin singlet state with vanishing spin nematic order, while the odd occupation densities show a spin nematic state with a finite nematic order parameter. This phenomenon of spin singlet (nematic) formation is now responsible for an even (odd) asymmetry in the MI phase and hence shows a first (second) order transition to the SF phase [24, 25, 30, 31, 110, 111, 117, 118, 130, 187]. However density matrix renormalization group (DMRG) studies indicate a signature of a dimerized phase and shows odd-even asymmetry for higher values of the AF interaction [119].

Besides, the use of hyperfine degrees of freedom as a short lattice dimension, known as the synthetic dimension, helps in realizing high synthetic magnetic field [49] and various density ordered SF phases in presence of spin-orbit coupling (SOC) [45, 169]. Later, the inclusion of long range extended interactions such as density-density [189] and spin-spin [173] extended interactions displays a charge (CDW) and spin density wave (SDW) pattern in the MI phase in the former case, while an antiferromagnetic SF (AFSF) which has both the crystalline and off-diagonal order in the latter. Moreover, the effects of magnetic fields [26, 41, 47, 74, 153, 160, 170], disorder [107, 144, 188], dipolar interaction [22, 175] and spin dynamics etc have now been studied extensively in the context of a spin-1 Bose gas.

Apart from studying such properties in presence of two body interactions cited above, recently, the consequences of higher body interaction, such as a repulsive

three body interaction on the ground state phase diagrams have been explored on a spin-1 ultracold Bose gas using MFA in chapter 6 and DMRG [193, 194] techniques. Interestingly, the mean field phase diagram still shows a spin nematic-singlet formation and hence an asymmetry in the MI phase in presence of both the two and three body interactions, while for a purely three body interaction such asymmetry is destroyed [199]. On the contrary, the DMRG studies show that there is neither any asymmetry, nor any spin singlet-nematic formation in the MI phase and there is a possible phase transition involved in the SF phase in presence of both the two and three body interactions [193, 194].

Besides the presence of such repulsive three body interaction, another form of three body interaction which is attractive in nature is proposed by Safavi-Naini *et al.* [106]. Such interaction can be observed by exciting a triple occupied state into an excited hyperfine state so that they can form a trimer state. Such type of attractive interaction was studied in the context of a spin-0 Bose gas where it is found to affect a particular MI lobe. Motivated by such interesting phenomena, it is worthwhile to explore the effects of an attractive multi-body (three body) interaction in a spinor Bose gas. We shall study the effects of an attractive three body interaction on the SBHM to see the consequences on the phase diagrams, particularly the existence of odd-even asymmetry in the MI lobes.

We organize this chapter as follows. The next section introduces the mean field Hamiltonian in presence of an attractive three body interaction potential. The third section deals with results obtained by us. At first, we have presented the mean field phase diagrams for different values of the attractive three body strength. Later we have outlined different order of phase transition involved in between the spin singlet-nematic MI and SF phases using the spin eigenvalue and spin nematic order parameters. The PMFA phase diagrams are also obtained to compare with the mean field phase diagrams.

7.1 Model

For spin-1 ultracold Bose gases loaded in an optical lattice, the Hamiltonian in presence an attractive three body interaction can be written as [17, 18, 106],

$$\begin{aligned}
 H = & -t \sum_{\langle ij \rangle} \sum_{\sigma} (a_{i\sigma}^{\dagger} a_{j\sigma} + h.c) - \mu \sum_i n_i + \frac{U_0}{2} \sum_i n_i(n_i - 1) \\
 & + \frac{U_2}{2} \sum_i (\mathbf{S}_i^2 - 2n_i) + U_3 \sum_i \delta_{n_i,3}
 \end{aligned} \tag{7.1}$$

where all other symbols carry the same meaning as discussed in section 2.2 of the chapter 2 and U_3 is the attractive three body interaction strength. In order to study the MI-SF phase transition related with Eq.(7.1), the hopping term is

decoupled using the SSMFT as discussed in section 2.4.1 of chapter 2 and the mean field Hamiltonians, H_i^{MF} is given by,

$$H^{MF} = \underbrace{-t \sum_{\sigma} (\psi_{\sigma} a_{\sigma} + h.c.) + t \sum_{\sigma} \psi_{\sigma}^2}_{H'} + \underbrace{\frac{U_0}{2} n(n-1) + \frac{U_2}{2} (\mathbf{S}^2 - 2n) - \mu n + U_3 \delta_{n,3}}_{H^0} \quad 7.2$$

Here, H^0 and H' correspond to the unperturbed and perturbation Hamiltonians respectively and the site index, i is removed due to homogeneity of the system. To obtain the equilibrium values of the SF order parameter, ψ^{eq} and local densities, ρ^{eq} in the ground state, Eq.(7.2) with $n_i = 7$ is diagonalized self consistently as discussed in section 2.4.1 of chapter 2. Finally, we obtain the equilibrium SF order parameter and local densities as (dropping the subscript eq from hereafter)

$$\begin{aligned} \psi_{\sigma} &= \langle \Psi^g | a_{\sigma} | \Psi^g \rangle & \psi &= \sqrt{\psi_+^2 + \psi_0^2 + \psi_-^2} \\ \rho_{\sigma} &= \langle \Psi^g | n_{\sigma} | \Psi^g \rangle & \rho &= \rho_+ + \rho_0 + \rho_- \end{aligned} \quad 7.3$$

7.2 Results

7.2.1 Antiferromagnetic case

7.2.1.1 MI lobes in the atomic limit

In order to see how such an attractive three body interaction affects the MI-SF phase transition, let us first consider the atomic limit, that is, $t = 0$ in Eq.(7.1). In the atomic limit, the system is completely in the insulating phase and hence the width of the MI lobe, (μ) is the difference between the upper (μ_+) and the lower (μ_-) values of the chemical potential for a given occupancy, n [107]. For $t = 0$, assuming a common eigenstate $|S, S_z, n\rangle$ for H^0 where the corresponding operators, S, S_z, n commute with each other, the energy eigenvalue, $E^0(S, n)$ of H^0 is given by,

$$E^0(S, n) = \frac{U_0}{2} n(n-1) + \frac{U_2}{2} [S(S+1) - 2n] - \mu n + U_3 \delta_{n,3} \quad 7.4$$

In the AF case, for the time being, we are assuming that the spin eigenvalue, $S = 0$ for the even and $S = 1$ for the odd MI lobes, as considered earlier without U_3 in Ref. [107]. The boundaries of the MI lobe (μ_{\pm}) can be obtained from the relation, $E^0(S_1, n-1) < E^0(S, n) < E^0(S_2, n+1)$, where $S_{1,2}$ are the two spin eigenvalues corresponding to $n \mp 1$ occupancies. For the MI lobe with $n = 3$, this inequality

yields the following condition,

$$2 + \frac{U_3}{U_0} < \frac{\mu}{U_0} < 3 - 2\frac{U_2}{U_0} - \frac{U_3}{U_0} \quad 7.5$$

Similarly for all other occupation densities, we have obtained the boundaries of each MI lobe separately and finally plotted them in Fig.7.1 for different values of U_3/U_0 .

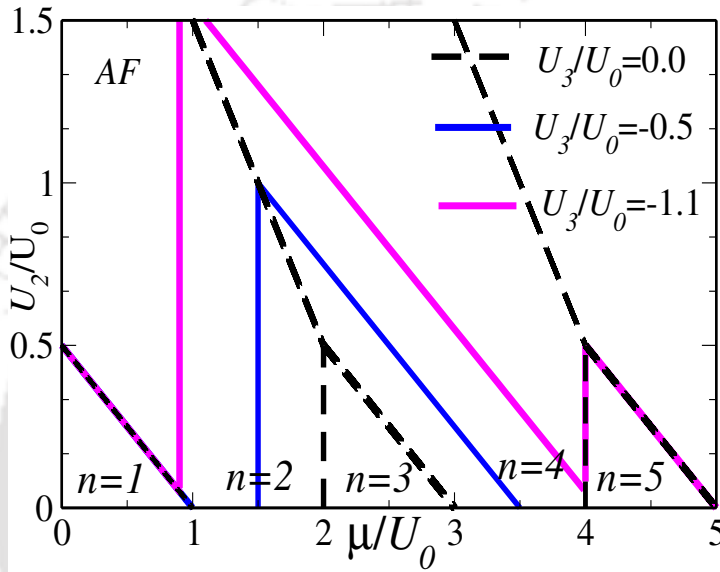


Figure 7.1: The width of the MI lobes in the atomic limit ($t = 0$) with $U_2/U_0 = 0.05$ for different values of U_3/U_0 . The plots show that the odd-even asymmetry is destroyed around the third ($\rho = 3$) MI lobe.

It shows that at a representative value for U_3 , namely, $U_3/U_0 = -0.5$, although there is no change in the first and the fifth MI lobes, but surprisingly the third MI lobe expands considerably, thereby engulfing the second ($\rho = 2$) and the fourth ($\rho = 4$) MI lobes. Also the critical value of U_2/U_0 at which all odd MI lobes disappear still remains at 0.5 [107] for the first and the fifth MI lobes, while for the third MI lobe, it corresponds to $U_2^c > U_0/2 - U_3$. Further, for a larger value of U_3 , namely, $U_3/U_0 = -1.1$, the third MI lobe grows compared to the other MI lobes by completely encroaching into the second and the fourth MI lobes. This implies that there exists a critical value of U_3 below which the second and the fourth MI lobes survive which is given by, $U_3^c/U_0 = 1 + 2U_2/U_0$. It is relevant to mention that for a scalar Bose gas, this critical value is of the order of 1, that is $U_3 \simeq -U_0$. While for a spinor Bose gas, this critical value depends on the two body spin dependent interaction, U_2 .

7.2.1.2 MFA phase diagrams

Now, to understand how such an attractive interaction modifies the odd-even asymmetry and hence the spin nematic-singlet formation in the MI phase, we shall compute the mean field phase diagrams by turning on the hopping strength, t/U_0 . The results are shown in Fig.7.2 (a) and (b).

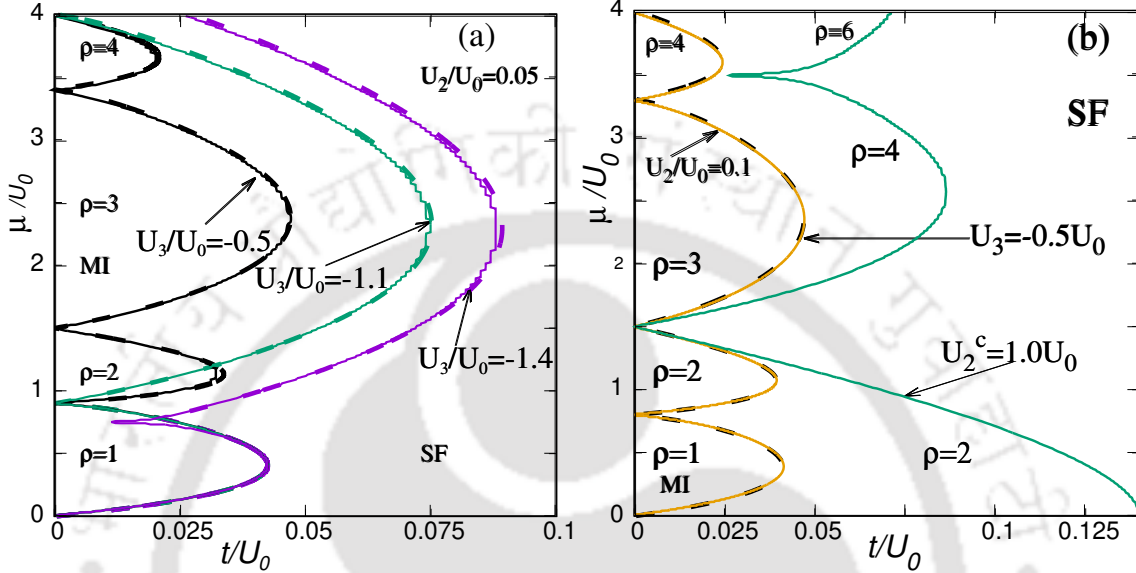


Figure 7.2: Phase diagrams from MFA (solid lines) and PMFA (dashed lines) for $U_2/U_0 = 0.05$ with attractive three body interaction potential, U_3/U_0 in (a). With increasing U_3/U_0 , the asymmetry is destroyed around the third MI lobe. The phase diagrams corresponding to the higher values of spin dependent interaction, namely at $U_2/U_0 = 0.1$ and at a critical value, $U_2^c/U_0 = 1.0$ in (b).

For $U_2/U_0 = 0.05$ [Fig.7.2(a)], we have found that at $U_3/U_0 = -0.5$, the third MI lobe grows considerably by encroaching into both the second and the fourth MI lobes, while the first MI lobe remains unaffected as seen from Fig.7.2. At $U_3/U_0 = -1.1$, the third MI lobe completely occupies the second and the fourth MI lobes, since the critical value of U_3/U_0 below which they exist corresponds to $1 + 2U_2/U_0$ as seen from Fig.7.1.

Also, we have checked that at the critical value of $U_2^c/U_0 = 1.0$ for $U_3/U_0 = -0.5$, the phase diagram only consists of all the even MI lobes, since all the odd MI lobes disappear at this critical value [Fig.7.2(b)]. At higher values of U_2 , namely, $U_2/U_0 = 0.1$, the phase diagram shows similar effects as that of Fig.7.2(a) different values of U_3/U_0 [Fig.7.2(b)]. Increasing U_3/U_0 leads to the stabilization of the third MI lobe and hence the critical tunneling strength, t_c/U_0 also increases corresponding to the MI-SF phase transition.

The phase diagrams in Fig.7.2(a) and (b) show that, unlike the repulsive three body interaction [see chapter 6], which retains the odd-even asymmetry in the MI lobes, here the attractive three body interaction diminishes the odd-even asymme-

try around the second and the fourth MI lobes. This typically raises one concern, namely, whether will there any such asymmetry sustain beyond the fourth MI lobe. To answer that, we have obtained the phase diagram corresponding to higher occupation densities and found that the chemical potential widths for the fifth ($\rho = 5$) as well as the sixth ($\rho = 6$) MI lobes remain unaltered for different values of U_3/U_0 . This certainly underscores the importance of such interaction potential solely around the third MI lobe and also indicates that the asymmetry being intact beyond the fourth MI lobe.

7.2.1.3 Spin eigenvalue and spin nematic order parameter

Further, in order to check if there is any phase transition involved with the SF phase, that is, from transverse polar (TP) to longitudinal polar (LP) state, we have shown the spin population fraction, ρ_σ/ρ as a function of the occupation densities, ρ with U_3/U_0 for $U_2/U_0 = 0.05$ in Fig.7.3. It indicates that the hyperfine fractions corresponding to $\sigma = \pm 1$ are equal, that is, $\rho_+ = \rho_-$. This is obvious since in absence of an external magnetic field, the total magnetization is conserved. Also no crossover is observed among the ρ_\pm/ρ and ρ_0/ρ components which suggests that the SF phase is completely in the TP state, as $\rho_\pm > \rho_0$. Further, at $U_3/U_0 = -0.5$, we have found that the spin singlet formation corresponding to all even MI lobes occur where all the spin populations are equal, that is, $\rho_\pm/\rho = \rho_0/\rho$ [31]. Besides, it shows that the asymmetry is present around the fifth and the sixth MI lobes at larger values of U_3/U_0 .

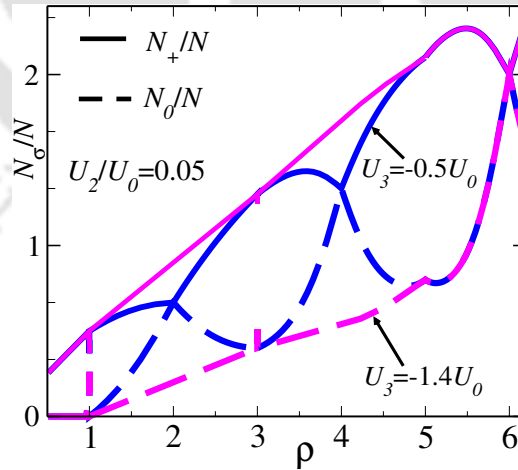


Figure 7.3: The population fraction, N_σ/N with occupation densities, ρ for $U_2/U_0 = 0.05$ with U_3/U_0 indicates that the spin singlet formation for the even MI lobes.

We have seen earlier that smaller values of attractive three body interaction show the spin singlet formation in the MI phase. It is therefore necessary to ascertain the order of phase transition as well as the spin eigenvalue variation from a spin singlet (nematic) MI phase to a SF phase. For $U_3/U_0 = -0.5$, the spin

eigenvalue, $\langle S^2 \rangle = 0$ for all the even MI lobes which indicates the formation of a spin singlet phase and it shows a first order phase transition to the SF phase Fig.7.4 (a). The spin eigenvalue, $\langle S^2 \rangle$ corresponding to the first ($\rho = 1$) is shown in Fig.7.5(a) and the third ($\rho = 3$) in Fig.7.5(b) MI lobes with U_3/U_0 for $U_2/U_0 = 0.05$. At both values of U_3 , the $\langle S^2 \rangle = 2$ indicates the existence of a spin nematic state corresponding to all odd MI lobes. Also, the phase transition from spin nematic MI to SF phase still continues to have a second order character for both the first ($\mu = 0.7$) and third ($\mu = 2.5$) MI phases at $U_3 = -0.5U_0$. Interestingly, at larger value of U_3 , namely, $U_3/U_0 = -1.4$, the first MI lobe ($\mu = 0.7$) shows a first order transition, while the third MI lobe displays a second order transition at $\mu = 1.2$ and a first order transition at $\mu = 2.5$ to the SF phase respectively [Fig.7.5 (a) and (b)]. Further, we have computed the SF order parameter and the ground state energy. They show similar kind of phase transition as pointed out above corresponding to different MI lobes for both values of U_3/U_0 .

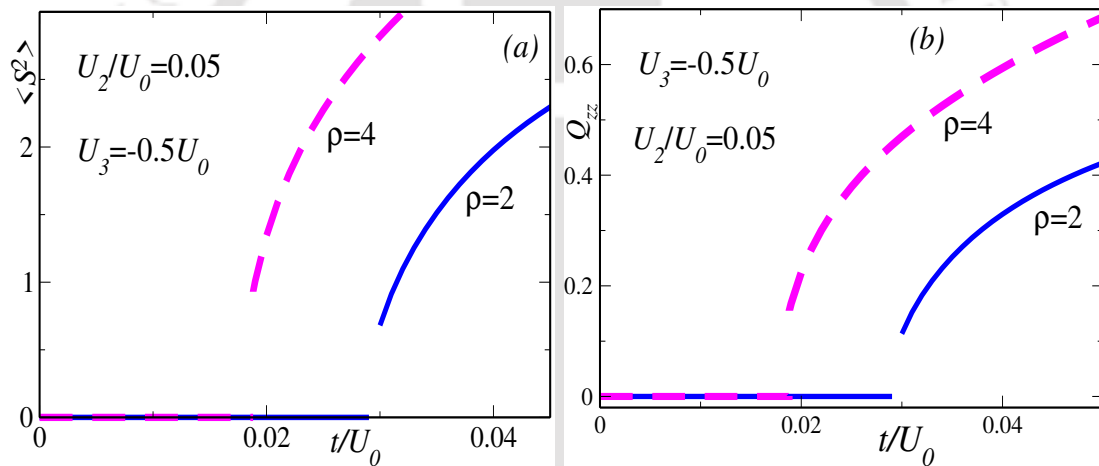


Figure 7.4: The total spin eigenvalue, $\langle S^2 \rangle$ in (a) and the spin nematic order parameter, Q_{zz} in (b) for $U_2/U_0 = 0.05$ corresponding to the second ($\rho = 2$) and the fourth ($\rho = 4$) MI lobes indicate the spin singlet formation at $U_3/U_0 = -0.5$.

Now we shall look into the magnetic properties which signify the spin anisotropy of the spin singlet-nematic MI phases in presence of an attractive three body interaction. For that purpose, we have again calculated the z-component of the spin nematic order parameter which is defined as, $Q_{zz} = \langle S_z^2 \rangle - (1/3)\langle S^2 \rangle$ [27, 34, 111, 160]. In the AF case, for the first and third MI lobes, Q_{zz} is finite in the MI phase and it shows a second order transition at $U_3 = -0.5U_0$, while a first as well as a second order phase transition for $U_3 = -1.4U_0$ to the SF phase as pointed out earlier by us [Fig.7.5 (c) and (d)]. For the spin singlet MI phase, the spin nematic order parameter vanishes since all the spin population fractions are equal, that is, $\rho_{\pm}/\rho = \rho_0/\rho$ and a first order transition to the SF phase is observed [Fig.7.4 (b)].

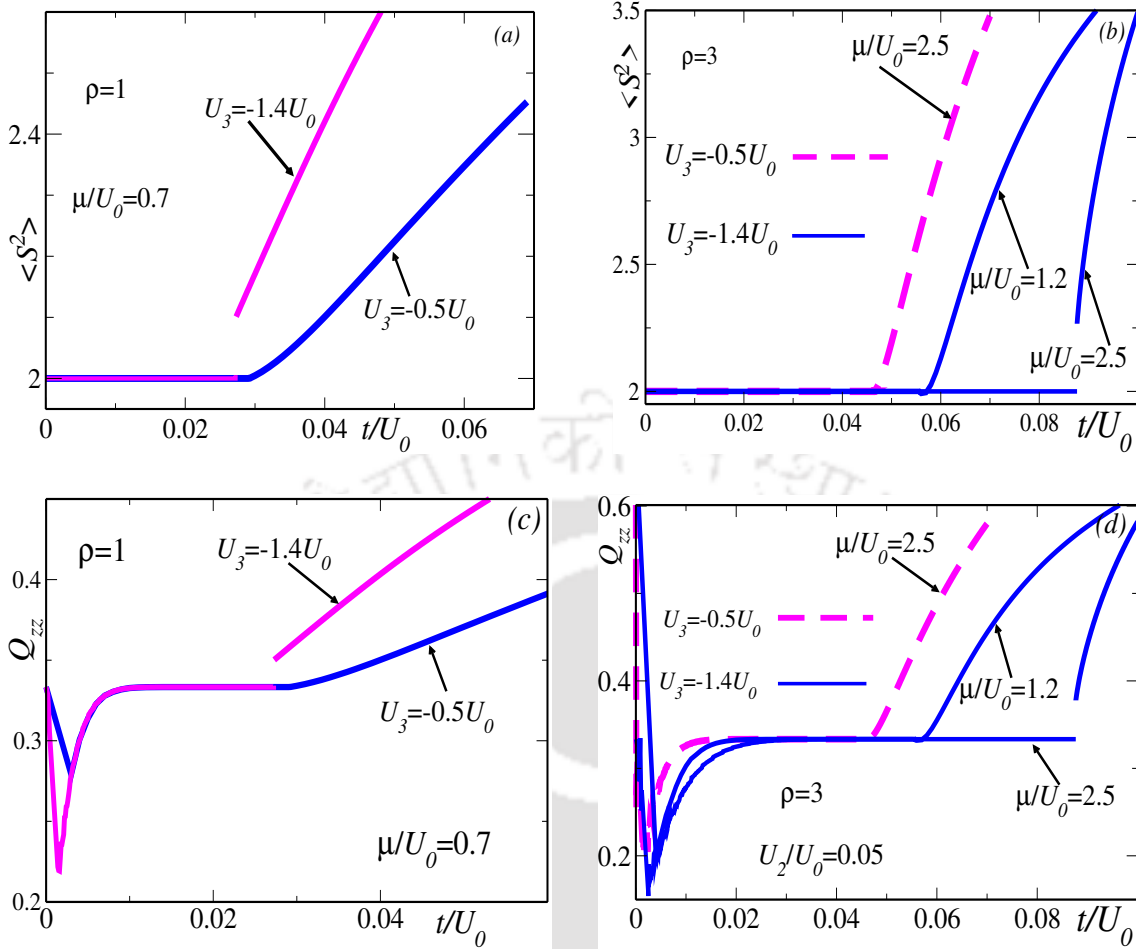


Figure 7.5: The total spin eigenvalue, $\langle S^2 \rangle$ and the spin nematic order parameter, Q_{zz} for $U_2/U_0 = 0.05$ corresponding to the first ($\rho = 1$) (left) and the third ($\rho = 3$) (right) odd MI lobes with $U_3/U_0 = -0.5$ and $U_3/U_0 = -1.4$. For the third MI lobe, we have found a second order phase transition at $\mu/U_0 = 1.2$ and a first order at $\mu/U_0 = 2.5$ for $U_3/U_0 = -1.4$.

7.2.1.4 PMFA phase diagrams

Since the spin eigenvalues, $S = 0$ for the even and $S = 1$ for the odd MI lobes in presence of three body interaction, we shall now focus on obtaining the analytic phase diagrams using perturbative mean field approaches (PMFA) to compare them with the numerical mean field phase diagram. Using H' as the perturbed Hamiltonian in Eq.(7.2), the ground state energy, E_n which includes the first and second order corrections, is expressed in a series of ψ [24] as,

$$E_n(\psi) = E^0 + C_2(U_0, U_2, \mu, n, U_3) \sum_{\sigma} \psi_{\sigma}^2 \quad 7.6$$

The boundary between the MI-SF phase is obtained by putting $C_2(U_0, U_2, \mu, n, U_3) = 0$ due to minimization of $E_n(\psi)$ with respect to ψ . Using Eq.(7.6), the boundary

equation corresponding to the third MI lobe ($\rho = 3$) is given by,

$$\left(\frac{1}{t}\right)_{n=3} = \frac{8/15}{\mu - 2U_0 + 3U_2 - U_3} + \frac{28/15}{3U_0 + U_2 - \mu - U_3} + \frac{5/3}{\mu - 2U_0 - U_3} + \frac{4/3}{3U_0 - 2U_2 - \mu - U_3} \quad 7.7$$

Similarly for other MI lobes, we can obtain the boundary equations and the resultant phase diagrams are shown in Fig.7.2 (a) and (b) (dashed lines).

At both values of U_2/U_0 , the PMFA phase diagrams are in excellent agreement with the MFA results for all odd and even MI lobes corresponding to all values of U_3/U_0 . However, we have checked that at smaller values of $U_2/U_0 \leq 0.03$, the MFA and the phase diagrams obtained via PMFA differ from each other slightly at the tip of the MI lobes, particularly it is prominent for the third MI lobe. Such deviation is due to inadequacy of the MFA to handle the fluctuations in reduced dimensions [24,30]. The above equation, which is quadratic in μ , also shows that the critical tunneling strength, t_c/U_0 for the location of the MI-SF phase transition now increases as the three body interaction potential is enhanced.

7.2.1.5 Phase diagram for $U_3 = -1.4U_0$

In Fig.7.5, the spin eigenvalue and the spin nematic order parameters display different orders of phase transition at $U_3/U_0 = -1.4$ which certainly necessitates a careful scrutiny of the complete phase diagram at different values of the chemical potential, μ . For that purpose, we have studied the behaviour of variational energy, E_v and the SF order parameter variation from the MI to the SF phase as a function of t/U_0 for both the $\rho = 1$ and $\rho = 3$ MI lobes with $\psi_+ = \psi_-$ and ψ_0 . For the first MI lobe ($\rho = 1$) at $\mu/U_0 = 0.75$, the variational energy, E_v shows a single minimum in the MI phase at $t/U_0 = 0.005$ [Fig.7.6 (a)]. As we approach toward the SF phase at $t/U_0 = 0.016$, four degenerate minima are formed [Fig.7.6 (b)]. Finally at $t/U_0 = 0.005$ indicates a first order transition due to discontinuous evolution of the global minima [Fig.7.6 (c)]. Similarly, E_v for the third ($\rho = 3$) MI lobe, that is, at $\mu/U_0 = 0.75 + \epsilon$, where $\epsilon = 0.001$, also demonstrates a first order phase transition at $t/U_0 = 0.04$ [Fig.7.6 (d)]. On the other hand, the variational energy for the first MI lobe at $\mu/U_0 = 0.25$ shows a global minima in the MI phase and its continuous evolution in the SF phase signifies a second order transition. Further the order parameter and the variational energy indicate an analogous behaviour near the vicinity of the third ($\rho = 3$) and the fifth ($\rho = 5$) MI lobes. Thus the final phase diagram depicting the first and second order transition is shown in Fig.7.7 where the solid line represents a second order, while the dashed line indicates a first order phase transition.

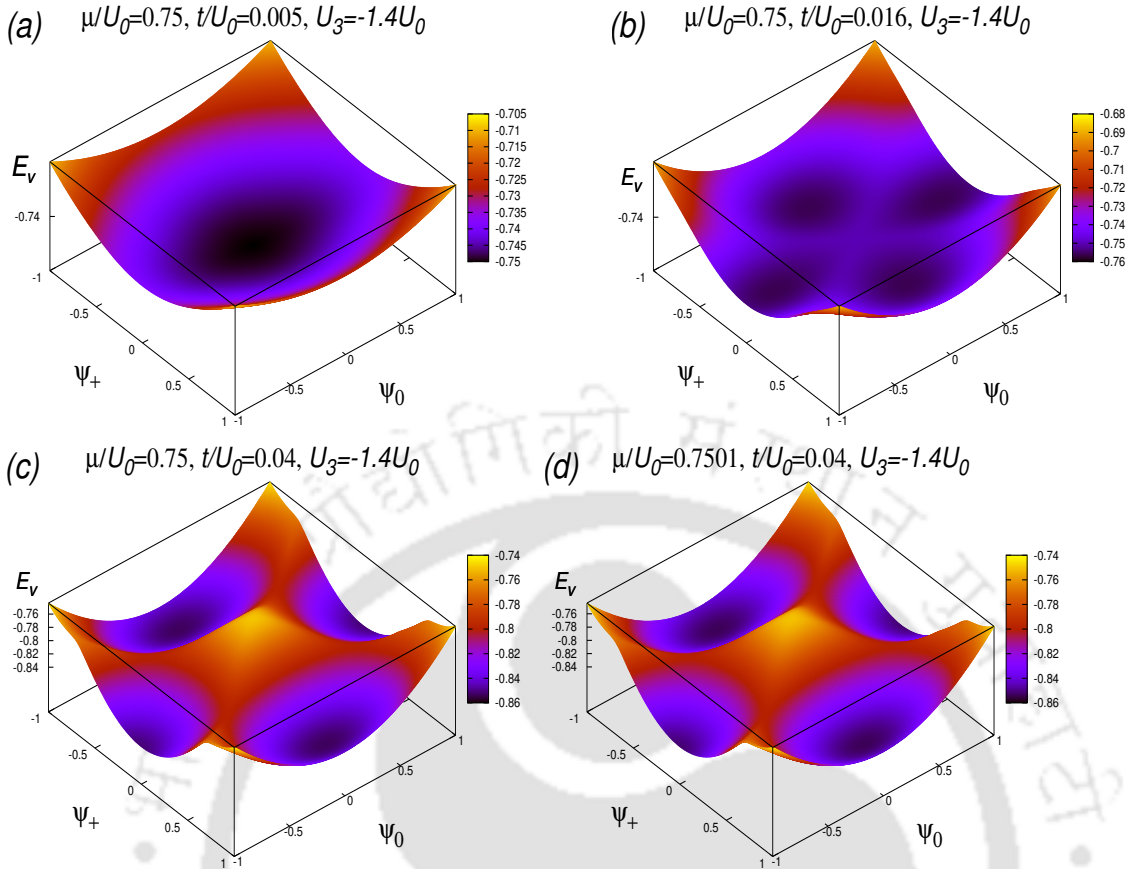


Figure 7.6: The variational energy (E_v) behaviour for the first MI lobe ($\rho = 1$) at $\mu/U_0 = 0.75$ in the MI phase at $zt/U_0 = 0.005$ in (a), near the MI-SF phase at $zt/U_0 = 0.016$ in (b) and finally in the SF phase at $zt/U_0 = 0.04$ in (c) for $U_3/U_0 = -1.4$. E_v shows a discontinuous transformation of the global minimum to four degenerate minima is a signature of first order transition for the first MI lobe ($\rho = 1$). The third MI lobe ($\rho = 3$) at $\mu/U_0 = 0.7501$ also shows first order transition from the MI to the SF phase in (d).

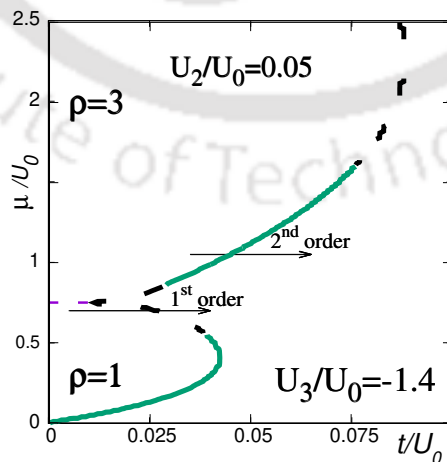


Figure 7.7: The detailed mean field phase diagram depicting the first (dashed line) and second (solid lines) order transition for $U_3/U_0 = -1.4$ with $U_2/U_0 = 0.05$.

7.2.2 Ferromagnetic case

The phase diagrams corresponding to the ferromagnetic case ($U_2/U_0 = -0.04$) for different values of U_3/U_0 are shown in [Fig.7.8] and they are identical to a spin-0 Bose gas. We have also found similar kinds of phase transition corresponding to different MI lobes at $U_3 = -1.4U_0$ which was pointed out earlier in Ref. [106].

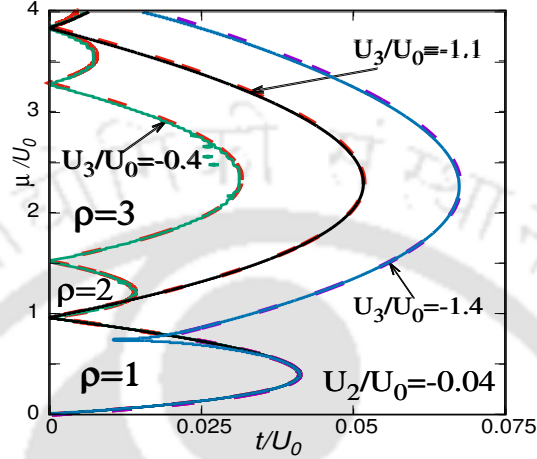


Figure 7.8: The MFA (solid lines) and PMFA (dashed lines) phase diagrams in the ferromagnetic case $U_2/U_0 = -0.04$ with U_3/U_0 . Both the MFA and PMFA phase diagrams are in complete agreement with each other.

7.3 Conclusion

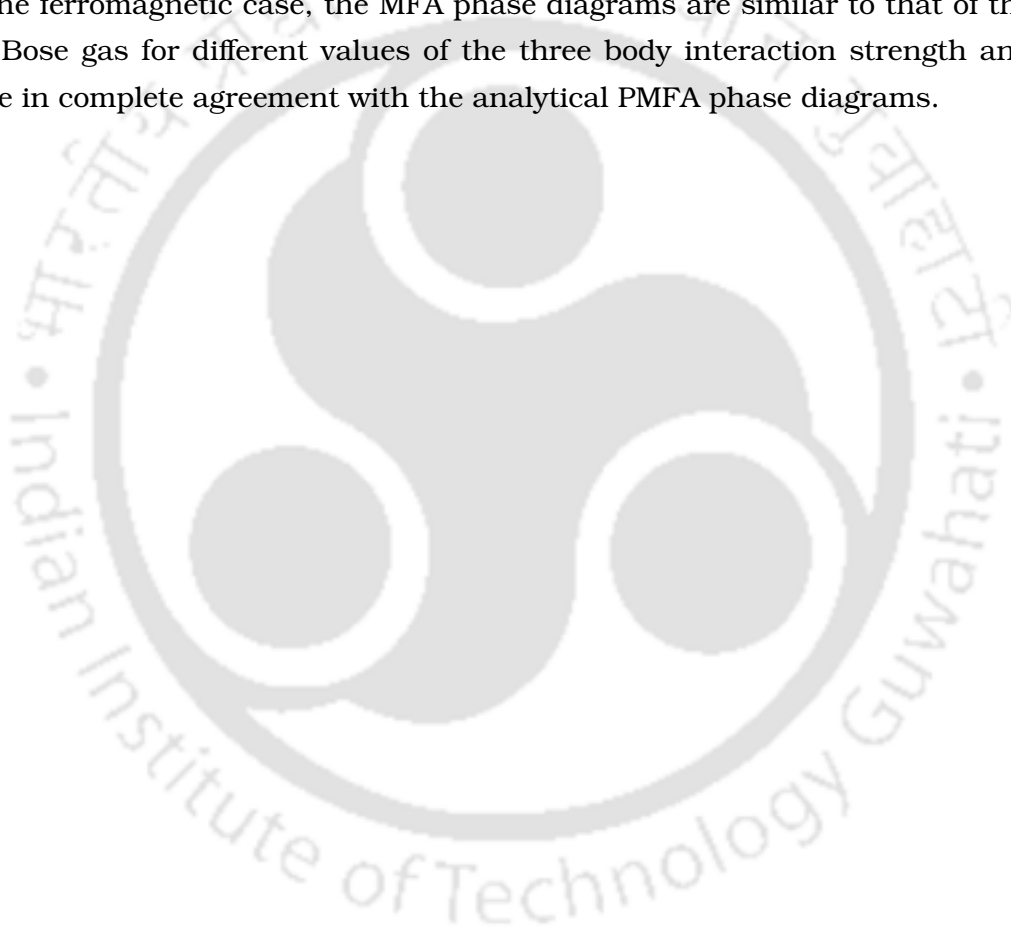
In this work, we have explored the consequences of an attractive three body interaction on the phase diagram of a SBHM using mean field and perturbative approaches. In the AF case, the third MI lobe expands by encroaching into the neighbouring second and fourth MI lobes which affects the odd-even asymmetry in the MI phase for smaller values of the three body interaction strength. However above the critical value of the three body strength, the third MI lobe predominantly occupies the whole phase diagram where it completely engulfs the neighbouring even MI lobes, thereby destroying such asymmetry around the second and the fourth MI lobes. Although the asymmetry remains intact beyond the fourth MI lobe at higher values of the potential strength.

The spin eigenvalue and the nematic order parameter shows the formation of the spin singlet and nematic state corresponding to the even and odd MI lobes respectively for smaller values of the interaction strength. Also the order parameters show that the phase transition to the SF phase still maintains a first and second order character from the spin singlet and nematic MI phases respectively.

At a considerable higher values of the three body strength, we have found a first as well as a second order transition at different location of the chemical

potential corresponding to the first and the third MI lobes. This was confirmed by carefully scrutinizing the variational ground state energy and the spin eigenvalue and spin nematic order parameter. The region in the vicinity of the first and third, as well as the third and the fifth MI lobes also show a first order phase transition which were subsequently confirmed from the behaviour of the variational energy and order parameters. Finally, all our MFA phase diagrams have splendid match with the analytical phase diagrams obtained using perturbative expansion (PMFA). Both the phase diagrams are in good agreement with each other however a small discrepancy is observed near the tip of the MI lobes for smaller values of the two body spin dependent interaction potential.

In the ferromagnetic case, the MFA phase diagrams are similar to that of the spin-0 Bose gas for different values of the three body interaction strength and they are in complete agreement with the analytical PMFA phase diagrams.



Chapter 8: Conclusions

A spinor system possesses an additional spin dependent interaction potential owing to the presence of different hyperfine spin degrees of freedom. This potential can have a positive, known as an antiferromagnetic (AF) or a negative, known as a ferromagnetic interaction. The spin dependent interaction potential has a direct role in determining various exotic phases of a spin-1 Bose gas which shows an edge in the study of the quantum magnetism compared to the scalar or spin-0 Bose gas. Motivated by this, this thesis involves an extensive theoretical exploration of the ground state phase properties of a spin-1 ultracold atom in an optical lattice. For our purpose and adequate to address the main objectives, we have used a mean field approach (MFA) to study the different features and properties of a spin-1 Bose Hubbard model (SBHM). The mean field calculations are suitably supported by a strong coupling perturbative expansion (PMFA) techniques. Various contextual issues discussed by including a random disorder, synthetic magnetic field, extended and multi-body interaction potentials etc. The formation of the spin nematic and singlet Mott insulating (MI) phases and hence the existence of an odd-even asymmetry in the MI lobes, as well as polar and ferromagnetic nature of the superfluid (SF) phase are noteworthy results obtained by us that are carefully scrutinized by computing various physical quantities, such as the SF density, ground state energies, spin eigenvalues and spin nematic order parameter in presence of such interactions.

At the beginning, we have considered a system of spin-1 ultracold atoms in presence of an on-site random disorder potential. The inclusion of disorder in the SBHM yields a glassy phase, known as the Bose glass (BG) phase along with the MI and SF phases. These three different types of phases have been characterized by an indicator which is defined as the fraction of the lattice sites having finite SF order parameter and non integer local densities. The indicator aids in the study of phase transition from one phase to another. The transition to a BG phase, either from a MI or a SF phase, is found to have an unusual similarity with the random percolation phenomena familiar in the context of statistical physics. A percolation threshold, at the onset of a SF phase in our interacting spinor Bose gas, is found to have a surprisingly close value to the one obtained in a non-interacting random site occupation problem. The only resemblance being the "random" disorder in our case, vis-a-vis a "random" occupation probability in a statistical model. The precise locations for the MI-BG and the BG-SF phase transition are done by computing the probability of having a SF percolating cluster using Hoshen-Kopelman (HK) algorithm. Further, the phase diagrams are obtained based on the critical values of the indicator that demarcate the boundaries existing among the three different phases. The resultant phase diagrams obtained by us using percolation

analysis are in good agreement with the existing phase diagrams obtained via the probabilistic mean field perturbative approximation (PMFA).

Apart from studying a random disorder, we have explored the consequences of a synthetic magnetic field on the spin singlet and nematic MI and the SF phases of the SBHM. For the sake of completeness, we have considered both the synthetic magnetic field which enters into the Hamiltonian via Peierl's coupling, as well as an external magnetic field that includes Zeeman coupling. We have found that the external and the synthetic magnetic fields compete against each other for the formation of spin singlet phases. In the AF case, low strengths of the external magnetic field favours spin singlet formation, while the synthetic field pushes the system towards an insulating phase. However, at large field strengths, the external magnetic field suppresses the spin singlet formation to destabilize the even MI lobes, but the synthetic magnetic field stabilizes the MI phase by destroying the phase coherence of the SF phase. Also the energy spectrum shows a symmetry with the magnetic flux for both the spin singlet and nematic phases. However an asymmetry is observed for the spin singlet phase at higher values of the flux strength. A signature of transverse polar and longitudinal ferro SF phases is demonstrated by computing the magnetization corresponding to both values of spin dependent interactions.

In the next chapter, we have investigated the appearances of various density ordered phases in the SBHM in presence of a long range interaction potential along with the usual short range two body interaction. The density-density extended interaction in the SBHM results in a charge density wave (CDW) along with the MI and SF phases. For small values of extended interaction strengths, a CDW phase appears to be sandwiched between the MI and the supersolid (SS) phases. On the contrary, when extended interaction is larger than the potential widths of the odd and even MI lobes, the CDW phase completely engulfs all the MI lobes. Since at this critical value, both the CDW and MI phases become degenerate and for the first time, a signature of spin singlet and nematic CDW insulating phases has been observed which is analogous to the spin singlet and nematic MI phases. The variation of the spin eigenvalues confirmed formation of the spin singlet and nematic CDW phases which oscillates between 0 and 1 replicating a spin density wave (SDW) pattern. The order parameters and the ground state energy show that the phase transition from the spin singlet CDW to SS phase found to be a first order, while a second order transition is observed from the spin nematic CDW to SS phase. Finally, we have obtained the analytic phase diagrams using PMFA and the boundary between the CDW-SS and MI-SF phases which are subsequently compared with the MFA results. Both the techniques yield results that are in qualitative agreement with each other.

The last two consecutive chapters are dedicated to study the effects of a multi-

body interaction on the SBHM. The first one deals with a three body interaction potential in addition to the s-wave dominated two body interaction strengths to study the signature of odd-even asymmetry in the MI lobes. In the AF case, at first we have considered both the two as well as a repulsive three body interaction potentials and found the spin nematic-singlet MI phase. The odd-even asymmetry remains intact in the MI lobes. This was confirmed by carefully analyzing the spin eigenvalue and spin nematic order parameters. Also the the phase transition still maintains a first and second order transition to the SF phase from the spin singlet and nematic MI phases respectively. For an attractive three body interaction potential, the phase diagram is similar to that of the repulsive case and also shows the spin singlet and nematic states corresponding to the even and odd MI lobes. However, for a purely three body repulsive interaction, the higher order MI lobes, except the first one, stabilize compared to the SF phase. However the spin nematic-singlet formation is observed beyond the second MI lobe. The spin eigenvalue vanishes for the fourth and corresponds to unity for the third MI lobe, while it shows an oscillatory behaviour for the second MI lobe. All the phase properties are carefully examined by computing the spin eigenvalues and the spin nematic order parameter. Finally all the mean field phase diagrams are compared with the PMFA phase diagrams. They are in good agreement with each other, except for a small mismatch near the tip of the MI lobes.

In addition to the above three body interaction potential, in the last chapter, we have studied the effects of an attractive three body interaction potential relevant to formation of trimer states in a SBHM. For smaller values of the attractive three body strength, the third MI lobe expands by invading into the regime of the neighbouring even MI lobes, which in turn, affects the asymmetry of the MI phase. At higher values of the three body strength, the third MI lobe completely captures the second and fourth MI lobes and thereby destroy the above mentioned asymmetry in its neighbourhood. However such asymmetry remains unhindered beyond the fourth MI lobe at higher values of the potential strength. The spin eigenvalue and the spin nematic order parameter show the formation of the spin singlet phase for the even MI lobes and indicate a first order transition to the SF phase. In a strong three body interaction limit, the first and the third MI lobes display both first and second order phase transition to the SF phase corresponding to different values of the chemical potential. This was confirmed by carefully scrutinizing the behaviour of the variational ground state energy and the spin eigenvalue and spin nematic order parameter. Finally we have obtained the PMFA phase diagrams to compare with the results obtained from the mean field calculation and they are found to be in agreement with each other.



Appendices





Appendix A: Matrix elements and the PMFA calculation

Here, we shall briefly outline the perturbative mean field approach (PMFA) to obtain the analytic boundary between the MI and the SF phases that was developed by *Tsuchiya et al.* [24]. Using the single site mean field decoupling approximation [Eq.(2.29)], the mean field Hamiltonian is written as [Eq.(2.31)],

$$H^{MF} = \underbrace{-zt \sum_{\sigma} (\psi_{\sigma} a_{\sigma}^{\dagger} + h.c.)}_{H'} + \underbrace{zt \sum_{\sigma} \psi_{\sigma}^2 - \mu n + \frac{U_0}{2} n(n-1) + \frac{U_2}{2} (S^2 - 2n)}_{H^0} \quad \text{A.1}$$

Since S^2 , S_z and n commute with each other thus the eigenstate of H^0 is described by $|S, m, n\rangle$ where

$$\begin{aligned} S^2 |S, m, n\rangle &= S(S+1) |S, m, n\rangle \\ H^0 |S, m, n\rangle &= E^0(S, n) |S, m, n\rangle \\ E^0(S, n) &= -\mu n + \frac{1}{2} U_0 n(n-1) + \frac{1}{2} U_2 [S(S+1) - 2n] \end{aligned} \quad \text{A.2}$$

Now expressing $|S, m, n\rangle$ in terms of the creation operator a_a^{\dagger} as,

$$\begin{aligned} |S, S, n\rangle &= \frac{1}{\sqrt{f(Q, S)}} (a_+^{\dagger})^S (\Theta^{\dagger})^{\mathcal{Q}} |vacuum\rangle \\ \Theta &= a_0^2 - 2a_+ a_-, \quad \mathcal{Q} = \frac{n-S}{2} \\ f(Q, S) &= \frac{S! \mathcal{Q}! 2^{\mathcal{Q}} (2\mathcal{Q} + 2S + 1)!!}{(2S + 1)!!} \end{aligned} \quad \text{A.3}$$

By comparing the expression for $|S, S, n\rangle$ and $|S+1, S+1, n+1\rangle$, we obtain,

$$a_+^{\dagger} |S, m, n\rangle = \sqrt{\frac{(S+1)(2S+2\mathcal{Q}+3)}{2S+3}} |S+1, S+1, n+1\rangle \quad \text{A.4}$$

Few commutation relations among S^{\pm} , a_{σ} and Θ^{\dagger} are given by,

$$\begin{aligned} [S^+, a_+] &= -\sqrt{2}a_0, \quad [S^-, a_+] = 0, \quad [S_z, a_+] = -a_1 \\ [S^+, a_0] &= -\sqrt{2}a_{-1}, \quad [S^-, a_0] = -\sqrt{2}a_+, \quad [S_z, a_0] = 0 \\ [S^+, a_-] &= 0, \quad [S^-, a_-] = -\sqrt{2}a_0, \quad [S_z, a_-] = -a_- \\ [a_+, \Theta^{\dagger}] &= -2a_-^{\dagger}, \quad [a_0, \Theta^{\dagger}] = 2a_0^{\dagger}, \quad [a_-, \Theta^{\dagger}] = -2a_+^{\dagger} \end{aligned} \quad \text{A.5}$$

By operating S^- in Eq.(A.4) and using the above commutation relations, the following equations can be derived as,

$$\begin{aligned} \alpha_{\pm} |0, 0, n\rangle &= -\sqrt{\frac{n}{3}} |1, \mp, n-1\rangle, & \alpha_0 |0, 0, n\rangle &= \sqrt{\frac{n}{3}} |1, 0, n-1\rangle \\ \alpha_{\pm}^{\dagger} |0, 0, n\rangle &= \sqrt{\frac{n+3}{3}} |1, \pm, n+1\rangle, & \alpha_0^{\dagger} |0, 0, n\rangle &= \sqrt{\frac{n+3}{3}} |1, 0, n+1\rangle \end{aligned} \quad \text{A.6}$$

Now the second order correction for the ground state energies corresponding to the even MI lobes ($\rho = 2, 4, 6 \dots$) using H' is given by,

$$E_q^2 = \sum_{q \neq i} \frac{|\langle q | H' | i \rangle|^2}{E_i^0 - E_q^0} \quad \text{A.7}$$

where $|i\rangle = |0, 0, n\rangle$ is the initial state for the even MI lobes with the spin eigenvalue $S = 0$ and $|q\rangle$ is the intermediate state. The following intermediate states are as follows,

$$\begin{aligned} |q\rangle &= |1, +1, n \pm 1\rangle \\ &= |1, -1, n \pm 1\rangle \\ &= |1, 0, n \pm 1\rangle \end{aligned} \quad \text{A.8}$$

For example H' acting on $|0, 0, n\rangle$ gives the following equation as,

$$\begin{aligned} H' |0, 0, n\rangle &= -zt \left[-\sqrt{\frac{n}{3}} \psi_+ |1, -1, n-1\rangle + \sqrt{\frac{n+3}{3}} \psi_+ |1, 1, n+1\rangle \right. \\ &\quad - \sqrt{\frac{n}{3}} \psi_- |1, 1, n-1\rangle + \sqrt{\frac{n+3}{3}} \psi_- |1, -1, n+1\rangle \\ &\quad \left. + \sqrt{\frac{n}{3}} \psi_0 |1, 0, n-1\rangle + \sqrt{\frac{n+3}{3}} \psi_0 |1, 0, n+1\rangle \right] \end{aligned} \quad \text{A.9}$$

Finally calculating all the matrix elements between $|1, m, n \pm 1\rangle$ and $|0, 0, n\rangle$, the corrected ground state energy after including the second order correction term (E^2) is given by,

$$E_n(\psi) = E^0 + E^1 + E^2 = E^0 + C_2(\mu, n, U_0, U_2, zt) \sum_{\sigma} \psi_{\sigma}^2 \quad \text{A.10}$$

where

$$C_2(\mu, n, U_0, U_2, zt) = zt + \frac{1}{3} \left[\frac{n+3}{\mu - U_0 n} + \frac{n}{-\mu + U_0(n-1) - 2U_2} \right] (zt)^2 \quad \text{A.11}$$

For the MI-SF phase boundary, the condition $C_2(\mu, n, U_0, U_2, zt) = 0$ gives the following equation for the even MI lobes,

$$\frac{1}{zt} = \frac{1}{3} \left[\frac{n+3}{nU_0 - \mu} + \frac{n}{\mu + 2U_2 - U_0(n-1)} \right] \quad \text{A.12}$$

Similarly, for the odd MI lobes with spin eigenvalue $S = 1$, the ground state, $|1, m, n\rangle$ has degeneracy for $m = \pm 1, 0$ and a second order degenerate perturbation theory can be used as the following,

$$\det \left[\langle 1, m, n | H' \frac{1}{E^0(1, n) - H^0} H' | 1, m', n \rangle - E_n^2 \delta_{mm'} \right] = 0 \quad \text{A.13}$$

Finally solving this equation, the boundary for the odd MI lobes is given by,

$$\frac{1}{zt} = \frac{(n+2)/3}{a} + \frac{4(n-1)/15}{a+3U_2} + \frac{(n+1)/3}{\beta-2U_2} + \frac{4(n+4)/15}{\beta+U_2} \quad \text{A.14}$$

where $a = \mu - (n-1)U_0$, $\beta = -\mu + nU_0$



Appendix B: Derivation of the repulsive three body interaction potential

The effective three body spinor interaction can be derived by assuming a virtual excitation to the excited trap levels of the isolated sites of a deep optical lattice as outlined in Ref. [192, 200, 201]. Atoms are held in the ground state of a site which can be approximated by an isotropic 3-dimensional oscillator potential of frequency ω_f . Then the Hamiltonian for spin-1 bosons is given by,

$$\begin{aligned} H_0 &= \epsilon_a a_{ma}^\dagger a_{ma} \\ \Gamma_0 &= \frac{1}{2} c_0 g_{a\beta, \gamma\delta} a_{ka}^\dagger a_{l\beta}^\dagger a_{ka} a_{l\beta} \\ \Gamma_2 &= \frac{1}{2} c_2 g_{a\beta, \gamma\delta} a_{ka}^\dagger a_{l\beta}^\dagger (\mathbf{S}_{km} \cdot \mathbf{S}_{ln}) a_{my} a_{n\delta} \end{aligned} \quad \text{B.1}$$

where a_{ma} annihilates an atom in the spin projection $m = +1, 0, -1$ and 3-dimensional harmonic oscillator state a . ϵ_a is the single particle energies and the real symmetric coefficient $g_{a\beta, \gamma\delta}$ is a 3-dimensional integral over the product of the four oscillator wave functions a, β, γ , and δ . For every spatial mode a , the spin wave function $|\{n_{-1}, n_0, n_1\}_a\rangle$ with $n_m = 0, 1, 2, \dots$ in the spin state m . The ground states P are formed by the orthonormal basis functions $|g\rangle = |\{n_{-1}, n_0, n_1\}_0, 0_{a \neq 0}\rangle$ for any value of n_m and where $0_{a \neq 0}$ indicates that there are no atoms in the excited spatial modes. Using H_0 as the zeroth-order Hamiltonian and $\Gamma_0 + \Gamma_2$ as the perturbation, the second order correction to the ground state energies for the ground motional states $|g'\rangle$ and $|g\rangle$ is given by,

$$\langle g' | \delta H^{(2)} | g \rangle = \frac{1}{2} \sum_{e \neq P} \langle g' | \Gamma_0 + \Gamma_2 | e \rangle \times \left[\frac{1}{E_g - E_e} + \frac{1}{E_{g'} - E_e} \right] \langle e | \Gamma_0 + \Gamma_2 | g \rangle \quad \text{B.2}$$

The sum over the excited states can be evaluated by realizing that only states $|e\rangle \propto a_{ka}^\dagger a_{l\beta}^\dagger a_{m0} a_{n0} |g\rangle$ with $a\beta \neq 00$ and $k+l = m+n$ contribute as both $\Gamma_0 + \Gamma_2$ conserve atom number. Inserting the normalized expression for $|e\rangle$ and performing the sums over $|e\rangle$ as well as those appearing in the potentials $\Gamma_0 + \Gamma_2$, then the Eq.(B.2) is given by,

$$\begin{aligned} \langle g' | \delta H^{(2)} | g \rangle &= - \sum_{a\beta \neq 00, \mu\nu} g_{00, \mu\nu} \frac{1}{\epsilon_a + \epsilon_\beta} g_{a\beta, 00} \times \left[\frac{1}{4} c_0^2 \langle g' | a_{m0}^\dagger a_{n0}^\dagger a_{m\mu} a_{n\nu} a_{ka}^\dagger a_{l\beta}^\dagger a_{k0} a_{l0} | g \rangle \right. \\ &\quad \left. + \frac{1}{2} c_0 c_2 \langle g' | a_{p0}^\dagger a_{o0}^\dagger (\mathbf{S}_{pm} \cdot \mathbf{S}_{on}) a_{m\mu} a_{n\nu} a_{ka}^\dagger a_{l\beta}^\dagger a_{k0} a_{l0} | g \rangle \right] \end{aligned} \quad \text{B.3}$$

By normal ordering the creation and annihilation operators in Eq.(B.3) and using the fact that the ground state P contains no atoms in the excited trap levels then,

$$\langle g' | \delta H^{(2)} | g \rangle = \langle g' | \delta H_{2B} + H_{3B} | g \rangle \quad \text{B.4}$$

where

$$\delta H_{2B} = Z_2 \left[-\frac{1}{2} c_0^2 a_{k_0}^\dagger a_{l_0}^\dagger a_{k_0} a_{l_0} - c_0 c_2 a_{m_0}^\dagger a_{n_0}^\dagger (\mathbf{S}_{mk} \cdot \mathbf{S}_{nl}) a_{k_0} a_{l_0} \right] \quad \text{B.5}$$

is a correction to the pairwise two body interaction and

$$H_{3B} = Z_3 \left[-c_0^2 a_{k_0}^\dagger a_{l_0}^\dagger a_{m_0}^\dagger a_{k_0} a_{l_0} a_{m_0} - 2c_0 c_2 a_{o_0}^\dagger a_{m_0}^\dagger a_{n_0}^\dagger (\mathbf{S}_{mk} \cdot \mathbf{S}_{nl}) a_{k_0} a_{l_0} a_{o_0} \right] \quad \text{B.6}$$

is an effective three body interaction. Here

$$Z_2 = \sum_{\mu \nu \neq 00} g_{00,\mu\nu} \frac{1}{\epsilon_\mu + \epsilon_\nu} g_{\mu\nu,00}$$

$$Z_3 = \sum_{\mu \neq 0} g_{00,\mu 0} \frac{1}{\epsilon_\mu} g_{\mu 0,00} \quad \text{B.7}$$

The sums in Z_2 diverge and must be regularized and renormalized [201]. That is, the bare coupling constant c_0 is defined such that, that, by combing the first and second order corrections, $c_0 g_{00,00} - c_0^2 Z_2$ is finite and is equal to U_0 . Similarly, the term $c_2 g_{00,00} - 2c_0 c_2 Z_2$ is finite and equal to U_2 . The sum in coefficient Z_3 of the effective three body Hamiltonian converges. Hence, the effective three body interaction can be redefined as,

$$H_{3B} = \frac{1}{6} W a_{k_0}^\dagger a_{l_0}^\dagger a_{m_0}^\dagger a_{k_0} a_{l_0} a_{m_0} + \frac{1}{6} V a_{o_0}^\dagger a_{m_0}^\dagger a_{n_0}^\dagger (\mathbf{S}_{mk} \cdot \mathbf{S}_{nl}) a_{k_0} a_{l_0} a_{o_0} \quad \text{B.8}$$

where,

$$W = -6U_0^2 \frac{1}{g_{00,00}^2} Z_3 \quad \text{and} \quad V = -12U_0 U_2 Z_3 = 2 \frac{U_2}{U_0} W \quad \text{B.9}$$

Here W and V are the three body spin independent and dependent interaction potentials respectively. For a spherically symmetric harmonic oscillator, $W = -1.34U_0^2/(\hbar\omega_f)$ [200]. Since $U_2 > 0$ for ^{23}Na atoms thus $V < 0$, while for ^{87}Rb atoms, $U_2 < 0$ and thus $V > 0$. Finally the three body interaction potential can be written in terms of the angular momentum operator $\mathbf{S} = (S_x, S_y, S_z)$ as,

$$H_3 = \frac{W}{6} n(n-1)(n-2) + \frac{V}{6} (\mathbf{S}^2 - 2n)(n-2) \quad \text{B.10}$$

Bibliography

- [1] D. Jaksch, C. Bruder, J. I. Cirac, C. W. Gardiner, and P. Zoller, *Phys. Rev. Lett.*, vol. 81, pp. 3108-3111, Oct 1998.
- [2] M. Greiner, O. Mandel, T. Esslinger, T. W. Hansch, and I. Bloch, *Nature*, vol. 415, p. 39, 2002.
- [3] S. Chu, *Rev. Mod. Phys.*, vol. 70, pp. 685-706, Jul 1998.
- [4] W. D. Phillips, *Rev. Mod. Phys.*, vol. 70, pp. 721-741, Jul 1998.
- [5] C. N. Cohen-Tannoudji, *Rev. Mod. Phys.*, vol. 70, pp. 707-719, Jul 1998.
- [6] T. Hänsch and A. Schawlow, *Optics Communications*, vol. 13, no. 1, pp. 68 - 69, 1975.
- [7] M. H. Anderson, J. R. Ensher, M. R. Matthews, C. E. Wieman, and E. A. Cornell, *Science*, vol. 269, no. 5221, pp. 198-201, 1995.
- [8] C. C. Bradley, C. A. Sackett, J. J. Tollett, and R. G. Hulet, *Phys. Rev. Lett.*, vol. 75, pp. 1687-1690, Aug 1995.
- [9] K. B. Davis, M. O. Mewes, M. R. Andrews, N. J. van Druten, D. S. Durfee, D. M. Kurn, and W. Ketterle, *Phys. Rev. Lett.*, vol. 75, pp. 3969-3973, Nov 1995.
- [10] Bose, *Zeitschrift für Physik*, vol. 26, no. 1, pp. 178-181, Dec 1924.
- [11] C. Chin, R. Grimm, P. Julienne, and E. Tiesinga, *Rev. Mod. Phys.*, vol. 82, pp. 1225-1286, Apr 2010.
- [12] M. Greiner, "Ultracold quantum gases in three-dimensional optical lattice potentials," Ph.D. dissertation, lmu, 2003.
- [13] A. Ashkin, *Proceedings of the National Academy of Sciences*, vol. 94, no. 10, pp. 4853-4860, 1997.
- [14] S. Chu, J. E. Bjorkholm, A. Ashkin, and A. Cable, *Phys. Rev. Lett.*, vol. 57, pp. 314-317, Jul 1986.
- [15] C. S. Adams, H. J. Lee, N. Davidson, M. Kasevich, and S. Chu, *Phys. Rev. Lett.*, vol. 74, pp. 3577-3580, May 1995.
- [16] D. M. Stamper-Kurn and M. Ueda, *Rev. Mod. Phys.*, vol. 85, pp. 1191-1244, Jul 2013.

- [17] T.-L. Ho, *Phys. Rev. Lett.*, vol. 81, pp. 742–745, Jul 1998.
- [18] T. Ohmi and K. Machida, *J. Phys. Soc. Jpn.*, vol. 67, no. 6, pp. 1822–1825, 1998.
- [19] D. M. Stamper-Kurn, M. R. Andrews, A. P. Chikkatur, S. Inouye, H.-J. Miesner, J. Stenger, and W. Ketterle, *Phys. Rev. Lett.*, vol. 80, pp. 2027–2030, Mar 1998.
- [20] H.-J. Miesner, D. M. Stamper-Kurn, J. Stenger, S. Inouye, A. P. Chikkatur, and W. Ketterle, *Phys. Rev. Lett.*, vol. 82, pp. 2228–2231, Mar 1999.
- [21] D. M. Stamper-Kurn, H.-J. Miesner, A. P. Chikkatur, S. Inouye, J. Stenger, and W. Ketterle, *Phys. Rev. Lett.*, vol. 83, pp. 661–665, Jul 1999.
- [22] S. Yi and H. Pu, *Phys. Rev. Lett.*, vol. 97, p. 020401, Jul 2006.
- [23] S. W. Seo, W. J. Kwon, S. Kang, and Y. Shin, *Phys. Rev. Lett.*, vol. 116, p. 185301, May 2016.
- [24] S. Tsuchiya, S. Kurihara, and T. Kimura, *Phys. Rev. A*, vol. 70, p. 043628, Oct 2004.
- [25] R. V. Pai, K. Sheshadri, and R. Pandit, *Phys. Rev. B*, vol. 77, p. 014503, Jan 2008.
- [26] F. Zhou, *Phys. Rev. Lett.*, vol. 87, p. 080401, Aug 2001.
- [27] E. Demler and F. Zhou, *Phys. Rev. Lett.*, vol. 88, p. 163001, Apr 2002.
- [28] S. K. Yip, *Phys. Rev. Lett.*, vol. 90, p. 250402, Jun 2003.
- [29] A. Imambekov, M. Lukin, and E. Demler, *Phys. Rev. Lett.*, vol. 93, p. 120405, Sep 2004.
- [30] T. Kimura, S. Tsuchiya, and S. Kurihara, *Phys. Rev. Lett.*, vol. 94, p. 110403, Mar 2005.
- [31] G. G. Batrouni, V. G. Rousseau, and R. T. Scalettar, *Phys. Rev. Lett.*, vol. 102, p. 140402, Apr 2009.
- [32] H. Sun, P. Xu, H. Pu, and W. Zhang, *Phys. Rev. A*, vol. 95, p. 063624, Jun 2017.
- [33] L. M. Symes and P. B. Blakie, *Phys. Rev. A*, vol. 96, p. 013602, Jul 2017.
- [34] A. Imambekov, M. Lukin, and E. Demler, *Phys. Rev. A*, vol. 68, p. 063602, Dec 2003.

- [35] Y. Li, L. He, and W. Hofstetter, *Phys. Rev. A*, vol. 93, p. 033622, Mar 2016.
- [36] F. Zhou, *EPL (Europhysics Letters)*, vol. 63, no. 4, p. 505, 2003.
- [37] M. Ueda, *Reports on Progress in Physics*, vol. 77, no. 12, p. 122401, 2014.
- [38] J. Jiang, L. Zhao, S.-T. Wang, Z. Chen, T. Tang, L.-M. Duan, and Y. Liu, *Phys. Rev. A*, vol. 93, p. 063607, Jun 2016.
- [39] K. H. Z. So and M. Ueda, *Phys. Rev. A*, vol. 96, p. 023628, Aug 2017.
- [40] L. de Forges de Parny and V. G. Rousseau, *Phys. Rev. A*, vol. 97, p. 023628, Feb 2018.
- [41] W. Zhang, S. Yi, and L. You, *New Journal of Physics*, vol. 5, no. 1, p. 77, 2003.
- [42] C. Frapolli, T. Zibold, A. Invernizzi, K. Jiménez-García, J. Dalibard, and F. Gerbier, *Phys. Rev. Lett.*, vol. 119, p. 050404, Aug 2017.
- [43] C. B. Dağ, S.-T. Wang, and L.-M. Duan, *Phys. Rev. A*, vol. 97, p. 023603, Feb 2018.
- [44] C. Wang, C. Gao, C.-M. Jian, and H. Zhai, *Phys. Rev. Lett.*, vol. 105, p. 160403, Oct 2010.
- [45] J. H. Pixley, S. S. Natu, I. B. Spielman, and S. Das Sarma, *Phys. Rev. B*, vol. 93, p. 081101, Feb 2016.
- [46] J.-G. Wang, L.-L. Xu, and S.-J. Yang, *Phys. Rev. A*, vol. 96, p. 033629, Sep 2017.
- [47] A. Celi, P. Massignan, J. Ruseckas, N. Goldman, I. B. Spielman, G. Juzeliūnas, and M. Lewenstein, *Phys. Rev. Lett.*, vol. 112, p. 043001, Jan 2014.
- [48] K. Sun, C. Qu, Y. Xu, Y. Zhang, and C. Zhang, *Phys. Rev. A*, vol. 93, p. 023615, Feb 2016.
- [49] G. I. Martone, F. V. Pepe, P. Facchi, S. Pascazio, and S. Stringari, *Phys. Rev. Lett.*, vol. 117, p. 125301, Sep 2016.
- [50] J. L. Helm, T. P. Billam, A. Rakonjac, S. L. Cornish, and S. A. Gardiner, *Phys. Rev. Lett.*, vol. 120, p. 063201, Feb 2018.
- [51] P. A. M. Dirac, *Proceedings of the Royal Society of London A: Mathematical, Physical and Engineering Sciences*, vol. 112, no. 762, pp. 661–677, 1926.

- [52] L. Pitaevskii and S. Stringari, *Bose-Einstein condensation and superfluidity*. Oxford University Press, 2016, vol. 164.
- [53] T. D. Lee and C. N. Yang, *Phys. Rev.*, vol. 112, pp. 1419–1429, Dec 1958.
- [54] I. Bloch, J. Dalibard, and W. Zwerger, *Rev. Mod. Phys.*, vol. 80, pp. 885–964, Jul 2008.
- [55] E. P. Gross, *Il Nuovo Cimento (1955-1965)*, vol. 20, no. 3, pp. 454–477, 1961.
- [56] L. Pitaevskii, *Sov. Phys. JETP*, vol. 13, no. 2, pp. 451–454, 1961.
- [57] I. Bloch, *Nature Physics*, vol. 1, no. 1, p. 23, 2005.
- [58] W. Ketterle and N. Van Druten, “Evaporative cooling of trapped atoms,” in *Advances in atomic, molecular, and optical physics*. Elsevier, 1996, vol. 37, pp. 181–236.
- [59] R. Grimm, M. Weidemüller, and Y. B. Ovchinnikov, “Optical dipole traps for neutral atoms,” in *Advances in atomic, molecular, and optical physics*. Elsevier, 2000, vol. 42, pp. 95–170.
- [60] D. J. Wineland, J. Dalibard, and C. Cohen-Tannoudji, *JOSA B*, vol. 9, no. 1, pp. 32–42, 1992.
- [61] V. I. Kukulkin, V. Krasnopolsky, and J. Horáček, *Theory of resonances: Principles and Applications*. Springer Science & Business Media, 2013, vol. 3.
- [62] A. J. Moerdijk, B. J. Verhaar, and A. Axellsson, *Phys. Rev. A*, vol. 51, pp. 4852–4861, Jun 1995.
- [63] E. R. I. Abraham, W. I. McAlexander, C. A. Sackett, and R. G. Hulet, *Phys. Rev. Lett.*, vol. 74, pp. 1315–1318, Feb 1995.
- [64] J. A.-S. MW Zwierlein, A. Schirotzek, C. Schunck, and W. Ketterle, *Nature (London)*, vol. 435, p. 1047, 2005.
- [65] L. Viverit, *Phys. Rev. A*, vol. 66, p. 023605, Aug 2002.
- [66] J. Hubbard, *Proc. R. Soc. London, Ser. A*, vol. 276, p. 238, 1963.
- [67] M. P. A. Fisher, P. B. Weichman, G. Grinstein, and D. S. Fisher, *Phys. Rev. B*, vol. 40, pp. 546–570, Jul 1989.
- [68] D. van Oosten, D. B. M. Dickerscheid, B. Farid, P. van der Straten, and H. T. C. Stoof, *Phys. Rev. A*, vol. 71, p. 021601, Feb 2005.

- [69] J. Wernsdorfer, “Interacting ultracold gases in optical lattices: non-equilibrium dynamics and effects of disorder,” Ph.D. dissertation, GUF, 2012.
- [70] M. D. Barrett, J. A. Sauer, and M. S. Chapman, *Phys. Rev. Lett.*, vol. 87, p. 010404, Jun 2001.
- [71] M.-S. Chang, C. D. Hamley, M. D. Barrett, J. A. Sauer, K. M. Fortier, W. Zhang, L. You, and M. S. Chapman, *Phys. Rev. Lett.*, vol. 92, p. 140403, Apr 2004.
- [72] H. Schmaljohann, M. Erhard, J. Kronjäger, M. Kottke, S. van Staa, L. Cacciapuoti, J. J. Arlt, K. Bongs, and K. Sengstock, *Phys. Rev. Lett.*, vol. 92, p. 040402, Jan 2004.
- [73] A. Görlitz, T. L. Gustavson, A. E. Leanhardt, R. Löw, A. P. Chikkatur, S. Gupta, S. Inouye, D. E. Pritchard, and W. Ketterle, *Phys. Rev. Lett.*, vol. 90, p. 090401, Mar 2003.
- [74] H. M. Hurst, J. H. Wilson, J. H. Pixley, I. B. Spielman, and S. S. Natu, *Phys. Rev. A*, vol. 94, p. 063613, Dec 2016.
- [75] B. C. Crooker, B. Hebral, E. N. Smith, Y. Takano, and J. D. Reppy, *Phys. Rev. Lett.*, vol. 51, pp. 666–669, Aug 1983.
- [76] T. Giamarchi and H. J. Schulz, *EPL (Europhysics Letters)*, vol. 3, no. 12, p. 1287, 1987.
- [77] B. V. Svistunov, *Phys. Rev. B*, vol. 54, pp. 16 131–16 134, Dec 1996.
- [78] F. Krüger, J. Wu, and P. Phillips, *Phys. Rev. B*, vol. 80, p. 094526, Sep 2009.
- [79] J.-W. Lee, M.-C. Cha, and D. Kim, *Phys. Rev. Lett.*, vol. 87, p. 247006, Nov 2001.
- [80] L. Pollet, N. V. Prokofev, B. V. Svistunov, and M. Troyer, *Phys. Rev. Lett.*, vol. 103, p. 140402, Sep 2009.
- [81] J. K. Freericks and H. Monien, *Phys. Rev. B*, vol. 53, pp. 2691–2700, Feb 1996.
- [82] L. Fallani, J. E. Lye, V. Guarrera, C. Fort, and M. Inguscio, *Phys. Rev. Lett.*, vol. 98, p. 130404, Mar 2007.
- [83] P. Horak, J.-Y. Courtois, and G. Grynberg, *Phys. Rev. A*, vol. 58, pp. 3953–3962, Nov 1998.

- [84] D. Clément, A. F. Varón, M. Hugbart, J. A. Retter, P. Bouyer, L. Sanchez-Palencia, D. M. Gangardt, G. V. Shlyapnikov, and A. Aspect, *Phys. Rev. Lett.*, vol. 95, p. 170409, Oct 2005.
- [85] M. White, M. Pasienski, D. McKay, S. Q. Zhou, D. Ceperley, and B. DeMarco, *Phys. Rev. Lett.*, vol. 102, p. 055301, Feb 2009.
- [86] R. Roth and K. Burnett, *Phys. Rev. A*, vol. 68, p. 023604, Aug 2003.
- [87] G. Roati, C. D'Errico, L. Fallani, M. Fattori, C. Fort, M. Zaccanti, G. Modugno, M. Modugno, and M. Inguscio, *Nature*, vol. 453, no. 7197, p. 895, 2008.
- [88] B. Damski, J. Zakrzewski, L. Santos, P. Zoller, and M. Lewenstein, *Phys. Rev. Lett.*, vol. 91, p. 080403, Aug 2003.
- [89] V. Schweikhard, I. Coddington, P. Engels, V. P. Mogendorff, and E. A. Cornell, *Phys. Rev. Lett.*, vol. 92, p. 040404, Jan 2004.
- [90] K. W. Madison, F. Chevy, W. Wohlleben, and J. Dalibard, *Phys. Rev. Lett.*, vol. 84, pp. 806–809, Jan 2000.
- [91] J. Abo-Shaeer, C. Raman, J. Vogels, and W. Ketterle, *Science*, vol. 292, no. 5516, pp. 476–479, 2001.
- [92] Y.-J. Lin, R. L. Compton, K. Jimenez-Garcia, J. V. Porto, and I. B. Spielman, *Nature*, vol. 462, p. 628, 2009.
- [93] S. Tung, V. Schweikhard, and E. A. Cornell, *Phys. Rev. Lett.*, vol. 97, p. 240402, Dec 2006.
- [94] W. V. Pogosov, A. L. Rakhmanov, and V. V. Moshchalkov, *Phys. Rev. B*, vol. 67, p. 014532, Jan 2003.
- [95] V. Pietilä and M. Möttönen, *Phys. Rev. Lett.*, vol. 103, p. 030401, Jul 2009.
- [96] T. Lahaye, C. Menotti, L. Santos, M. Lewenstein, and T. Pfau, *Reports on Progress in Physics*, vol. 72, no. 12, p. 126401, 2009.
- [97] A. Griesmaier, J. Werner, S. Hensler, J. Stuhler, and T. Pfau, *Phys. Rev. Lett.*, vol. 94, p. 160401, Apr 2005.
- [98] B. Pasquiou, E. Maréchal, G. Bismut, P. Pedri, L. Vernac, O. Gorceix, and B. Laburthe-Tolra, *Phys. Rev. Lett.*, vol. 106, p. 255303, Jun 2011.

- [99] O. Dutta, M. Gajda, P. Hauke, M. Lewenstein, D.-S. Lühmann, B. A. Malomed, T. Sowiński, and J. Zakrzewski, *Reports on Progress in Physics*, vol. 78, no. 6, p. 066001, 2015.
- [100] M. Iskin, *Phys. Rev. A*, vol. 83, p. 051606, May 2011.
- [101] T. Ohgoe, T. Suzuki, and N. Kawashima, *Phys. Rev. B*, vol. 86, p. 054520, Aug 2012.
- [102] P. Sengupta, L. P. Pryadko, F. Alet, M. Troyer, and G. Schmid, *Phys. Rev. Lett.*, vol. 94, p. 207202, May 2005.
- [103] F. Ferlino, S. Knoop, M. Berninger, W. Harm, J. P. D’Incao, H.-C. Nägerl, and R. Grimm, *Phys. Rev. Lett.*, vol. 102, p. 140401, Apr 2009.
- [104] B. Paredes, T. Keilmann, and J. I. Cirac, *Phys. Rev. A*, vol. 75, p. 053611, May 2007.
- [105] S. Will, T. Best, U. Schneider, L. Hackermuller, D.-S. Lühmann, and I. Bloch, *Nature*, vol. 465, p. 197, 2010.
- [106] A. Safavi-Naini, J. von Stecher, B. Capogrosso-Sansone, and S. T. Rittenhouse, *Phys. Rev. Lett.*, vol. 109, p. 135302, Sep 2012.
- [107] M. Łacki, S. Paganelli, V. Ahufinger, A. Sanpera, and J. Zakrzewski, *Phys. Rev. A*, vol. 83, p. 013605, Jan 2011.
- [108] D. van Oosten, P. van der Straten, and H. T. C. Stoof, *Phys. Rev. A*, vol. 63, p. 053601, Apr 2001.
- [109] K. Sheshadri, H. R. Krishnamurthy, R. Pandit, and T. V. Ramakrishnan, *EPL (Europhysics Letters)*, vol. 22, no. 4, p. 257, 1993.
- [110] M. Snoek and F. Zhou, *Phys. Rev. B*, vol. 69, p. 094410, Mar 2004.
- [111] L. de Forges de Parny, F. Hébert, V. G. Rousseau, and G. G. Batrouni, *Phys. Rev. B*, vol. 88, p. 104509, Sep 2013.
- [112] T.-L. Ho and S. K. Yip, *Phys. Rev. Lett.*, vol. 84, pp. 4031–4034, May 2000.
- [113] P. Sengupta, M. Rigol, G. G. Batrouni, P. J. H. Denteneer, and R. T. Scalettar, *Phys. Rev. Lett.*, vol. 95, p. 220402, Nov 2005.
- [114] F. Becca, M. Capello, M. Fabrizio, and S. Sorella, *Phys. Rev. Lett.*, vol. 99, p. 056402, Aug 2007.

- [115] M. Capello, F. Becca, M. Fabrizio, and S. Sorella, *Phys. Rev. B*, vol. 77, p. 144517, Apr 2008.
- [116] Y. Toga, H. Tsuchiura, M. Yamashita, K. Inaba, and H. Yokoyama, *Journal of the Physical Society of Japan*, vol. 81, no. 6, p. 063001, 2012.
- [117] L. de Forges de Parny, M. Traynard, F. Hébert, V. G. Rousseau, R. T. Scalettar, and G. G. Batrouni, *Phys. Rev. A*, vol. 82, p. 063602, Dec 2010.
- [118] L. de Forges de Parny, F. Hébert, V. G. Rousseau, R. T. Scalettar, and G. G. Batrouni, *Phys. Rev. B*, vol. 84, p. 064529, Aug 2011.
- [119] M. Rizzi, D. Rossini, G. De Chiara, S. Montangero, and R. Fazio, *Phys. Rev. Lett.*, vol. 95, p. 240404, Dec 2005.
- [120] S. Bergkvist, I. P. McCulloch, and A. Rosengren, *Phys. Rev. A*, vol. 74, p. 053419, Nov 2006.
- [121] B. K. Alavani, A. Das, and R. V. Pai, *Journal of Physics B: Atomic, Molecular and Optical Physics*, vol. 51, no. 14, p. 145302, 2018.
- [122] A. Wagner, C. Bruder, and E. Demler, *Phys. Rev. A*, vol. 84, p. 063636, Dec 2011.
- [123] D. W. S. Carvalho, A. Foerster, and M. A. Gusmão, *Phys. Rev. A*, vol. 91, p. 033608, Mar 2015.
- [124] Q. Zhu, Q.-f. Sun, and B. Wu, *Phys. Rev. A*, vol. 91, p. 023633, Feb 2015.
- [125] J. Stenger, S. Inouye, D. M. Stamper-Kurn, H.-J. Miesner, A. P. Chikkatur, and W. Ketterle, *Nature*, vol. 396, p. 345, 1998.
- [126] J.-M. Hou and M.-L. Ge, *Phys. Rev. A*, vol. 67, p. 063607, Jun 2003.
- [127] T. Kuwamoto, K. Araki, T. Eno, and T. Hirano, *Phys. Rev. A*, vol. 69, p. 063604, Jun 2004.
- [128] J. E. Lye, L. Fallani, M. Modugno, D. S. Wiersma, C. Fort, and M. Inguscio, *Phys. Rev. Lett.*, vol. 95, p. 070401, Aug 2005.
- [129] A. E. Niederle and H. Rieger, *Phys. Rev. A*, vol. 91, p. 043632, Apr 2015.
- [130] S. S. Natu, J. H. Pixley, and S. Das Sarma, *Phys. Rev. A*, vol. 91, p. 043620, Apr 2015.
- [131] U. Bissbort, R. Thomale, and W. Hofstetter, *Phys. Rev. A*, vol. 81, p. 063643, Jun 2010.

- [132] U. Bissbort and W. Hofstetter, *EPL (Europhysics Letters)*, vol. 86, no. 5, p. 50007, 2009.
- [133] A. E. Niederle and H. Rieger, *New Journal of Physics*, vol. 15, no. 7, p. 075029, 2013.
- [134] M. Makivić, N. Trivedi, and S. Ullah, *Phys. Rev. Lett.*, vol. 71, pp. 2307–2310, Oct 1993.
- [135] N. Prokof'ev and B. Svistunov, *Phys. Rev. Lett.*, vol. 92, p. 015703, Jan 2004.
- [136] J. Kisker and H. Rieger, *Phys. Rev. B*, vol. 55, pp. R11981–R11984, May 1997.
- [137] D. S. Rokhsar and B. G. Kotliar, *Phys. Rev. B*, vol. 44, pp. 10328–10332, Nov 1991.
- [138] i. m. c. G. Söyler, M. Kiselev, N. V. Prokof'ev, and B. V. Svistunov, *Phys. Rev. Lett.*, vol. 107, p. 185301, Oct 2011.
- [139] Barman, Apurba, Dutta, Sunayana, Khan, Ayan, and Basu, Saurabh, *Eur. Phys. J. B*, vol. 86, no. 7, p. 308, 2013.
- [140] D. Stauffer and A. Aharony, *Introduction To Percolation Theory*. Taylor & Francis, 1994. [Online]. Available: <https://books.google.co.in/books?id=v66pllej5QC>
- [141] J. Hoshen and R. Kopelman, *Phys. Rev. B*, vol. 14, pp. 3438–3445, Oct 1976.
- [142] K. V. Krutitsky, A. Pelster, and R. Graham, *New Journal of Physics*, vol. 8, no. 9, p. 187, 2006.
- [143] D. Morita, T. Kubo, Y. Tokura, and M. Yamashita, *Phys. Rev. A*, vol. 93, p. 063625, Jun 2016.
- [144] S. N. Nabi and S. Basu, *J. Phys. B: At. Mol. Opt. Phys.*, vol. 49, no. 12, p. 125301, 2016.
- [145] L. Wen, Q. Sun, H. Q. Wang, A. C. Ji, and W. M. Liu, *Phys. Rev. A*, vol. 86, p. 043602, Oct 2012.
- [146] L. Chen, H. Pu, and Y. Zhang, *Phys. Rev. A*, vol. 93, p. 013629, Jan 2016.
- [147] A. A. Svidzinsky and S. T. Chui, *Phys. Rev. A*, vol. 68, p. 043612, Oct 2003.

- [148] N. Uesugi and M. Wadati, *J. Phys. Soc. Jpn.*, vol. 72, no. 5, pp. 1041–1048, 2003.
- [149] K. Kis-Szabó, P. Szépfalussy, and G. Szirmai, *Phys. Rev. A*, vol. 72, p. 023617, Aug 2005.
- [150] G. Lang and E. Witkowska, *Phys. Rev. A*, vol. 90, p. 043609, Oct 2014.
- [151] M. Matuszewski, *Phys. Rev. A*, vol. 82, p. 053630, Nov 2010.
- [152] M. Matuszewski, T. J. Alexander, and Y. S. Kivshar, *Phys. Rev. A*, vol. 80, p. 023602, Aug 2009.
- [153] M. Koashi and M. Ueda, *Phys. Rev. Lett.*, vol. 84, pp. 1066–1069, Feb 2000.
- [154] D. Jaksch and P. Zoller, *New Journal of Physics*, vol. 5, no. 1, p. 56, 2003.
- [155] I. Coddington, P. C. Haljan, P. Engels, V. Schweikhard, S. Tung, and E. A. Cornell, *Phys. Rev. A*, vol. 70, p. 063607, Dec 2004.
- [156] T. A. Zaleski and T. P. Polak, *Phys. Rev. A*, vol. 83, p. 023607, Feb 2011.
- [157] A. R. Kolovsky, *Europhysics Letters*, vol. 93, no. 2, p. 20003, 2011.
- [158] A. Cichy, K. Cichy, and T. P. Polak, *Annals of Physics*, vol. 354, p. 89, 2015.
- [159] M. O. Oktel, M. Niță, and B. Tanatar, *Phys. Rev. B*, vol. 75, p. 045133, Jan 2007.
- [160] F. Zhou, M. Snoek, J. Wiemer, and I. Affleck, *Phys. Rev. B*, vol. 70, p. 184434, Nov 2004.
- [161] Y. Kawaguchi and M. Ueda, *Reports on Progress in Physics*, vol. 520, no. 5, p. 253, 2012.
- [162] D. R. Hofstadter, *Phys. Rev. B*, vol. 14, pp. 2239–2249, Sep 1976.
- [163] M. Niemeyer, J. K. Freericks, and H. Monien, *Phys. Rev. B*, vol. 60, pp. 2357–2362, Jul 1999.
- [164] E. Yukawa and M. Ueda, *Phys. Rev. A*, vol. 86, p. 063614, Dec 2012.
- [165] Z. Pu, J. Zhang, S. Yi, D. Wang, and W. Zhang, *Phys. Rev. A*, vol. 93, p. 053628, May 2016.

- [166] Y. M. Liu, Y. Z. He, and C. G. Bao, *Phys. Rev. A*, vol. 92, p. 043617, Oct 2015.
- [167] J. Lovegrove, M. O. Borgh, and J. Ruostekoski, *Phys. Rev. A*, vol. 93, p. 033633, Mar 2016.
- [168] E. M. Bookjans, A. Vinit, and C. Raman, *Phys. Rev. Lett.*, vol. 107, p. 195306, Nov 2011.
- [169] S. S. Natu, X. Li, and W. S. Cole, *Phys. Rev. A*, vol. 91, p. 023608, Feb 2015.
- [170] S. N. Nabi and S. Basu, *EPL (Europhysics Letters)*, vol. 116, no. 4, p. 46001, 2016.
- [171] C. D. L., P. R. M., P. A., V.-C. A., T. D., and S. I. B., *arXiv*, p. 1501.05984, 2015.
- [172] W. Zhang, Y. Yang, L. Guo, C. Ding, and T. C. Scott, *Phys. Rev. A*, vol. 91, p. 033613, Mar 2015.
- [173] C.-C. Chang, V. G. Rousseau, R. T. Scalettar, and G. G. Batrouni, *Phys. Rev. B*, vol. 92, p. 054506, Aug 2015.
- [174] S. Yi, L. You, and H. Pu, *Phys. Rev. Lett.*, vol. 93, p. 040403, Jul 2004.
- [175] Y. Kawaguchi, H. Saito, and M. Ueda, *Phys. Rev. Lett.*, vol. 97, p. 130404, Sep 2006.
- [176] B. Naylor, A. Reigue, E. Maréchal, O. Gorceix, B. Laburthe-Tolra, and L. Vernac, *Phys. Rev. A*, vol. 91, p. 011603, Jan 2015.
- [177] K. Aikawa, A. Frisch, M. Mark, S. Baier, R. Grimm, and F. Ferlaino, *Phys. Rev. Lett.*, vol. 112, p. 010404, Jan 2014.
- [178] M. Lu, N. Q. Burdick, and B. L. Lev, *Phys. Rev. Lett.*, vol. 108, p. 215301, May 2012.
- [179] J. W. Park, S. A. Will, and M. W. Zwierlein, *Phys. Rev. Lett.*, vol. 114, p. 205302, May 2015.
- [180] M. Yamashita and M. W. Jack, *Phys. Rev. A*, vol. 76, p. 023606, Aug 2007.
- [181] J. Kurdestany, R. Pai, and R. Pandit, *Ann. Phys. (Berlin)*, vol. 524, pp. 234–244, 2012.
- [182] M. Iskin and J. K. Freericks, *Phys. Rev. A*, vol. 79, p. 053634, May 2009.

- [183] A. Barman and S. Basu, *Journal of Physics B: At. Mol. Opt. Phys.*, vol. 47, no. 2, p. 025302, 2014.
- [184] S. Baier, M. J. Mark, D. Petter, K. Aikawa, L. Chomaz, Z. Cai, M. Baranov, P. Zoller, and F. Ferlaino, *Science*, vol. 352, no. 6282, pp. 201–205, 2016.
- [185] M. Lu, N. Q. Burdick, S. H. Youn, and B. L. Lev, *Phys. Rev. Lett.*, vol. 107, p. 190401, Oct 2011.
- [186] K. Aikawa, A. Frisch, M. Mark, S. Baier, A. Rietzler, R. Grimm, and F. Ferlaino, *Phys. Rev. Lett.*, vol. 108, p. 210401, May 2012.
- [187] T. Kimura, *Phys. Rev. A*, vol. 87, p. 043624, Apr 2013.
- [188] K. D. McAlpine, S. Paganelli, S. Ciuchi, A. Sanpera, and G. De Chiara, *Phys. Rev. B*, vol. 95, p. 235128, Jun 2017.
- [189] S. N. Nabi and S. Basu, *Annalen der Physik*, vol. 530, no. 1, p. 1700245, 2018.
- [190] B.-l. Chen, X.-b. Huang, S.-p. Kou, and Y. Zhang, *Phys. Rev. A*, vol. 78, p. 043603, Oct 2008.
- [191] J. Silva-Valencia and A. M. C. Souza, *Phys. Rev. A*, vol. 84, p. 065601, Dec 2011.
- [192] K. W. Mahmud and E. Tiesinga, *Phys. Rev. A*, vol. 88, p. 023602, Aug 2013.
- [193] A. F. Hincapie-F, R. Franco, and J. Silva-Valencia, *Phys. Rev. A*, vol. 94, p. 033623, Sep 2016.
- [194] A. Hincapie-F, R. Franco, and J. Silva-Valencia, *arXiv preprint arXiv:1707.08195*, 2017.
- [195] C. J. Pethick and H. Smith, *Bose-Einstein Condensation in Dilute Gases*. Cambridge, England: Cambridge University Press, 2002.
- [196] T. D. Kühner, S. R. White, and H. Monien, *Phys. Rev. B*, vol. 61, pp. 12 474–12 489, May 2000.
- [197] T. Sowiński, *Phys. Rev. A*, vol. 85, p. 065601, Jun 2012.
- [198] S. Ejima, F. Lange, H. Fehske, F. Gebhard, and K. z. Münster, *Phys. Rev. A*, vol. 88, p. 063625, Dec 2013.

- [199] S. N. Nabi and S. Basu, *EPL (Europhysics Letters)*, vol. 121, no. 4, p. 46002, 2018.
- [200] P. R. Johnson, E. Tiesinga, J. V. Porto, and C. J. Williams, *New Journal of Physics*, vol. 11, no. 9, p. 093022, 2009.
- [201] E. Tiesinga and P. R. Johnson, *Phys. Rev. A*, vol. 83, p. 063609, Jun 2011.





Curriculum vitae

Sk Noor Nabi was born on 13th February, 1991 in Uchahar, India. He did his B.Sc. with Physics Honours in 2011 from Midnapore College under Vidyasagar University and M.Sc. in physics from Indian Institute of Technology Guwahati in 2013. He had enrolled into the Ph.D programme at Indian Institute of Technology Guwahati in 2013. He had received gold medal award in 2012 for securing 1st position in B.Sc Physics Honours from Vidyasagar University. He had also received best poster award in 2015 in the 60th Department of Atomic Energy-Solid State Physics Symposium (DAE-SSPS). He had qualified CSIR-UGC NET in 2013 and Graduate Aptitude Test in Engineering (GATE) in 2014. He has earned the Senior Research Fellowship in 2015 by Indian Institute of Technology Guwahati.





B.O.O.O.O.1

